

Studies on Atmospheric Pressure Chemical Ionization and
Tandem Mass Spectrometry of Sulfur-containing Compounds from Petroleum

by

Lisandra Cubero Herrera

Submitted in partial fulfillment of the requirements
for the degree of Doctor of Philosophy

at

Dalhousie University
Halifax, Nova Scotia
August 2007

© Copyright by Lisandra Cubero Herrera, 2007



Library and
Archives Canada

Bibliothèque et
Archives Canada

Published Heritage
Branch

Direction du
Patrimoine de l'édition

395 Wellington Street
Ottawa ON K1A 0N4
Canada

395, rue Wellington
Ottawa ON K1A 0N4
Canada

Your file Votre référence

ISBN: 978-0-494-31482-1

Our file Notre référence

ISBN: 978-0-494-31482-1

NOTICE:

The author has granted a non-exclusive license allowing Library and Archives Canada to reproduce, publish, archive, preserve, conserve, communicate to the public by telecommunication or on the Internet, loan, distribute and sell theses worldwide, for commercial or non-commercial purposes, in microform, paper, electronic and/or any other formats.

The author retains copyright ownership and moral rights in this thesis. Neither the thesis nor substantial extracts from it may be printed or otherwise reproduced without the author's permission.

AVIS:

L'auteur a accordé une licence non exclusive permettant à la Bibliothèque et Archives Canada de reproduire, publier, archiver, sauvegarder, conserver, transmettre au public par télécommunication ou par l'Internet, prêter, distribuer et vendre des thèses partout dans le monde, à des fins commerciales ou autres, sur support microforme, papier, électronique et/ou autres formats.

L'auteur conserve la propriété du droit d'auteur et des droits moraux qui protègent cette thèse. Ni la thèse ni des extraits substantiels de celle-ci ne doivent être imprimés ou autrement reproduits sans son autorisation.

In compliance with the Canadian Privacy Act some supporting forms may have been removed from this thesis.

Conformément à la loi canadienne sur la protection de la vie privée, quelques formulaires secondaires ont été enlevés de cette thèse.

While these forms may be included in the document page count, their removal does not represent any loss of content from the thesis.

Bien que ces formulaires aient inclus dans la pagination, il n'y aura aucun contenu manquant.


Canada

DALHOUSIE UNIVERSITY

To comply with the Canadian Privacy Act the National Library of Canada has requested that the following pages be removed from this copy of the thesis:

Preliminary Pages

Examiners Signature Page (pii)

Dalhousie Library Copyright Agreement (piii)

Appendices

Copyright Releases (if applicable)

A mis padres

Table of Contents

List of Tables	viii
List of Figures	xiv
List of Schemes	xxi
Abstract	xxii
List of Abbreviations and Symbols Used	xxiii
Acknowledgments	xxv
 Chapter 1. Introduction	 1
1.1. Introduction	1
1.2. Sulfur-containing Compounds in Petroleum	2
1.2.1. Catalyst-based Hydrodesulfurization (HDS) Process	5
1.2.2. Non-HDS Based Technologies	9
1.3. Chromatography	10
1.3.1. Gas Chromatography	11
1.3.2. Liquid Chromatography	12
1.3.3. Supercritical Fluid Chromatography	14
1.4. Mass Spectrometry	16
1.4.1. Ion Sources	17
1.4.1.1. Electron Ionization	17
1.4.1.2. Chemical Ionization	18
1.4.1.3. Atmospheric Pressure Chemical Ionization	20
1.4.1.4. Electrospray Ionization	22
1.4.2. Mass Analyzers	24
1.4.2.1. The Quadrupole Mass Filter	24
1.4.2.2. The Quadrupole Ion Trap	26
1.4.3. Tandem Mass Spectrometry (MS/MS)	29
1.4.3.1. MS/MS in the Quadrupole Mass Filter	29
1.4.3.2. MS/MS in the Quadrupole Ion Trap	31
1.5. Research Objectives	33

Chapter 2. Selective Adsorbents for Sulfur Compounds.....	35
2.1. Introduction	35
2.1.1. Separation through Complexation with Metal Ions	36
2.1.2. Support Materials	38
2.1.2.1. Silica Gel.....	38
2.1.2.2. Alumina	39
2.1.2.3. Zeolites.....	40
2.2. Experimental	43
2.3. Results and Discussion.....	43
2.3.1. Na/zeolite Y, Cu(II)/zeolite Y and Reduced Cu(II)/zeolite Y Adsorbents	44
2.3.2. Cu(II)/SiO ₂ Adsorbents.....	46
2.3.3. PdCl ₂ /Al ₂ O ₃ Adsorbent.....	47
2.3.4. PdCl ₂ /SiO ₂ Adsorbent.....	48
 Chapter 3. MS and MS/MS of Selected Sulfur Compounds	 55
3.1. Introduction	55
3.2. Experimental	55
3.2.1. Experimental—ESI(+)—MS	58
3.2.2. Experimental—APCI(+)—MS.....	58
3.2.3. Experimental—APCI(+)—MS/MS	61
3.2.4. Experimental—Gaussian Calculations	63
3.3. Results and Discussion.....	64
3.3.1. ESI(+)—MS of DBT and TA	64
3.3.2. APCI <i>versus</i> ESI.....	68
3.3.2.1. APCI(+)—MS of DBT, PY, FLU and CAR.....	70
3.3.2.2. Limits of Detection.....	77
3.3.2.3. Linear Dynamic Ranges.....	79
3.3.2.4. Studies of Mixtures of PACs.....	84
3.3.2.5. Measurement of the Ionization Current	89
3.3.2.6. Total Ion Current Studies	96

3.3.2.7. Ionization Mechanisms in APCI(+)	98
3.3.2.8. Calculations using Gaussian	122
3.3.3. MS/MS of Selected Sulfur Compounds	141
3.3.3.1. APCI(+)-MS/MS of Model Compounds	155
3.3.3.2. SRM Experiments	171
Chapter 4. Conclusion	197
4.1. Conclusions	197
4.2. Future Work	201
Appendix A. Calculation of Flow Rates	204
Appendix B. Calculation of Proton Affinities	205
Appendix C. Summary of Thermodynamic Data	208
Appendix D. Examples of Potential Energy Curves	210
Appendix E. Derivation of Equations (3.8), (3.9) and (3.10)	212
Reference List	218

List of Tables

Table 2.1. PdCl ₂ /SiO ₂ adsorbents with different PdCl ₂ loadings.....	48
Table 2.2. Recovery (%) of DBT and PHEN	54
Table 3.1. Polycyclic aromatic compounds (PACs) used as standards.....	56
Table 3.2. Experimental conditions for the determination of LODs and calibration curves in MeCN and in MeOH (B: bath gas, S: sheath gas, N: nebulizer gas)	60
Table 3.3. Experimental conditions for studies on mixtures of PACs in MeCN and in MeOH (B: bath gas, S: sheath gas, N: nebulizer gas)	61
Table 3.4. Limits of detection (mol L ⁻¹) in MeCN at different solvent flow rates	78
Table 3.5. Limits of detection (mol L ⁻¹) in MeOH at different solvent flow rates	78
Table 3.6. Linear range of response (mol L ⁻¹) in MeCN at different solvent flow rates.....	79
Table 3.7. Linear range of response (mol L ⁻¹) in MeOH at different solvent flow rates.....	80
Table 3.8. Mixture ion currents for DBT as % of ion currents for DBT alone in MeCN.....	87
Table 3.9. Mixture ion currents for DBT as % of ion currents for DBT alone in MeOH.....	87
Table 3.10. Species and total ion counts (TIC) for PACs in MeCN (relative standard deviation in % shown in parentheses, n = 5).....	97

Table 3.11. Species and total ion counts (TIC) for PACs in MeOH (relative standard deviation in % shown in parentheses, n = 5).....	97
Table 3.12. Species and total ion counts (TIC) for PACs in toluene (relative standard deviation in % shown in parentheses, n = 5).....	97
Table 3.13. Concentration of solvent, water and analyte relative to N ₂ for MeCN, MeOH and toluene at different solvent rates ([N ₂]:[Solvent]:[Water]:[Analyte]).....	105
Table 3.14. Thermodynamic data for analytes, solvents and nitrogen gas.....	106
Table 3.15. Theoretical ΔH values (in eV) for reactions (6) and (7).....	108
Table 3.16. Experimental ΔH values (in eV) for reaction (11)	111
Table 3.17. Experimental ΔH values (in eV) for reaction (12)	112
Table 3.18. Experimental ΔH values (in eV) for reaction (13)	112
Table 3.19. Experimental ΔH values (in eV) for reaction (14)	114
Table 3.20. Experimental ΔH values (in eV) for reaction (16)	115
Table 3.21. Experimental ΔH values (in eV) for reaction (17)	116
Table 3.22. Ionization data—Solvent comparison for a given analyte.....	117
Table 3.23. Ionization data—Analyte comparison for a given solvent.....	118
Table 3.24. Thermochemical model—Analyte and solvent comparison.....	118

Table 3.25. Thermodynamic quantities for the clustering reactions $(S)_{n-1}H^+ + S \rightarrow (S)_nH^+$ where S is either MeCN or MeOH. (Note: ΔE , ΔH° and ΔG° in kJ mol^{-1} , ΔS° in $\text{J mol}^{-1} \text{K}^{-1}$, E is the electronic energy in hartree, $\Delta E_{n-1,n}$ is the stabilization energy calculated as $\Delta E_{n-1,n} = E((S)_nH^+) - E((S)_{n-1}H^+) - E(S)$).....	131
Table 3.26. Electronic energy (E_e) for AH^+ species and (toluene) H^+	132
Table 3.27. Thermodynamic data for the $AH^+ + S \rightarrow (S)AH^+$ reaction where S: MeCN or MeOH and A: DBT, PY, CAR or FLU (ΔE° , ΔH° and ΔG° in kJ mol^{-1})	133
Table 3.28. Thermodynamic quantities for the $SH^+ + nS \rightarrow (S)_nSH^+$ ($n = 1-2$) clustering reaction where S: MeCN or MeOH (ΔE° , ΔH° and ΔG° in kJ mol^{-1})	133
Table 3.29. Thermodynamic data for the $A + (S)_nSH^+ \rightarrow AH^+ + (n+1)S$ ($n = 0-2$) proton transfer reaction in MeOH (ΔH° and ΔG° in eV)	137
Table 3.30. Thermodynamic data for the $A + (S)_nSH^+ \rightarrow (S)AH^+ + nS$ ($n = 0-2$) proton transfer reaction in MeOH (ΔH° and ΔG° in eV)	138
Table 3.31. Thermodynamic data for the $A + (S)_nS^{+\bullet} \rightarrow A^{+\bullet} + (n+1)S$ ($n = 0-2$) charge exchange reaction in MeOH (ΔH° and ΔG° in eV)	138
Table 3.32. Thermodynamic data for the $A + (S)_nS^{+\bullet} \rightarrow (S)A^{+\bullet} + nS$ ($n = 0-2$) charge exchange reaction in MeOH (ΔH° and ΔG° in eV)	139
Table 3.33. Thermodynamic data for the $A + (S)_nSH^+ \rightarrow AH^+ + (n+1)S$ ($n = 0-2$) proton transfer reaction in MeCN (ΔH° and ΔG° in eV)	139
Table 3.34. Thermodynamic data for the $A + (S)_nSH^+ \rightarrow (S)AH^+ + nS$ ($n = 0-2$) proton transfer reaction in MeCN (ΔH° and ΔG° in eV)	140
Table 3.35. Thermodynamic data for the $A + (S)_nS^{+\bullet} \rightarrow A^{+\bullet} + (n+1)S$ ($n = 0-2$) charge exchange reaction in MeCN (ΔH° and ΔG° in eV)	140
Table 3.36. Thermodynamic data for the $A + (S)_nS^{+\bullet} \rightarrow (S)A^{+\bullet} + nS$ ($n = 0-2$) charge exchange reaction in MeCN (ΔH° and ΔG° in eV)	141

Table 3.37. Fractional abundances (T) within precursor-ion mass spectrum.....	147
Table 3.38. Fractional abundances (T) among precursor-ion mass spectra.....	149
Table 3.39. Fractional abundances (T) within neutral loss mass spectrum.....	150
Table 3.40. Fractional abundances (T) among neutral loss mass spectra.....	151
Table 3.41. Fractional abundances (T) of precursor ions.....	152
Table 3.42. Fractional abundances (T) in product-ion spectra	154
Table 3.43. Relative peak heights within and among product-ion mass spectra.....	155
Table 3.44. Theoretical (T) and experimental (E) abundance ratios (%) within and among neutral loss spectra for TA (10 eV and 35 V cone).....	173
Table 3.45. Theoretical (T) and experimental (E) abundance ratios (%) within and among product-ion spectra for TA (5 eV and 35 V cone)	173
Table 3.46. Theoretical (T) and experimental (E) abundance ratios (%) within and among precursor-ion spectra for TA (10 eV and 35 V cone)	174
Table 3.47. Theoretical (T) and experimental (E) abundance ratios (%) within and among product-ion spectra for MA (10 eV and 25 V cone).....	174
Table 3.48. Theoretical (T) and experimental (E) abundance ratios (%) within and among neutral loss spectra for MA (5 eV and 15 V cone)	175
Table 3.49. Theoretical (T) and experimental (E) abundance ratios (%) within and among precursor-ion spectra for MA (10 eV and 20 V cone)	175

Table 3.50. Experimental (E) abundance ratios (%) within and among product-ion spectra for MA at 10 eV and 20 eV collision energy (25 V cone)	176
Table 3.51. Experimental (E) abundance ratios (%) within and among precursor-ion spectra for TA at 10 eV and 20 eV collision energy (35 V cone)	176
Table 3.52. Fractional abundances (T) of all precursor ions	185
Table 3.53. Precursors of 184 (Q3 set to m/z 184, Q1 scanned, P: product ion)	186
Table 3.54. Fractional abundance within precursor-ion of m/z 184 spectrum at low and high resolution	187
Table 3.55. Precursors of 185 (Q3 set to m/z 185, Q1 scanned, P: product ion)	188
Table 3.56. Fractional abundance within precursor-ion of m/z 185 spectrum at low and high resolution	189
Table 3.57. Constant neutral loss of 32 (Q1 and Q3 are both scanned with a constant difference of m/z 32 between them, P: product ion).....	189
Table 3.58. Fractional abundance within constant neutral loss of 32 u spectrum at low and high resolution	190
Table 3.59. Constant neutral loss of 33 (Q1 and Q3 are both scanned with a constant difference of m/z 33 between them, P: product ion).....	191
Table 3.60. Fractional abundance within constant neutral loss of 33 u spectrum at low and high resolution	192
Table 3.61. Theoretical (T) and experimental (E) abundance ratios (%) within and among product-ion spectra for TA (LCQ)	193
Table 3.62. Theoretical (T) and experimental (E) abundance ratios (%) within and among product-ion spectra for MA (LCQ).....	193

Table A1. Density and molecular weight of MeCN, MeOH, toluene and water.....	204
Table B1. Proton affinities of model compounds at the B3LYP and the PBE1PBE levels of theory and different basis sets	207
Table C1. Summary of thermodynamic properties for the species of N ₂ , MeCN, MeOH and toluene at the B3LYP/6–31G(<i>d</i>) level of theory.....	208
Table C2. Summary of thermodynamic properties for the species of DBT, PY, CAR and FLU at the B3LYP/6–31G(<i>d</i>) level of theory.....	209

List of Figures

Figure 1.1. General classes and structures of representative sulfur compounds (for each class) found in petroleum	4
Figure 1.2. Relative reactivity of sulfur compounds in HDS	6
Figure 1.3. Stationary phases in gas chromatography.....	12
Figure 1.4. Diagram of an EI ion source (Adapted from a drawing by Dr. Louis Ramaley).....	17
Figure 1.5. Diagram of a Micromass Quattro APCI source. Drawing by Dr. Louis Ramaley. BG: bath gas, CE: counter electrode, CN: corona needle, NG: nebulizer gas, S: solvent or sample, SC: sampling cone, SG: sheath gas, SH: source heater, PH: probe heater, MP: mechanical rotary oil pump and TP: turbomolecular pump.....	21
Figure 1.6. Quadrupole mass filter: side (a) and end (b) views (Adapted from a drawing by Dr. Louis Ramaley).....	24
Figure 1.7. Cross-sectional view of the quadrupole ion trap	26
Figure 1.8. Triple quadrupole mass spectrometer (QqQ). (Adapted from a drawing by Dr. Louis Ramaley)	29
Figure 1.9. MS/MS scan modes in a triple quadrupole mass spectrometer	30
Figure 2.1. The framework of zeolites, (M^+ is a monovalent charge balancing cation)	40
Figure 2.2. Representation of the zeolite Y structure and occupancy sites for charge-balancing cations	42
Figure 2.3. UV spectra of DBT and PHEN (2 mg L ⁻¹ each in hexanes).....	44

Figure 2.4. Apparatus used for the reduction and regeneration of adsorbents with hydrogen	45
Figure 2.5. Calibration curves for DBT in hexanes (▲252 nm and ■ 232 nm)	50
Figure 2.6. Calibration curves for PHEN in hexanes (▲252 nm and ■ 232 nm)	50
Figure 2.7. Calibration curves for DBT in MeCN (▲252 nm and ■ 232 nm)	51
Figure 2.8. Calibration curves for PHEN in MeCN (▲252 nm and ■ 232 nm)	51
Figure 2.9. Elution with hexanes (F1, 10 mL), 0.02 mg of DBT and PHEN (each)	52
Figure 2.10. Elution with MeCN (F2, 1 mL), 0.02 mg of DBT and PHEN (each)	52
Figure 2.11. Elution with hexanes (F1, 10 mL), 0.1 mg of DBT and PHEN (each)	53
Figure 2.12. Elution with MeCN (F2, 10 mL), 0.1 mg of DBT and PHEN (each)	53
Figure 3.1. ESI(+) spectrum of DBT and TA in MeCN (1 g L ⁻¹ , each). Mass range: 150–300 <i>m/z</i> , scan time: 0.6 s, 45 V cone).....	64
Figure 3.2. ESI(+) spectra of DBT and TA in the presence of Ag ⁺ at 20 V (A), 30 V (B) and 40 V (C) cone voltages. Electrospray needle voltage: 1.5 kV, solvent: MeCN, 5 µL of solution of silver triflate (0.3 g L ⁻¹) were added to 5 µL of solution of DBT and TA (1 g L ⁻¹ , each). Mass range: 150–550 <i>m/z</i> , scan time: 1.5 s.....	67
Figure 3.3. APCI(+) response for DBT (○) and PY (■) in a DBT/PY mixture. DBT (constant: 0.02 g L ⁻¹) and PY (variable, range: 0.0–0.3 g L ⁻¹)	69

Figure 3.4. APCI(+) mass spectra of DBT at 40 V (A) and 50 V (B) cone.....	70
Figure 3.5. APCI(+) mass spectra of PY (impure) at 40 V cone in MeCN (A) and MeOH (B)	71
Figure 3.6. APCI(+) mass spectra of FLU at 5 V cone showing analyte and solvent clusters in MeCN (A) and MeOH (B)	72
Figure 3.7. APCI(+) mass spectra of FLU at 30 V (A), 40 V (B) and 50 V (C) cone	74
Figure 3.8. APCI(+) mass spectra of CAR at 5 V (A), 40 V (B) and 50 V (C) cone	75
Figure 3.9. Ion counts for M^{+} , MH^{+} and $[M^{+} + MH^{+}]$ of CAR at different gas flow rates (sLph) and cone voltages. Conditions: solvent (MeCN, 0.5 mL min ⁻¹), [CAR] = 1.0e-6 mol L ⁻¹ , bath gas (B), sheath gas (S), nebulizer gas (N)	76
Figure 3.10. Linear region (low concentration range) of calibration curves in MeCN for DBT (■), FLU (□), PY (○) and CAR (●) (solvent rate: 0.02 mL min ⁻¹).....	80
Figure 3.11. Linear region (low concentration range) of calibration curves in MeCN for DBT (■), FLU (□), PY (○) and CAR (●) (solvent rate: 0.5 mL min ⁻¹).....	81
Figure 3.12. Non-linear region (high concentration range) of calibration curves in MeCN for DBT (■), FLU (□), PY (○) and CAR (●) (solvent rate: 0.5 mL min ⁻¹).....	81
Figure 3.13. Calibration curves for M^{+} of DBT in MeOH (A) and in MeCN (B) at different solvent rates: 0.02 mL min ⁻¹ (○), 0.1 mL min ⁻¹ (■) and 0.5 mL min ⁻¹ (□)	83
Figure 3.14. Calibration curves for DBT and CAR in MeOH (0.5 mL min ⁻¹) at different probe temperatures: 200 °C (○), 350 °C (■) and 450 °C (□).....	84

Figure 3.15. APCI(+) mass spectra of DBT alone (C), PY (impure) alone (B) and a 1:1 mixture of DBT:PY (A) in MeCN, [DBT] = [PY] = $5.0\text{e-}4 \text{ mol L}^{-1}$	85
Figure 3.16. Effect of DBT on PY in MeCN: Ion counts for $\text{M}^{+\bullet}$ of PY alone (●) and in DBT/PY mixture (○)	88
Figure 3.17. Effect of DBT on CAR in MeCN: ion counts for MH^{+} of CAR alone (●) and in DBT/CAR mixture (○)	89
Figure 3.18. Expansion of the corona discharge region.....	90
Figure 3.19. Ionization current as a function of the corona needle voltage in N_2 alone at different gas flow rates.....	91
Figure 3.20. Ionization current as a function of the corona needle voltage for N_2 , MeCN, MeOH and toluene at 0.02 mL min^{-1} (A) and 0.5 mL min^{-1} (B). Conditions: B (200 sLph), S (200 sLph) N (45 sLph)	92
Figure 3.21. Ionization current as a function of the corona needle voltage for MeOH alone and MeOH with DBT (linear region, [DBT] = $6.6\text{e-}6 \text{ mol L}^{-1}$) at different solvent flow rates: 0.02 mL min^{-1} (A) and 0.5 mL min^{-1} (B)	93
Figure 3.22. Ionization current as a function of the corona needle voltage for MeOH alone and MeOH with DBT (non-linear region, [DBT] = $2.0\text{e-}2 \text{ mol L}^{-1}$) at different solvent flow rates: 0.02 mL min^{-1} (A) and 0.5 mL min^{-1} (B)	93
Figure 3.23. Ionization current as a function of the corona needle voltage for MeCN alone and MeCN with DBT (linear region, [DBT] = $6.6\text{e-}6 \text{ mol L}^{-1}$) at different solvent flow rates: 0.02 mL min^{-1} (A) and 0.5 mL min^{-1} (B)	94
Figure 3.24. Ionization current as a function of the corona needle voltage for MeCN alone and MeCN with DBT (non-linear region, [DBT] = $2.0\text{e-}2 \text{ mol L}^{-1}$) at different solvent flow rates: 0.02 mL min^{-1} (A) and 0.5 mL min^{-1} (B)	94

Figure 3.25. Ionization current as a function of the corona needle voltage for toluene alone and toluene with DBT (linear region, [DBT] = $6.6\text{e-}6 \text{ mol L}^{-1}$) at different solvent flow rates: 0.02 mL min^{-1} (A) and 0.5 mL min^{-1} (B)	95
Figure 3.26. Ionization current as a function of the corona needle voltage for toluene alone and toluene with DBT (non-linear region, [DBT] = $2.0\text{e-}2 \text{ mol L}^{-1}$) at different solvent flow rates: 0.02 mL min^{-1} (A) and 0.5 mL min^{-1} (B).....	95
Figure 3.27. Ionization mechanisms in APCI(+) with nitrogen as source gas (M: molecule, A: analyte, S: solvent). (Not drawn to scale)	99
Figure 3.28. Background spectrum of toluene at 40 V cone. Conditions: solvent flow rate (0.5 mL min^{-1}), B (200 sLph), S (200 sLph) and N (45 sLph).....	101
Figure 3.29. Background spectra of MeCN at 5 V (A), 30 V (B) and 40 V (C) cone. Conditions: solvent flow rate (0.5 mL min^{-1}), B (400 sLph), S (200 sLph) and N (45 sLph)	102
Figure 3.30. Background spectra of MeOH at 5 V (A), 30 V (B) and 40 V (C) cone. Conditions: solvent flow rate (0.5 mL min^{-1}), B (400 sLph), S (200 sLph) and N (45 sLph)	103
Figure 3.31. Efficiency of proton transfer vs. charge exchange for DBT, PY, FLU and CAR as a function of solvent.....	122
Figure 3.32. Optimized geometries of toluene, (toluene) H^+ and (toluene) $^{+*}$. Selected bond lengths in Å.....	123
Figure 3.33. Optimized geometries of (MeCN) $_n\text{H}^+$ and (MeCN) $_n^{+*}$ (n=1–3) clusters. Selected bond lengths are in Å and angles in degree.....	124
Figure 3.34. Optimized geometries of (MeOH) $_n\text{H}^+$ and (MeOH) $_n^{+*}$ (n=1–3) clusters. Selected bond lengths in Å and angles in degree.....	125
Figure 3.35. Optimized geometries of DBT species. Selected bond lengths in Å.....	126

Figure 3.36. Optimized geometries of PY species. Selected bond lengths in Å.....	127
Figure 3.37. Optimized geometries of CAR species. Selected bond lengths in Å.....	128
Figure 3.38. Optimized geometries of FLU species. Selected bond lengths in Å.....	129
Figure 3.39. MS/MS and full-scan spectra of BT (IC: ion counts). Collision energy (eV) and cone voltage (V) for each experiment: 10, 55 (A); 10, 40 (B); 13, 43 (C); 11, 43 (D); 10, 50 (E); 10, 60 (F); 12, 43 (G); 10, 55 (H) and 50 V (I).....	158
Figure 3.40. MS/MS and full-scan spectra of DBT (IC: ion counts). Collision energy (eV) and cone voltage (V) for each experiment: 15, 70 (A); 10, 40 (B); 20, 50 (C); 15, 55 (D); 10, 50 (E); 10, 50 (F); 10, 60 (G); 15, 55 (H); 20, 50 (I) and 60 V (J).....	159
Figure 3.41. MS/MS and full-scan spectra of MDBT (IC: ion counts). Collision energy (eV) and cone voltage (V) for each experiment: 10, 60 (A); 15, 50 (B); 10, 60 (C); 10, 60 (D); 10, 60 (E), 10, 35 (F); 15, 45 (G); 15, 55 (H); 15, 50 (I); 15, 50 (J); 10, 60 (K) and 60 V (L).....	160
Figure 3.42. MS/MS and full-scan spectra of DMDBT. Collision energy (eV) and cone voltage (V): 20, 55 (A); 15, 60 (B); 20, 50 (C); 20, 50 (D); 10, 55 (E); 10, 55 (F); 15, 55 (G); 15, 55 (H); 15, 55 (I); 10, 60 (J); 20, 50 (K); 20, 50 (L); 20, 50 (M); 10, 60 (N); 15, 40 (O); 10, 55 (P); 10, 55 (Q) and 60 V (R)	161
Figure 3.43. MS/MS and full-scan spectra of TA. Collision energy (eV) and cone voltage (V) for each experiment: 10, 60 (A); 20, 35 (B); 15, 55 (C) and 40 V (D)	171
Figure 3.44. MS/MS and full-scan spectra of MA. Collision energy (eV) and cone voltage (V) for each experiment: 5, 25 (A); 5, 15 (B); 5, 20 (C) and 20 V (D)	172
Figure 3.45. Collision process between an ion (m_p) and a neutral target (m_t)	177

Figure 3.46. Product-ion mass spectra of m/z 169 (A and B) and precursor-ion mass spectra of m/z 95 (C and D) at different collision energies: 5 eV (A), 15 eV (B), 5 eV (C) and 20 eV (D) (MA, 15 V cone) 182

Figure 3.47. Product-ion mass spectra of TA obtained with the LCQ: products of m/z 216 (A), products of m/z 217 (B), products of m/z 218 (C) and products of m/z 219 (D) 194

Figure 3.48. Product-ion mass spectra of MA obtained with the LCQ: products of m/z 168 (A), products of m/z 169 (B), products of m/z 170 (C) and products of m/z 171 (D) 195

Figure D1. Coordinates used to obtain potential energy curves for $[(\text{MeCN})_2\text{H}]^+$ 210

Figure D2. Potential energy surfaces for $[(\text{MeCN})_2\text{H}]^+$ as a function of the N–H distance (R_2) and parametric in the N–N distance (R_1) 210

Figure D3. Potential energy curves for two $[(\text{MeOH})_2\text{H}]^+$ isomers 211

List of Schemes

Scheme 3.1. Fragmentation pathways for BT	156
Scheme 3.2. Fragmentation pathways for DBT	156
Scheme 3.3. Fragmentation pathways for MDBT	157
Scheme 3.4. Fragmentation pathways for DMDBT	157
Scheme 3.5. Possible fragmentation mechanisms for BT.....	163
Scheme 3.6. Possible fragmentation reaction for DBT involving the loss of sulfur	164
Scheme 3.7. Possible fragmentation paths for DBT leading to the ions at m/z 183, 140 and 139.....	165
Scheme 3.8. Possible fragmentation pathway leading to m/z 165 for MDBT	166
Scheme 3.9. Possible fragmentation pathway leading to m/z 153 for MDBT	167
Scheme 3.10. Cleavage of the phenylic bond in DMDBT to form ion at m/z 197.....	168
Scheme 3.11. Possible fragmentation pathways for the formation of the ion at m/z 178 for DMDBT	170

Abstract

The presence of polycyclic aromatic sulfur heterocycles (PASHs) in transportation fuels is being increasingly regulated because of their impact on the environment and refining processes. Methods for the analysis of PASHs are constantly being improved to meet the new environmental regulations requiring a reduction in the amount of sulfur. However, the successful analysis of PASHs is hindered by complex matrices, many similar compounds and low level concentrations.

This thesis is an investigation of atmospheric pressure ionization (API) methods and tandem mass spectrometry (MS/MS) for improving the detection of PASHs in the presence of similar compounds that may cause interference. Several adsorbents based on reduced metals supported on different materials were also examined for the enrichment of PASHs in selected fractions to aid their future identification.

For API methods conventional wisdom holds that nonlinear response and interferences are more serious with electrospray ionization than with atmospheric pressure chemical ionization (APCI). However, during the APCI analysis of PASHs from petroleum we observed serious, unexpected nonlinearity and matrix effects. To understand better the parameters that influence APCI, especially ionization mechanisms, representative polycyclic aromatic compounds (PACs) from petroleum —dibenzothiophene, pyrene, carbazole, and fluorenone— were observed under various conditions. Linear ranges and limits of detection were determined in acetonitrile and methanol using flow injection. Model compounds displayed linear regions for calibration curves at low concentrations with negative deviations from linearity at high concentrations. In the linear response region, the presence of a second analyte did not affect the response of dibenzothiophene, whereas in the nonlinear region interactions between PACs were observed. The relative ionization efficiency of the model analytes differed markedly among solvents and followed the order: toluene > acetonitrile > methanol. These results were explained considering solvation effects and limiting reagent ion concentrations.

MS/MS in a triple quadrupole instrument was used to study fragmentation processes of model PASHs. Neutral losses of S, HS[•] and CS were found to occur from these compounds and the precise losses were structure dependent. Selected reaction monitoring experiments were also performed to confirm fragmentation patterns through the use of natural abundance ratios in MS/MS spectra.

List of Abbreviations and Symbols Used

ac	Alternating current
APCI	Atmospheric pressure chemical ionization
b. p.	Boiling point
BT	Benzo[<i>b</i>]thiophene
CAR	Carbazole
CI	Chemical ionization
CID	Collision induced dissociation
DBT	Dibenzo[<i>b,d</i>]thiophene
dc	Direct current
DMDBT	4,6-Dimethyldibenzo[<i>b,d</i>]thiophene
e-number	Scientific notation indicating 10 ^{-number}
EI	Electron ionization
ESI	Electrospray ionization
eV	Electron volt
FA	Fractional abundance
FCC	Fluid catalytic cracking
FLU	Fluoren-9-one
FPD	Flame photometric detector
GC	Gas chromatography
GC/MS	Gas chromatography/mass spectrometry
HDS	Hydrodesulfurization
HPLC	High-performance liquid chromatography
IC	Ion counts
LC	Liquid chromatography
LC/MS	Liquid chromatography/mass spectrometry
M ⁺	Molecular ion
MA	2-Mercaptoacetanilide
MALDI	Matrix assisted laser desorption ionization
MDBT	4-Methyldibenzo[<i>b,d</i>]thiophene

MH ⁺	Protonated molecule
MS	Mass spectrometry
ms	Millisecond
MS/MS	Tandem mass spectrometry
M. W.	Molecular weight
<i>m/z</i>	Mass-to-charge ratio
NCI	Negative-ion chemical ionization
NP-LC	Normal-phase liquid chromatography
PAC	Polycyclic aromatic compound
PAH	Polycyclic aromatic hydrocarbon
PASH	Polycyclic aromatic sulfur heterocycle
PCI	Positive-ion chemical ionization
PY	Pyrene
ppmw	Parts per million by weight
QIT	Quadrupole ion trap
QMF	Quadrupole mass filter
QqQ	Triple quadrupole mass spectrometer
RF	Radio frequency
RP-LC	Reversed-phase liquid chromatography
SCD	Sulfur chemiluminiscence detector
SFC	Supercritical fluid chromatography
SIM	Selected ion monitoring
sLph	Standard liters per hour
SRM	Selected reaction monitoring
T	Total fractional abundance
TA	Thianthrene
TIC	Total ion counts
u	Unified atomic mass unit
UV	Ultraviolet
V	Volt or voltage

Acknowledgements

I am indebted to those people who contributed to the research and the making of this thesis. In the first place I would like to thank Dr. Louis Ramaley for providing me with direction and for being a constant source of knowledge and support throughout these years. I consider myself very fortunate for having had him as my supervisor. I am also obliged to Dr. J. Stuart Grossert whose help and advice have been of great value in this study.

I acknowledge my co-supervisor, Dr. Robert D. Guy, and my external examiner, Dr. Rebecca Jockusch, for reading the whole thesis so thoroughly. Their comments will add value both to the thesis and the manuscript that we are currently writing. I am also grateful to Dr. Robert L. White and Dr. Alan A. Doucette for agreeing to be on my examining committee on such a short notice and for their helpful remarks on this work.

I would like to express my gratitude to Mike Boutilier and Richard Conrad for their assistance with the nitrogen tanks that I regularly needed to carry out my research work. I also appreciate the help provided during these years by the secretaries of the Department of Chemistry, Giselle Andrews and Cheryl Stanton.

I warmly thank my lab mates John Tran, Mark Wall, Diane Mataija, Hannes Hochreiner and Najat Bahroun. Thanks to Wilber Menéndez, Carlos González, Gianna Alemán, Kerry Chambers and Evelyn Keirstead for their unconditional friendship.

My family deserve special mention for their encouragement and love.

Thank you Reinaldo, my best friend, for always being there.

I recognize that this research would not have been possible without the financial support of the Department of Chemistry at Dalhousie University and MDS Sciex.

1.1. Introduction

Polycyclic aromatic compounds (PACs) are widely distributed in the environment and can arise from natural sources, spills of oil-derived materials, and combustion processes (Kolakowski 1999). PACs form a broad class of compounds that consists of polycyclic aromatic hydrocarbons (PAHs), their derivatives and their heteroatomic (–O, –S, –N) analogues. In recent years, special attention has been paid to the identification and quantification of polycyclic aromatic sulfur heterocycles (PASHs) because of their impact on the environment, refining processes, and quality of fuel products.

The removal of sulfur from refinery streams includes two approaches: catalyst-based hydrodesulfurization (HDS) and non-HDS processes (Song 2003). Currently, the HDS technology is the most widely used approach. The HDS process is highly effective in removing thiols, sulfides and disulfides but it is less efficient for PASHs. Moreover, the reactivity of PASHs under HDS conditions depends on the presence and the position of alkyl substituents. A survey of HDS and non-HDS based technologies is given in Chapter 1.

Environmental regulations requiring a reduction in the amount of sulfur in transportation fuels are driving the need for better analytical methods. In general, the lack of standards, the complexity of the samples, and the low concentration of PASHs hinder the successful analysis of sulfur-containing compounds. Separation methods such as gas chromatography (GC) (Nero 2003), liquid chromatography (LC) (Rudzinski 2003a) and supercritical fluid chromatography (SFC) (Andersson *et al.* 2006) coupled to a selective detector, such as the mass spectrometer, have been applied to the analysis of PASHs, and analytical protocols involving them are constantly being improved to minimize these problems. Although the basic concepts of GC, LC and SFC are summarized below in Chapter 1, LC on a stationary phase containing transition metals was the only chromatography used in the thesis. The principal aspects of chemical ionization (CI) are explained because of the similarities between CI and

atmospheric pressure chemical ionization (APCI). However, CI was not employed in the experimental work.

1.2. Sulfur-containing Compounds in Petroleum

Petroleum or crude oil is a highly complex mixture predominantly composed of hydrocarbons. The major classes of hydrocarbons found in petroleum include alkanes, cycloalkanes and aromatics (Speight 1980, pp 52,60). Compounds containing sulfur, nitrogen, oxygen and transition metals such as vanadium and nickel are encountered in comparatively lesser amounts (Nadkarni 2003, pp 27–56).

After carbon and hydrogen, sulfur is commonly the third most abundant element found in crude oils (Speight 1980, pp 50–51). The sulfur content in crude oils may range from 0.05 to 5% w/w, depending upon the geologic history, and in some unusual cases can be higher (13.9% in a crude oil in Rozel Point, Utah) (Thompson 1980, pp 189–208). The majority of the sulfur present in crude oils is predominantly bonded to carbon, with elemental sulfur and hydrogen sulfide representing only minor portions of the total sulfur amount (Kropp and Fedorak 1998). Speight has suggested that sulfur compounds are formed by a thermal reaction between elemental sulfur, and possibly also hydrogen sulfide, and hydrocarbons (Speight 1980, pp 13–14).

Generally, the greater the density of a crude oil, the higher its sulfur content. Crude oils from the most ancient deposits appear to have low sulfur contents. High-sulfur oils are frequently found in layers buried at a depth of 1.5–2.0 km, while low-sulfur oils are often found in layers buried at a lesser depth (Aksenov and Kamyanov 1980, pp 1). The distribution and types of sulfur-containing compounds vary with the boiling range (Kropp and Fedorak 1998) and among crudes of diverse origin (Speight 1980, pp 65–66).

The sulfur content usually increases as the cut point of the petroleum fraction rises (Aksenov and Kamyanov 1980, pp 2–13). However, the middle boiling point fractions may contain more sulfur than the higher fractions as a result of thermal degradation of the higher molecular weight sulfur compounds

during distillation (Speight 1980, p 67). Representative structures of the various types of sulfur compounds encountered in petroleum are shown in Figure 1.1 (Kropp and Fedorak 1998).

The sulfur present in fractions with boiling points lower than 150 °C exists primarily in the form of thiols, sulfides, disulfides, thiophene and thiophenes substituted with one or two methyl groups. Disulfides are not considered as generally being present in petroleum but may form after oxidation of thiols during processing (Speight 1980, p 69). In fractions having boiling points between 150 and 250 °C, these same types of compounds but of higher molecular mass are encountered along with mono-, bi- and tri-cyclic sulfides, arene thiols, alkyl aryl sulfides, thienothiophenes, thiophenes with up to four short alkyl chains and benzothiophenes.

The major sulfur-containing compounds in fractions with boiling points between 250 and 540 °C are substituted thiophenes, benzothiophenes, dibenzothiophenes, naphthothiophenes, benzonaphthothiophenes and phenanthrothiophenes. These compounds are known as polycyclic aromatic sulfur heterocycles (PASHs) or thiaarenes. Sulfur compounds in fractions with higher boiling points (>540 °C) may constitute approximately half of the total sulfur content of crude oils. Approximately 80% of the sulfur present in these fractions is estimated to form part of thiophene rings that are condensed to form larger and more complex PASHs (Kropp and Fedorak 1998).

PASHs may have biological activity since they are the sulfur-containing analogs of polycyclic aromatic hydrocarbons (PAHs) and the carcinogenic, and mutagenic potential of PAHs is well-documented (Jacob 1990, pp 70–71). However, although some studies have revealed the mutagenic and carcinogenic potential of PASHs, the biological activity of these compounds does not always correlate with that of the isosteric PAHs. The biological activity of PASHs suggests that these compounds may contribute significantly to the impact of oil spills on contaminated environments (Kropp and Fedorak 1998).

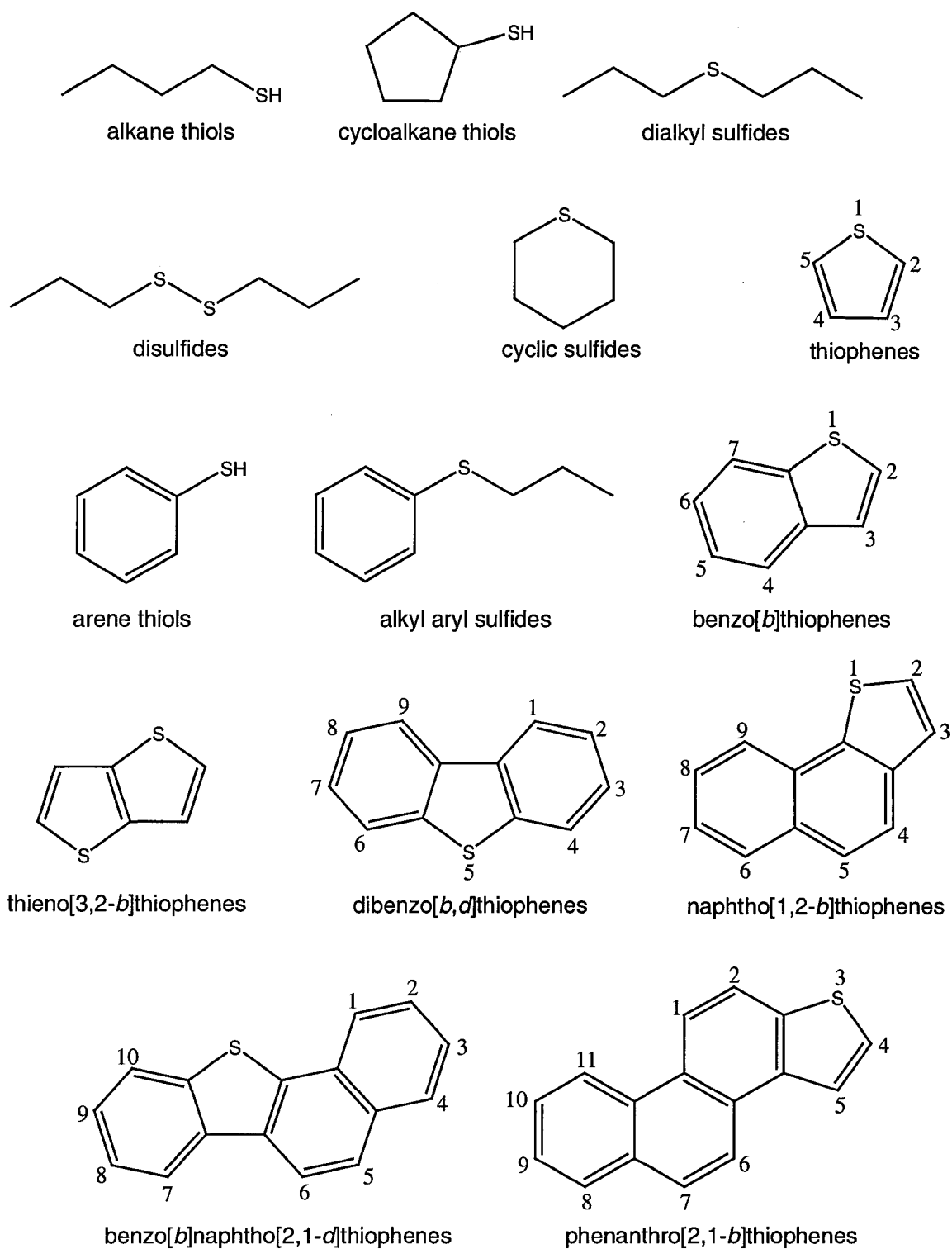


Figure 1.1. General classes and structures of representative sulfur compounds (for each class) found in petroleum.

Knowledge of the types and distribution of sulfur compounds in petroleum is fundamental for the development of improved methods for the removal of sulfur from crude oils. The removal of sulfur from petroleum products is important because sulfur in fuels transforms into sulfur dioxide on combustion, which is believed to promote the corrosion of engine parts (Speight 1980, pp 65–67). Furthermore, reaction of sulfur dioxide with atmospheric oxygen and water forms sulfuric acid resulting in acid rain (Rudzinski 2003a, p 314), which affects aquatic life and vegetation. Sulfur dioxide can also react atmospheric components to form airborne sulfate particles, which are an important component of urban smog and are considered health hazards (Environment Canada web site: <http://www.ec.gc.ca/acidrain/acidair.html>, access date: January 11, 2007). Therefore, governments are proposing environmental regulations to reduce the sulfur content in petroleum products. Currently, the desulfurization of refinery streams includes two approaches: a) catalyst-based hydrodesulfurization (HDS) processes and b) non-HDS based technologies. These two processes will be briefly discussed in the following sections.

1.2.1. Catalyst-based Hydrodesulfurization (HDS) Process

HDS is the most widely used refining process and often involves a molybdenum sulfide catalyst supported on alumina, usually combined with promoter metals such as cobalt and nickel: Co–Mo/Al₂O₃ or Ni–Mo/Al₂O₃. The catalyst transforms sulfur compounds, under a high pressure of hydrogen (1.38–20.70 MPa) and high temperatures (290–425 °C), to hydrocarbons and H₂S (Song 2003).

Figure 1.2 (Song 2003) shows the types of sulfur compounds present in gasoline, jet fuel and diesel fuel and their relative reactivity in HDS as a function of ring size and the position of alkyl substitutions on the ring. In general, the reactivity of sulfur compounds under HDS conditions is governed by the strength of the C–S bond, the position of the alkyl substituents and the electron density on the sulfur atom (Song 2003).

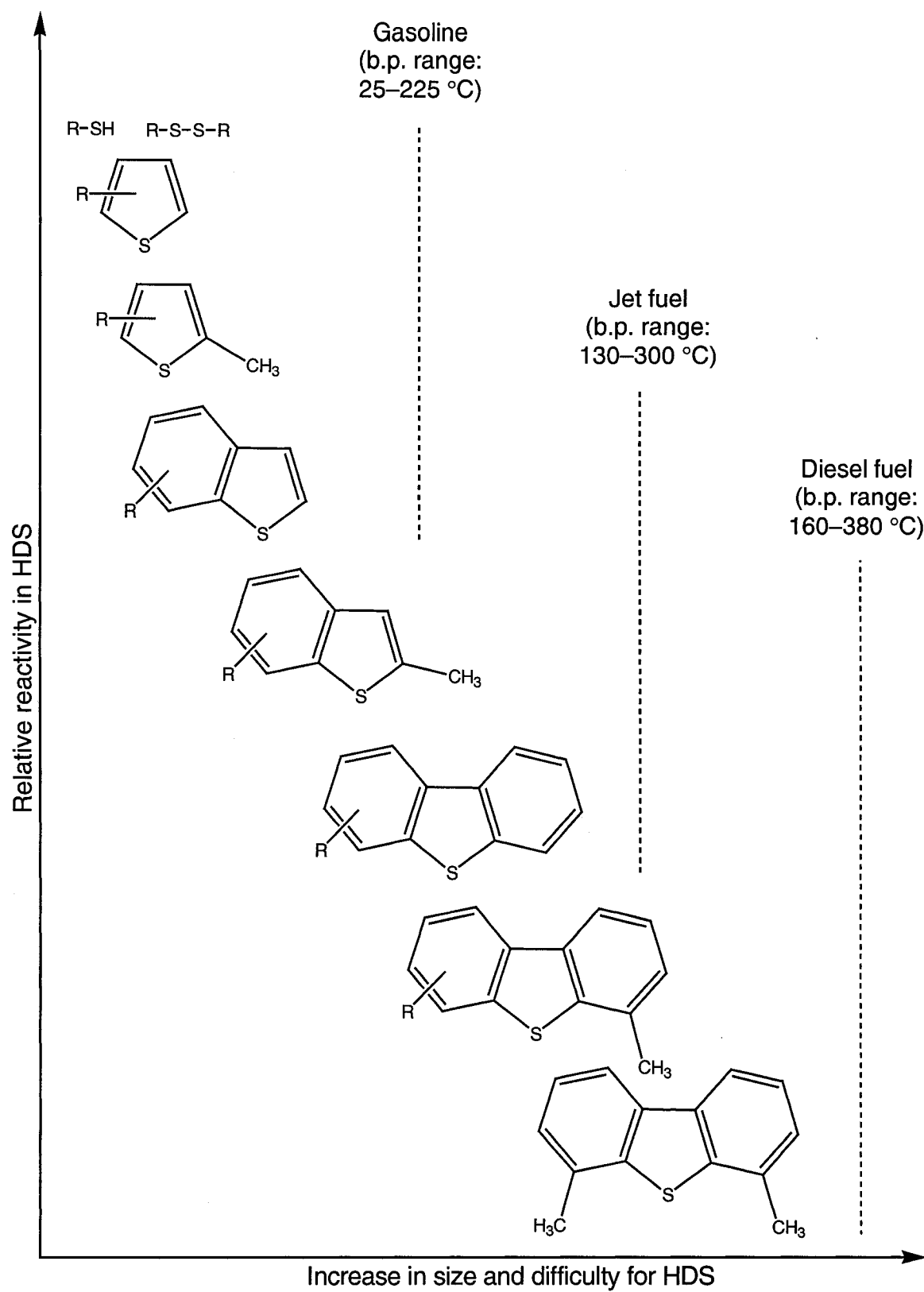


Figure 1.2. Relative reactivity of sulfur compounds in HDS.

Furthermore, the H_2S produced from sulfur compounds with higher reactivity probably influences the HDS of less reactive ones by reducing the activity of conventional Co–Mo/ Al_2O_3 or Ni–Mo/ Al_2O_3 catalysts (Ma *et al.* 1994) and/or decreasing the hydrogen partial pressure inside the reactor (Bej 2004a).

Thiols, sulfides and disulfides are very reactive in conventional HDS because they have weaker C–S bonds and higher electron density on the sulfur atom (Song 2003). As a result, they react by the hydrogenolysis route, which involves direct C–S bond breaking. Generally, the removal of sulfur compounds over Co–Mo/ Al_2O_3 catalysts occurs through the direct hydrogenolysis pathway (Song 2003; Bej *et al.* 2004b).

The reactivity of the 1- to 3-ring sulfur compounds decreases in the order thiophenes > benzothiophenes > dibenzothiophenes. Dialkyl dibenzothiophenes in heavier fractions, mainly 4,6-dialkyldibenzo[*b,d*]thiophene (4,6- R_2DBT), are the sulfur compounds most difficult to remove during the HDS process (Bej *et al.* 2004b; Ma *et al.* 1994). The relative reactivity for 4,6- R_2DBTs over Ni–Mo/ Al_2O_3 catalysts decreases in the order $\text{R} = -\text{CH}_3 > -\text{CH}_2\text{CH}_3 > -(\text{CH}_2)_3\text{CH}_3 > -(\text{CH}_2)_2\text{CH}_3$ (Breysee *et al.* 2003). For the dimethyl series of DBT, the ease of HDS over Co–Mo/ Al_2O_3 catalysts has the following order 2,8-dimethylDBT > 3,7-dimethylDBT > 4,6-dimethylDBT (Bej *et al.* 2004b). According to Ma and co-workers, 2,8-dimethylDBT and 3,7-dimethylDBT are more reactive than DBT, while PASHs with four condensed rings such as alkylated phenanthrothiophenes and benzonaphthothiophenes appear to be more reactive than 4,6- R_2DBT over Ni–Mo/ Al_2O_3 catalysts (Ma *et al.* 1996).

The low reactivity of 4,6- R_2DBT has been mainly attributed to the steric hindrance of the alkyl groups, which make the sulfur atom inaccessible to the active sites of the catalyst (Bej *et al.* 2004b). Thus, desulfurization of 4,6- R_2DBT proceeds primarily *via* the hydrogenation pathway, which involves complete hydrogenation of one phenyl ring before C–S bond breaking, rather than direct hydrogenolysis (Perspective 2003). Ni–Mo/ Al_2O_3 catalysts generally have higher hydrogenation ability than Co–Mo/ Al_2O_3 and also perform better than Co–Mo/ Al_2O_3 at high pressure and low temperature conditions, thus facilitating HDS

by the hydrogenation pathway (Song 2003). As compared to Ni–Mo/Al₂O₃ catalysts, Co–Mo/Al₂O₃ catalysts are more efficient for the removal of dibenzo[*b,d*]thiophene (DBT), while both catalysts have almost equal activity for the removal of 4-methylDBT. On the contrary, 4,6-dimethylDBT can be removed more efficiently over Ni–Mo/Al₂O₃ catalysts (Bej *et al.* 2004b).

Four different approaches have been attempted for decreasing the steric hindrance of the alkyl groups and increasing the reactivity of 4,6–R₂DBT. These include hydrogenation of one of the phenyl rings in 4,6–R₂DBT, shifting positions of the methyl groups from the 4,6 to the 3,7 or to the 2,8 positions through isomerization, removal of one or both alkyl groups through dealkylation, and scission of the C–C bond in the thiophenic ring. The catalysts required for directing HDS through the aforementioned pathways must have a) a high hydrogenation capability, which can be enhanced by incorporating a suitable metal such as Ni, W, Pt, Pd and Ru, and b) acidic properties, which can be achieved by using supports other than alumina, *e.g.* zeolites, to favor the routes of isomerization and dealkylation, which are acid-catalyzed (Bej *et al.* 2004b; Breysee *et al.* 2003).

The sulfur content in diesel fuel can be reduced to 300–500 ppmw using conventional HDS. Most of the developed countries are planning to reduce the allowed limit of sulfur in diesel fuel to 10–15 ppmw in the near future (Fujikawa 2006). However, reduction of sulfur levels to less than 15 ppmw is difficult using the current HDS process because the remaining sulfur compounds in diesel fuel with 500 ppmw of sulfur are the refractory 4,6–R₂DBTs.

In the case of gasoline, the key to deep desulfurization, from the current level of 330 to a future level of 30 ppmw or less, is sulfur removal from fluid catalytic cracking (FCC) naphtha. FCC naphtha, which is a major blend component of gasoline (about 25–40%), contributes up to 90–98% of the sulfur present in gasoline and also has a high content of alkenes. Although the amount of sulfur in gasoline can be reduced to 30 ppmw using the current HDS technology, the major problem for deep desulfurization of gasoline is that

conventional HDS significantly reduces the octane number due to saturation of alkenes in FCC naphtha (Song 2003; Ma *et al.* 2002).

Although the use of more severe HDS conditions and/or catalysts of higher activity are some ways to lower the amount of sulfur in fuels and meet the new environmental regulations (Bej 2004a), novel processes including non-HDS based technologies, have been researched in order to achieve deep desulfurization of fuels under milder conditions and with less hydrogen consumption while preserving the quality of liquid fuels.

1.2.2. Non-HDS Based Technologies

Non-HDS based technologies for the removal of refractory sulfur compounds include any of the following processes: alkylation, extraction, precipitation or adsorption.

The boiling point of thiophenic compounds in gasoline can be shifted to a higher value by alkylation of sulfur compounds with alkenes present in the refinery stream and catalysts such as AlCl_3 or ZnCl_2 deposited on silica and/or alumina supports. The alkylated sulfur compounds are later separated by distillation. Under the conditions employed, alkylation of sulfur compounds occurs more rapidly than that of aromatic hydrocarbons. However, the alkylated thiophenes may require more drastic hydrotreating conditions to eliminate sulfur (Babich and Moulijn 2003).

In desulfurization via extraction, sulfur-containing compounds are selectively dissolved in an appropriate solvent, for example acetone, ethanol, polyethylene glycols, and they are separated from the refinery stream by liquid/liquid extraction. Before liquid/liquid extraction, sulfur compounds can be oxidized to sulfones to increase their solubility in polar solvents. The organosulfur compounds are later separated from the solvent by distillation and the solvent is recycled (Babich and Moulijn 2003).

Desulfurization by precipitation is based on the formation of charge transfer complexes between alkylated DBTs and π -acceptors such as 2,4,5,7-tetranitrofluorenone (TNF). The insoluble complex is later removed by filtration

and the excess of TNF is recovered using a solid adsorbent. However, one treatment only removes 20% of the sulfur present and the role of other compounds that might form π -complexes such as PAHs has not been thoroughly studied (Babich and Moulijn 2003; Breysee *et al.* 2003).

Removal of sulfur compounds by adsorption involves two approaches a) reactive adsorption and b) selective adsorption. In the first approach, metals or metal oxides (Ni/ZnO, NiO/ZnO) on a solid sorbent (silica, alumina) react with sulfur, at elevated temperature (343–413 °C) and low hydrogen pressure (7–21 atm) (1 atm = 101.3 kPa), to form the metal sulfide without hydrogenation of aromatics. The sulfur is later burned off the sorbent, and the sorbent is regenerated using hydrogen. After reactive adsorption, the hydrocarbon portion of the molecule is released back into the process stream. The sulfur content in gasoline can be reduced to 10 ppmw using this procedure (Song 2003).

Desulfurization by selective adsorption is based on the removal of sulfur by selective interaction of sulfur compounds with a solid adsorbent, in the presence of PAHs, under ambient conditions without using hydrogen. Several adsorbents based on complexes of transition metals (Ni(II), Cu(I) and Ag(I)) supported on silica, alumina or zeolites, have been used for selective adsorption desulfurization. Sulfur compounds are recovered by washing the sorbent with a suitable solvent. The sorbent can be regenerated by oxidation, reduction or solvent washing (Ma *et al.* 2002; Song 2003).

1.3. Chromatography

Chromatography is a physical separation method in which the components in a mixture are selectively distributed between two immiscible phases: a mobile and a stationary phase. Chromatographic methods are normally categorized by the mobile phase: *e.g.* gas chromatography (GC), liquid chromatography (LC) or supercritical fluid chromatography (SFC). A chromatographic system consists of the following component parts: a device for sample introduction, a mobile phase delivery system, a column containing the

adsorbent (stationary phase), a detector and an electronic device to control all these components and register data.

In the following sections the basic principles of gas, liquid and supercritical fluid chromatography will be briefly described.

1.3.1. Gas Chromatography

In gas chromatography (GC) the sample, dissolved in an appropriated solvent, is vaporized and transported through the column by the flow of a chemically inert gas, *e.g.* helium or nitrogen. Unlike other types of chromatography, the mobile phase does not interact with the analyte. The stationary phase may be either a solid or a liquid. However, gas-liquid chromatography is employed for most applications in GC.

Both packed and capillary columns are used in GC, though the latter type is almost always applied to the separation of complex mixtures due to higher resolving power. The introduction of liquid samples onto capillary columns is a critical step in the chromatographic analysis because of limitations on sample size (100 ng/ μ L per component). Split and splitless injection are among the most popular injection techniques for capillary GC. Most commonly, a single injector permits both operation modes. In splitless injection, all of the sample and solvent is passed onto the column. As a result, there is no sample discrimination and direct quantification can be accomplished in trace and major component analyses. However, the method may cause peak broadening and loss of resolution. In split mode, most of the sample flows to waste, and only a small portion passes onto the column. Typical split ratios are in the range of 1:10 to 1:100 and thus relatively large volumes, compared to splitless mode, can be injected *e.g.* 1 μ L. However, sample loss and discrimination, as well as limited precision and accuracy, are among the most important disadvantages of the technique (Niessen 2001, pp 3–4).

A typical capillary column contains a liquid stationary phase that is chemically attached to the inner surface of a thin fused silica tube, which has an external polyimide coating. The most stable and widely used liquid stationary

phases are based on a polysiloxane backbone where the substitution of the polymer, typically with methyl, phenyl and/or cyano-propyl groups, generates the desired polarity, Figure 1.3 (Scott 1998, p 46; de Zeeuw and Luong 2002).

A stationary phase with a polarity that matches that of the sample is generally selected. Under this condition, the components in the sample elute in the order of their boiling points. If the sample has a broad boiling range, the temperature of the column is increased either continuously or in steps to alter solute retention and speed up the analysis (Skoog and Leary 1992, pp 616–617).

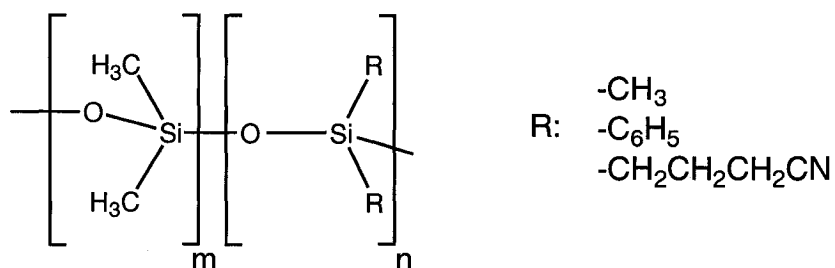


Figure 1.3. Stationary phases in gas chromatography.

GC detectors for the selective determination of sulfur-containing compounds include the flame photometric detector (FPD) (Dressler 1986, pp 133–137; Cheskis *et al.* 1993) and the sulfur chemiluminescence detector (SCD) (Yan 1999; Yan 2002).

The separating capability of capillary GC for a wide variety of samples is presently unparalleled. However, the technique is restricted to the analysis of small, volatile and thermally stable substances.

1.3.2. Liquid Chromatography

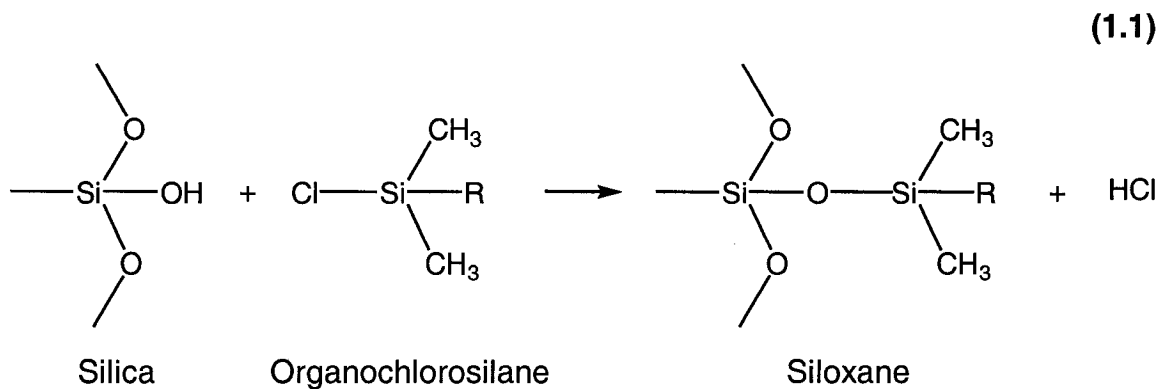
Liquid chromatography (LC) is suitable for separating nonvolatile, thermally labile and water-soluble substances, which are not amenable to GC analysis.

In high-performance liquid chromatography (HPLC), the mobile phase is delivered under high pressure (up to 400 bar) ($1 \text{ bar} = 10^5 \text{ Pa}$) through the

chromatographic column. In contrast to capillary GC, in which different types of injectors are available, the device for sample introduction in HPLC consists of a loop (from 5 μL to 500 μL) into which the sample is introduced using a conventional syringe. Separations in HPLC are most commonly carried out using packed columns. Typically, columns are constructed from stainless steel tubes (Skoog and Leary 1992, pp 634).

Depending on the nature of the compounds to be analyzed (molecular weight and solubility in water) as well as their interaction with the stationary phase, separation can take place as a result of various and sometimes mixed mechanisms: partition, adsorption, ion exchange or size exclusion (Niessen 1999, pp 11–12).

Partition chromatography has become the most widely used of the four types of liquid chromatographic modes. The technique has been successfully applied to the analysis of polar compounds having a molecular weight less than 3000 u. The most widely used stationary phases in partition chromatography are of the bonded-phase type. Bonded-phase materials are commonly siloxanes formed by reaction of silica with an organochlorosilane (1.1).



Partition chromatography can be classed as normal-phase (NP) or reversed-phase (RP) depending upon the relative polarities of the mobile and stationary phases. In normal-phase liquid chromatography (NP-LC), the mobile phase is non-polar while the bonded-phase coating contains a polar functional group (e.g. R: $-(\text{CH}_2)_3\text{NH}_2$ in equation (1.1)). In reversed-phase liquid chromatography (RP-LC), on the contrary, the mobile phase is relatively polar

and the stationary phase is non-polar (*e.g.* .R: $-(\text{CH}_2)_7\text{CH}_3$ or $-(\text{CH}_2)_{17}\text{CH}_3$ in equation (1.1)). The majority of HPLC analyses employ reversed-phase systems. Usually, a bonded-phase material, the polarity of which matches that of the analyte, and a mobile phase of different polarity are carefully selected to carry out the chromatographic separation in a reasonable time (Niessen 1999, pp 5–8; Skoog and Leary 1992, pp 642–645). A mobile phase gradient, generated by mixing two or more solvents, is the easiest way of altering the analyte retention in LC. Gradient elution is extensively employed in the analysis of complex mixtures.

Another important LC method, adsorption or liquid-solid chromatography, is fundamentally a NP technique. The most commonly used stationary phase in adsorption chromatography is silica and the technique is best suited to the analysis of relatively non-polar compounds having a molecular weight less than 5000 u. However, the principal strength of adsorption chromatography is its ability to separate isomers (Skoog and Leary 1992, pp 651–654).

Ultraviolet (UV) and fluorescence detectors are among the most frequently used after liquid chromatographic separation (Ramaley and Campbell 2000; Scott 1986, pp 89–108). Although both detectors are selective to analytes containing chromophores, fluorescence detection is more selective and sensitive than absorption methods. This is because, firstly, a small number of compounds fluoresce naturally and secondly, as the excitation and emission wavelengths do not coincide, the analyte can be identified using both. The sensitivity of fluorometric methods is also higher because fluorescence detectors measure the analyte's emitted light directly, in contrast to UV detectors which measure small differences in the intensities of the incident and transmitted light beams.

1.3.3. Supercritical Fluid Chromatography

A supercritical fluid is an element or a substance above its critical pressure and critical temperature (Skoog and Leary 1992, pp 670–671). The most commonly used mobile phase for supercritical fluid chromatography (SFC) is carbon dioxide, although ammonia and sulfur dioxide have also been

employed. The use of carbon dioxide has some advantages: in addition to being relatively inert, its critical temperature (31.3 °C) and pressure (72.9 atm) lie well within the limits of HPLC instrumentation. Further, substances with low critical temperatures are useful for separating thermally unstable analytes (Skoog and Leary 1992, pp 672–673).

Both packed and capillary columns have been used in SFC. Capillary SFC uses detectors like those employed in GC. In capillary SFC, the stationary phase is bonded to the capillary wall, and not simply adhered to the inner wall as in some capillary GC columns, so it cannot be stripped off by the passing supercritical fluid.

Instruments and packed columns for SFC are similar to those for HPLC. Injection in packed column SFC is usually achieved by means of a conventional HPLC injection system. Unlike HPLC, SFC uses a thermostated column oven to control the temperature of the mobile phase, and a restrictor to control the pressure in the column (Sanagi and Smith 1988, pp 29–36).

The mobile phase is pumped as a liquid and heated at constant pressure before passing into the column. Increasing the pressure in SFC increases the density of the supercritical fluid causing a rise in its solvating power, which shortens the elution time of the analytes. Pressure programming in SFC produces analogous results to those obtained with gradient elution in LC and temperature programming in GC. The retention behaviour in SFC can also be altered by adding polar modifiers such as methanol or acetonitrile. Chemists have observed that the addition of small amounts of modifier is usually enough to alter separations in packed column SFC whereas the influence of modifier in capillary SFC is proportional to its concentration. However, no explanation for this behavior has been given (Smith 1999a).

Several of the detectors used in GC and HPLC can be used in SFC, including FPD, SCD, UV and fluorescence detectors. The coupling of SFC to mass spectrometry has been one of the most successful applications of the technique since a supercritical mobile phase can be more easily evaporated into the MS source than most LC solvents (Smith 1999a).

Capillary SFC is of importance because it permits the separation of very high-molecular-mass analytes, *e.g.* alkanes of up to 100 carbon atoms, which are too involatile to be handled by GC. However, capillary SFC does not equal GC in speed and efficiency. Further, although packed column SFC is essentially a normal-phase technique and cannot compete with RP-LC for samples that require RP separation, SFC provides faster, and often more efficient separations of samples than NP techniques. In this regard, SFC has provided enhanced separation of chiral analytes with respect to NP-LC by increasing analyte-stationary phase interactions (Smith 1999a).

1.4. Mass Spectrometry

Mass spectrometers have the following component parts: an inlet system, an ion source, a mass analyzer, a detector, a pumping system and a computer to control all these components and perform data analysis.

The pumping system maintains the instrument at a reduced pressure (10^{-5} – 10^{-8} Torr) (1 Torr = 133.3 Pa), which prevents the ions from colliding with residual gas molecules along the path from the ion source to the detector.

Samples in the gas, liquid or solid states are introduced into the ionization region by means of the inlet system. Once in the ion source, the components of the sample are converted into ions by bombardment with electrons, atoms, ions, molecules or photons, depending on the ionization method. The ions produced are then accelerated into the mass analyzer, which separates them on the basis of their mass-to-charge (m/z) ratio. After ion separation, the ion beam is transformed into a usable signal by the detector/amplifier system and this signal is converted into appropriate data by the computer.

In the following sections, four ionization modes and two types of mass analyzers will be described. These will be the components of most use in the proposed thesis research.

1.4.1. Ion Sources

1.4.1.1. Electron Ionization

In an electron ionization (EI) ion source (Figure 1.4), sample molecules are ionized in the gas phase by collision with electrons. Therefore, EI mode is best suited for the analysis of volatile and thermally stable compounds, with molecular weights less than 1000 u. Samples are commonly introduced into the source *via* a gas chromatograph or a direct probe inlet, in which solids and less volatile liquids are volatilized prior to ionization (Ashcroft 1997, pp 60–73). In GC/MS applications, the capillary column is passed directly from the GC oven into the ion source of the mass spectrometer via a heated transfer line.

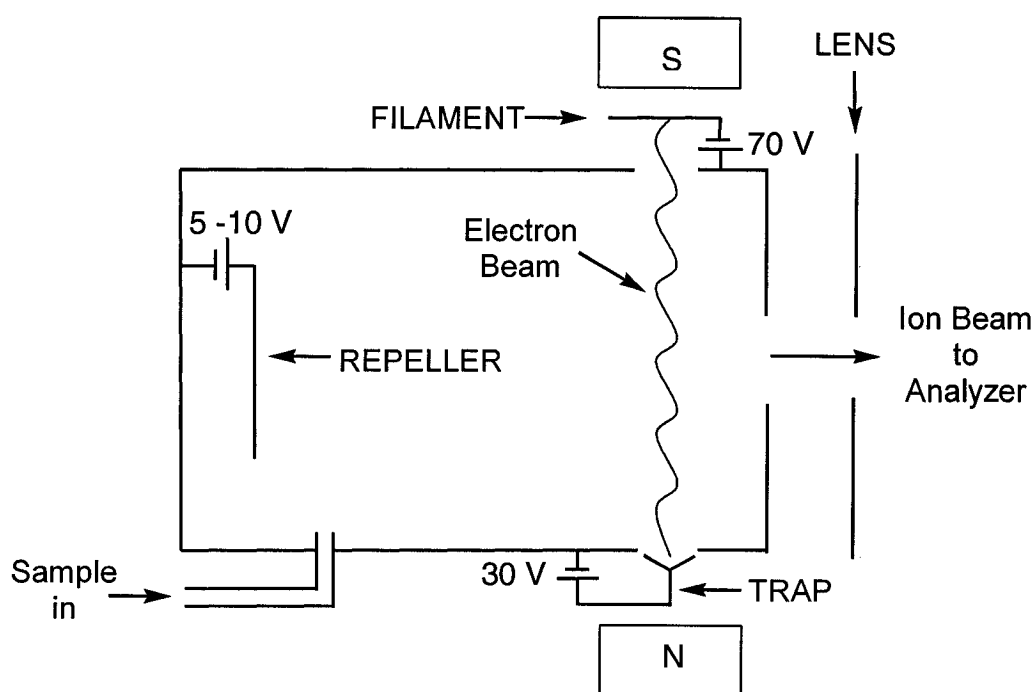


Figure 1.4. Diagram of an EI ion source (Adapted from a drawing by Dr. Louis Ramaley).

Electrons are emitted from a heated rhenium or tungsten filament. The emitted electrons are accelerated through a voltage difference, normally of 70 V towards the source block and collected by the trap located at the opposite side of the block. After introduction of the sample into the path of the electron beam, the

primary ionization process is the formation of a molecular ion **(1.2)** (M represents the analyte molecule and $M^{+•}$ is the molecular ion).



In EI mode, the source is maintained at low pressure (10^{-8} bar) so that the $M^{+•}$ ions formed have a very low probability of interacting with other molecules before leaving the ion source. Therefore, only unimolecular reactions are observed under EI conditions and EI mass spectra are highly reproducible (McLafferty and Tureček 1993, p 115).

EI is considered a “hard” ionization method because the energy gained by the ionizing electrons is much greater than the bond dissociation energies of the molecules. Therefore, extensive fragmentation of the sample molecules may occur, which can lead to structural information about the analyte (McLafferty and Tureček 1993, pp 6–7).

The source may be heated from about 100 °C to 250 °C to maintain the sample in the gas phase and the source clean. A magnetic field positioned across the ion chamber focuses the electron beam and causes it to spiral from the filament to the trap, increasing the efficiency of ionization. Negative ions, which may result from electron capture processes, have low abundance under EI conditions. Therefore, EI is mainly a positive ionization process (Ashcroft 1997, p 75). Negative ions are not detected because a repeller forces only the positive ions out of the source in the direction of the mass analyzer.

1.4.1.2. Chemical Ionization

The technique of chemical ionization (CI) was introduced by Munson and Field in 1966 (Munson and Field 1966). In CI mode, samples are ionized in the gas phase by collision with ionized reagent gas molecules. Therefore, the method is useful for ionizing volatile compounds, and the inlet systems are analogous to those used in EI mode. EI and CI ion sources are also similar, but the CI source uses a smaller exit slit to maintain a higher pressure in the source

(up to 1 Torr) while maintaining a low pressure in the analyzer (10^{-5} – 10^{-8} Torr) (Skoog and Leary 1992, p 444).

A reagent gas, commonly methane, isobutane or ammonia, is introduced into the CI ion source in a large concentration with respect to the analyte. Therefore, the electron beam ionizes almost exclusively the reagent molecules, and radical molecular ions of the reagent gas are formed. These radical ions may fragment and/or interact with neutral molecules of the reagent gas to yield reagent ions that ionize the analyte.

Ionization of the sample molecules in positive-ion CI (PCI) may occur by proton transfer, charge exchange, electrophilic addition or hydride abstraction (Munson 2000), equations (1.3) to (1.6).



In PCI, the major reaction of analyte molecules of higher proton affinity than that of the reagent gas is proton transfer to generate protonated molecules MH^+ (1.3). However, samples with very low proton affinities may ionize by hydride abstraction to yield $[\text{M} - \text{H}]^+$ ions (1.6). If the sample molecules are somewhat less basic than the reagent gas ions, then the reagent gas ion (X^+) may attach to the analyte to form the adduct $[\text{M} + \text{X}]^+$ (1.5). An alternative to proton transfer is ionization by charge transfer with reagents that do not contain available hydrogens, *e.g.* He, Ar, N_2 , to produce molecular ions of the analyte and EI-like spectra (1.4).

CI can also be used to produce negative ions either by ion/molecule reactions or by electron capture. In negative-ion CI (NCI), ion/molecule reactions include adduct ion formation, proton abstraction to give deprotonated molecules $[\text{M} - \text{H}]^-$ and charge exchange (Ashcroft 1997, pp 74–82).

Negative ions may also form as a result of electron/molecule interactions. In the presence of a gas at relatively high pressures, electrons are considerably decelerated and some types of molecules can capture an electron to form negative ions. Although this reaction is an important means of ionizing analytes that contain electronegative atoms, electron capture does not directly involve a reagent gas ion and, therefore, it is not considered a chemical ionization process (Sparkman 2000, pp 9–10; Harrison 1992, pp 24–27).

CI is classified as a “soft” ionization technique because little excess energy may be put into the analyte molecules when they are ionized and in many cases little fragmentation takes place. Consequently, the CI spectra are generally dominated by adduct ions, produced by ion/molecule reactions, from which the molecular mass of the analyte can be inferred (de Hoffman *et al.* 1996, p 15).

1.4.1.3. Atmospheric Pressure Chemical Ionization

Although Horning developed atmospheric pressure chemical ionization (APCI) in the 1970s (Horning *et al.* 1973), the technique did not gain popularity as an LC/MS interface until the widespread success of electrospray ionization (ESI) sources in the late 1980’s (Thomson 1998). APCI is a “soft” ionization technique applied to the analysis of a great variety of compounds. Although APCI is better suited for the analysis of less polar compounds and solvents compared to ESI, the technique is not as effective as ESI for the analysis of biopolymers with the mass limit for APCI considered to be below 2000 u (Abian 1999; Ardrey 2003, p 125).

APCI and ESI require liquid samples. APCI commonly accepts solvent flow rates of up to 2 mL min⁻¹ without requiring a flow split. Methanol, ethanol, hexane, toluene and acetonitrile are examples of solvents used in APCI studies (Cole 1997, pp 324–327).

A diagram of the APCI source used in this thesis is shown in Figure 1.5. The Quattro APCI source uses three concentric, separate gas streams: the nebulizer, the sheath and the bath gas flows.

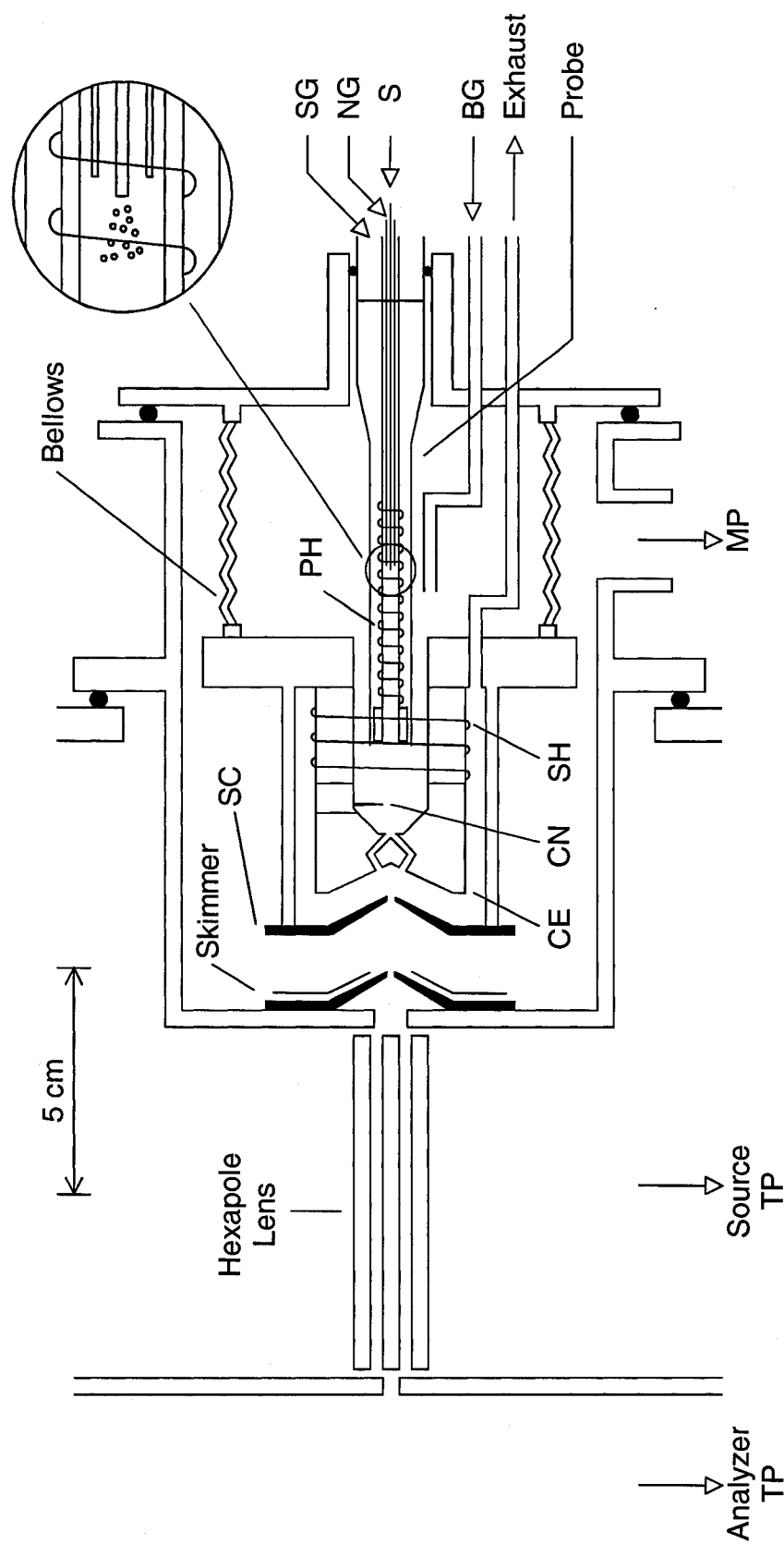


Figure 1.5. Diagram of a Micromass Quattro APCI source. Drawing by Dr. Louis Ramaley. BG: bath gas, CE: counter electrode, CN: corona needle, NG: nebulizer gas, S: solvent or sample, SC: sampling cone, SG: sheath gas, SH: source heater, PH: probe heater, MP: mechanical rotary oil pump and TP: turbomolecular pump.

Examples of source gases that have been used in APCI–MS are nitrogen, air and carbon dioxide (Kolakowski *et al.* 2004). The importance of these gas streams will be explained briefly.

The column effluent, or a liquid sample, enters the APCI source through a thin silica capillary. The nebulizer gas flows past this capillary and transforms the sample into a stream of small droplets, which are vaporized by heat from the probe heater. The sheath gas flows throughout the outside of this heater and its purpose is to cool the probe sheath. The nebulizer and the sheath gases are mixed at the tip of the heated nebulizer probe. The bath gas flows past the probe and prevents molecules of solvent or analyte from depositing on the relatively cool surfaces of the APCI source.

The mixture of nebulizer, sheath and bath gases, analyte and solvent, enters the atmospheric-pressure ion source where the solvent molecules are ionized by electrons generated by application of a high voltage to a corona discharge needle. The solvent thus acts as a reagent gas and the ionization mechanisms are similar to those in CI. However, APCI ions are formed under equilibrium conditions, whereas CI products are formed under kinetically controlled conditions (Niessen 1999, pp 249–250). Finally, the ions generated pass through a “pepper pot” counter electrode and are transferred, through several stages of differential pumping separated by cones from the atmospheric pressure ion source towards the high vacuum of the mass analyzer.

The assembly of the corona needle, the counter electrode and the first cone is attached to a bellows, which allows some movement between the first and second cones. Other than this, all other components of the Quattro APCI source, including the corona needle, are fixed in position.

1.4.1.4. Electrospray Ionization

The phenomenon of electrospray has been known since the late 1910's (Zeleny 1917; Niessen 1999, pp 285–286). However, the technique gained celebrity in the late 1980's, when Fenn reported the formation of multiply-charged ions under electrospray ionization (ESI) conditions (Fenn *et al.* 1989).

The electrospray process has been described elsewhere (Herbert and Johnstone 2003, pp 55–60; de Hoffman *et al.* 1996, pp 27–31). In ESI, a stream of solvent containing the analyte is passed through a narrow-bore capillary or electrospray needle into an atmospheric pressure ion source. Unlike APCI, ESI commonly tolerates solvent flow rates from nL min^{-1} levels to 0.2 mL min^{-1} (de Hoffman 1996, pp 104–105).

In ESI a source very similar to that described for APCI (Figure 1.5) is employed. However, as primary ionization does not occur by means of a corona needle, this device is absent in an ESI source. The liquid emerging from the capillary is dispersed into an aerosol of highly charged droplets, known as the electrospray, by applying a potential difference of 3–6 kV between the needle and the counter electrode. To aid the evaporation of the solvent and reduce the number of cluster ions, a flow of gas, *e.g.* nitrogen, is directed across the electrospray. The evaporation of the solvent produces a reduction in the droplet size and a charge density increment. When the number of electrostatic charges on the drop surface becomes large relative to the droplet size an explosion occurs and smaller droplets are produced. This process repeats itself until ions are released from the droplets (ion evaporation) or all the solvent has evaporated to leave the ion in the gas phase (ion desolvation). Ions are formed by protonation or deprotonation of the analyte or by adduct formation with solvent ions, which reflect acid-base equilibria in solution. The technique is thus better suited for the analysis of compounds already ionized or that can be ionized in the liquid phase. Therefore, the yield of ions can be improved by using polar solvents such as water or acetic acid, or by adding an electrolyte to the solution. Multiply-charged ions of the type $[\text{M} + n\text{H}]^{n+}$ are frequently produced, which makes ESI a valuable tool for measuring accurately the mass of large molecules with a wide range of mass analyzers, including quadrupoles (Abian 1999).

ESI is a “soft” ionization technique, which accomplishes the transfer of ions from solution to the gas phase. Therefore, it is a suitable interface for coupling LC to MS, although it can be used equally well for single substances by first dissolving them in an appropriate solvent. ESI is a reasonably sensitive

technique for analyzing large (over 100,000 u), polar, basic, thermally labile and non-volatile compounds (Abian 1999; de Hoffman *et al.* 1996, p 206).

1.4.2. Mass Analyzers

1.4.2.1. The Quadrupole Mass Filter

The principles of the quadrupole mass filter (QMF) were first described in the early 1950's by Paul and Steinwedel (Paul and Steinwedel 1953, taken from de Hoffmann *et al.* 1996, p 42). The device in practice usually consists of four cylindrical metal rods positioned in a radial array, Figure 1.6.

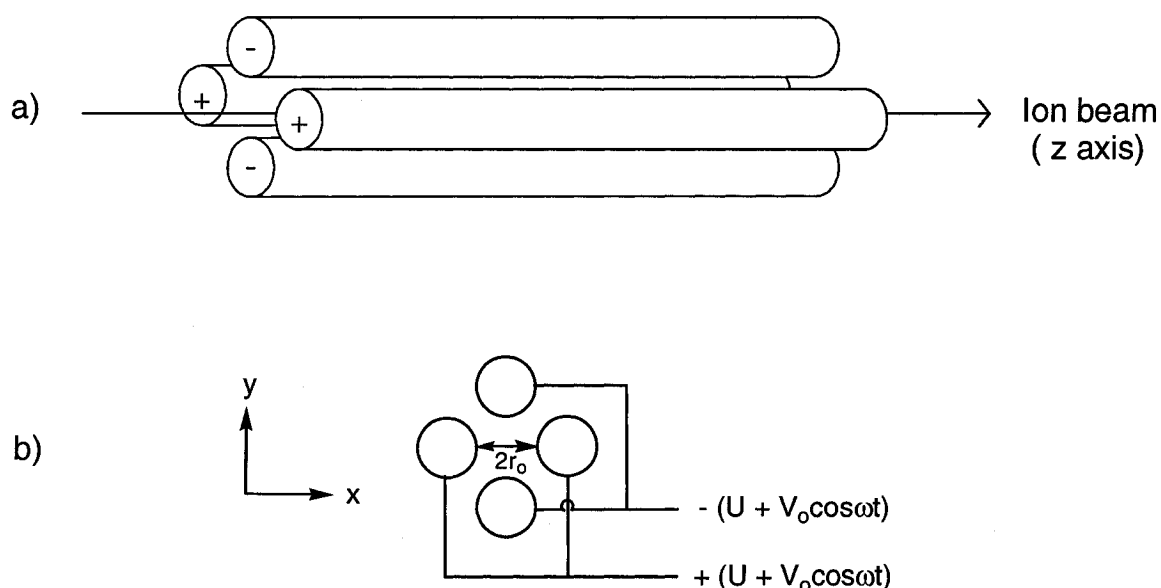


Figure 1.6. Quadrupole mass filter: side (a) and end (b) views (Adapted from a drawing by Dr. Louis Ramaley).

The filtering action of the QMF for an ion with a given m/z value is achieved by applying both dc (constant) and ac (sinusoidal) voltages to the rods (Miller and Denton 1986). At every moment, the voltage applied to adjacent rods is equal in magnitude but opposite in sign. This voltage (V) is given by $V = U + V_0 \cos \omega t$, where U is the dc voltage and $V_0 \cos \omega t$ represents a radio frequency (RF) voltage of amplitude V_0 and angular frequency ω . Note that the two RF voltages are arranged to be 180° out of phase with respect to each other.

As a result of the applied voltage, the ions entering the quadrupole begin to oscillate in both the X–Z and Y–Z planes. In order for an ion to traverse the rods and reach the detector, it must remain stable in both the X–Z and the Y–Z planes. The voltage applied to the rods creates a low pass mass filter in the Y–Z plane and a high pass mass filter in the X–Z plane. At given U and V_0 values, only ions of a specific m/z will have stable trajectories and will be transmitted. All other ions will oscillate with increasing amplitude until eventually they collide with one of the rods. A mass spectrum can thus be obtained by increasing U and V_0 while holding their ratio constant.

As m/z ratios depend upon easily controllable variables such as U and V_0 , the QMF can be programmed to scan over a very small mass range, thereby allowing ions of specific m/z ratios to pass through the analyzer and rejecting all others. This process, known as selected ion monitoring (SIM), offers enhanced sensitivity and specificity over the full-scan experiment since the mass analyzer can remain for a longer time at given values of U and V_0 and thus m/z value (Smith and Busch 1999b, p 15). Mass scanning can be performed very quickly (< 100 ms) over several hundred mass units, and this feature make QMFs ideal detectors for chromatography (Skoog and Leary 1992, p 429). Further, coupling of quadrupoles to atmospheric-pressure inlet systems is easy since ions are accelerated through relatively low voltages (5–10 V) before entering the mass filter (Herbert and Johnstone 2003, p 185).

The resolution of the QMF can be set electronically, by varying the value of U/V_0 , rather than mechanically through the use of slits. They are usually operated at a resolution sufficient to separate two peaks one mass unit apart, often up to m/z 4000 (Volmer and Sleno 2005a). Unit mass resolution may be preserved even when analyzing ions with wide velocity distributions, in contrast to sector instruments. However, quadrupoles provide lower mass resolution than double focusing instruments. Further, the efficiency of transmission of ions through quadrupoles decreases as m/z ratios increase, leading to a relative loss in sensitivity at higher masses (de Hoffmann *et al.* 1996, pp 46–47; Herbert and Johnstone 2003, pp 185–186).

1.4.2.2. The Quadrupole Ion Trap

The quadrupole ion trap (QIT) was developed in parallel with the quadrupole mass filter (QMF) by Paul and Steinwedel in the early 1950's (Paul and Steinwedel 1953, taken from de Hoffmann *et al.* 1996, p 42). However, the QIT was not widely used for MS until the 1980's when Stafford and co-workers made two major improvements that led to the creation of commercial QIT mass spectrometers. First, they created the mass-selective instability mode where ions over a wide m/z range are trapped and then sequentially ejected from the ion trap (Stafford *et al.* 1984) and second, they discovered that introducing helium gas into the trapping volume greatly improved the resolution of the QIT (Louris *et al.* 1987). Three hyperbolic electrodes, consisting of a ring, an entrance end-cap, and an exit end-cap, form the core of the QIT (Figure 1.7). These electrodes create a cavity that uses a three-dimensional quadrupole electrodynamic field to trap ions.

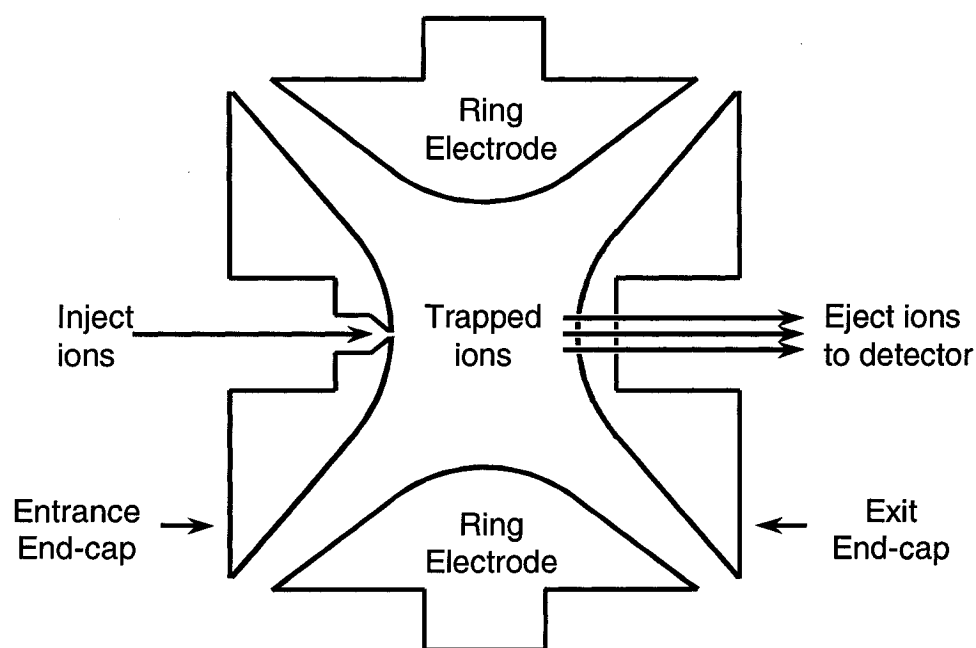


Figure 1.7. Cross-sectional view of the quadrupole ion trap.

Ions may enter the trap through an electrostatic ion gate, which pulses open and closed, or through a combination of radio frequency potentials applied to the ring electrode. The pulsed transmission of ions into the trap distinguishes QITs from beam instruments such as QMFs where ions continually enter and leave the mass analyzer. Although a trapping instrument, the QIT can be interfaced with various ionization methods, including pulsed ionization methods like matrix-assisted laser desorption ionization (MALDI) (Chambers *et al.* 1993) as well as continuous-beam sources such as ESI (van Berkel *et al.* 1990) and APCI (Hogenboom *et al.* 1998).

The ion trap is typically filled with helium to a pressure of about 10^{-3} Torr. Because of the presence of helium, the pressure inside the ion trap is high relative to other mass analyzers ($\sim 10^{-3}$ vs. 10^{-7} – 10^{-11} Torr). Collisions with helium cause all ions to migrate to the center of the trap and dampen their kinetic energy. This is referred to as *collisional cooling*. By condensing the ions to the center of the trap, ion loss is reduced and thus, sensitivity is improved. In addition, better resolution is achieved since ions form a packet that can be ejected more coherently than a diffuse cloud of ions (Louris *et al.* 1987).

Ions are confined to stable trajectories in the trap by using a suitable radio frequency (RF) voltage applied to the ring electrode. A full-scan spectrum is obtained by sequentially ejecting ions from low m/z to high m/z . This is performed by scanning the amplitude of the RF voltage to make the trajectories of ions sequentially unstable. Ions are ejected through holes in the exit end-cap. This mode of operation is known as mass-selective instability (Stafford *et al.* 1984). The mass resolution of the QIT depends, among other factors, on the number of RF cycles that ions spend interacting with the electrostatic field and on the number of ions in the trap. Typical operation of commercial QIT mass spectrometers gives unit mass resolution for mass ranges of up to 5000 m/z (Stafford 2002). However, better than unit mass resolution can be achieved by scanning at lower speed over a reduced m/z range.

An advantage of QIT mass spectrometers is that ions can be accumulated over relatively long periods of time to increase the number of ions detected and

consequently, the detection sensitivity. However, an important limitation is the dependency of ion stabilities upon the number of ions present in the trap at the same time. Space charging arises from the presence of too many ions in the trap, which causes a distortion of the electrostatic field. In addition, ions affected by space-charge will be forced by Coulombic repulsions to spread out into a larger cloud. This leads to an overall reduction in performance, *e.g.* mass shifts, broadening of peaks, and loss in sensitivity. Further, if the trap is filled with both matrix ions (large number) and analyte ions (very small number), the dynamic range for the detection of the analyte of interest will be reduced. Initial pre-scans are usually performed to count the ions entering the trap so that the amount of time that ions are allowed to accumulate in the trap (ion injection time) is dependent on the ion flux. This guarantees only a certain number of ions get in the trap (Volmer and Sleno 2005b).

The QIT offers high sensitivity in full-scan mode because of its ion-trapping capabilities. However, the sensitivity enhancement in the selected ion monitoring mode (SIM) is not very pronounced in comparison to the full-scan mode and, sometimes, mass spectrometrists point out that the QIT has full-scan detection limits similar to those of a QMF operated in the SIM mode. This is because the duty cycles in QITs and QMFs are different. The duty cycle in QMFs is defined as the fraction of time the detector is actually measuring ions (duty cycle in % = [ion detection time / total scan time] x 100). At unit mass resolution in a scan of 200 u, the QMF has a duty cycle of approximately 0.5 % whereas QMFs operated in SIM mode can be set to spend almost all of the scan time looking at a specific m/z ion (duty cycle close to 100 %), thus improving signal-to-noise ratios. Both full-scan and SIM modes on the QIT, on the contrary, are composed of different events occurring in sequence, *i.e.* ion injection, ion isolation and analysis. The duty cycle in QITs is determined by the trapping time, not the scanning time. Since trapping times can be of the same order of magnitude as the other times, the effective duty cycle for QITs are higher than for QMFs in full-scan mode, accounting for the higher sensitivity of QITs. On the

other hand, very little improvement in duty cycle is achieved in SIM mode for QITs, so little difference is observed over QMFs in SIM mode.

1.4.3. Tandem Mass Spectrometry (MS/MS)

1.4.3.1. MS/MS in the Quadrupole Mass Filter

Tandem mass spectrometry (MS/MS) is a technique in which ions are selected in the first stage (or step) of analysis, subjected to fragmentation and their fragments analyzed in a second mass analysis stage (or step). MS/MS is accomplished in beam instruments, such as the QMF, by placing mass analyzers in series, Figure 1.8.

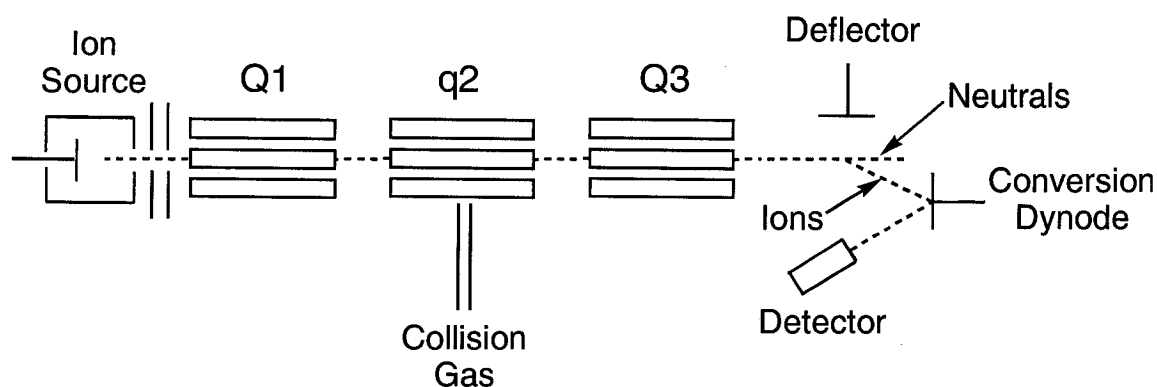


Figure 1.8. Triple quadrupole mass spectrometer (QqQ). (Adapted from a drawing by Dr. Louis Ramaley).

In this set-up, the first and third quadrupoles (Q1 and Q3) act as true mass filters, while the central one (q2) is operated without the dc voltage. In this RF-only mode, no mass separation occurs, therefore q2 acts as collision cell and ion guide. In MS/MS, the ions selected in Q1 collide with an inert gas in q2, usually argon, in a process known as collision-induced dissociation (CID). Typically in these instruments, ions undergo many collisions in q2 and the fragments produced by the collisions are guided into Q3 where they are analyzed.

The ionization method selected for an MS/MS experiment, especially when analyzing mixtures, must produce ideally as few ions of different m/z ratios as possible per component in the mixture. Therefore, “soft” ionization techniques

such as CI, ESI, APCI and MALDI, which tend to give few fragment ions, are preferable to “hard” ionization techniques such as EI. Further, higher sensitivity and lower detection limits may be achieved if the ion current for a given analyte is concentrated in one ion of a specific m/z value and not diluted among several ions of different m/z values (Busch *et al.* 1988, pp 8–9).

MS/MS may provide better sensitivity and detection limits than a single stage of mass spectrometry when analyzing mixtures. This improvement arises because the first stage of mass analysis “filters” out much of the chemical noise, which increases the signal-to-noise ratios for the ions observed in the MS/MS experiment (de Hoffmann *et al.* 1996, pp 128–131).

There are four types of MS/MS analyses: precursor-ion, neutral loss, product-ion and selected reaction monitoring (SRM) scans (Figure 1.9) (de Hoffmann *et al.* 1996, p 50). The first two scans permit identifying compound classes, whilst the third one is useful for detecting unknown compounds in mixtures.

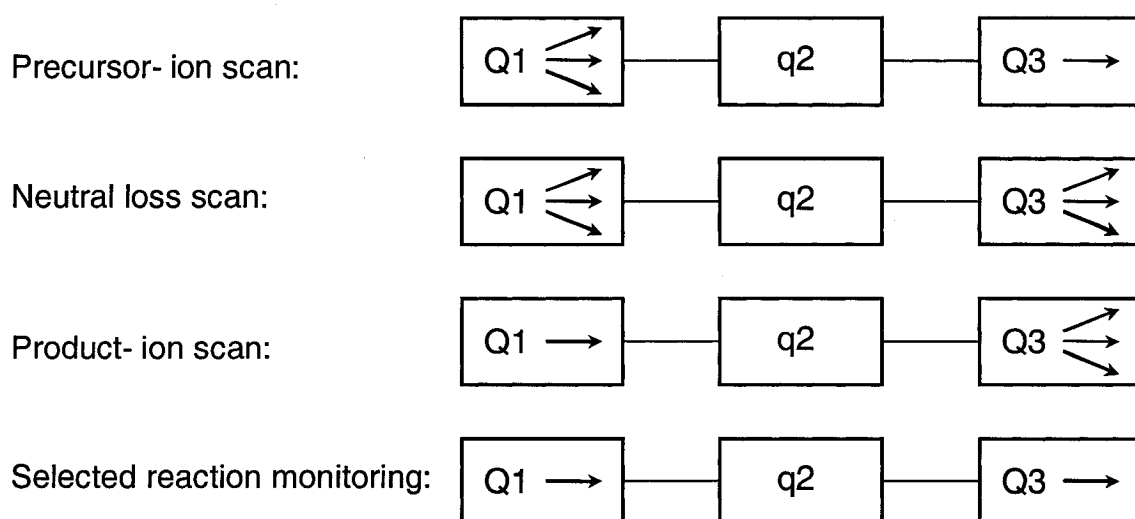


Figure 1.9. MS/MS scan modes in a triple quadrupole mass spectrometer.

Precursor-ion spectra are obtained by selecting an ion of a specific m/z value in Q3 and scanning Q1 over the mass range of expected precursor ions.

This analysis is useful for detecting all precursor ions that fragment to give a common product ion.

In a constant neutral loss scan, Q1 and Q3 are scanned with a constant mass difference, which corresponds to the mass of the neutral fragment. This type of analysis identifies all precursor ions formed from a complex mixture that fragment by loss of the specified neutral fragment.

Product-ion spectra are obtained by setting Q1 to the m/z value of the precursor ion and scanning Q3 over the mass range of expected fragment ions. This scan is especially useful for identifying compounds present in complex mixtures and unresolved chromatographic peaks (Busch *et al.* 1988, p 11).

Lower detection limits for a targeted compound can be achieved if selected reaction monitoring (SRM) is performed. In this MS/MS experiment, the first analyzer is set to pass only the precursor ion, and the third analyzer is set to pass a specific product ion. Therefore, the fragmentation pattern of the compound under study must be known before this type of scan is performed. Although SRM is less specific than any of the above scans, it provides increased specificity over selected ion monitoring (SIM), since many precursor ions can have the same mass but can give rise to different product ions.

1.4.3.2. MS/MS in the Quadrupole Ion Trap

MS/MS in ion-trapping instruments is performed *via* a tandem-in-time method, rather than tandem-in-space. This means that each stage of MS/MS on the QIT is performed in the same analyzer, sequentially in time. In contrast, a beam instrument, such as a triple quadrupole (QqQ), uses one analyzer for each stage of MS/MS. Therefore, in ion-trapping instruments multiple stages of MS/MS (MS^n) can be performed without instrumental modifications, with the number of MS/MS stages limited only by the ion intensity (Payne and Glish 2005). A limitation of the QIT, though, is that certain scan modes of QqQ mass spectrometers, namely simple precursor-ion and neutral loss scans, are currently not possible.

The sequence of events that conforms an MS/MS experiment on an ion trap is called a *microscan*. The time periods that conform a *microscan* for a QIT operating in product-ion mode are: ion injection, isolation of the desired precursor ion, excitation of the precursor ion, and detection of the product ions. To isolate a precursor ion, ions of both lower and higher m/z than that of the precursor must be ejected from the trap. Lower m/z ions are ejected *via* mass-selective instability (explained earlier p 27) and higher m/z ions are ejected using resonance ejection (Kaiser *et al.* 1989). Ion ejection *via* resonance is possible because each m/z ion oscillates in the trap with a characteristic frequency, known as the secular frequency. This frequency is used to increase the kinetic energy of selected ions by resonance. Resonance is induced by matching the frequency of a supplementary AC voltage applied to the end-cap electrodes to the secular frequency of the ion. Ions oscillating at the frequency of the supplementary AC voltage will become unstable and will be ejected from the trap.

Activation of the isolated precursor ion is usually achieved *via* resonance excitation (March *et al.* 1990). This procedure employs the same phenomenon of resonance as the resonance ejection method discussed above. However, in order to increase the kinetic energy of the precursor ion without ejecting it from the trap, a low-amplitude tickle voltage is applied to the end-cap electrodes. After excitation, ions are activated by collisions with helium damping gas. These collisions convert the kinetic energy of the precursor ion to internal energy that induces its dissociation. The resulting product ions are then ejected mass selectively for detection. Further product ion isolation and dissociation steps may be incorporated into the duty cycle to perform more stages of MSⁿ.

As the precursor and product ions have different secular frequencies, the fragment ions will no longer be in resonance with the excitation frequency and, since they cannot pick up further energy no second-generation product ions will be produced. Therefore, exact relationships between precursor and product ions can be determined and the “genealogical” mapping of the entire fragmentation process can be obtained (Volmer and Sleno 2005b). The linked information

between precursor and fragment ions is usually difficult to assess in QqQ because product ions tend to undergo further collisions to give additional products. Consequently, QITs tend to yield collision-induced dissociation spectra with a limited number of fragment ions, in comparison to QqQ spectra.

Collision energies in QIT and QMF mass spectrometers are similar in magnitude, typically in the 1–100 eV range. Helium is typically the collision gas in the QIT, whereas argon is commonly used in triple quadrupoles. With heavier gases such as argon, more kinetic energy can be converted to internal energy per collision and this leads to a different internal energy distribution and notable differences in MS/MS spectra (de Hoffmann *et al.* 1996, pp 134–136; Payne and Glish 2005).

1.5. Research Objectives

New environmental regulations requiring a reduction in the amount of sulfur in fuels are driving the need for better analytical methods. New analytical methods must be rapid, sensitive and selective. These methods need to be sensitive because of the lower levels being analyzed and selective because structural features create differences in the ability to remove sulfur using the current HDS technology.

PASHs are commonly present with a complex mixture of PAHs in petroleum samples. Finding procedures for the detection and quantification of PASHs in the presence of PAHs is extremely difficult because 1) PASHs are usually present in lower concentration compared to the PAHs and 2) the physico-chemical properties of PAHs and PASHs are so similar that poor class separation is usually achieved using the current workup schemes for the analysis of aromatic compounds.

One approach to obtain better sensitivity is to concentrate sulfur-containing compounds prior to detection. This can be achieved by using adsorbents that interact specifically with sulfur. Selectivity can be enhanced if a selective detector, such as the mass spectrometer, is employed after chromatographic separation.

The objectives of this work are two fold: 1) to develop adsorbents that interact specifically with sulfur to pre-concentrate and separate sulfur-containing compounds from PAHs in complex mixtures and 2) to investigate various MS ionization methods and tandem mass spectrometry to determine if better sensitivity and/or selectivity for the analysis of PASHs can be obtained.

The first objective was addressed first and an adsorbent system was developed as explained later. Observations made while addressing the second objective lead away from developing specific methods for the analysis of PASH compounds and into an investigation of ionization mechanisms and details of tandem mass spectrometry. Therefore, testing the adsorbent system on real-world samples was not carried out.

The observations mentioned above lead to changing the objectives of this work to 1) determining the APCI ionization mechanism for model PACs in solvents useful for LC/MS (which involved theoretical thermodynamic calculations), 2) investigating the mechanism of collisional dissociation of PASHs and 3) investigating the use of naturally occurring heavy isotopes in tandem mass spectrometry.

Chapter 2. Selective Adsorbents for Sulfur Compounds

2.1. Introduction

The use of selective adsorbents to pre-concentrate sulfur compounds in oil samples is important because sulfur-containing compounds may be present in very complex mixtures and/or in very small amounts. Furthermore, adsorbents for the removal of PASHs from crude oils must interact selectively with sulfur in the presence of large excesses of non-sulfur-containing aromatic compounds. The objective of this part of the thesis is to develop adsorbents that interact specifically with sulfur to pre-concentrate sulfur compounds and separate PASHs from similar compounds, for example PAHs, that can interfere with the analysis of PASHs.

Transition metals are important as catalysts in the chemical and petrochemical industries (<http://www.stillwaterpalladium.com/uses.html>, access date: January 29, 2007). Sulfur compounds are well known to act as inhibitors of the catalyst activity. Of all the transition metals used as catalysts, palladium appears to be the most liable to sulfur poisoning (Environmental Protection Agency staff paper on gasoline sulfur issues, <http://www.epa.gov/oms/regs/ld-hwy/tier-2/sulf-ppr.pdf>, access date: January 30, 2007). This toxicity could be related to the ability of sulfur to form strong bonds with the catalyst surface. Several studies have demonstrated substantial overlap of the sulfur *p*-states with the palladium surface *d*-band which creates a strong covalent bond between sulfur and palladium (Rodriguez *et al.* 1998).

The affinity of sulfur for transition metals can be conveniently used in order to develop adsorbents to separate sulfur-containing compounds from other polycyclic aromatic compounds. Transition metals such as Pd, Cu and Ag, supported on silica gel, alumina and zeolites have been used for the selective adsorption of PASHs in the presence of PAHs. The advantages and drawbacks of several procedures developed for the group separation of PASHs and PAHs through complexation with metal ions will be described briefly.

2.1.1. Separation through Complexation with Metal Ions

Pyell and co-workers (Pyell *et al.* 1997) tested a chelating silica gel column loaded with Ag(I) or Pd(II) cations as a stationary phase for the separation of PASHs (number of condensed rings ≤ 3) and PAHs. Their results showed that the Pd(II) loaded column was more selective towards PASHs than the Ag(I) loaded phase. The capacity ratio (k') for the PASHs investigated with the Pd(II) column was greatly enlarged ($k' > 10$) in comparison to the capacity ratio of PAHs on the same column ($k' \leq 1$) and of PASHs on the unloaded column ($k' \leq 1$). PASHs can be eluted from the column with isopropanol or hexane.

Nishioka and co-workers (Nishioka *et al.* 1986) developed a method for the isolation of PASHs from the aromatic fractions of coal-derived materials using 5% palladium chloride deposited on silica gel as sorbent. According to the procedure, PAHs eluted from the column with the first 30 mL of eluent (chloroform/hexane, 1:1 v/v), while PASHs eluted with the next 50 mL. However, the principal inconvenience of the method is that PASHs elute in the form of PdCl₂/PASH complexes that need to be destroyed with diethylamine prior to GC analysis, if hydrogen is used as a carrier gas, to avoid reduction of the more reactive PASHs. To analyze the samples directly and avoid adding diethylamine, Andersson (Andersson 1987) used a small amount of an aminopropyl-bonded silica phase at the exit of the PdCl₂/silica column developed by Nishioka to retain all the PdCl₂ and destroy the PdCl₂/PASH complexes. The authors observed, though, that PASHs with a terminal thiophene ring attached less strongly to the PdCl₂/silica gel adsorbent, with or without the aminopropyl-bonded silica phase and, as a result, some of the benzothiophenes eluted along with the PAHs. Later studies suggest (Nishioka 1988) that the strength of the sulfur–Pd interaction is correlated with the Hückel π –electron density. PASHs with higher π –electron densities are more strongly retained by the PdCl₂/silica column. The π –electron density of benzothiophene is 1.663 and that of dibenzothiophene is 1.722; benzothiophene interacts less strongly with PdCl₂ and as previously observed, eluted together with the PAH fraction.

McKinley and Angelici (McKinley and Angelici 2003a) developed a procedure to extract DBT and 4,6-Me₂DBT (411 ppmw sulfur each) from simulated, hydrotreated petroleum feedstocks, by selective adsorption on AgNO₃/silica gel (1.734 grams, 10% w/w of AgNO₃). The results showed that about 98% of the initial PASH amount was retained on the adsorbent and could be recovered using diethyl ether as eluent. However, the selectivity of the adsorbent towards PAHs was not studied.

Yang and co-workers (Yang *et al.* 2003b) tested silver- and copper-exchanged faujasite-type zeolites (Ag(I) or Cu(I)-zeolite Y) as adsorbents for the deep desulfurization of commercial fuels at ambient temperature and pressure. Their results indicated that both Ag(I) and Cu(I)-zeolite Y could adsorb thiophene preferentially over benzene and that Cu(I) is stronger than Ag(I) in binding with thiophene. The sulfur content in diesel fuels was reduced from 430 to less than 0.2 ppmw using Cu(I)-zeolite Y at a sorbent capacity of 34 cm³ of clean fuel produced per gram of sorbent. The authors claimed that the sorbent binds thiophenic compounds selectively by π -complexation. The mechanism of π -complexation involves electron donation from the π orbital of thiophene to the vacant s orbital of metals (σ -donation) and simultaneously, back-donation of electrons from the d orbitals of the metal to the π^* orbital of thiophene (π -back donation). They suggested that σ -donation is more important for thiophene while π -back donation is predominant for benzene. Although the authors have shown by theoretical calculations that the π -complexation strength is higher for thiophene compared to benzene, it is not clear how the adsorbent can be selective towards PASHs due to π -complexation. The authors have noted, though, that the performance of the adsorbent decreases when aromatic compounds are present in the fuel, probably due to competitive adsorption between sulfur compounds and aromatics by π -complexation (Hernández-Maldonado and Yang 2003).

As opposed to the mechanism of π -complexation proposed by Hernández-Maldonado and Yang, McKinley and Angelici (McKinley and Angelici

2003a) have suggested that Ag^+ coordinates to dibenzothiophene through the sulfur atom. In order to characterize the interaction between Ag^+ and DBT, the authors recorded the ^1H and ^{13}C NMR spectra of free DBT and DBT/ AgBF_4 (1:1) in d_6 -acetone at 200 K. The small but measurable difference between the chemical shifts of free DBT and DBT in the DBT/ AgBF_4 solution was consistent with what has been reported previously for well-characterized transition metal complexes of DBT, which coordinate to the metal ion through the sulfur atom ($\Delta\text{ppm} < 4$ in ^{13}C NMR) (McKinley and Angelici 2003b). The authors claim that if Ag^+ were coordinated through the phenyl ring of DBT, much larger, upfield chemical shifts in the ^1H and ^{13}C NMR spectra would be expected ($\Delta\text{ppm} \sim 90$ in ^{13}C NMR), as observed in $[\text{Ru}(\text{NH}_3)_5(\text{benzothiophene})]^{2+}$ complexes, in which benzothiophene is coordinated to the metal ion through the olefin group at C2–C3 (McKinley and Angelici 2003b).

In the following section, the principal characteristics and common applications of silica gel, alumina and zeolites will be summarized. These will be the support materials used in the thesis research.

2.1.2. Support Materials

2.1.2.1. Silica Gel

Silica gel is a porous, amorphous form of silica. Silica, SiO_2 , is a mineral that occurs naturally in several forms. Commercially, silica gel is prepared by mixing a solution of sodium silicate and a mineral acid (HCl or H_2SO_4), (2.1) (Yang 2003a, p 132). As a result, finely divided particles of hydrated SiO_2 are produced, which polymerize on standing into a white jelly-like precipitate or silica gel. The resulting gel is then washed, dried and activated.

(2.1)



Silica gel consists of a three-dimensional network of contiguous spherical particles (10–1000 Å in diameter, Iler 1979 p 462) or short chains of particles linked rigidly together (Iler 1979, pp 462, 479, 533). The structure of silica gel is

primarily composed of polymerized siloxane (Si–O–Si) bonds, internal OH groups in the silica structure and four basic types of surface silanol groups (*i.e.* isolated, H-bonded, geminal and vicinal) (Yang 2003a, pp 134–135). The surface silanol groups are the primary sites for adsorption of water and other polar compounds, *via* hydrogen bond formation (Yang 2003a, p 137). Furthermore, silica gel has relatively large pores (20–2000 Å, Iler 1979, p 481) and the hydrogen-bonded water can be easily removed by heating at 150 °C (Iler 1979, p 505).

Because of its large capacity for water (~40 % by weight) and ease in regeneration, silica gel is most commonly used as a desiccant (Yang 2003a, p 131). In addition, modified silica gels with a monomolecular layer of organic ligand, are increasingly used as stationary phases in chromatography.

2.1.2.2. Alumina

Alumina or Al_2O_3 is produced on a commercial scale from bauxite *via* the Bayer process. Bauxite is a mineral composed primarily of gibbsite ($\alpha\text{-Al}_2\text{O}_3\cdot 3\text{H}_2\text{O}$), bohemite ($\alpha\text{-Al}_2\text{O}_3\cdot \text{H}_2\text{O}$), diaspore ($\beta\text{-Al}_2\text{O}_3\cdot \text{H}_2\text{O}$) and a mixture of iron, silicon and titanium oxides. In the Bayer process, the hydrated aluminas are selectively dissolved in NaOH and separated from the other insoluble oxides. After separation from the insoluble bauxite residue, the hydrated aluminas transform into different forms of Al_2O_3 upon heat treatment (Yang 2003a, pp 146–149).

Unlike silica gel, activated alumina is crystalline. Among the aluminas, $\gamma\text{-Al}_2\text{O}_3$ is the form most commonly used as an adsorbent and in catalytic applications. As opposed to silicas, Lewis acid sites (Al^{3+} sites that can accept electrons) are usually abundant on aluminas. Therefore, aluminas are selective toward Lewis bases such as alcohols, aldehydes, ethers and ammonia. In addition to having Lewis acid sites, aluminas with fully hydrated surfaces have also Brønsted acid sites (OH groups that can donate protons) (Yang 2003a, pp 149–151).

Because NaOH is used to extract alumina from bauxite, activated aluminas always contain Na_2O , typically 0.3% by weight. However, the Na_2O

content can be increased by impregnating solutions of alkali bicarbonates on alumina followed by decomposition at 500 °C. Alkalized alumina, with 1–10% by weight of alkali oxides, is a commercial sorbent for CO₂ removal (Yang 2003a, pp 152–154).

Aluminas are also used for the removal of ions from water. At pH values below the zero point charge (ZPC), the alumina surface has a net positive charge that can be counter-balanced by adsorbing anions, while at pH values above the ZPC, cations will be adsorbed. The zero point charge (ZPC) is the pH value, typically between 8 and 10, at which the net charge on the surface of activated alumina is zero (Yang 2003a, pp 150–152). Because of its properties, alumina has been employed more frequently than silica gel as a sorbent.

2.1.2.3. Zeolites

Zeolites are crystalline aluminosilicates, which contain micropores occupied by exchangeable cations and water molecules. Because of their unique porous properties, zeolites have found application in several areas, for example, in petrochemical cracking, in water softening and purification, and in the separation and removal of gases and solvents (Christie *et al.* 2002).

The framework of zeolites (Figure 2.1) is made up of tetrahedra with silicon or aluminum atoms (denoted as T atoms) in the middle, and oxygen atoms at the corners. Each of the four oxygen atoms is shared by two tetrahedra, with no two aluminum atoms sharing the same oxygen (Ramamurthy 2000). As opposed to aluminum atoms, two silicon atoms may reside next to each other. For this reason, the proportion of aluminum in zeolites is always lower than that of silicon.

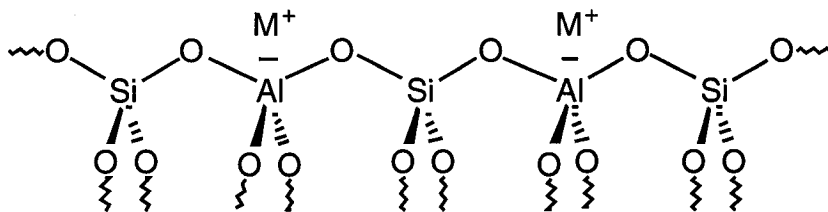


Figure 2.1. The framework of zeolites, (M^+ is a monovalent charge balancing cation).

As each aluminum-containing tetrahedron has a net charge of -1 , the total framework charge of zeolites is negative and must be counter-balanced by a cation. Although a wide range of ions such as Cu^{2+} and NH_4^+ may be exchanged into zeolites, the most favored charge balancing cations in natural zeolites are alkaline or alkaline earth metal cations (Na^+ , K^+ , Ca^{2+} , Mg^{2+} and Ba^{2+}). The negative charge can be also balanced by incorporating protons into the zeolite framework. Therefore, zeolites may act as acid catalysts, and this property is used to initiate reactions (e.g. catalytic cracking, isomerization and alkylation) in molecules present in their pores and cavities (Christie *et al.* 2002).

The formula of a zeolite can be expressed as $\text{M}_p\text{D}_q[\text{Al}_p + 2q \text{ Si}_r\text{O}_{2p + 4q + 2r}] \cdot s \text{ H}_2\text{O}$. As such, the zeolite framework requires twice as many oxygen atoms as T atoms, while charge balance requires that the number of aluminum atoms equals the sum of the monovalent ions (represented as M_p) plus twice the number of divalent ions (represented as D_q). The single $(\text{AlO}_4)^{-5}$ and $(\text{SiO}_4)^{-4}$ tetrahedra are considered the primary building blocks of the zeolite framework. These tetrahedra are linked together to form secondary building units (SBUs) and the entire zeolite framework is usually made up of one type of SBU.

Since this research deals with Y zeolites, only a description of the internal structure of Y zeolites will be provided. Zeolite Y belongs to the faujasite family (termed FAU according to IUPAC rules). In a conventional Y zeolite, the silicon content exceeds the aluminum content by a ratio of about 2.5 to 1. Zeolite Y has the following unit cell composition: $\text{M}_{56}(\text{AlO}_2)_{56}(\text{SiO}_2)_{136} \cdot 253\text{H}_2\text{O}$, where M is a monovalent ion. The framework of zeolite Y is composed of sodalite cages, which are linked through hexagonal prisms (Figure 2.2).

Assembly of the sodalite cages forms a spherical supercage, which is about 13 Å in diameter. A unit cell of zeolite Y consists of eight supercages. Sodalite cages and hexagonal prisms are too small to accommodate most organic molecules, whereas the spherical supercages are large enough to accommodate relatively large organic molecules. The supercage is accessible through four ring windows or pores, which are 7.4 Å in diameter and contain 12 T atoms each (Figure 2.2) (Ramamurthy 2000). As a result, the supercages form a

three-dimensional network with each supercage connected to four others in a tetrahedral-like assembly.

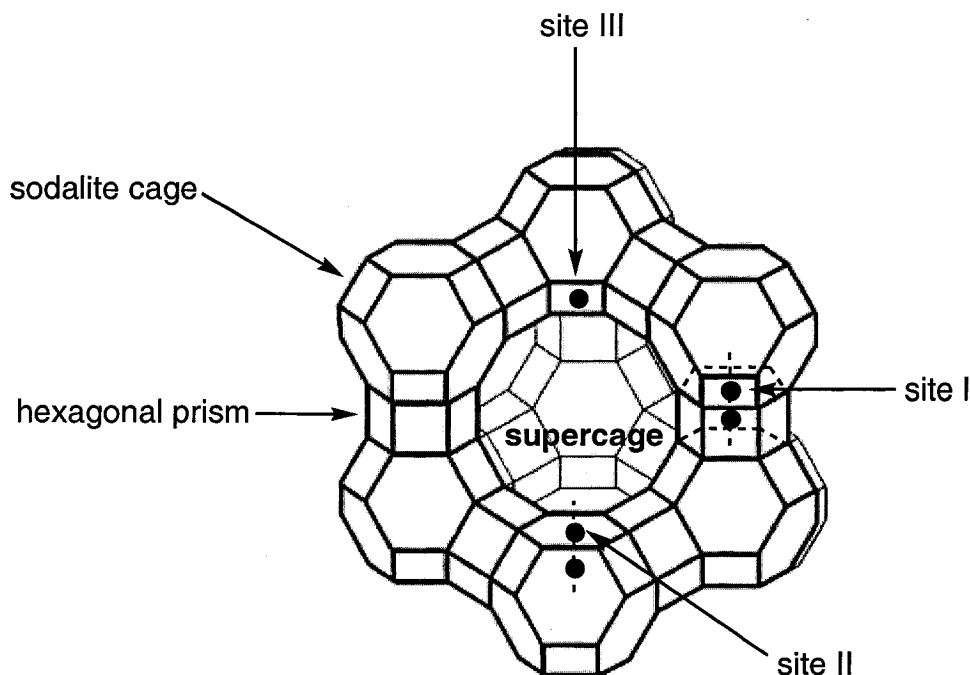


Figure 2.2. Representation of the zeolite Y structure and occupancy sites for charge-balancing cations.

Charge-balancing cations can occupy three different positions in zeolite Y (Figure 2.2). The first type (site I) with 16 cations per unit cell, is located on the hexagonal prism faces between the sodalite cages. The second type (site II) with 32 cations per unit cell, is located in the open hexagonal faces of the sodalite cages. Finally, the third type (site III), with 8 cations per unit cell, is located on the walls of the large supercage cavity. Only cations at sites II and III are accessible to the organic molecules adsorbed within a supercage (Ramamurthy 2000; Kaduk and Faber 1995).

Zeolites are highly hydrophilic. They may take up water to as much as 20 % or more of their weight at ambient conditions (Hernández-Maldonado and Yang 2003). Water molecules are coordinated to the framework cations and hydrogen bonded to the framework oxygen. However, water can be removed by heating at 400–500 °C for several hours. The framework of zeolites generally

remains intact upon heating because of its high thermal stability (Christie *et al.* 2002).

2.2. Experimental

All solvents and chemicals were used without further purification. The solvents acetonitrile, hexanes (Optima grade) and dichloromethane (Pesticide grade) were purchased from Fisher (Nepean, ON, Canada). Isopropanol (Reagent grade) was provided by ACP Chemicals (Montreal, Quebec, Canada). The copper salts CuSO_4 , $\text{Cu}(\text{NO}_3)_2 \cdot 3\text{H}_2\text{O}$ and the solution of PdCl_2 in HCl (5 %) were obtained from Fisher (Fair Lawn, NJ, USA). Cupric chloride ($\text{CuCl}_2 \cdot 2\text{H}_2\text{O}$) (Reagent grade) was purchased from Anachemia (Toronto, ON, Canada). Dibenzothiophene (DBT), phenanthrene (PHEN), silica gel (60–100 mesh, 150 Å, grade 645) and sodium-exchanged faujasite Y type zeolite (Na/zeolite Y) were obtained from Aldrich (Milwaukee, WI, USA). Alumina (basic Al_2O_3 for column chromatography, 90 active) was provided by Brinkmann Instruments LTD (Rexdale, ON, Canada). Deionized water was used as obtained from a Barnstead NANOpure purifier (Fisher, Nepean, ON, Canada).

2.3. Results and Discussion

The adsorbents used in this study include Na/zeolite Y, Cu(II)/zeolite Y, reduced Cu(II)/zeolite Y, $\text{Cu}(\text{NO}_3)_2/\text{SiO}_2$, $\text{CuSO}_4/\text{SiO}_2$, $\text{CuCl}_2/\text{SiO}_2$, $\text{PdCl}_2/\text{Al}_2\text{O}_3$ and $\text{PdCl}_2/\text{SiO}_2$ (the preparation of these materials is explained below). Each adsorbent (0.3 grams placed in a 5" Pasteur pipette) was first equilibrated with hexanes.

Dibenzothiophene (DBT) and phenanthrene (PHEN) were used as model compounds to study the specificity of the adsorbents. After equilibration, 1 mL of a solution containing either DBT (20 mg L^{-1} in hexanes) or both DBT and PHEN (20 mg L^{-1} each in hexanes) was added to the column. The selectivity of the adsorbents was tested by using (in this order) hexanes, dichloromethane (CH_2Cl_2), acetonitrile (MeCN) and isopropanol to elute the model compounds.

DBT and PHEN were detected off-line by recording their UV spectra using an HP 8452A Diode Array Spectrophotometer. The UV spectra of DBT and PHEN are shown in Figure 2.3. Phenanthrene was selected on the following basis: a) it is a PAH with three conjugated aromatic rings as DBT and b) the absorbance value for λ_{\max} in the UV spectrum of both DBT and PHEN (2 mg L^{-1} each in hexanes) lies between 0.2 and 0.8. Every attempt at using Na/zeolite Y, Cu(II)/zeolite Y, reduced Cu(II)/zeolite Y, $\text{Cu}(\text{NO}_3)_2/\text{SiO}_2$, $\text{CuSO}_4/\text{SiO}_2$, $\text{CuCl}_2/\text{SiO}_2$, $\text{PdCl}_2/\text{Al}_2\text{O}_3$ as adsorbents for the isolation of PASHs failed for the reasons given below.

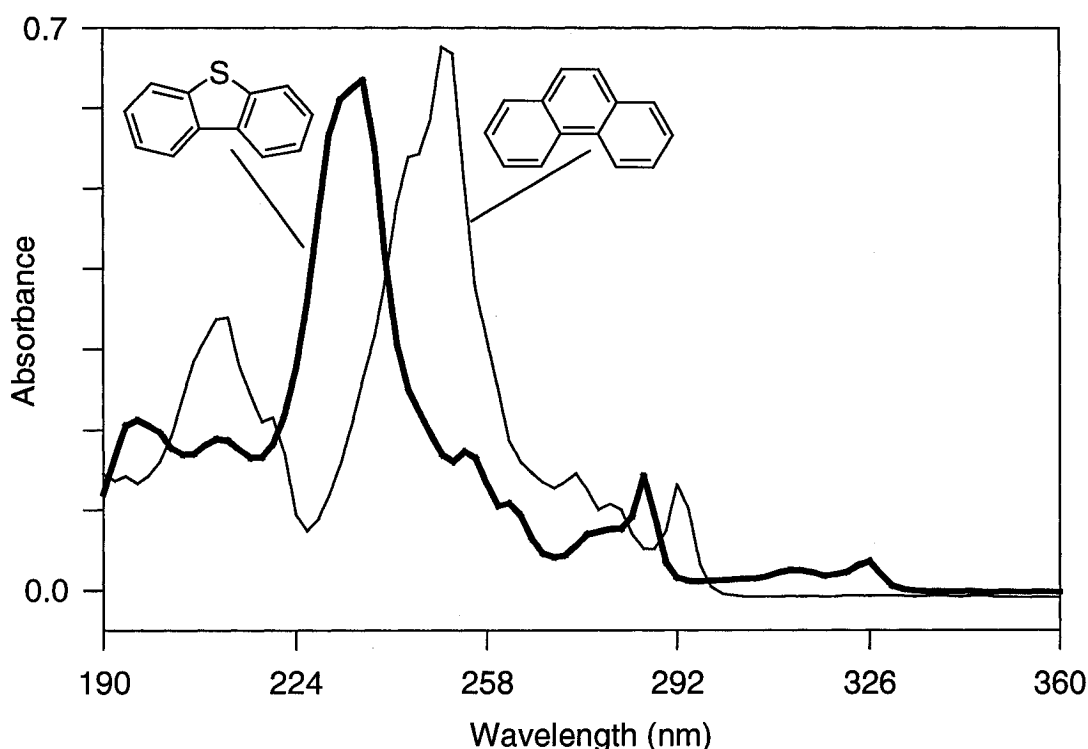


Figure 2.3. UV spectra of DBT and PHEN (2 mg L^{-1} each in hexanes).

2.3.1. Na/zeolite Y, Cu(II)/zeolite Y and Reduced Cu(II)/zeolite Y Adsorbents

The copper cation forms of Y zeolite (Cu(II)/zeolite Y) were prepared (Hernández–Maldonado and Yang 2003b) by first ion-exchanging 1.03 grams of Na/zeolite Y (zeolite Y was previously heated at 450°C for 24 hours) with 17 mL of a $\text{Cu}(\text{NO}_3)_2 \cdot 3\text{H}_2\text{O}$ aqueous solution (1 mol L^{-1}). The mixture was stirred at

room temperature for 50 hours. The adsorbent was recovered by filtration and washed with a large excess of deionized water. After drying at 100 °C for at least 24 hours, the zeolite, originally white in color, was light blue.

Na/zeolite Y and Cu(II)/zeolite Y adsorbents behaved similarly. DBT (0.02 mg) was held on both and could be eluted with 1 mL CH_2Cl_2 and not with hexanes (2 mL). This result shows that DBT seems to be held in the cavities of the zeolite Y as opposed to an interaction with Cu(II). Cu(II) on zeolite Y was then reduced in the presence of hydrogen at high temperature. The adsorbent (0.3 g) in a 5" Pasteur pipette was heated with a Bunsen burner while a flow of hydrogen passed through it (Figure 2.4).

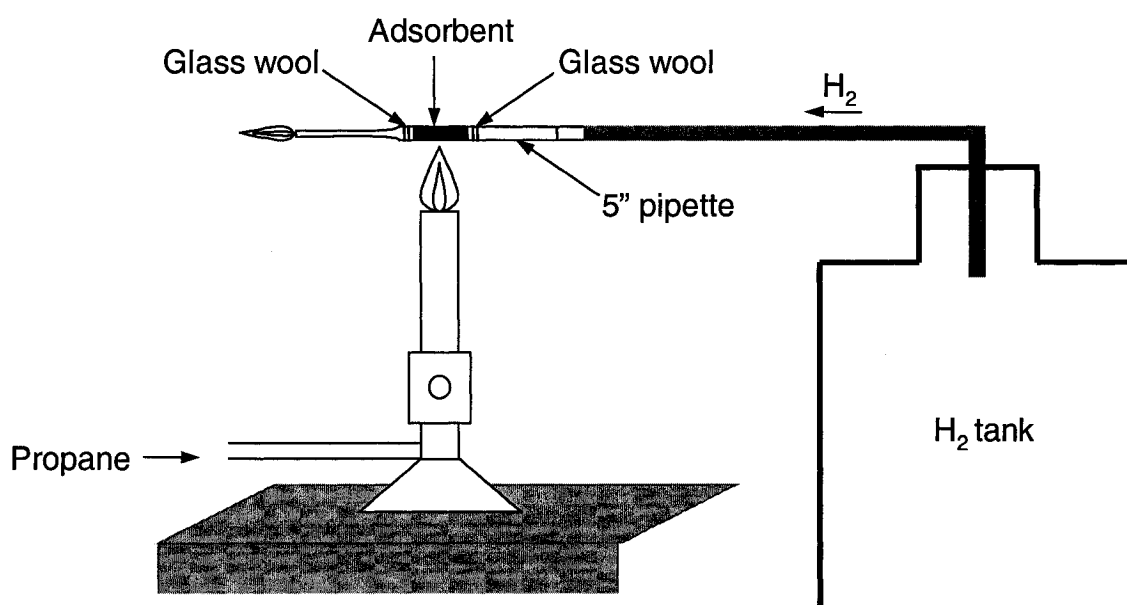


Figure 2.4. Apparatus used for the reduction and regeneration of adsorbents with hydrogen.

After reduction, the adsorbent, originally light blue, was light green. The change in color indicates reduction. However, no additional studies were done to establish the final oxidation state. DBT was more strongly retained on the reduced form of Cu(II)/zeolite Y than on the Na/zeolite Y and the Cu(II)/zeolite Y forms. However, the adsorbent disaggregates (becomes a finely dispersed powder which is not held in the column) when more polar solvents, such as

MeCN or isopropanol, were used to elute DBT. The ability of the adsorbent to work in MeCN is important given that MeCN is commonly used as a solvent in HPLC and as a modifier in SFC. High resolution separations of sulfur-containing compounds in complex samples can be performed by SFC/GC.

2.3.2. Cu(II)/SiO₂ Adsorbents

Cu(II)/SiO₂ adsorbents were prepared by adding 1 mL of deionized water and 3.2 mL of an aqueous solution of Cu(NO₃)₂•3H₂O (or CuCl₂•2H₂O or CuSO₄) (1 M each), to 4 grams of silica gel. The adsorbent was dried in the oven at 120 °C for 24 hours. The Cu(NO₃)₂/SiO₂ phase had a blue-greenish color after drying, CuCl₂/SiO₂ was yellow-green and CuSO₄/SiO₂ was light blue.

Most of the DBT (0.02 g) eluted with 2 mL of hexanes when using the Cu(NO₃)₂/SiO₂ column. The color of the Cu(NO₃)₂/SiO₂ adsorbent changed from blue-green to reddish with a bright metallic luster upon reduction with hydrogen and heat. Because of the appearance of the adsorbent, it was thought that Cu(II) was probably reduced to metallic copper. DBT was more strongly retained on the reduced form of the adsorbent than on the Cu(II) phase—it did not elute with 2 mL of hexanes and eluted completely with 2 mL of CH₂Cl₂. The adsorbent was then regenerated by flushing CH₂Cl₂ through it. However, DBT was less retained on the column when the procedure was repeated—some of the DBT eluted with 2 mL of hexanes.

Since CH₂Cl₂ was probably competing with DBT for the active sites in the adsorbent, the solvent was eliminated by passing nitrogen or hydrogen gas at high temperature through the column (Figure 2.4). After doing so, reproducible results were obtained. However, when MeCN was used to elute DBT from the column, a broad band ($\Delta\lambda = 30$ nm) with λ_{max} at 200 nm, was observed in the UV spectrum. The nature of the compound that caused the band was not determined, but it was not present in MeCN before the solvent was passed through the column. However, flushing MeCN through the column did not eliminate it. As this compound could interfere with the analysis of DBT when using MeCN, other copper salts were tested.

The $\text{CuCl}_2/\text{SiO}_2$ and $\text{CuSO}_4/\text{SiO}_2$ phases were not tested in the oxidized form. Both adsorbents were reduced under hydrogen at high temperature. Upon reduction, the $\text{CuCl}_2/\text{SiO}_2$ phase turned first into light blue and finally to red/brown color with no shiny appearance. In addition, reduction of the $\text{CuCl}_2/\text{SiO}_2$ adsorbent took longer than in the case of the $\text{CuSO}_4/\text{SiO}_2$ and the $\text{Cu}(\text{NO}_3)_2/\text{SiO}_2$ columns. DBT was not retained on the reduced form of the $\text{CuCl}_2/\text{SiO}_2$ adsorbent —unlike the reduced $\text{Cu}(\text{NO}_3)_2/\text{SiO}_2$ phase, DBT eluted completely from the reduced $\text{CuCl}_2/\text{SiO}_2$ column with 3 mL of hexanes.

Upon reduction, the $\text{CuSO}_4/\text{SiO}_2$ adsorbent changed from light blue to very dark brown with some, but much less, metallic luster than the reduced $\text{Cu}(\text{NO}_3)_2/\text{SiO}_2$ adsorbent. However, reduction took place very rapidly as in the case of the $\text{Cu}(\text{NO}_3)_2/\text{SiO}_2$ phase. DBT was more strongly retained on the reduced $\text{CuSO}_4/\text{SiO}_2$ column than on the reduced $\text{CuCl}_2/\text{SiO}_2$ phase —DBT did not elute from the reduced $\text{CuSO}_4/\text{SiO}_2$ column with 3 mL of hexanes. DBT eluted from the reduced $\text{CuSO}_4/\text{SiO}_2$ column with either 1 mL of MeCN or 1 mL of CH_2Cl_2 and reproducible results were obtained when the column was regenerated with hydrogen or nitrogen at high temperature. The broad band observed in the UV spectrum, when the reduced $\text{Cu}(\text{NO}_3)_2/\text{SiO}_2$ adsorbent and MeCN were used, was absent when DBT eluted from the reduced $\text{CuSO}_4/\text{SiO}_2$ column with MeCN. PHEN was added to the column along with DBT to test the selectivity of the adsorbent towards PAHs. PHEN was slightly less retained on the column than DBT —some of the PHEN eluted with 3 mL of hexanes. DBT and PHEN could elute completely with either 1 mL of MeCN or 1 mL of CH_2Cl_2 . However, after column regeneration with hydrogen or nitrogen, none of the PHEN eluted with hexanes. PHEN eluted along with DBT in the MeCN fraction, and they could not be separated to any extent after the first regeneration of the column.

2.3.3. $\text{PdCl}_2/\text{Al}_2\text{O}_3$ Adsorbent

$\text{PdCl}_2/\text{Al}_2\text{O}_3$ adsorbent was prepared by addition of 0.8 mL of PdCl_2 in HCl (5 % solution) and 3 mL of deionized water to 4 grams of basic alumina. The

resultant slurry was yellow-light brown. The mixture was dried in the oven at 110 °C over night and after drying the adsorbent was reddish-brown.

PdCl_2 adsorbed on alumina dissolves in relatively polar solvents such as MeCN and isopropanol. To prevent stripping of the PdCl_2 from the column, the $\text{PdCl}_2/\text{Al}_2\text{O}_3$ adsorbent was treated with 1 mL of NaOH solution (1 M) and 3 mL of deionized water. After drying in the oven at 110 °C, the adsorbent was grayish-brown. Although this formulation of Pd(II) was not stripped off the column with MeCN, the adsorbent had similar selectivity for DBT and PHEN. A small fraction of both compounds eluted with hexanes, and most of the PHEN and the DBT eluted completely with 1 mL of MeCN. The $\text{PdCl}_2/\text{Al}_2\text{O}_3$ adsorbent treated with $\text{NaOH}_{(\text{aq})}$, was reduced under hydrogen at high temperature. The column rapidly turned grey upon reduction and became somewhat shiny. However, the reduced and non-reduced forms of the column showed similar behaviour. DBT and PHEN were held to the same extent onto the column and both eluted almost completely with the first mL of MeCN.

2.3.4. $\text{PdCl}_2/\text{SiO}_2$ Adsorbent

$\text{PdCl}_2/\text{SiO}_2$ adsorbents were prepared by addition of 1 mL of PdCl_2 in HCl (5 % solution, density: 1.053 g mL^{-1}) and deionized water to silica gel followed by drying at 120 °C for 24 hours (Table 2.1).

Table 2.1. $\text{PdCl}_2/\text{SiO}_2$ adsorbents with different PdCl_2 loadings.

Adsorbent	PdCl_2 % (w/w)	Volume of deionized water (mL)	Mass of silica gel (g)
A	5.3	1	1
B	2.6	3	2
C	1.3	7	4

DBT was more strongly retained on the $\text{PdCl}_2/\text{SiO}_2$ adsorbent (1.3 % w/w PdCl_2) than on the Cu(II)/zeolite Y and Cu(II)/SiO_2 columns —comparatively less DBT eluted from the $\text{PdCl}_2/\text{SiO}_2$ adsorbent with 2 mL of CH_2Cl_2 . However,

the Pd(II) salt dissolved in MeCN or isopropanol when these solvents were used to elute DBT. Therefore, Pd(II) was reduced under hydrogen at high temperature. After reduction, the adsorbent, originally dark red turned black. Palladium adsorbed on silica could be in three different forms, finely divided palladium metal, Pd metal with absorbed hydrogen or palladium hydride.

Calibration curves of DBT and PHEN in hexanes and MeCN (Figure 2.5 to 2.8) were obtained at 232 and 252 nm (λ_{\max} for DBT and PHEN, respectively) to study the selectivity of the reduced form of the PdCl₂/SiO₂ adsorbent and to determine the recovery and the reproducibility of the analysis for different loadings of Pd(II) salt on silica gel. The relative standard deviation ($n = 5$) for the slope and intercept of each curve was about 3 % and 30 %, respectively.

Figures 2.9 to 2.12 show the selectivity of the reduced adsorbent towards DBT and PHEN with different loadings of Pd(II) and different amounts of DBT and PHEN (either 0.02 mg each or 0.1 mg each on column). Prior to UV analysis, F1 and F2 were diluted to 10 mL (when 0.02 mg of DBT and PHEN, each, was used) or to 50 mL (when 0.1 mg was used) in volumetric flasks. F1 and F2 are the fractions collected after elution of the test compounds with hexanes and MeCN, respectively.

The concentrations of DBT and PHEN in F1 and F2 were calculated according to (2.2) and (2.3), respectively. (C: concentration (mol L⁻¹), λ_1 : 232 nm, λ_2 : 252 nm, ϵ : molar absorptivity (L mol⁻¹cm⁻¹), b: cell length (1 cm) and A: absorbance).

(2.2)

$$C_{\text{DBT}} = \frac{A_{\lambda_2}(\epsilon_{\text{PHEN}})_{\lambda_1} - A_{\lambda_1}(\epsilon_{\text{PHEN}})_{\lambda_2}}{b[(\epsilon_{\text{DBT}})_{\lambda_2}(\epsilon_{\text{PHEN}})_{\lambda_1} - (\epsilon_{\text{PHEN}})_{\lambda_2}(\epsilon_{\text{DBT}})_{\lambda_1}]}$$

(2.3)

$$C_{\text{PHEN}} = \frac{A_{\lambda_1}(\epsilon_{\text{DBT}})_{\lambda_2} - A_{\lambda_2}(\epsilon_{\text{DBT}})_{\lambda_1}}{b[(\epsilon_{\text{DBT}})_{\lambda_2}(\epsilon_{\text{PHEN}})_{\lambda_1} - (\epsilon_{\text{PHEN}})_{\lambda_2}(\epsilon_{\text{DBT}})_{\lambda_1}]}$$

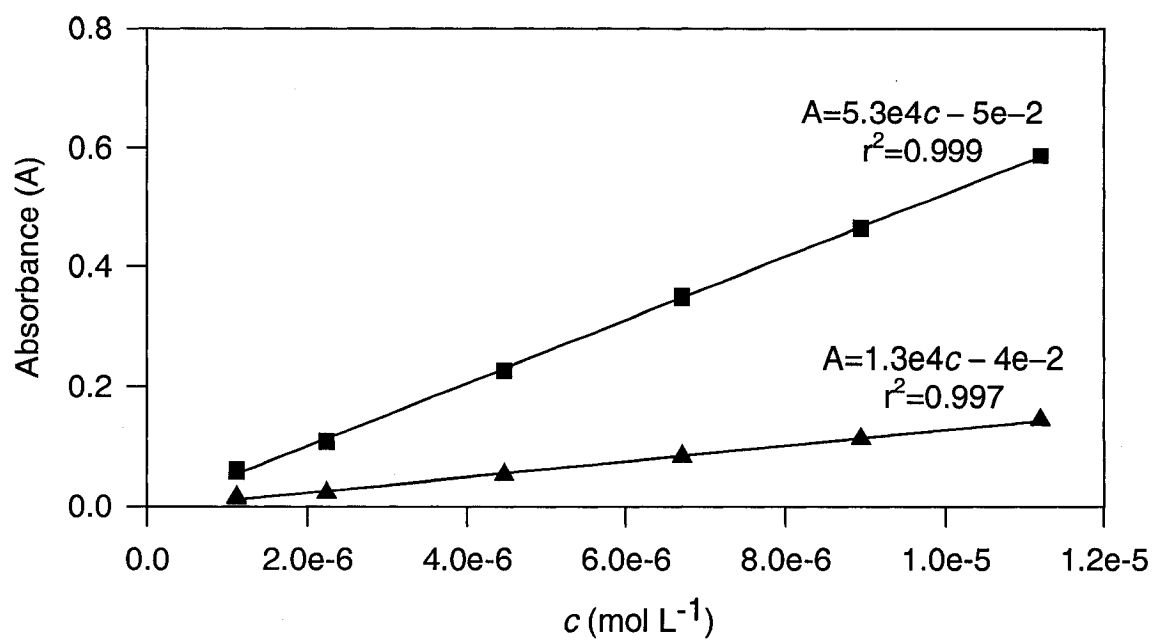


Figure 2.5. Calibration curves for DBT in hexanes (▲ 252 nm and ■ 232 nm).

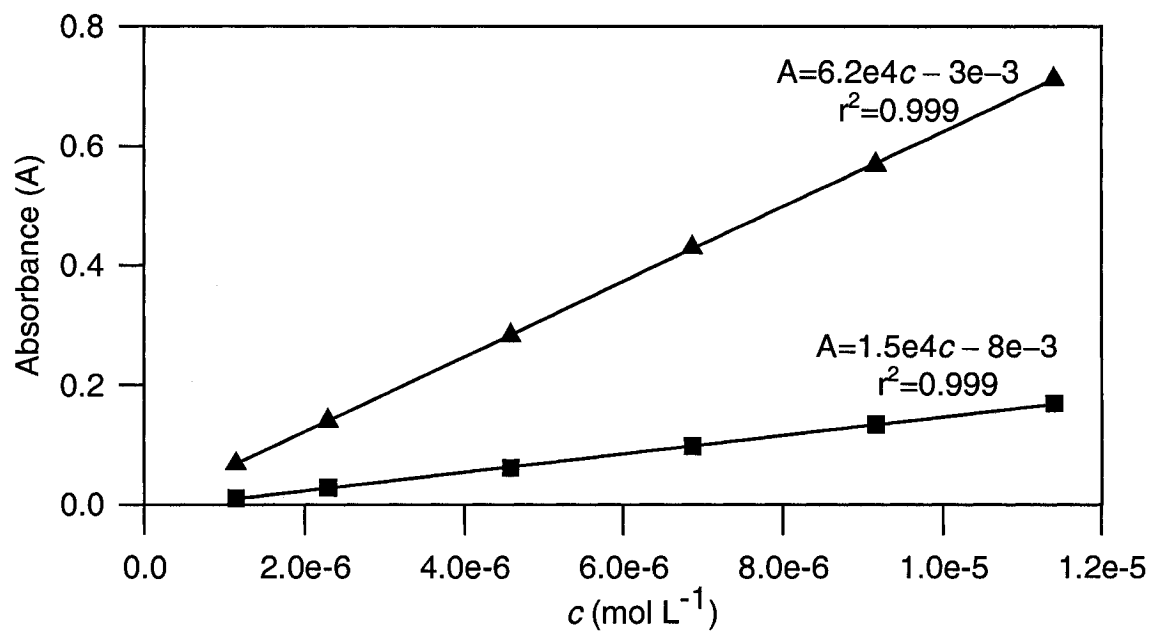


Figure 2.6. Calibration curves for PHEN in hexanes (▲ 252 nm and ■ 232 nm).

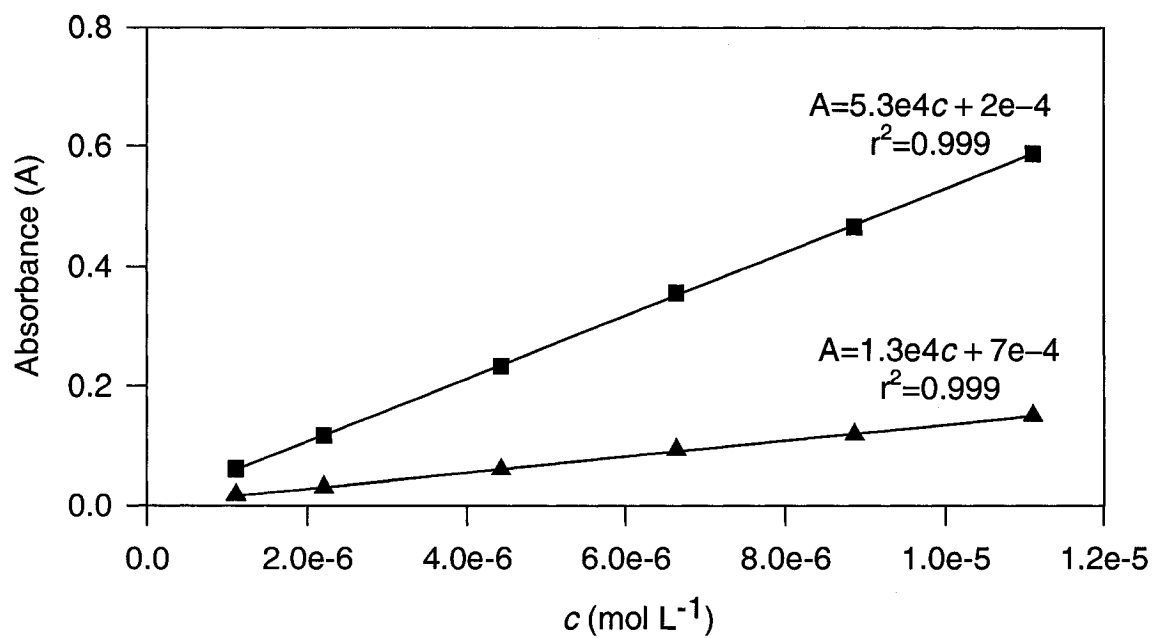


Figure 2.7. Calibration curves for DBT in MeCN (▲ 252 nm and ■ 232 nm).

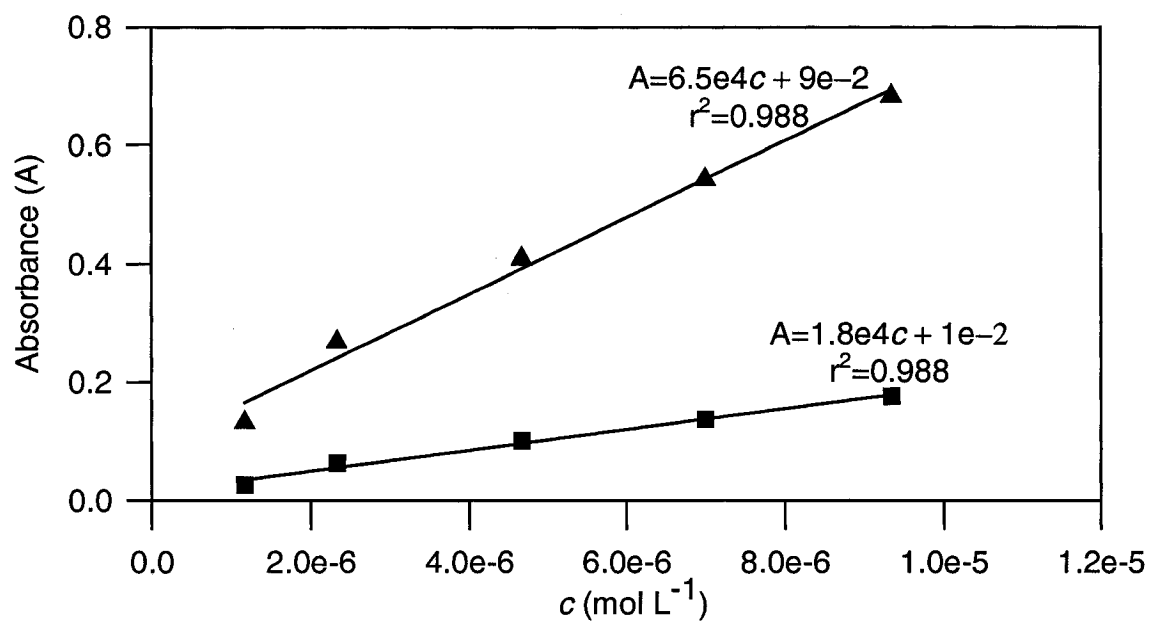


Figure 2.8. Calibration curves for PHEN in MeCN (▲ 252 nm and ■ 232 nm).

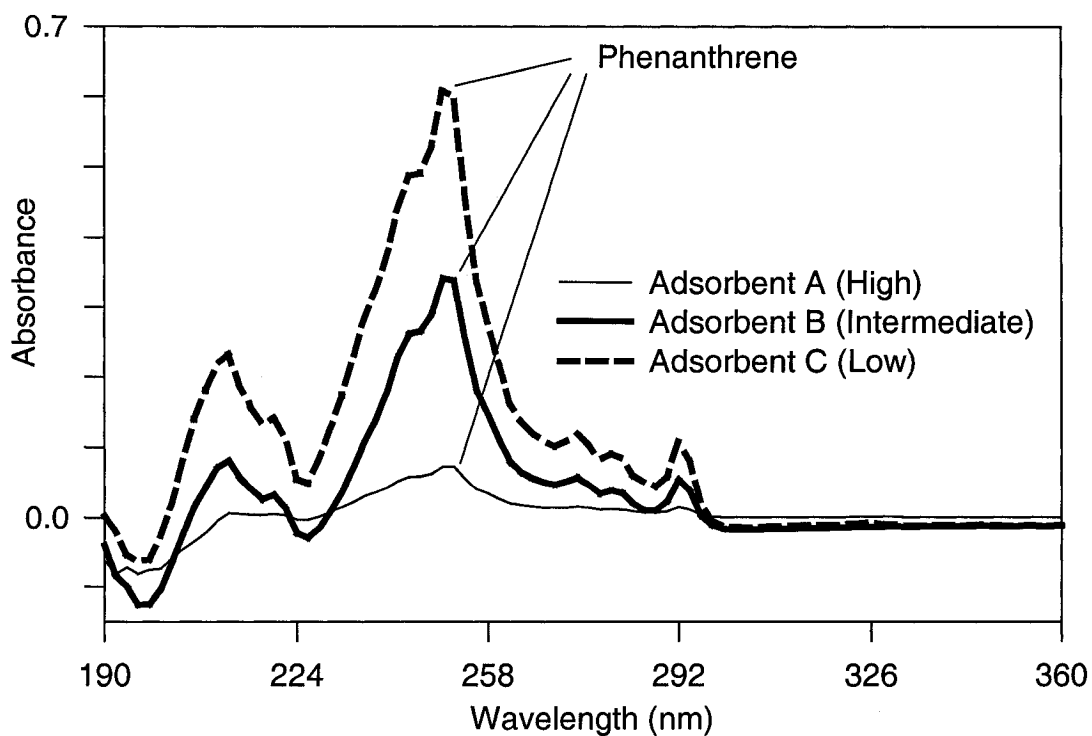


Figure 2.9. Elution with hexanes (F1, 10 mL), 0.02 mg of DBT and PHEN (each).

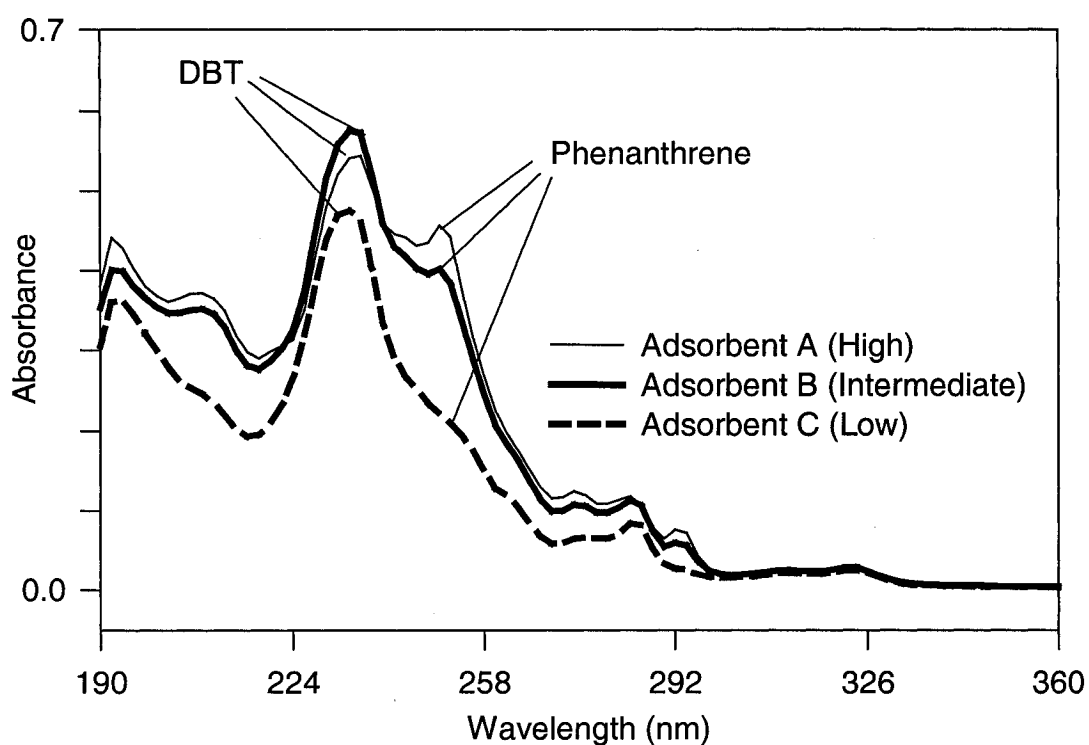


Figure 2.10. Elution with MeCN (F2, 1 mL), 0.02 mg of DBT and PHEN (each).

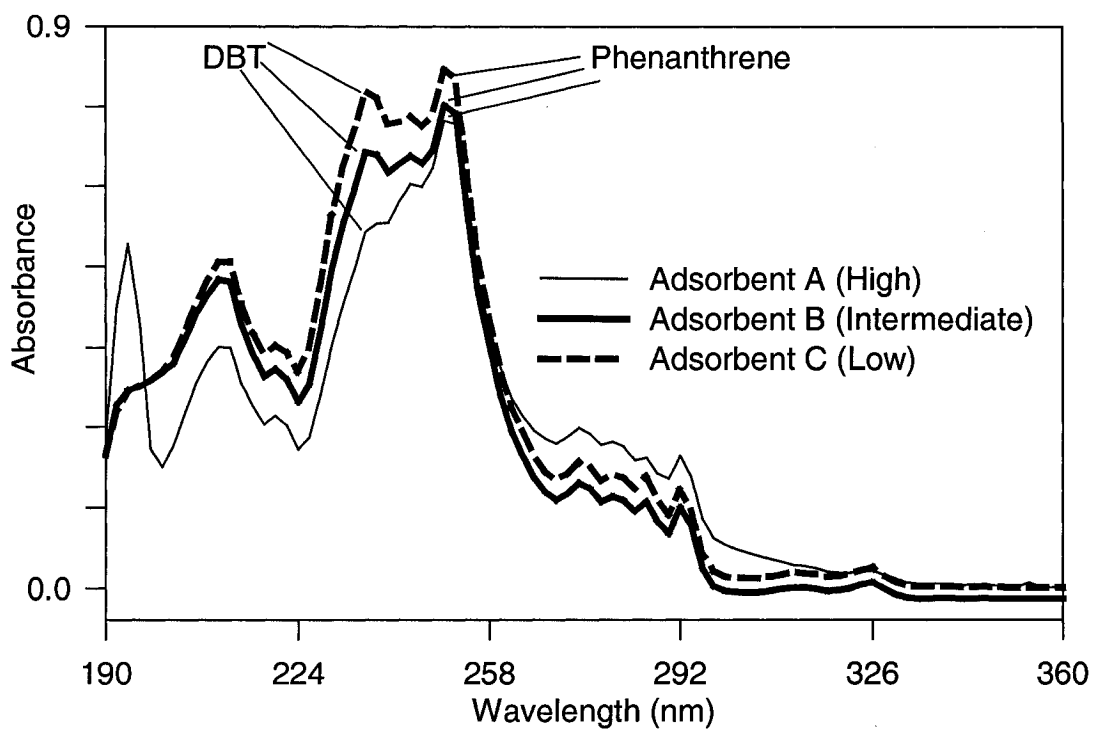


Figure 2.11. Elution with hexanes (F1, 10 mL), 0.1 mg of DBT and PHEN (each).

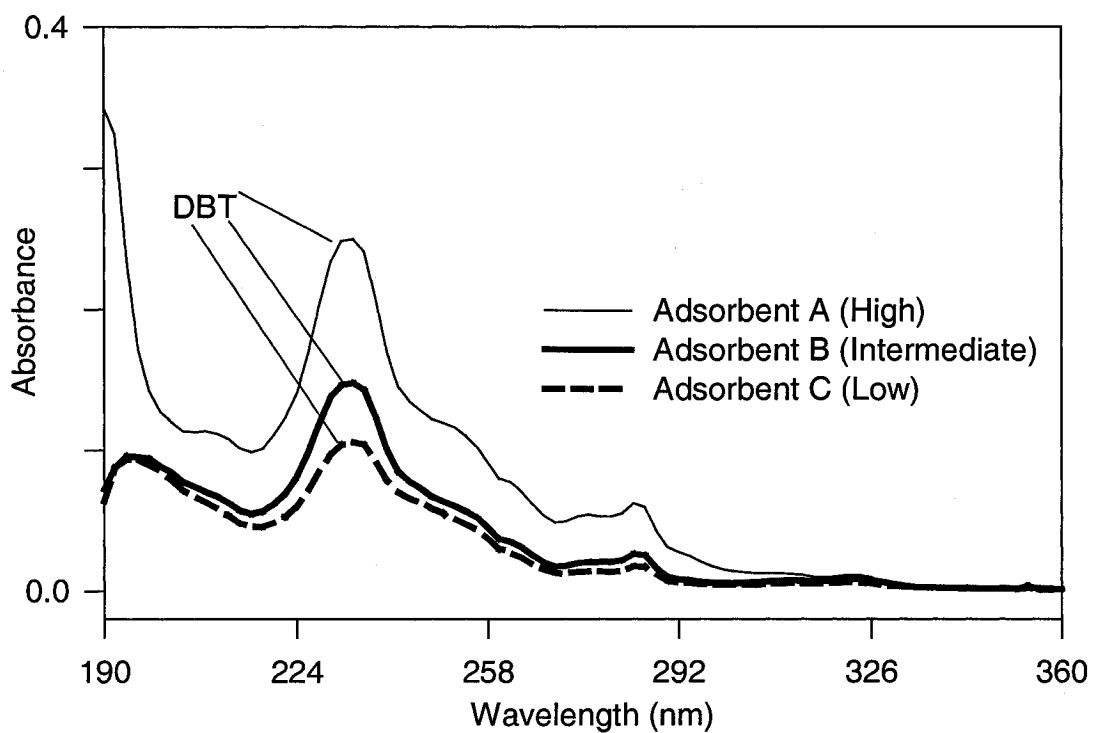


Figure 2.12. Elution with MeCN (F2, 10 mL), 0.1 mg of DBT and PHEN (each).

Figures 2.9 through 2.12 show that the interaction between sulfur and Pd adsorbed on SiO_2 is not strong enough to afford a clean separation between DBT and PHEN. For higher amounts of DBT and PHEN (0.1 mg each) loaded on the adsorbent, better separation is obtained when the Pd content is higher ($\text{PdCl}_2/\text{SiO}_2 - \text{A}$). However, for lower amounts of DBT and PHEN (0.02 mg each) loaded on the adsorbent, better separation is obtained when the Pd content is lower ($\text{PdCl}_2/\text{SiO}_2 - \text{C}$). Therefore, preparation of the adsorbent with optimum amount of Pd on silica depends on the concentration of sulfur-containing compounds in the samples to be analyzed or may be related to the total concentration of PACs.

The adsorbents could be regenerated with hydrogen and heat. Table 2.2 shows the reproducibility and the recovery of DBT and PHEN after 4 consecutive regenerations and for 0.1 or 0.02 mg of DBT and PHEN loaded on column. The recovery was obtained by summing the amount of each compound that eluted in the fraction of hexanes (F1) and in the fraction of MeCN (F2).

As shown in Table 2.2, recoveries of DBT and PHEN for adsorbents with higher Pd(II) content ($\text{PdCl}_2/\text{SiO}_2 - \text{A}$) are lower. The higher the content of Pd(II), the more strongly retained are DBT and PHEN on the column. For higher PdCl_2 loading on silica gel, for example 10.5 % (w/w), DBT and PHEN (0.02 mg each) were so strongly retained on the reduced form of the column that they did not elute with CH_2Cl_2 , MeCN or isopropanol.

Table 2.2. Recovery (%) of DBT and PHEN.

DBT and PHEN (each)	$\text{PdCl}_2/\text{SiO}_2 - \text{A}$		$\text{PdCl}_2/\text{SiO}_2 - \text{B}$		$\text{PdCl}_2/\text{SiO}_2 - \text{C}$	
	DBT	PHEN	DBT	PHEN	DBT	PHEN
0.1 mg	88 ± 2	86 ± 5	98 ± 3	98 ± 1	104 ± 1	103 ± 1
0.02 mg	76 ± 2	59 ± 4	87 ± 5	91 ± 6	98 ± 6	100 ± 3

Of all the adsorbents tested, the reduced form of $\text{PdCl}_2/\text{SiO}_2$ was the most selective to DBT, *i.e.* PHEN and DBT were separated to a greater extent. However, no complete separation of DBT and PHEN was achieved.

Chapter 3. MS and MS/MS of Selected Sulfur Compounds

3.1. Introduction

Electron ionization mass spectrometry at 60–80 eV has been the technique most commonly used in the characterization and identification of sulfur-containing compounds (Jacob 1990 p 18). Other ionization techniques such as chemical ionization (Hunt and Shabanowitz 1982), electrospray ionization (Rudzinski *et al.* 2003b) and atmospheric pressure chemical ionization (Rudzinski 2003a) in the positive-ion mode have been applied to the identification of sulfur compounds to a lesser extent.

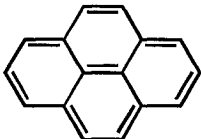
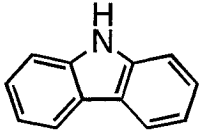
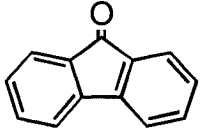
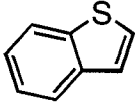
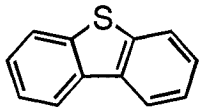
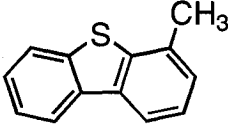
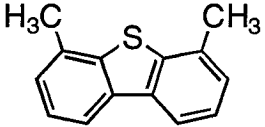
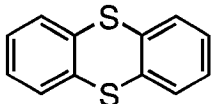
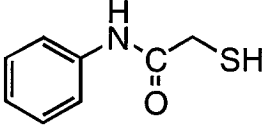
The general purpose of Chapter 3 is to investigate the response of PASHs to electrospray ionization (ESI) and atmospheric pressure chemical ionization (APCI) for improving the detection of sulfur-containing compounds. The capabilities of MS/MS for the selective identification of PASHs in the presence of similar compounds that do not contain sulfur will be also examined.

3.2. Experimental

A list of the polycyclic aromatic compounds used as standards in ESI(+)-MS, APCI(+)-MS and APCI(+)-MS/MS studies is given in Table 3.1. All solvents and chemicals, except pyrene, were used as provided. Pyrene (PY) contained an impurity which was extracted with 10% aqueous HCl (Fisher, Nepean, ON, Canada). PY was later purified by liquid chromatography using silica gel (Aldrich, 60–100 mesh, 150 Å, grade 645) as stationary phase and toluene as eluent.

Acetonitrile (MeCN) (HPLC grade), methanol (MeOH) (HPLC grade), toluene (HPLC grade) and acetic acid (reagent grade) were purchased from Fisher (Nepean, ON, Canada). Ammonium acetate (reagent grade) was obtained from the Nichols Chemical Company (Montreal, Quebec, Canada). Triethylamine (reagent grade) was provided by Fisher (Fair Lawn, NJ, USA). Iodine (reagent grade) was purchased from Anachemia (Toronto, ON, Canada).

Table 3.1. Polycyclic aromatic compounds (PACs) used as standards.

PAC name	Molecular Formula	Monoisotopic Mass (u)
 pyrene (PY)	C ₁₆ H ₁₀	202.0782
 carbazole (CAR)	C ₁₂ H ₉ N	167.0734
 fluoren-9-one (FLU)	C ₁₃ H ₈ O	180.0575
 benzo[b]thiophene (BT)	C ₈ H ₆ S	134.0190
 dibenzo[b,d]thiophene (DBT)	C ₁₂ H ₈ S	184.0346
 4-methyldibenzo[b,d]thiophene (MDBT)	C ₁₃ H ₁₀ S	198.0503
 4,6-dimethyldibenzo[b,d]thiophene (DMDBT)	C ₁₄ H ₁₂ S	212.0659
 thianthrene (TA)	C ₁₂ H ₈ S ₂	216.0067
 2-mercaptoacetanilide (MA)	C ₈ H ₉ NOS	167.0405

Dibenzo[*b,d*]thiophene (DBT) (98%), pyrene (PY) (98%), carbazole (CAR) (puriss.), fluoren-9-one (FLU) (98%), thianthrene (TA) (97%), benzo[*b*]thiophene (BT) (95%), silver triflate ($\text{F}_3\text{CSO}_3^-\text{Ag}^+$) and 4,6-dimethyldibenzo[*b,d*]thiophene (DMDBT) (97%) were obtained from Aldrich (Milwaukee, WI, USA). 4-Methyldibenzo[*b,d*]thiophene (MDBT) (96%) was purchased from Aldrich (St. Louis, MO, USA) and 2-mercaptoacetanilide (MA) was provided by Eastman Chemical Co. Inc. (Rochester, NY, USA).

Toluene was the single compound detected in a sample of toluene (either diluted with dichloromethane or neat) analyzed by gas chromatography coupled to mass spectrometry (Perkin-Elmer Autosystem XL instrument controlled by TurboMass and TurboChrom software). Operating conditions were: ionization method: EI(+) (70 eV energy), source temperature: 200 °C, carrier gas: helium (1 mL min⁻¹), column: 5% phenyl methylsiloxane (Supelco, 0.25 mm i.d., 30 m length, film thickness: 0.5 µm), temperature programming: 40 °C (1 min) up to 80 °C (1 °C min⁻¹), 80 °C (1 min) up to 280 °C (5 °C min⁻¹), 280 °C (1 min).

The majority of the mass spectra were obtained with a Micromass VG Quattro I triple quadrupole (QqQ) mass spectrometer (Micromass UK Ltd, Manchester, UK) running under MassLynx v3.4 software. The mass spectrometer was used in ESI(+) and APCI(+) modes. A diagram of the Quattro II atmospheric pressure ionization (API) interface employed is shown on page 26. The solvent ions were used to tune the mass spectrometer in ESI and APCI modes (analyte ions were not used for this purpose to avoid contamination of the instrument).

The nitrogen gas used for operation of the mass spectrometer in API mode was obtained from evaporation of liquid nitrogen contained in a 160-L pressurized Dewar flask. Liquid nitrogen was generated in the Chemistry Department by membrane separation of nitrogen from air followed by liquefaction.

The accurate mass of the impurity isolated from commercial pyrene was measured on a Consolidated Electrodynamics Corporation double focusing magnetic sector mass spectrometer model 21-110B. The sample was volatilized

using a heated solids probe (probe temperature = 64 °C) and ionized by EI(+) at 70 eV energy. The source temperature was 170 °C. The accurate mass of the molecular ion was measured with peak matching using perfluorokerosene as an internal calibration standard (reference ion: $C_6F_7^+$, reference mass: 204.9888 u). The standard deviation of mass measurement was ± 0.0008 u from 100 to 300 m/z . The resolution setting of the instrument was between 5000 and 10,000 using the 10 % valley definition.

3.2.1. Experimental—ESI(+)-MS

DBT, TA and PY were used as reference compounds in ESI(+)-MS studies. Ammonium acetate, acetic acid, triethylamine and iodine were tested in order to improve the detection sensitivity of sulfur-containing compounds in ESI. Solutions of model PACs in MeCN (1 g L^{-1} each) were introduced into the ESI source by flow-injection techniques using a syringe pump (Pump 11, Harvard Apparatus, Holliston, MA), a model 7125 injector (Rheodyne, from Supelco, Oakville, Ontario, Canada), and a 10-mL syringe (Hamilton Co, Reno, NE). Polyetheretherketone (PEEK) tubing (1/16" o.d., Chromatographic Specialties, Brockville, ON) was used to make all tubing connections.

Regular operating parameters in ESI(+)-MS studies were (unless otherwise noted): electrospray needle voltage: 4.0 kV, source temperature = 100 °C, solvent: MeCN, solvent flow rate = 0.02 mL min^{-1} , sample injection volume = 0.01 mL, bath gas flow = 75 sLph (sLph: standard liters per hour) and nebulizer gas flow = 17 sLph.

3.2.2. Experimental—APCI(+)-MS

DBT, PY, CAR and FLU were used as model PACs in APCI(+)-MS experiments. Stock solutions of each PAC were made up in MeCN and in MeOH to obtain calibration curves of the selected PACs in both solvents. Each stock solution was diluted with the same solvent to yield analytical solutions with concentrations in the range from $\sim 1\text{e-}8\text{ mol L}^{-1}$ to $\sim 1\text{e-}3\text{ mol L}^{-1}$ in MeCN and from $\sim 4\text{e-}6\text{ mol L}^{-1}$ to $\sim 5\text{e-}2\text{ mol L}^{-1}$ in MeOH. Solutions of PY in MeOH were

prepared in the concentration range from $4\text{e-}6 \text{ mol L}^{-1}$ to $2\text{e-}2 \text{ mol L}^{-1}$ due to the relatively low solubility of PY in MeOH and the difficulty of preparing solutions with concentrations higher than $2\text{e-}2 \text{ mol L}^{-1}$. (Note: scientific notation is used throughout the thesis, $3\text{e-}2$ indicates 3×10^{-2} , and $5\text{e}3$ indicates 5×10^3).

Binary mixtures of model PACs (DBT/PY, DBT/FLU, DBT/CAR) were prepared in MeCN and in MeOH to study the interactions of these compounds in APCI over a wide concentration range. In all experiments, the amount of DBT was held constant and PY, CAR or FLU were mixed with DBT to form solutions with final molar ratios (DBT to PAC) of 3:1, 1:1 and 1:3. For the low concentrations, the concentration of DBT was $1\text{e-}6 \text{ mol L}^{-1}$ in MeCN and $1\text{e-}4 \text{ mol L}^{-1}$ in MeOH. At the higher concentrations, the concentration of DBT was $5\text{e-}4 \text{ mol L}^{-1}$ in MeCN and $1\text{e-}2 \text{ mol L}^{-1}$ in MeOH. In the case of the DBT/PY mixture in MeOH, the concentration of DBT was $8\text{e-}3 \text{ mol L}^{-1}$. In all cases, solutions of each PAC alone with concentrations that matched that of the PAC in the mixture were also prepared.

The above solutions were introduced into the APCI source by flow injection using an Agilent 1100 binary pump (Mississauga, Ontario, Canada), a Rheodyne injector and 1/16" o.d. PEEK tubing. Regular operating parameters in APCI(+)-MS were: corona needle voltage = 4.0 kV, source temperature = 90 °C and probe temperature = 200 °C. The cone voltage and the flows of bath (B), sheath (S) and nebulizer (N) gas were optimized for each PAC at different solvent flow rates in order to obtain maximum sensitivity. Experimental conditions used for the determination of limits of detection (LODs) and calibration curves for the model PACs varied in MeCN and in MeOH (Table 3.2).

Limits of detection and calibration curves were obtained at solvent flow rates of 0.02, 0.1 and 0.5 mL min^{-1} using sample loops of 0.02, 0.1 and 0.5 mL, respectively, both in MeCN and in MeOH. The ionization current was measured in MeCN, MeOH and toluene using the above solvent flow rates and sample injection volumes. The remainder of the studies (analysis of mixtures of PACs and determination of the total ion current for each PAC in MeCN, MeOH and toluene) were carried out at 0.5 mL min^{-1} using a sample loop of 0.5 mL.

Table 3.2. Experimental conditions for the determination of LODs and calibration curves in MeCN and in MeOH (B: bath gas, S: sheath gas, N: nebulizer gas).

Solvent	PAC	Solvent flow rate (mL min ⁻¹)	Gas flow rate (sLph)	Cone (V)
MeCN	DBT	0.02	B (150), S (75), N (45)	30
		0.1	B (75), S (75), N (45)	40
		0.5	B (75), S (75), N (45)	50
	PY	0.02	B (75), S (75), N (45)	50
		0.1	B (75), S (75), N (45)	50
		0.5	B (400), S (350), N (45)	50
	CAR	0.02	B (75), S (75), N (45)	40
		0.1	B (75), S (75), N (45)	50
		0.5	B (75), S (75), N (45)	50
	FLU	0.02	B (50), S (50), N (45)	30
		0.1	B (200), S (200), N (45)	30
		0.5	B (400), S (350), N (45)	40
MeOH	DBT	0.02	B (200), S (350), N (45)	40
		0.1	B (200), S (350), N (45)	40
		0.5	B (200), S (350), N (45)	40
	PY	0.02	B (200), S (350), N (45)	40
		0.1	B (200), S (350), N (45)	40
		0.5	B (200), S (350), N (45)	40
	CAR	0.02	B (200), S (350), N (45)	40
		0.1	B (200), S (350), N (45)	40
		0.5	B (200), S (350), N (45)	40
	FLU	0.02	B (200), S (350), N (45)	30
		0.1	B (200), S (350), N (45)	30
		0.5	B (200), S (350), N (45)	30

The experimental conditions used for the measurement of the ionization current were: [DBT] = $6.6\text{e-}6$ mol L⁻¹ or $2.0\text{e-}2$ mol L⁻¹, B (200 sLph), S (200 sLph) and N (45 sLph). In total ion current studies (TIC), the following conditions were used: [PAC] = $1.0\text{e-}5$ mol L⁻¹, B (200 sLph), S (200 sLph) and N (45 sLph).

Experimental conditions for the analysis of mixtures of PACs in MeCN and in MeOH are shown in Table 3.3.

Table 3.3. Experimental conditions for studies on mixtures of PACs in MeCN and in MeOH (B: bath gas, S: sheath gas, N: nebulizer gas).

Solvent	PAC mixture	Gas flow rate (sLph)	Cone (V)
MeCN	DBT/PY	B (450), S (350), N (45)	50
	DBT/CAR	B (200), S (350), N (45)	40
	DBT/FLU	B (200), S (350), N (45)	40
MeOH	DBT/PY	B (450), S (350), N (45)	50
	DBT/CAR	B (200), S (350), N (45)	40
	DBT/FLU	B (200), S (350), N (45)	40

Single ion monitoring (SIM) was used for the determination of LODs, and for the analysis of each PAC alone and in mixtures of PACs. A dwell time of 1 s at m/z 172 (background setting) and at the m/z values of both the molecular ion and the protonated molecule for all PACs was employed. Full-scan data were also obtained (mass range: 30–250 m/z). The sample was injected after twenty five scans of background were acquired, and data acquisition was continued until five scans after the total ion current had returned to the baseline. An average background was subtracted from the average analytical signal (five scans) and the responses (in counts) at the observed m/z values were recorded.

3.2.3. Experimental—APCI(+)-MS/MS

DBT, BT, MDBT, DMDBT, TA and MA were used as standards in APCI(+)-MS/MS experiments. MS/MS spectra were obtained on either a Finnigan LCQ Duo ion trap or a Micromass Quattro triple quadrupole (QqQ) mass spectrometer. Both mass spectrometers were operated in APCI(+) mode. Samples were introduced into the APCI source by flow injection techniques using

MeCN as solvent (solvent flow rate: 0.1 mL min^{-1} , sample injection volume: 0.1 mL).

The LCQ instrument was tuned manually using TA and MA as reference compounds. Instrumental parameters were: corona needle voltage = 4.5 kV , probe temperature = $450 \text{ }^{\circ}\text{C}$, capillary voltage = 35 V , capillary temperature = $150 \text{ }^{\circ}\text{C}$, source voltage = 0 V , sheath gas: nitrogen, sheath gas flow rate = 30 arbitrary units, damping and collision gas: helium (Praxair, Mississauga, ON, Canada). The collision energy was progressively increased until both precursor and product ions were observed. The normalized collision energy for TA was 37% and that for MA, 20% . Product-ion spectra of TA and MA were acquired in full-scan mode using a mass span of 0.4 u (optimal) and an ion injection time of 200 ms . Data for the mass spectra were based on 50 scans and each scan was the average of five microscans. Xcalibur software was used for data acquisition and processing. Solutions of TA and MA were prepared in MeCN. The following concentrations were used: $[\text{MA}] = 2.0\text{e-}4 \text{ mol L}^{-1}$ and $[\text{TA}] = 1.2\text{e-}3 \text{ mol L}^{-1}$.

The QqQ instrument was operated under the following conditions: corona needle voltage = 4.0 kV , source temperature = $90 \text{ }^{\circ}\text{C}$, probe temperature = $250 \text{ }^{\circ}\text{C}$, bath gas flow = 250 sLph , sheath gas flow = 250 sLph and nebulizer gas flow = 40 sLph , collision gas: argon (Liquid Carbonic Corp., Pittsburgh, PA, USA), collision gas pressure $\sim 6\text{e-}7 \text{ bar}$. Precursor-ion, product-ion and constant neutral loss scans were obtained in full scan mode for DBT, BT, MDBT, DMDBT, TA and MA. Eight-scan functions (scan time = 0.65 s) were set up for all the analyses. Analyte concentrations of $1.0\text{e-}2 \text{ mol L}^{-1}$ were used. MS/MS scans were also performed in selected reaction monitoring mode (SRM) for TA and MA. Pairs of mass-selected ions were analyzed using a dwell time of 0.05 s and a mass span of 0.2 u . The collision energy ($5\text{--}10 \text{ eV}$) and the cone voltage ($15\text{--}35 \text{ V}$) were variable for each compound and type of MS/MS analysis. Solutions with concentrations of $2.0\text{e-}3 \text{ mol L}^{-1}$ (MA) and $1.2\text{e-}3 \text{ mol L}^{-1}$ (TA) were employed.

3.2.4. Experimental—Gaussian Calculations

Calculations were carried out using the Gaussian 03 suite of programs (Gaussian 2003) on a Pentium 4 (CPU 3.40 GHz) under a Windows XP operating system. The structures of neutral molecules and ions in the ground state were fully optimized using the B3LYP functional and the 6–31G(*d*) basis set. In spite of the limitations imposed by the use of small basis sets, we were obliged to use the 6–31G(*d*) basis set since the more extensive basis sets are not practical for studies of larger systems. The B3LYP functional is composed of Becke's three-parameter hybrid exchange functional (B3) (Becke 1993) and the correlation functional of Lee, Yang, and Parr (LYP) (Lee *et al.* 1988). The B3LYP functional was selected because it yields reliable results at moderate computational cost even for larger systems (Boyd and Boyd 2007). The unrestricted B3LYP method was employed in the geometry optimization of odd electrons ions (spin multiplicity: doublet), while the restricted method was used for neutral molecules and even electron ions (spin multiplicity: singlet).

In the following A represents an analyte molecule and S a solvent molecule. In order to obtain minimum-energy geometries for both $(S)_{n=0-2}S^{+\bullet}$ and $(S)_{n=0-2}SH^+$ clusters (S: MeOH or MeCN), we used as input structures those reported by previous studies on clusters of MeOH and MeCN (Hirao *et al.* 1982a, Hirao *et al.* 1982b and Kolakowski *et al.* 2004). In some cases, different symmetries for a given structure were tried and potential energy curves were produced to find optimal dihedral angles and bond lengths (Appendix D).

Vibrational frequencies for A, $A^{+\bullet}$ and AH^+ , $(S)_{n=0-2}S^{+\bullet}$, $(S)_{n=0-2}SH^+$, $(S)A^{+\bullet}$ and $(S)AH^+$ species (where A is DBT, PY, CAR or FLU and, S is MeOH or MeCN) were computed at the B3LYP/6-31G(*d*) level to confirm that the optimized structures were a minimum on the potential energy surface (no imaginary frequencies). Thermodynamic data ($T = 298.15$ K and $P = 1$ atm) (Tables C1 and C2, Appendix C) were obtained at the same level of theory in order to calculate ΔH and ΔG of the charge exchange and proton transfer reactions considering solvation. The following energy conversions were used: 1 hartree = 27.2114 eV = 2625.500 kJ mol⁻¹ = 627.510 kcal mol⁻¹ (Janoschek 2001). Unless

otherwise noted, all calculations were performed with the default parameters of Gaussian.

3.3. Results and Discussion

3.3.1. ESI(+)-MS of DBT and TA

Molecular ions ($M^{\bullet+}$) were observed in the positive-ion ESI spectrum of DBT and TA in MeCN, Figure 3.1. This is unusual since radical ions are typically not formed by electrospray ionization. For ESI(+), proton transfer is the common ionization mechanism and protonated molecules (MH^+) are the ionic species normally observed. The ion observed at m/z 184 in Figure 3.1 could be the $M^{\bullet+}$ ion of DBT (an ion at m/z 184 is also observed in the ESI(+) spectrum of DBT alone) and/or an ion that results from the loss of sulfur from the $M^{\bullet+}$ ion of TA (the loss of sulfur is observed for TA alone). The formation of radical ions has been reported by van Berkel and co-workers (van Berkel *et al.* 1991) who observed molecular ions as the single ionic species in the positive-ion ESI mass spectrum of Ni(II) octaethylporphyrin sprayed from toluene/methanol/trifluoroacetic acid (60/40/0.2% v/v/v). In contrast to the divalent metal porphyrin, the free-base porphyrin forms protonated molecules rather than $M^{\bullet+}$ ions.

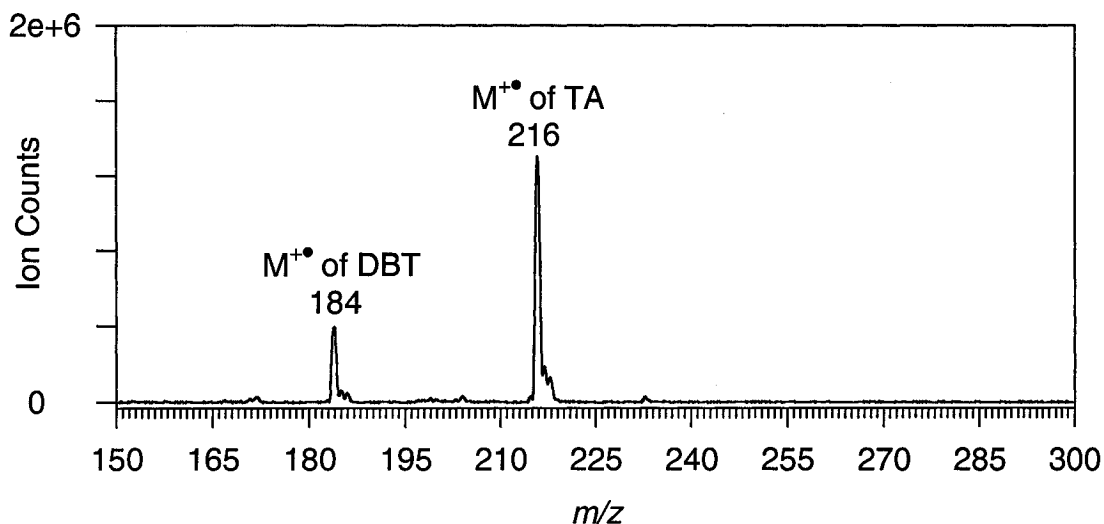


Figure 3.1. ESI(+) spectrum of DBT and TA in MeCN (1 g L^{-1} , each). Mass range: 150–300 m/z , scan time: 0.6 s, 45 V cone).

Van Berkel and Asano (van Berkel and Asano 1994) also described the formation of molecular ions of polycyclic aromatic hydrocarbons (PAHs) and thianthrene in the presence of electron-transfer reagents, such as trifluoroacetic acid and antimony pentafluoride, and found that the ionization efficiency and selectivity were dependent on the oxidizing strength of the reagent used. More recently, Rudzinski *et al.* (Rudzinski *et al.* 2003b) reported the formation of molecular ions of DBT, DMDBT and TA by charge transfer from the sulfur compounds to Pd(II) chloride. However, the molecular ions of the investigated PASHs were not observed in the absence of Pd(II).

As PAHs are not easily ionized under electrospray conditions, this technique was used to study if selective ionization of PASHs would occur in the presence of PAHs. Ions at m/z 184, 202 and 216, which correspond to the molecular ions of DBT, PY and TA, respectively, were observed in the ESI(+) spectrum of PY, DBT and TA in MeCN (1 g L^{-1} each) (spectrum not shown). However, whereas the peak at m/z 216 was the most intense in the spectrum, those at m/z 184 and 202 were of low and comparable intensity. In the absence of TA, the ions at m/z 184 and 202 were still of low intensity, indicating that the formation of the molecular ions of PY and DBT is not favored under the conditions used. The ionization energy (IE) for these compounds increases in the order: $\text{IE}_{\text{PY}} (7.4 \text{ eV}) < \text{IE}_{\text{TA}} (7.9 \text{ eV}) < \text{IE}_{\text{DBT}} (8.1 \text{ eV})$, indicating that ionization occurs most probably in the liquid-phase rather than in the gas-phase (Values of ionization energy were taken from <http://www.webbook.nist.gov>, access date: February 5, 2007). Molecules may be ionized by donation of an electron to a solvent molecule or a contaminant in the solution that has a relative high electron affinity or by an electrochemical oxidation in the electrospray needle.

When using ESI, higher sensitivity and lower detection limits are usually achieved for compounds that exist already as ions in solution or that can be ionized by acid/base chemistry or metal complexation. Therefore, in an attempt to increase the ionization efficiency of DBT, several reagents were added to the mixture of DBT and TA prior to introduction into the ESI source. The compounds tested included ammonium acetate, acetic acid, iodine and triethylamine.

However, similar results to those previously observed for the mixture of DBT and TA without reagent compound added (Figure 3.1) were obtained when ammonium acetate and acetic acid were used. The ionization efficiency of both compounds was lower when iodine was added, and in the case of triethylamine, the peaks corresponding to DBT and TA were not observed.

The possibility of forming adduct ions by complexation reactions of PASHs with Ag(I) was also examined. The ESI(+) mass spectra of DBT and TA in the presence of silver triflate and at different cone voltages are shown in Figure 3.2. However, no improvement in sensitivity was obtained for DBT under these conditions.

There are two naturally occurring isotopes of silver, ^{107}Ag and ^{109}Ag , with natural abundance of 51.8% and 48.2%, respectively. Therefore, the adduct ions that contain silver are recognized in the spectra because of their characteristic isotopic patterns (two peaks separated by two m/z units with approximately the same intensity, *e.g.* m/z 189/191, m/z 323/325, m/z 364/366 and m/z 539/541).

The most abundant peak in the spectrum of Figure 3.2 (A) is observed at m/z 189/191, which corresponds to the $[\text{2MeCN} + \text{Ag}]^+$ adduct ion formed by two MeCN molecules and one silver ion. Increasing the cone voltage from 20 to 40 V considerably reduces the amount of the ion at m/z 189/191. The facile dissociation of the ion at m/z 189/191 indicates that $[\text{2MeCN} + \text{Ag}]^+$ is a weakly bound complex.

The most intense peak in the spectra obtained at 30 and 40 V cone voltages (Figure 3.2 B and C) is the ion at m/z 323/325, which corresponds to the $[\text{TA} + \text{Ag}]^+$ adduct ion formed by the thianthrene molecule and the silver ion. The relatively low intensity of the peak at m/z 216 relative to the peak at m/z 323/325, shows that the formation of the $[\text{TA} + \text{Ag}]^+$ adduct ion is preferred over the formation of the molecular ion of TA (m/z 216).

The presence of copper in the ion structure is recognized from its characteristic isotopic pattern, *i.e.* two peaks in the isotopic cluster separated by two mass units and an experimental relative peak height ratio of about 70:30.

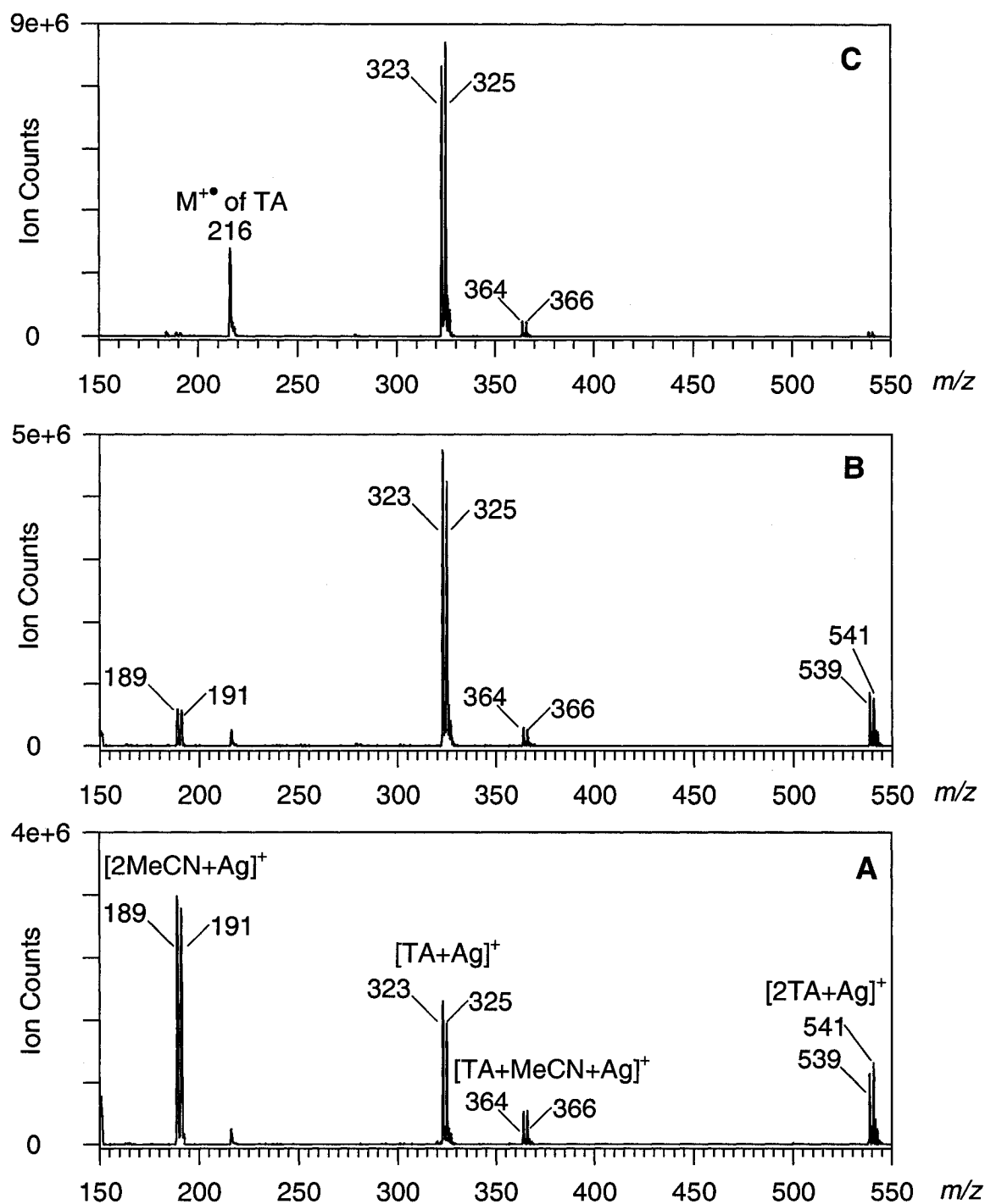


Figure 3.2. ESI(+) spectra of DBT and TA in the presence of Ag^+ at 20 V (A), 30 V (B) and 40 V (C) cone voltages. Electrospray needle voltage: 1.5 kV, solvent: MeCN, 5 μL of solution of silver triflate (0.3 g L^{-1}) were added to 5 μL of solution of DBT and TA (1 g L^{-1} , each). Mass range: 150–550 m/z , scan time: 1.5 s.

A peak (0.6% of the base peak) at m/z 279/281 in the spectra at 30 and 40 V cone voltages presumably corresponds to a $[TA + Cu]^+$ complex formed by thianthrene and copper (I). Copper is usually present in MeCN and adduct ions of copper and MeCN have been previously observed in ESI(+) mode. Copper has two naturally occurring isotopes, ^{63}Cu and ^{65}Cu , with natural abundance of 69.2% and 30.8%, respectively.

3.3.2. APCI versus ESI

APCI and ESI are liquid introduction API techniques that often complement each other, ESI being better suited for the analysis of polar or ionic compounds, and APCI usually being the best choice for non-polar analytes. However, linear response is reported to be less likely with ESI than with APCI and matrix effects are much more serious with ESI. Previous studies (Kearle and Tang 1993) have shown that the relationship between ESI-MS response and analyte ion concentration is typically linear from the limit of detection up to about $1e-6$ mol L^{-1} . Linear response over a wide concentration range is an attractive feature of APCI and has been reported by several authors (Anacleto *et al.* 1995; Hayen *et al.* 2002).

Recently, Roussis and Fedora (Roussis and Fedora 2002) compared the ability of APCI and ESI to quantify polar and ionic compounds in petroleum products. They obtained relative linear dynamic ranges of three orders of magnitude for both techniques and higher sensitivity for ESI than for APCI. However, their results showed non-linear response to ESI at higher concentrations. For APCI, linearity was obtained in the range of concentrations studied (maximum analyzed mass of compound: 0.3 mg) and the authors recommended the use of APCI for quantitative LC/MS applications.

While studying the application of APCI to the analysis of PASHs in petroleum samples, we observed 1) that the signal for dibenzothiophene decreases when increasing amounts of some other compounds, such as pyrene, are added to a mixture of both PACs and 2) that the response becomes non-linear at higher concentrations (Figure 3.3).

In this section of the thesis, the ability of positive-ion APCI to quantify PASHs over a wide range in concentration and in the presence of similar compounds that may cause interference will be examined. Dibenzothiophene (DBT), carbazole (CAR), and fluorenone (FLU) were chosen as model heteroaromatic compounds, and pyrene (PY) was selected as a model polycyclic aromatic hydrocarbon found in petroleum samples. The majority of the experiments were carried out in acetonitrile (MeCN) and methanol (MeOH), since these are the normal solvents used in reverse phase LC separations. In an attempt to explain the much lower ionization sensitivity in MeOH compared to MeCN, some experiments were carried out using toluene as a solvent of low polarity and ionization energy.

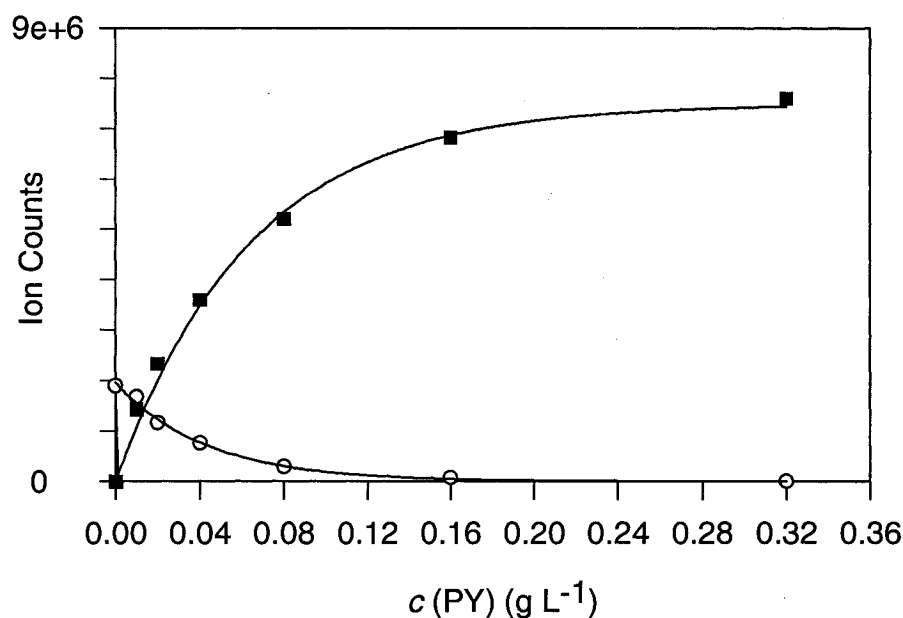


Figure 3.3. APCI(+) response for DBT (\circ) and PY (\blacksquare) in a DBT/PY mixture. DBT (constant: 0.02 g L^{-1}) and PY (variable, range: $0.0\text{--}0.3 \text{ g L}^{-1}$).

Our objectives are three fold: 1) to determine limits of detection and linear dynamic ranges of model PACs in MeCN and in MeOH at different solvent flow rates, 2) to study the effect on DBT of adding various amounts of PY, CAR and FLU in MeCN and in MeOH, both in the linear and non-linear regions of response and 3) to study mechanisms of ionization of representative PACs in APCI.

3.3.2.1. APCI(+) MS of DBT, PY, FLU and CAR

In general, the intensity of the ions formed in the APCI source was dependent on solvent, cone voltage, gas and solvent flow rates. Both molecular ions, $M^{+\bullet}$, and protonated molecules, MH^+ , were observed in the majority of the APCI(+) mass spectra of the model PACs (Figures 3.4 through 3.8, conditions: solvent flow rate = 0.5 mL min^{-1} , B = 400 sLph, S = 200 sLph and N = 45 sLph, $[PAC] = 5.0 \times 10^{-4} \text{ mol L}^{-1}$).

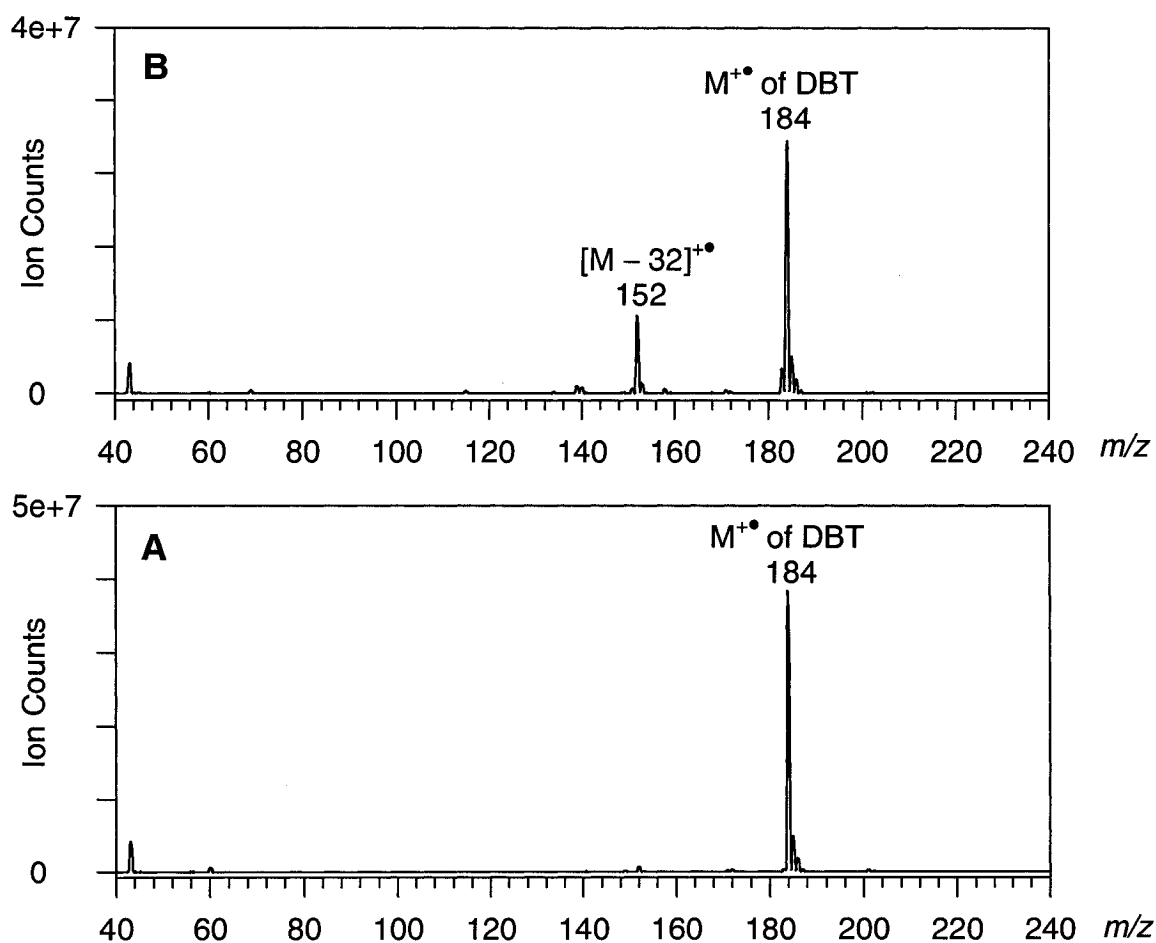


Figure 3.4. APCI(+) mass spectra of DBT at 40 V (A) and 50 V (B) cone.

On the whole, PACs showed different abilities to ionize by either charge or proton transfer. The APCI(+) spectra of DBT were found to be dominated by the

molecular ion (m/z 184) (Figure 3.4) and this was the unique species observed in MeCN and in MeOH. In toluene, the protonated molecule (m/z 185) was detected in addition to the M^{+*} ion.

The ion counts for the M^{+*} species increased when increasing values of cone voltage were used and maximum intensity was obtained at 40 V cone. At 50 V cone, fragmentation of the M^{+*} ion to m/z 152 was detected (Figure 3.4 B). Tandem mass spectrometry confirmed that m/z 152 originates from m/z 184 and that the fragmentation corresponds to the loss of sulfur (32 u). The loss of sulfur is characteristic of PASHs and has been reported elsewhere (Jacob 1990).

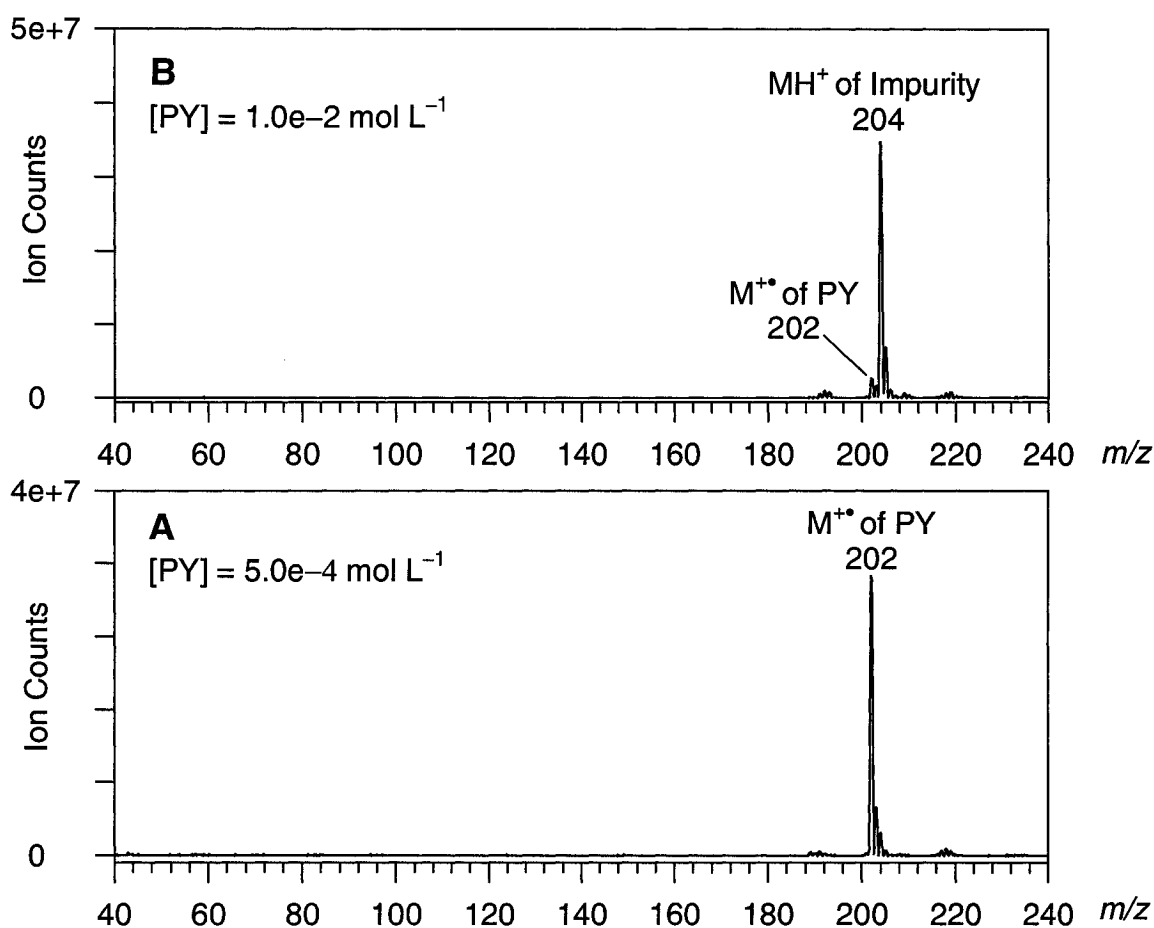


Figure 3.5. APCI(+) mass spectra of PY (impure) at 40 V cone in MeCN (A) and MeOH (B).

For PY, the M^{+*} ion was the only species detected in MeCN (Figure 3.5 A). In MeOH and in toluene both the M^{+*} (m/z 202) and the MH^{+} ions (m/z 203)

For PY, the $M^{+•}$ ion was the only species detected in MeCN (Figure 3.5 A). In MeOH and in toluene both the $M^{+•}$ (m/z 202) and the MH^+ ions (m/z 203) were observed. As mentioned in the experimental section, commercial PY contained an impurity (m/z 203) that reacted with $HCl_{(aq)}$ and that produced an abundant MH^+ ion (m/z 204) in MeOH (Figure 3.5 B). Analysis by EI(+)-MS of an isolated sample of the impurity showed that the $M^{+•}$ peak of the impurity has an accurate mass of 203.0740 ± 0.008 u, indicating a nitrogen-containing compound with chemical composition $C_{15}H_9N$ (calculated mass 203.0735 u), most probably one of the three possible azapyrene isomers.

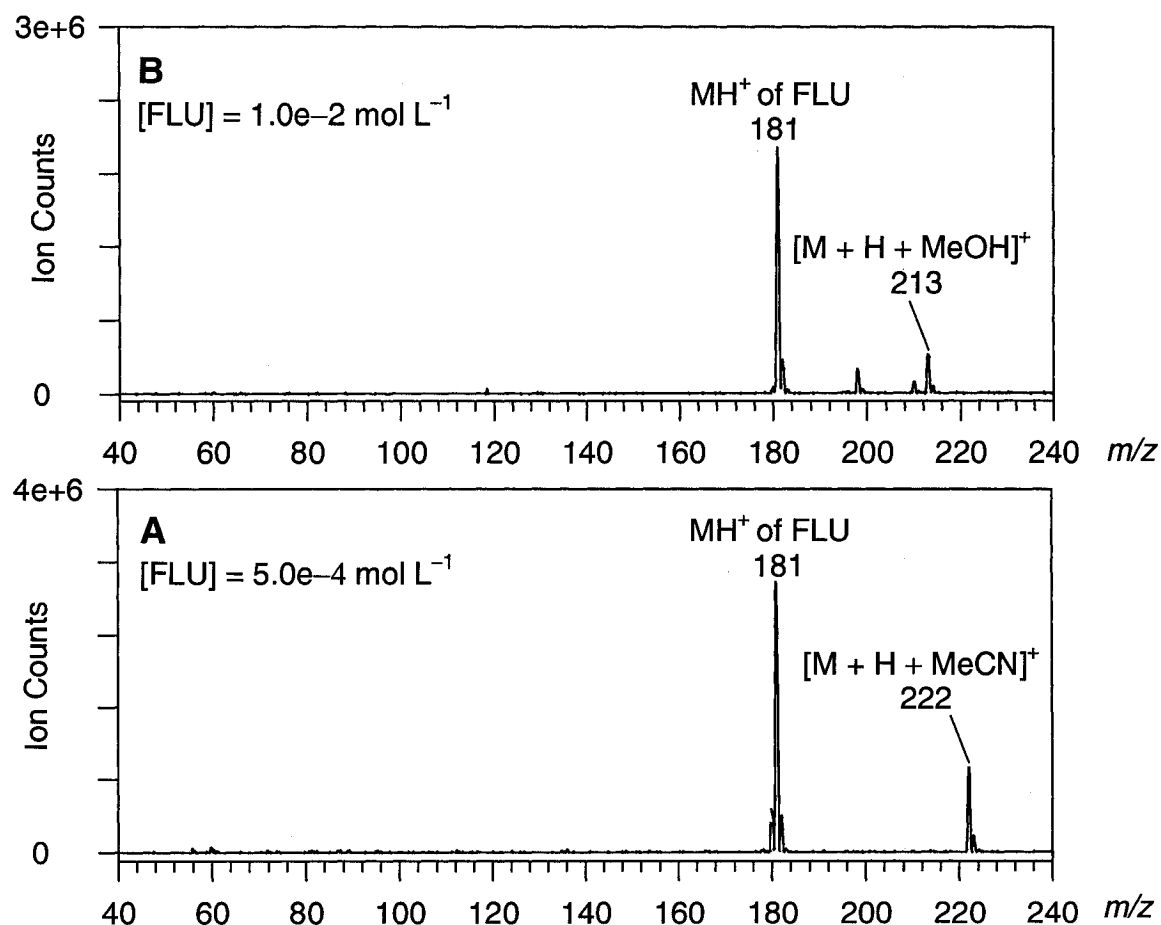


Figure 3.6. APCI(+) mass spectra of FLU at 5 V cone showing analyte and solvent clusters in MeCN (A) and MeOH (B).

The $M^{+•}$ (m/z 180) and the MH^+ (m/z 181) ions of FLU were the species observed in the APCI(+) spectra of FLU (Figure 3.6). At 5 V cone, adduct ions of FLU and the solvent were detected in MeOH at m/z 213 ($[FLU+MeOH+H]^+$) and in MeCN at m/z 222 ($[FLU+MeCN+H]^+$) which dissociated very easily when the cone voltage was increased. The protonated molecule was the predominant ion formed under the majority of conditions studied and the $M^{+•}$ ion was minor.

In general, the counts of $M^{+•}$ and MH^+ ions of FLU decreased when the cone voltage was increased from 30 to 50 V and maximum intensity was obtained for both species at 30 V cone (Figure 3.7).

At 30 V and higher cone voltages, fragment ions were detected at m/z 152 and m/z 153 in the spectra of FLU (Figure 3.7 B and C). MS/MS showed that the ions observed at m/z 152 and 153 are produced by the loss of CO (28 u) from $M^{+•}$ and MH^+ , respectively. The loss of CO has been previously observed in EI(+)-MS of ketones (Gross 2004 pp 283–284).

The main species detected in the APCI(+) spectra of CAR were the $M^{+•}$ (m/z 167) and the MH^+ (m/z 168) ions (Figure 3.8). An adduct ion of CAR and the solvent (m/z 209), which dissociated readily when increasing the cone voltage, was observed in MeCN ($[CAR + MeCN + H]^+$) at 5 V cone (Figure 3.8 A). However, the similar adduct ion in MeOH ($[CAR + MeOH + H]^+$) was not detected under the experimental conditions used.

The relative intensity of the $M^{+•}$ and the MH^+ ions for CAR was highly dependent on cone voltage. Figure 3.9 shows the ion counts for $M^{+•}$ and MH^+ of CAR at different gas flow rates and cone voltages. At 40 V cone the main species formed is the MH^+ ion, while at 50 V the $M^{+•}$ ion was predominant. The top panel on Figure 3.9 shows that the total ion counts (sum of MH^+ and $M^{+•}$ species) at 40 V and 50 V cone are very similar. The relatively constant sum intensity $[M^{+•} + MH^+]$ at 40 and 50 V cone suggests that the process $MH^+ \rightarrow M^{+•}$ probably occurs at 50 V cone.

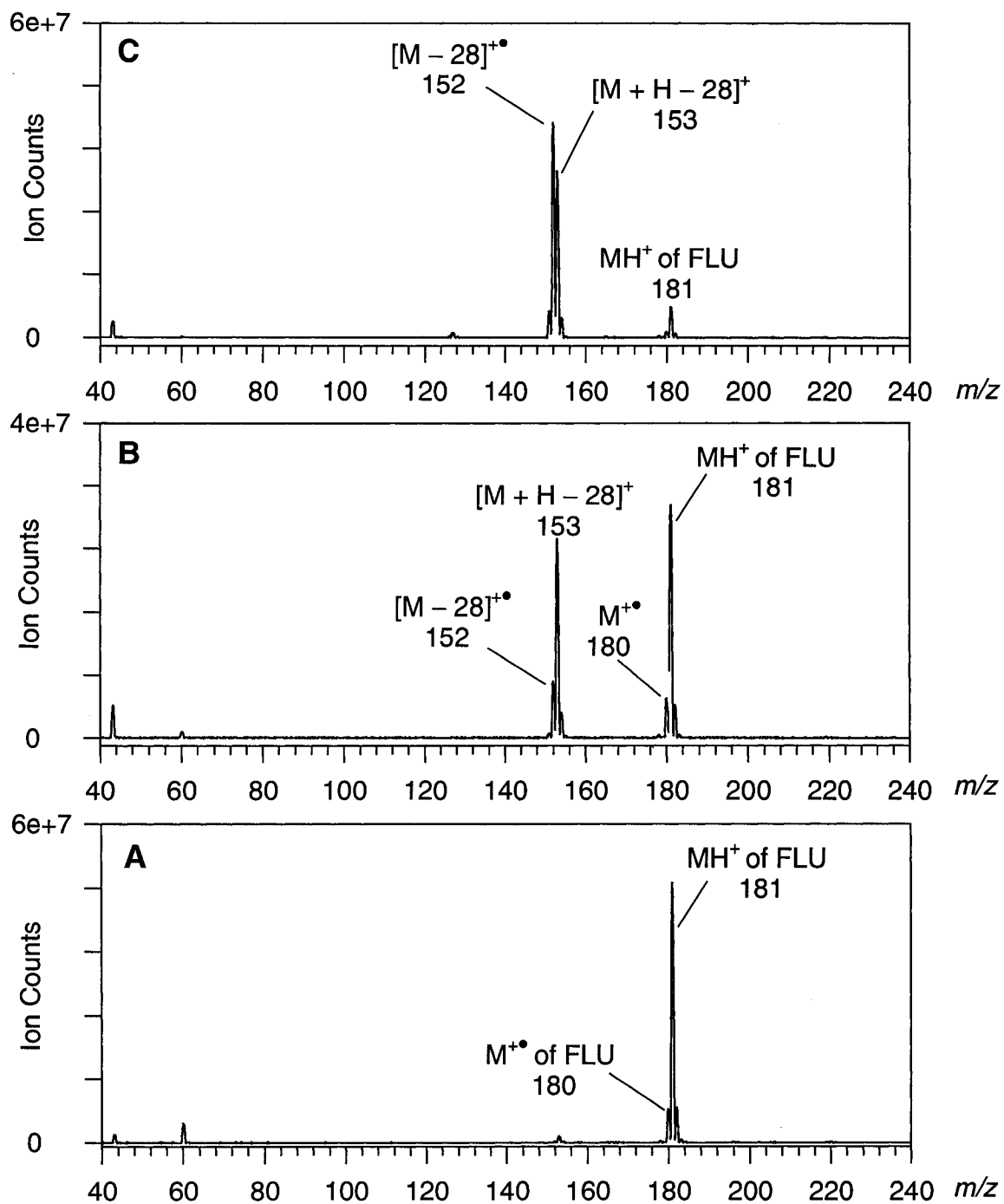


Figure 3.7. APCI(+) mass spectra of FLU at 30 V (A), 40 V (B) and 50 V (C) cone.

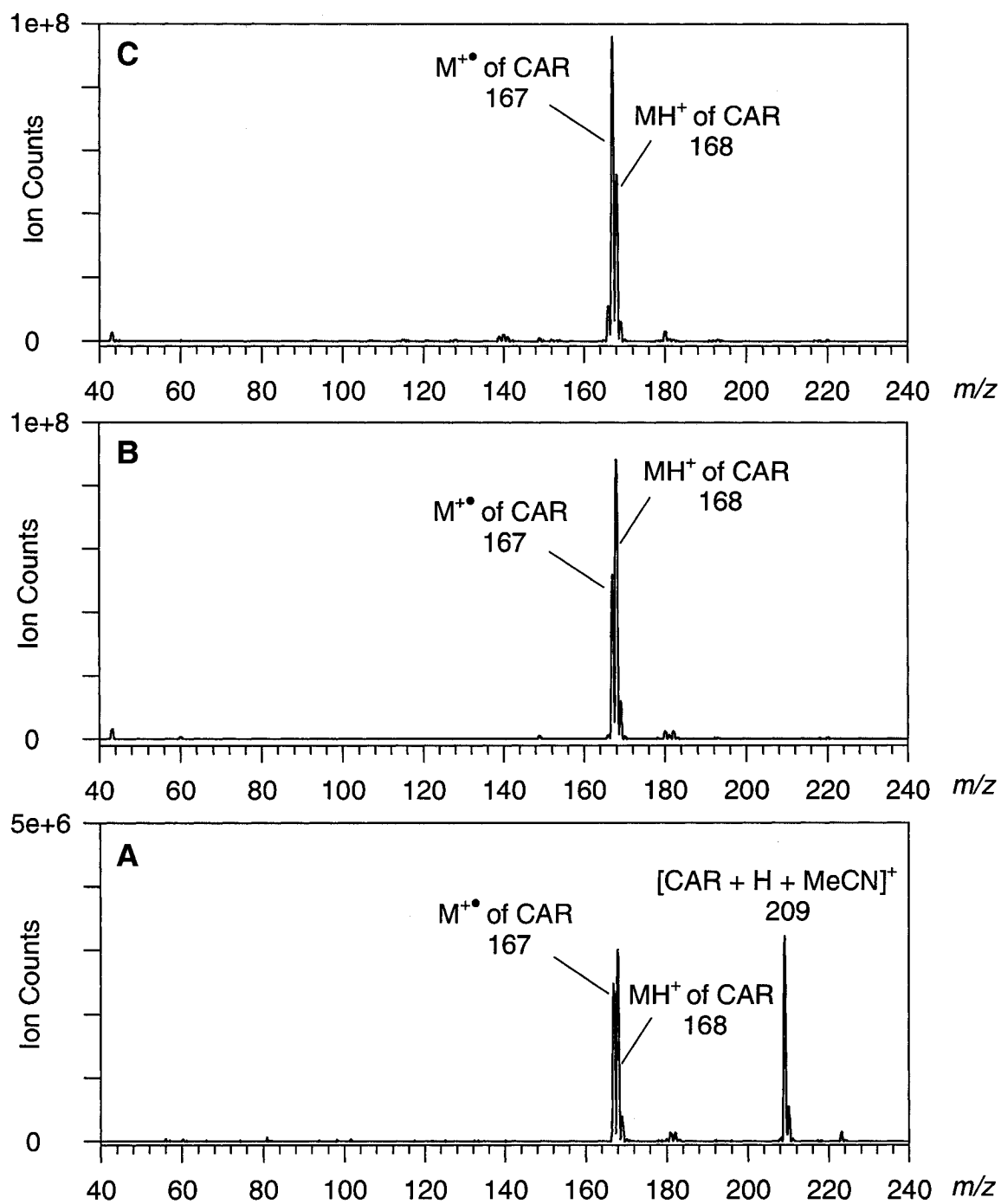


Figure 3.8. APCI(+) mass spectra of CAR at 5 V (A), 40 V (B) and 50 V (C) cone.

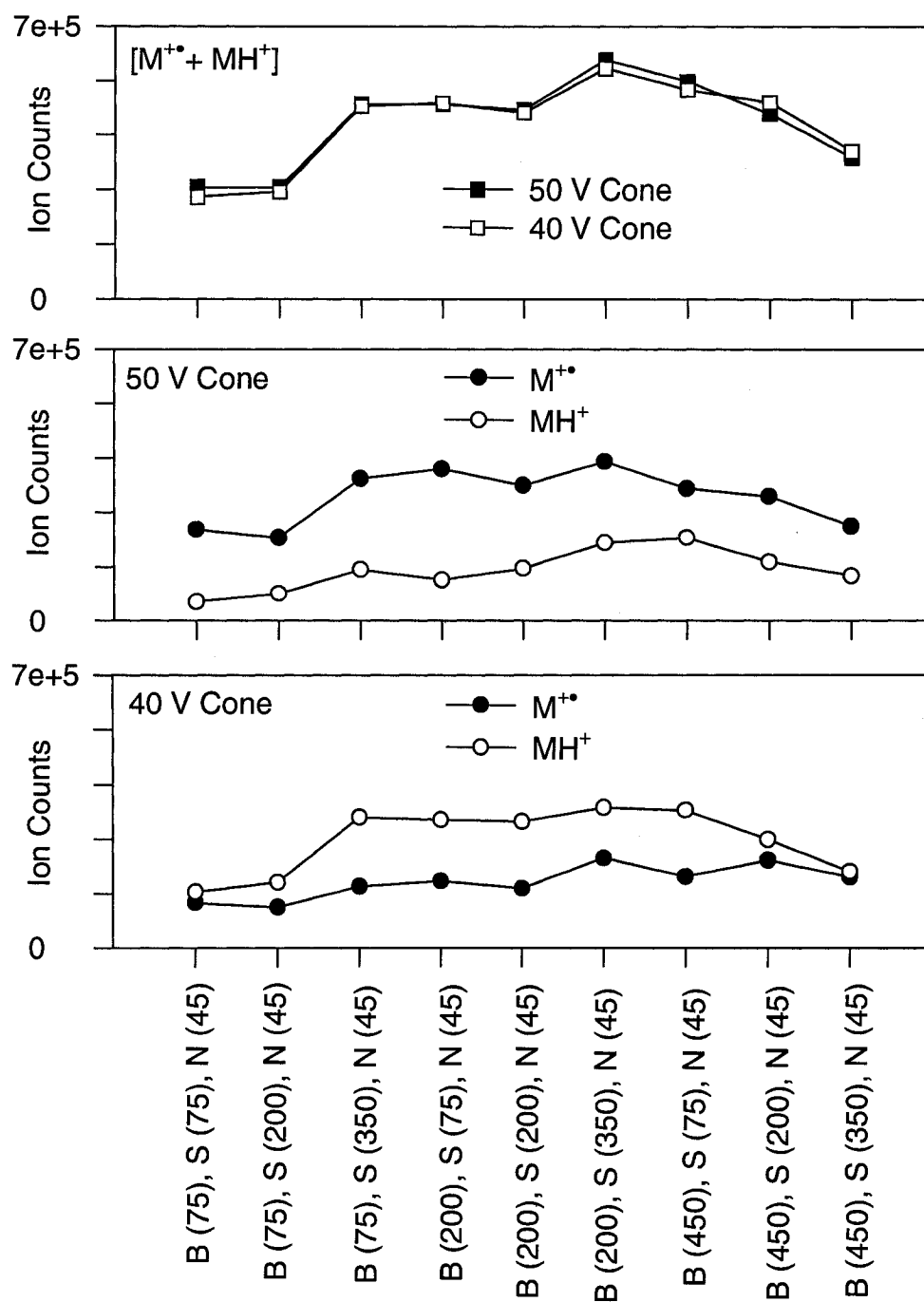


Figure 3.9. Ion counts for M^{++} , MH^+ and $[M^{++} + MH^+]$ of CAR at different gas flow rates (sLph) and cone voltages. Conditions: solvent (MeCN, 0.5 mL min^{-1}), $[CAR] = 1.0e-6 \text{ mol L}^{-1}$, bath gas (B), sheath gas (S), nebulizer gas (N).

The results obtained demonstrate that the cone voltage is one of the key parameters affecting the relative intensity of the ions observed in the APCI(+) mass spectra of model PACs. The cone voltage is the voltage applied between the sampling cone and the skimmer cone in the API ion source (Figure 1.5) and directly affects in-source fragmentation of analytes. Between the first and second cones, the pressure is in the millibar range and the main species present are analyte ions, solvent ions, gas ions and gas molecules. When the cone voltage is increased ions are accelerated, they gain energy in the cone region and fragmentation occurs by colliding with residual nitrogen molecules. The above mass spectra show that the degree of fragmentation in the APCI ion source can be enhanced, and thus structural information can be obtained, by increasing the cone voltage.

3.3.2.2. Limits of Detection

Limits of detection (LODs) of the model PACs were determined in MeCN and in MeOH (Tables 3.4 and 3.5, respectively). LODs are reported as the concentration of analyte (in mol L⁻¹) that produces a signal of twice (± 0.2 , $n=5$) the background.

In MeCN, the source gas flow rate and the cone voltage were varied until the best signal-to-noise ratio was obtained and optimal conditions were different for all PACs (Table 3.2). In general, relatively low cone voltages minimize the fragmentation of the analyte M⁺ and MH⁺ ions, thus improving signal-to-noise ratios. In contrast, higher cone voltages reduce the ion counts for the background and thus enhance signal-to-noise ratios. For example, ions formed between the solvent and the analyte (adduct ions) decompose easily at relatively high cone voltages. The reduction of adduct ions increases signal-to-noise ratios since it avoids spreading out the sample over a number of different ions. Overall, sensitivity is probably best at an intermediate cone voltage.

Table 3.4. Limits of detection (mol L^{-1}) in MeCN at different solvent flow rates.

PAC	Ion [m/z]	0.02 mL min ⁻¹	0.1 mL min ⁻¹	0.5 mL min ⁻¹
DBT	M ⁺ [184]	2.8e-7	3.4e-8	7.9e-9
PY	M ⁺ [202]	8.4e-8	1.6e-8	5.2e-9
CAR	M ⁺ [167]	1.5e-7	7.3e-9	4.6e-9
FLU	MH ⁺ [181]	1.3e-7	2.6e-8	2.0e-8

Table 3.5. Limits of detection (mol L^{-1}) in MeOH at different solvent flow rates.

PAC	Ion [m/z]	0.02 mL min ⁻¹	0.1 mL min ⁻¹	0.5 mL min ⁻¹
DBT	M ⁺ [184]	6.4e-6	3.1e-6	2.7e-6
PY	MH ⁺ [203]	1.2e-6	5.8e-6	1.9e-5
CAR	MH ⁺ [168]	2.7e-7	2.9e-6	1.2e-5
FLU	MH ⁺ [181]	1.8e-7	1.9e-7	2.9e-7

In MeCN, LODs decreased as solvent flow rate increased, and this seemed to apply both to M⁺ and MH⁺ ions. In MeOH, the gas flow rate and the cone voltage were kept constant for each PAC and the signal-to noise-ratio was not optimized (Table 3.2). Under these circumstances, LODs decreased as solvent flow rate increased for the M⁺ of DBT and the opposite trend was observed for PACs that form predominantly MH⁺ (CAR, PY and FLU). In general, LODs were not affected to a large extent (not even doubled) when the cone voltage or the gas flow rate differed from the values reported in Table 3.2.

Under the conditions used, LODs in MeCN are lower, and thus better than in MeOH. The limit of detection is defined by the signal-to-noise ratio. Under the same experimental conditions, the noise levels in the spectra taken in MeOH and in MeCN are very similar. However, the total ion counts for each PAC (sum of M⁺ and MH⁺ ions) are lower in MeOH than in MeCN. Reasons for this are proposed later in the thesis.

3.3.2.3. Linear Dynamic Ranges

Calibration curves of model PACs were obtained in both MeCN and MeOH to determine linear ranges of response. The linear dynamic range refers to the range of concentration of the analyte for which the relationship between the analyte concentration and the measured signal is linear. The upper concentration limit for the linear range was determined when adding the next higher concentration caused a clear decrease in the slope as determined by linear least square fitting. Linear ranges of response in MeCN and in MeOH are shown in Tables 3.6 and 3.7, respectively. The APCI(+) response to PACs is quite linear to the upper limit for all of the shown data. In many cases the response can be considered almost linear well above the upper limits listed. Linear ranges of at least three orders of magnitude, starting at the limits of detection, were obtained in MeCN. In MeOH, linear ranges of three orders of magnitude or less were observed. In general, linear ranges extended to higher concentrations in MeOH than in MeCN (for example, the upper limit of the linear range in MeOH at 0.5 mL min⁻¹ is about 5e-4 mol L⁻¹ vs. 5e-6 mol L⁻¹ in MeCN).

Calibration curves showing only the linear region (low concentration range) of response for DBT, PY, CAR and FLU in MeCN at 0.02 mL min⁻¹ and at 0.5 mL min⁻¹ are presented in Figures 3.10 and 3.11, respectively. The relative standard deviation for the linear portion of curves was about 3% for the slope and 60% for the intercept (n = 3).

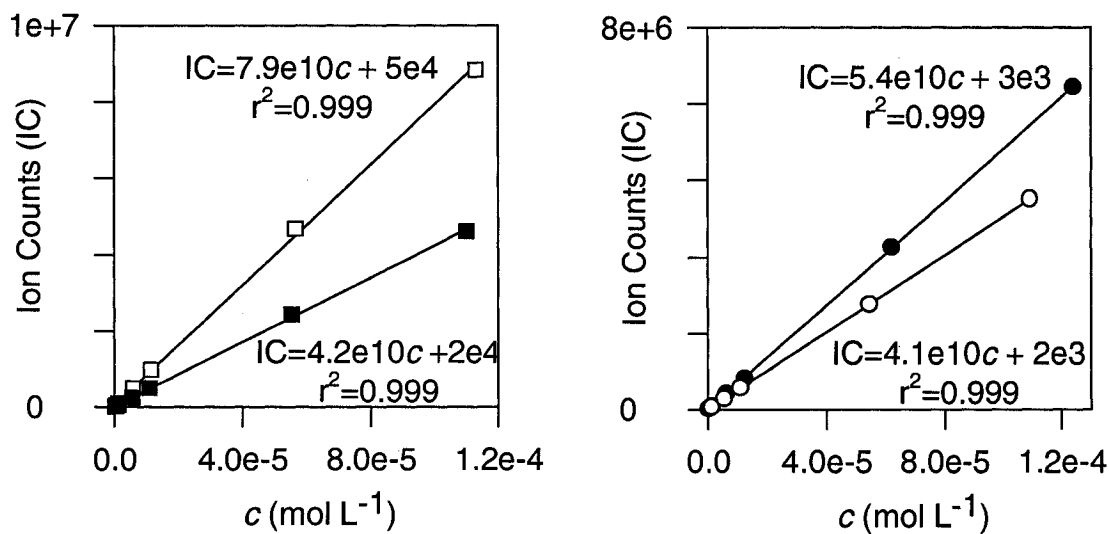
Table 3.6. Linear range of response (mol L⁻¹) in MeCN at different solvent flow rates.

PAC	Ion [m/z]	0.02 mL min ⁻¹	0.1 mL min ⁻¹	0.5 mL min ⁻¹
DBT	M ⁺ [184]	2.8e-7 to 1.1e-4	3.4e-8 to 1.1e-5	7.9e-9 to 5.5e-6
PY	M ⁺ [202]	8.4e-8 to 1.1e-4	1.6e-8 to 1.1e-5	5.2e-9 to 5.5e-6
CAR	M ⁺ [167]	1.5e-7 to 1.2e-4	7.3e-9 to 1.2e-5	4.6e-9 to 6.2e-6
	MH ⁺ [168]	4.7e-7 to 1.2e-4	2.9e-8 to 1.2e-5	1.8e-8 to 6.2e-6
FLU	M ⁺ [180]	3.9e-7 to 1.1e-4	1.8e-7 to 5.6e-5	5.6e-8 to 5.6e-6
	MH ⁺ [181]	1.3e-7 to 1.1e-4	2.6e-8 to 5.6e-5	2.0e-8 to 5.6e-6

Table 3.7. Linear range of response (mol L^{-1}) in MeOH at different solvent flow rates.

PAC	Ion [m/z]	0.02 mLmin^{-1}	0.1 mLmin^{-1}	0.5 mLmin^{-1}
DBT	$\text{M}^{+\bullet}$ [184]	$6.4\text{e-}6$ to $2.1\text{e-}2$	$3.1\text{e-}6$ to $4.1\text{e-}3$	$2.7\text{e-}6$ to $5.4\text{e-}4$
PY	$\text{M}^{+\bullet}$ [202]	$6.1\text{e-}6$ to $4.2\text{e-}4$	$1.8\text{e-}6$ to $4.2\text{e-}4$	$2.5\text{e-}5$ to $4.2\text{e-}4$
	MH^+ [203]	$1.2\text{e-}6$ to $4.2\text{e-}4$	$5.8\text{e-}6$ to $4.2\text{e-}4$	$1.9\text{e-}5$ to $4.2\text{e-}4$
CAR	$\text{M}^{+\bullet}$ [167]	$7.5\text{e-}7$ to $2.1\text{e-}3$	$2.9\text{e-}6$ to $2.1\text{e-}3$	$1.5\text{e-}5$ to $5.3\text{e-}4$
	MH^+ [168]	$2.7\text{e-}7$ to $2.1\text{e-}3$	$2.9\text{e-}6$ to $2.1\text{e-}3$	$1.2\text{e-}5$ to $5.3\text{e-}4$
FLU	$\text{M}^{+\bullet}$ [180]	$5.5\text{e-}5$ to $4.4\text{e-}4$	$3.2\text{e-}5$ to $4.4\text{e-}4$	$2.5\text{e-}5$ to $4.4\text{e-}4$
	MH^+ [181]	$1.8\text{e-}7$ to $4.4\text{e-}4$	$1.9\text{e-}7$ to $4.4\text{e-}4$	$2.9\text{e-}7$ to $4.4\text{e-}4$

Model PACs displayed linear regions for calibration curves at low concentrations with negative deviations from linearity at high concentrations. Figure 3.12 shows the non-linear portion (high concentration range) of representative calibration curves in MeCN at 0.5 mL min^{-1} .

**Figure 3.10.** Linear region (low concentration range) of calibration curves in MeCN for DBT (■), FLU (□), PY (○) and CAR (●) (solvent rate: 0.02 mL min^{-1}).

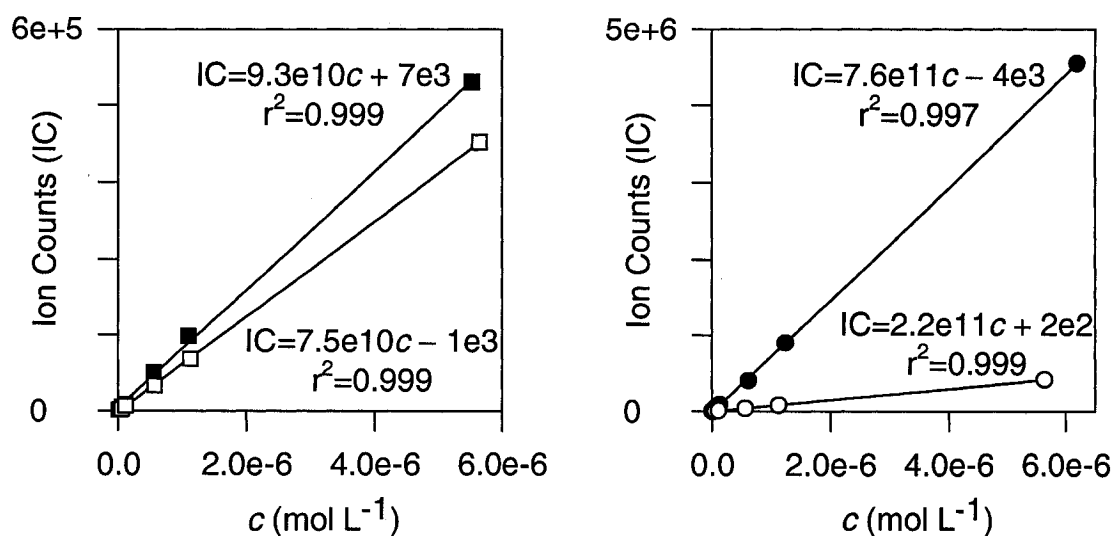


Figure 3.11. Linear region (low concentration range) of calibration curves in MeCN for DBT (■), FLU (□), PY (○) and CAR (●) (solvent rate: 0.5 mL min⁻¹).

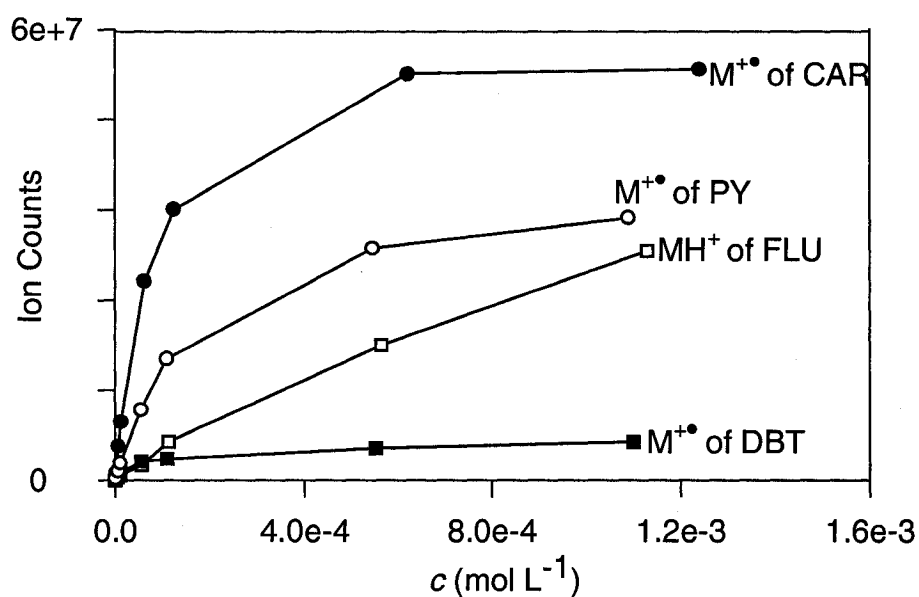


Figure 3.12. Non-linear region (high concentration range) of calibration curves in MeCN for DBT (■), FLU (□), PY (○) and CAR (●) (solvent rate: 0.5 mL min⁻¹).

The behavior observed at the low and high concentration ranges of the calibration curves is consistent with a model that postulates that a limited number of reagent ions ($S^{+\bullet}$ and SH^+) are formed in the corona discharge. For

relatively low concentrations of analyte in the ion source a large number of reagent ions are available to ionize the analyte and as a result, the counts for M^{+} and MH^{+} ions will increase linearly with the analyte concentration (no saturation occurs). However, at some critical concentration, the analyte will begin to use up a significant fraction of all of the available reagent ions, the number of reagent ions will significantly decrease and the response will become non-linear (saturation occurs).

The calibration curve data show that linear ranges extend to higher concentrations at lower solvent flow rates (Tables 3.6 and 3.7). This again can be explained as an effect of analyte concentration in the ion source. If gas flow rate is held constant, then the concentrations of both analyte and solvent molecules in the ion source are directly proportional to solvent flow rate. Therefore, there will be more analyte molecules in the ion source at higher solvent flow rates, though the ratio of analyte to solvent molecules will be the same. Since the number of reagent ions that form in the corona discharge is very similar at different solvent flow rates and more analyte molecules are present in the ion source at higher solvent flow rates, the non-linearity will start at some critical concentration of analyte, for which the formation of analyte ions begins to significantly decrease the number of reagent ions, and this critical concentration will be reached sooner at higher solvent flow rates.

To study the effect of the probe temperature on the analyte signal, calibration curves were obtained using higher probe temperatures (Figure 3.14). At probe temperatures higher than 200 °C, the ion counts for M^{+} and MH^{+} species increased, however, the linear range of response did not extend to higher concentrations. These results are expected since vaporization of analyte and solvent molecules is more efficient at higher probe temperatures and the ion counts for M^{+} and MH^{+} species will increase with the increase of molecules in the vapor phase. However, an increase in the number of molecules in the source would cause the analyte signal to saturate sooner, and therefore no improvement in linearity would be obtained.

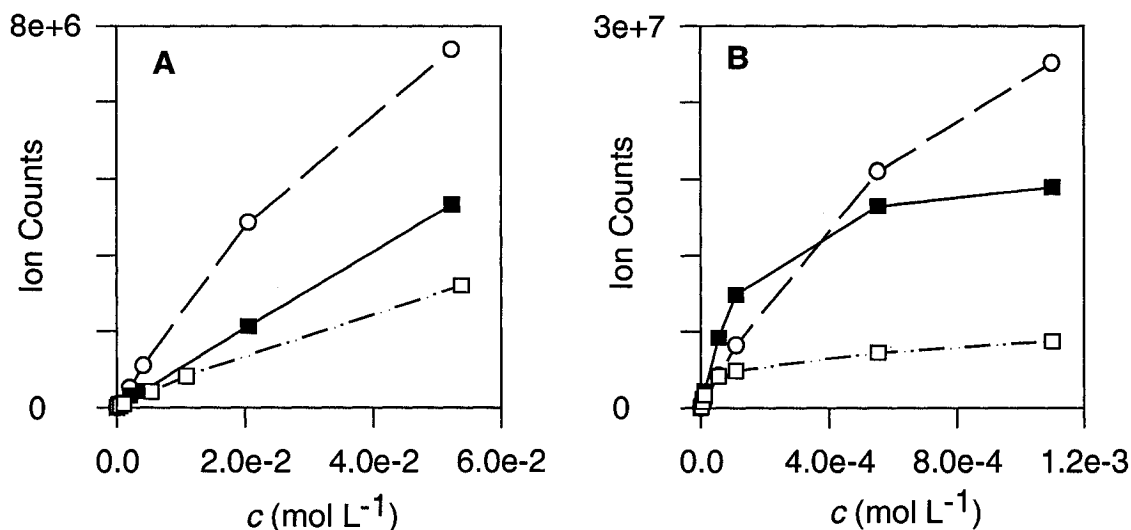


Figure 3.13. Calibration curves for M^{**} of DBT in MeOH (A) and in MeCN (B) at different solvent rates: 0.02 mL min⁻¹ (○), 0.1 mL min⁻¹ (■) and 0.5 mL min⁻¹ (□).

Calibration curves at different solvent flow rates (Figure 3.13) show that deviations from linearity are not as severe as low solvent flow rates for both MeCN and MeOH. This could be explained as an effect of the residence time of reagent ions at different solvent flow rates. As ionization in the corona discharge is current-limited, the number of ions that form in the discharge will be almost the same irrespective of the solvent flow rate. However, the number of solvent molecules that are not ionized will be higher at higher solvent flow rates. As a result, the chances of a solvent reagent ion, S^{+*} , colliding with a solvent molecule, S , according to $S^{+*} + S \rightarrow SH^+ + [S - H]^+$, will be fewer at lower solvent flow rates. Therefore, S^{+*} will stay longer in the ion source at lower solvent flow rates and the chances for the analyte to be ionized by charge exchange, $S^{+*} + M \rightarrow S + M^{+*}$, will be greater at lower solvent flow rates and hence, deviations from linearity will not be as severe for M^{+*} ions. The non-linearity may be caused by one or more of the following: (1) a limit in reagent ion concentration and (2) the residence time of reagent ions in the ion source.

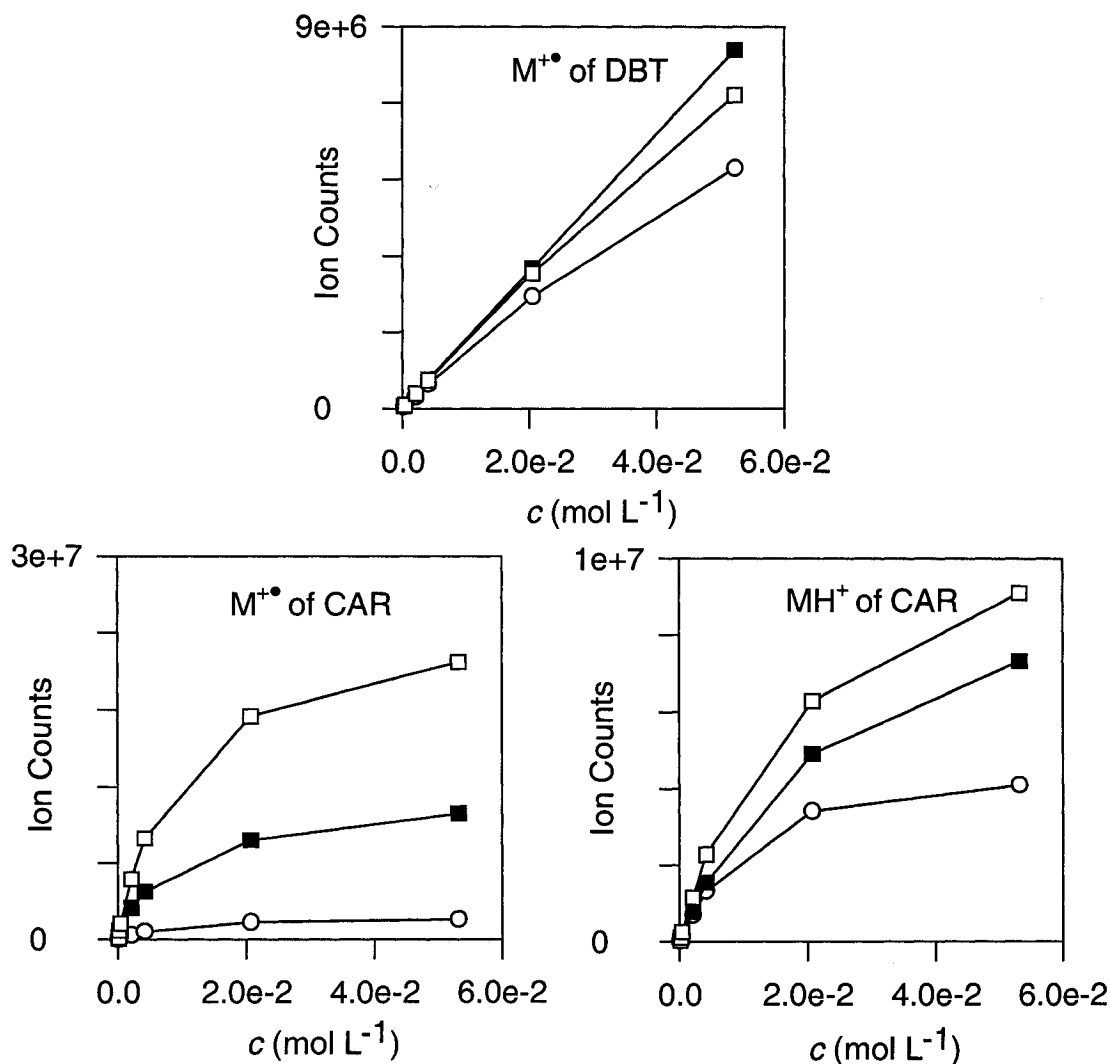


Figure 3.14. Calibration curves for DBT and CAR in MeOH (0.5 mL min^{-1}) at different probe temperatures: $200 \text{ }^{\circ}\text{C}$ (\circ), $350 \text{ }^{\circ}\text{C}$ (\blacksquare) and $450 \text{ }^{\circ}\text{C}$ (\square).

3.3.2.4. Studies of Mixtures of PACs

This study was undertaken when we observed that the signal for DBT decreased when increasing amounts of PY were added to a mixture of the two PACs. The APCI(+) mass spectra of DBT and PY alone, and a 1:1 mixture of DBT/PY are displayed in Figure 3.15.

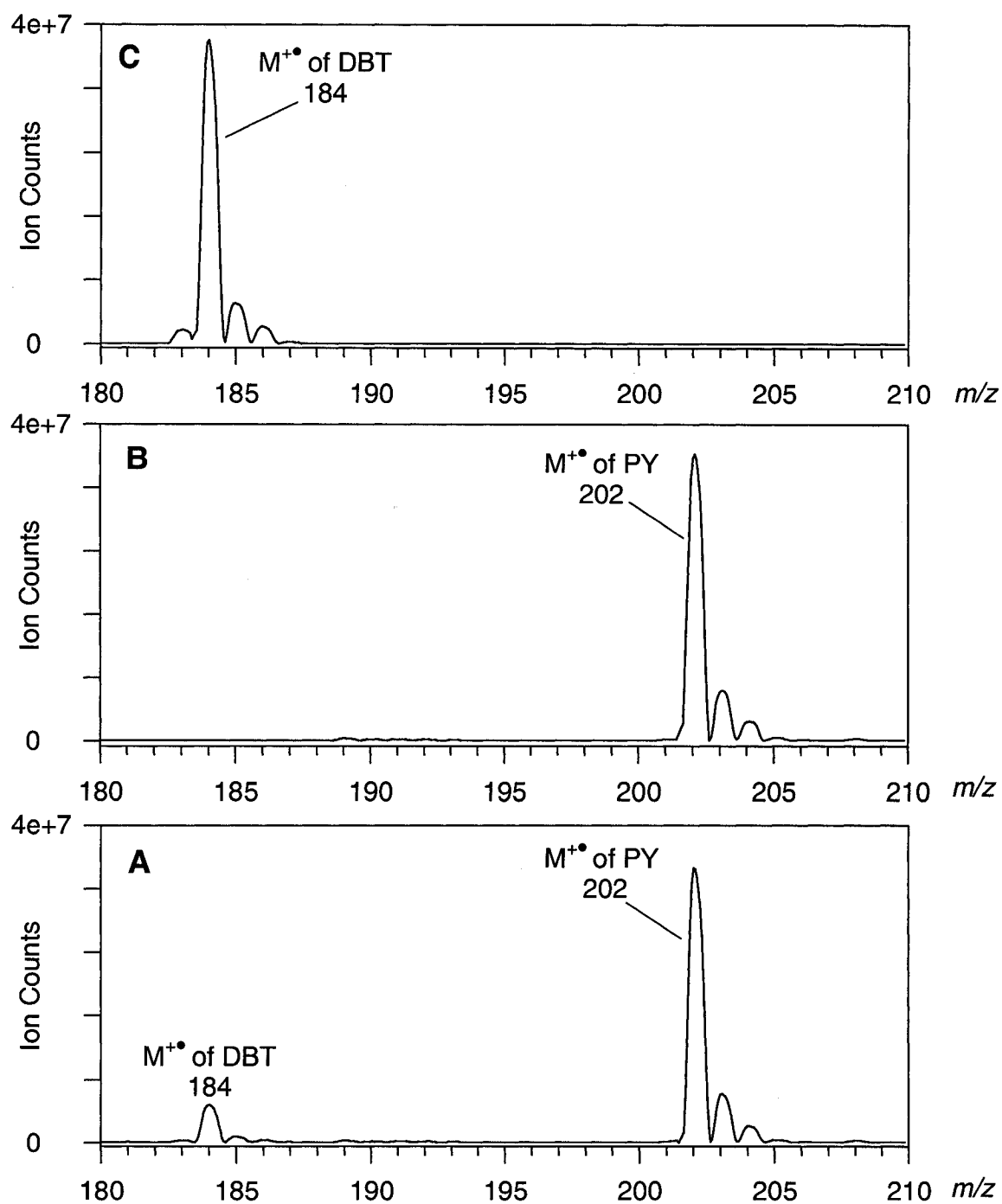


Figure 3.15. APCI(+) mass spectra of DBT alone (C), PY (impure) alone (B) and a 1:1 mixture of DBT:PY (A) in MeCN, $[DBT] = [PY] = 5.0 \times 10^{-4} \text{ mol L}^{-1}$.

Figure 3.15 shows that the counts for the $M^{+•}$ ion of DBT (m/z 184) are lower in the presence of PY compared to DBT alone (the concentrations of both PACs are sufficiently high to be in the non-linear portion of calibration curves). We decided then to study mixtures of two PACs to determine the effect of different compounds on one another in the event that two analytes are not resolvable by chromatography. DBT was always one of the pair of PACs and its concentration was not varied since we were interested in determining what effect other PAC would have on the response of DBT. The other PAC was added at concentrations equal to approximately 1/3 of that of DBT, equal to that of DBT, and 3 times that of DBT. Two concentration ranges were studied, one low enough to be in the linear range of response of calibration curves and one high enough to be in the non-linear region.

The effects on DBT of adding various amounts of PY, CAR and FLU in MeCN and in MeOH are shown in Tables 3.8 and 3.9, respectively. The data shown are the mixture ion currents for DBT as % of ion currents for DBT alone both in the linear and non-linear portions of calibration curves. The values were calculated according to equation (3.1) (the concentration of DBT alone and in the mixture is the same).

$$\frac{\text{Ion counts for } M^{+•} \text{ of DBT in mixture}}{\text{Ion counts for } M^{+•} \text{ of DBT alone}} \times 100 \quad (3.1)$$

The results in MeCN are more clear cut than those in MeOH, but the trends in both solvents are the same. In MeCN almost no interactions were observed in the linear region and serious interactions were observed in the non-linear region. In MeOH interference was greater in the linear region and not as serious in the non-linear region (as compared to MeCN), but there was still more interference in the non-linear region.

Table 3.8. Mixture ion currents for DBT as % of ion currents for DBT alone in MeCN.

PAC	Concentration of DBT (mol L ⁻¹)		DBT:PAC 3:1	DBT:PAC 1:1	DBT:PAC 1:3
PY	Linear	1e-6	101 %	101 %	98 %
	Non-linear	5e-4	44 %	14 %	2 %
CAR	Linear	1e-6	102 %	98 %	96 %
	Non-linear	5e-4	30 %	6 %	2 %
FLU	Linear	1e-6	97 %	98 %	97 %
	Non-linear	5e-4	97 %	94 %	85 %

Table 3.9. Mixture ion currents for DBT as % of ion currents for DBT alone in MeOH.

PAC	Concentration of DBT (mol L ⁻¹)		DBT:PAC 3:1	DBT:PAC 1:1	DBT:PAC 1:3
PY	Linear	1e-4	95 %	78 %	66 %
	Non-linear	8e-3	64 %	45 %	33 %
CAR	Linear	1e-4	96 %	78 %	63 %
	Non-linear	1e-2	57 %	45 %	38 %
FLU	Linear	1e-4	99 %	99 %	105 %
	Non-linear	1e-2	91 %	76 %	63 %

If two (or more) analytes are present simultaneously in the ion source, then these will compete for the reagent ions. When the concentrations of analytes are in the linear region of response, a large number of reagent ions are available and there is very little or no interference between two ions present at the same time in the source. Therefore, in the linear region, the presence of a second analyte has little effect on the response of DBT. In the non-linear regions, the analyte molecules must compete for reagent ions and interference will be observed if a limited number of reagent ions are formed in the plasma. In fact, the presence of the second PAC decreased the response of DBT (ion counts) and the sum of the ion counts of the two analytes was approximately equal to the ion counts of a single analyte. Like the calibration curve data, the

ion competition data also agree with a model that postulates that a limited number of reagent ions exist in the plasma and that competition arises when the ionization of analyte begins to use a significant fraction of reagent ions.

In terms of the ability to compete, both PY and CAR in MeCN and MeOH were more successful than DBT in reacting with reagent ions. FLU (which ionizes mainly by proton transfer while DBT ionizes by charge exchange) seemed less able to compete with DBT. From ionization energy data, this result is consistent with the expected order of ease of charge exchange for the model PACs: PY [7.4] ~ CAR [7.6] < FLU [8.3] ~ DBT [8.4] (ionization energies in eV are shown in brackets).

The other question would be to ask about the effects of adding DBT to other PACs. In this regard there was universally no effect observed at the low concentration ranges and very little effect noted at the high concentrations ranges either (Figures 3.16 and 3.17).

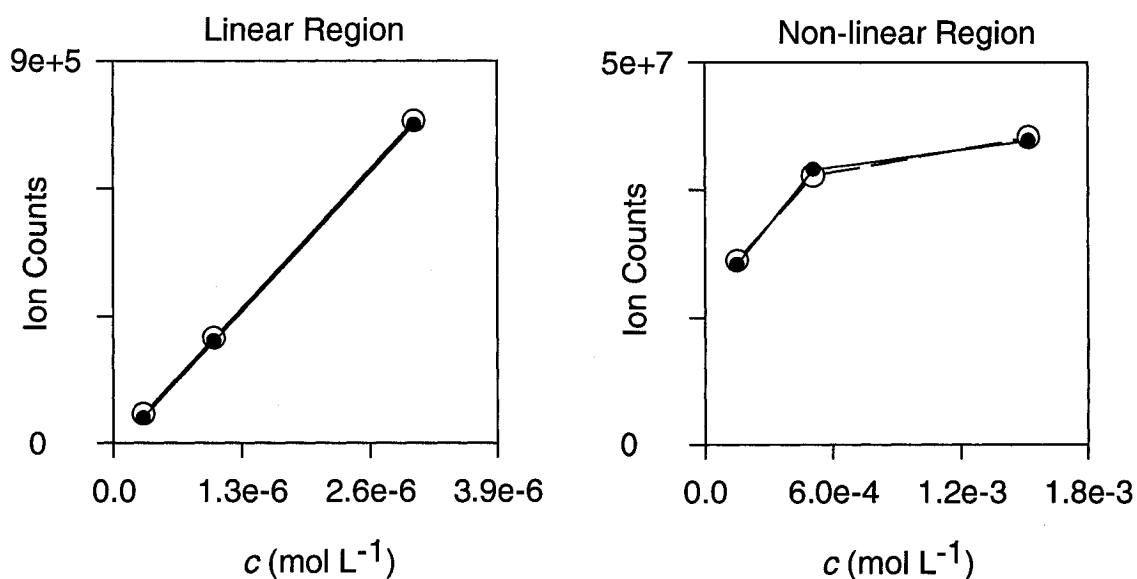


Figure 3.16. Effect of DBT on PY in MeCN: Ion counts for M⁺ of PY alone (●) and in DBT/PY mixture (○).

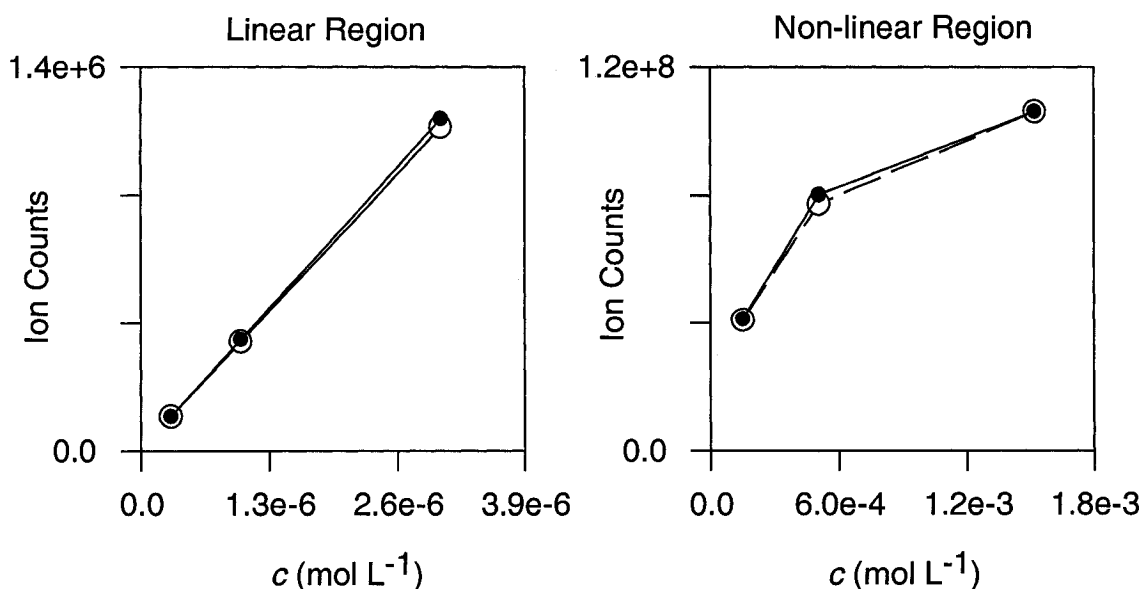


Figure 3.17. Effect of DBT on CAR in MeCN: ion counts for MH^+ of CAR alone (\bullet) and in DBT/CAR mixture (\circ).

3.3.2.5. Measurement of the Ionization Current

Both the calibration curve data and the ion competition data (the results in which two PACs are studied in the same sample) agree with a model which postulates that a maximum number of reagent ions are formed in the corona discharge. In order to test this idea, the ionization current was measured under different conditions.

A corona discharge occurs near the tip of a sharp needle when a high voltage is applied to the needle (Figure 3.18). Primary reagent ions are created in the high electric fields by abstraction of electrons from molecules ($\text{M} \rightarrow \text{M}^{+\bullet} + \text{e}^-$) and by collision of high velocity electrons with other molecules ($\text{M} + \text{e}^- \rightarrow \text{M}^{+\bullet} + 2\text{e}^-$). In a positive corona discharge the electrons migrate to the needle. The needle current is directly proportional to the flow of ions and electrons in the discharge.

The Quattro instrument has no inherent ability to measure corona needle currents. Therefore, a 5000 ohm resistor was inserted in series in the corona needle circuit. The voltage across this resistor was measured using a battery powered voltmeter. Current was calculated using this voltage and Ohm's law.

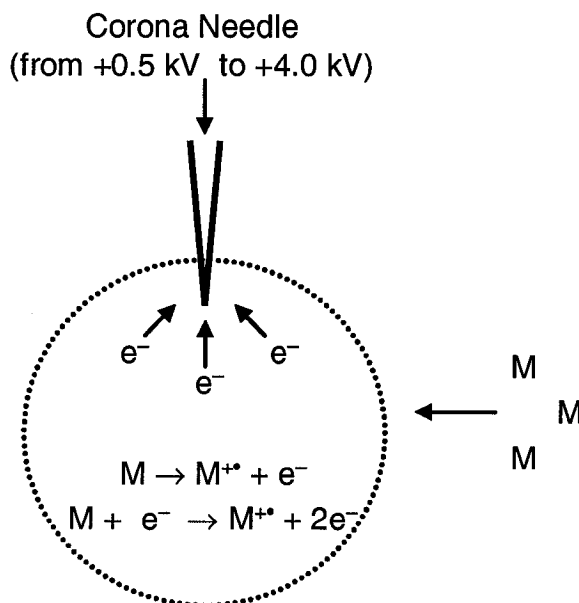


Figure 3.18. Expansion of the corona discharge region.

The ionization current was measured as a function of the corona needle voltage for three scenarios: (1) N_2 alone, (2) N_2 and solvent, and (3) N_2 , solvent and analyte. In all experiments the needle voltage was varied from +0.5 kV to +4.0 kV in steps of 0.5 kV. Figure 3.19 shows the ionization current in N_2 alone as a function of the corona needle voltage for different combinations of bath, sheath and nebulizer gas flow rates. The values of source gas rate (in sLph) given in the legend of the figure correspond to the total gas flow rate (sum of bath, sheath and nebulizer gas rates) and the standard deviation for the ionization current (N_2 alone) was $\pm 0.04 \mu A$ ($n = 3$).

Figure 3.19 shows that the ionization current increases when the corona needle voltage increases for different source gas flow rates. This happens because at higher needle voltages, the electrons are accelerated to higher velocities and secondary ionization occurs more readily. Consequently, the flow of electrons through the corona needle, and the measured current, will be also higher. However, the measured ionization current decreases at a given corona needle voltage with higher source gas flow rates. At high N_2 flow rates the electrons produced in the corona discharge are more easily swept from the

surroundings of the corona needle. They drift more and because fewer electrons reach the needle, the measured current decreases.

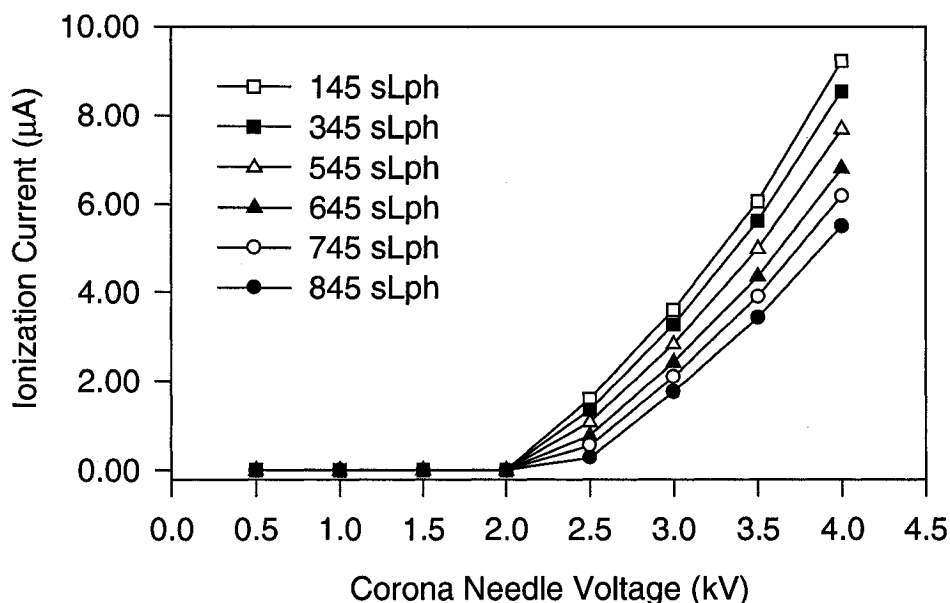


Figure 3.19. Ionization current as a function of the corona needle voltage in N_2 alone at different gas flow rates.

Ionization current curves for N_2 , MeCN, MeOH and toluene at a given N_2 gas flow rate and two different solvent flow rates (0.02 and 0.5 mL min^{-1}) are shown in Figure 3.20. The standard deviation for the ionization current was $\pm 0.04 \text{ } \mu\text{A}$ in MeCN and MeOH, and $\pm 0.1 \text{ } \mu\text{A}$ in toluene ($n = 3$). At a given corona needle voltage and low solvent flow rates, the ionization current and thus, the number of ions produced in the discharge is very similar in N_2 , MeCN, MeOH and toluene. At higher solvent flow rates, the ionization current values diverge more but the magnitude of these deviations do not account for the large differences observed among solvents in TIC studies (see below, Tables 3.10 to 3.12). This indicates that the number of ions produced in the discharge is not as important in the formation of the M^{+*} and MH^+ analyte ions as is the nature of the reagent ions. Moreover, the ionization current follows the order: MeOH > MeCN > toluene, which is opposite to the order observed in TIC studies (toluene > MeCN > MeOH) and which differs from the expected order of ease of charge exchange

($\text{N}_2^{+\bullet} + \text{S} \rightarrow \text{N}_2 + \text{S}^{+\bullet}$) from ionization energy data: toluene [8.8] > MeOH [10.8] > MeCN [12.2] (ionization energies in eV are shown in brackets).

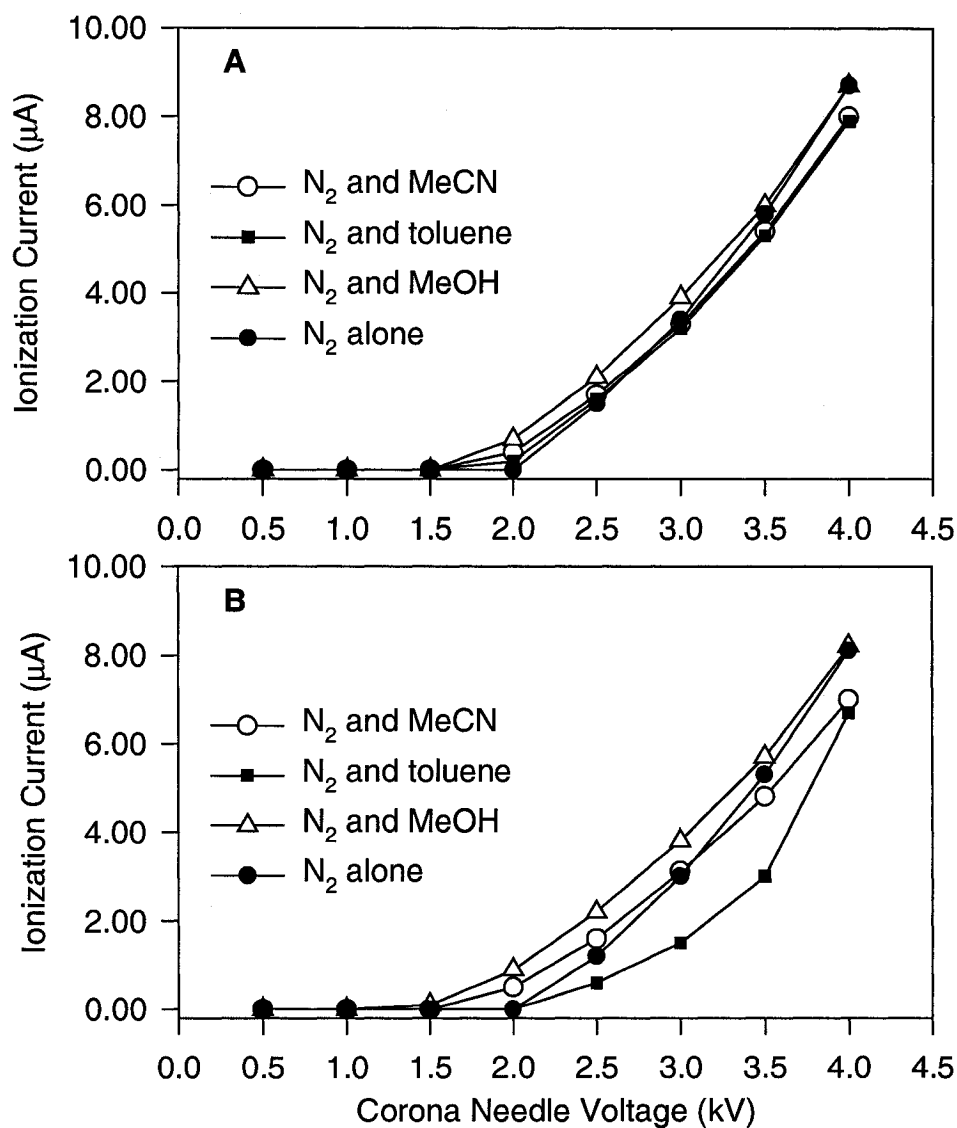


Figure 3.20. Ionization current as a function of the corona needle voltage for N₂, MeCN, MeOH and toluene at 0.02 mL min⁻¹ (A) and 0.5 mL min⁻¹ (B). Conditions: B (200 sLph), S (200 sLph) N (45 sLph).

The ionization current was also measured in the presence of analyte using DBT as test PAC. Ionization current curves in MeOH, MeCN and toluene at different solvent flow rates, for low (linear region) and high (non-linear region) concentrations of DBT are shown in Figures 3.21 through 3.26.

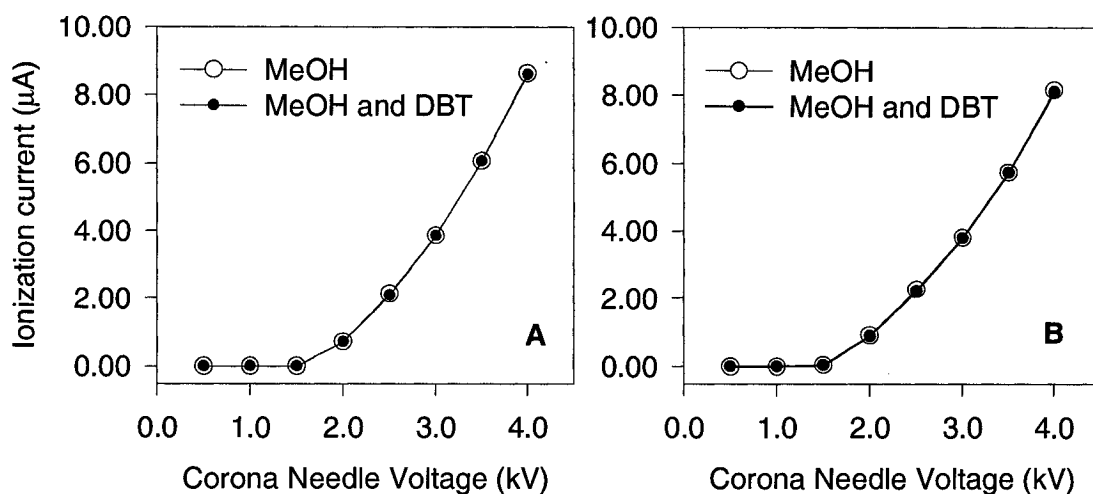


Figure 3.21. Ionization current as a function of the corona needle voltage for MeOH alone and MeOH with DBT (linear region, $[DBT] = 6.6 \times 10^{-6} \text{ mol L}^{-1}$) at different solvent flow rates: 0.02 mL min^{-1} (A) and 0.5 mL min^{-1} (B).

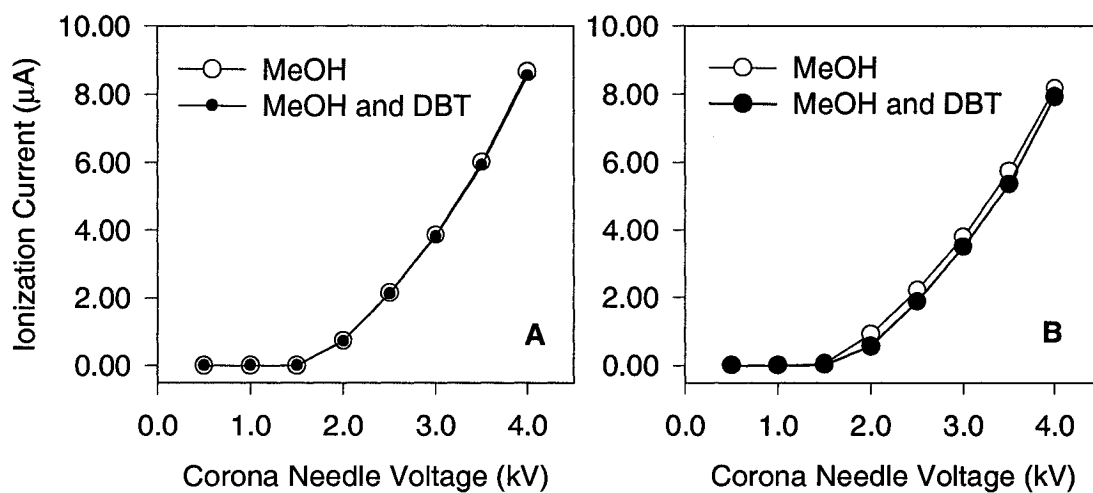


Figure 3.22. Ionization current as a function of the corona needle voltage for MeOH alone and MeOH with DBT (non-linear region, $[DBT] = 2.0 \times 10^{-2} \text{ mol L}^{-1}$) at different solvent flow rates: 0.02 mL min^{-1} (A) and 0.5 mL min^{-1} (B).

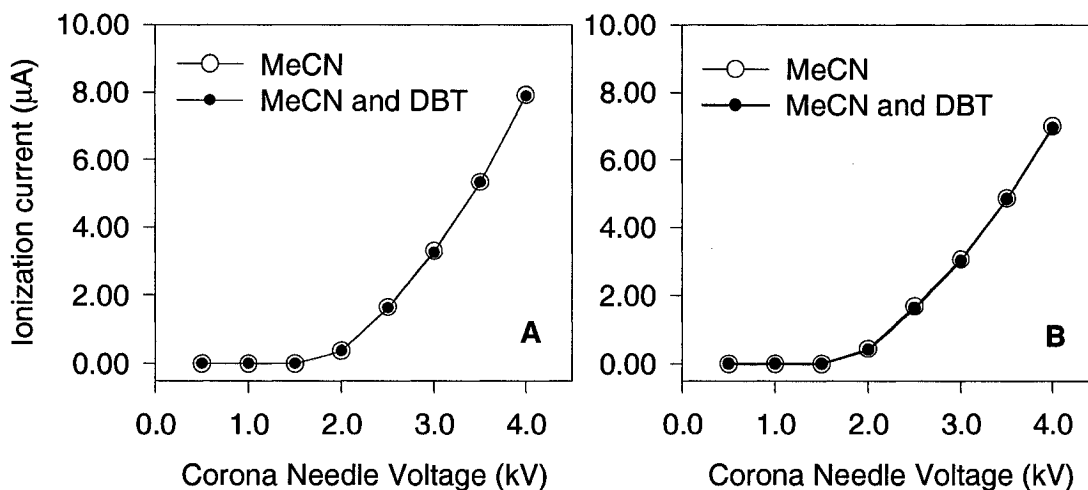


Figure 3.23. Ionization current as a function of the corona needle voltage for MeCN alone and MeCN with DBT (linear region, $[\text{DBT}] = 6.6 \times 10^{-6} \text{ mol L}^{-1}$) at different solvent flow rates: 0.02 mL min^{-1} (A) and 0.5 mL min^{-1} (B).

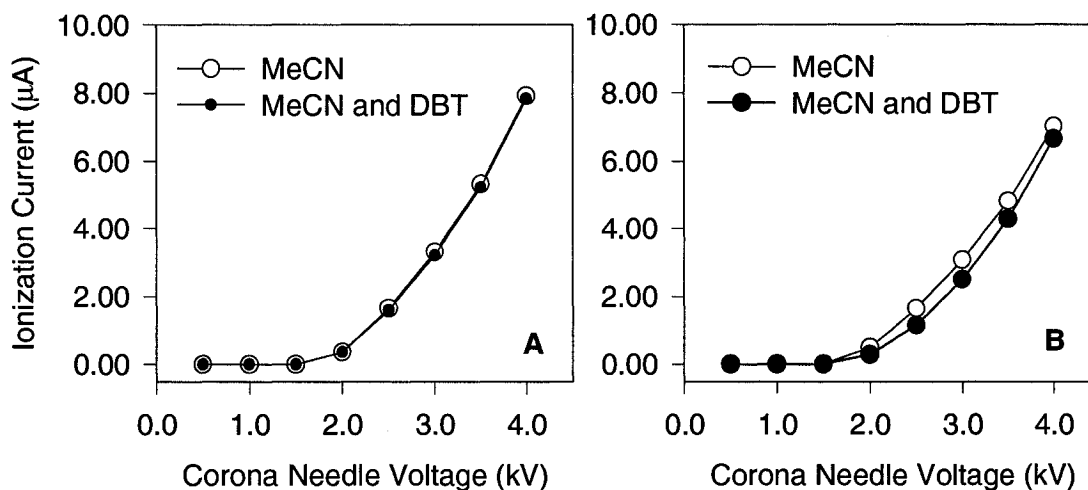


Figure 3.24. Ionization current as a function of the corona needle voltage for MeCN alone and MeCN with DBT (non-linear region, $[\text{DBT}] = 2.0 \times 10^{-2} \text{ mol L}^{-1}$) at different solvent flow rates: 0.02 mL min^{-1} (A) and 0.5 mL min^{-1} (B).

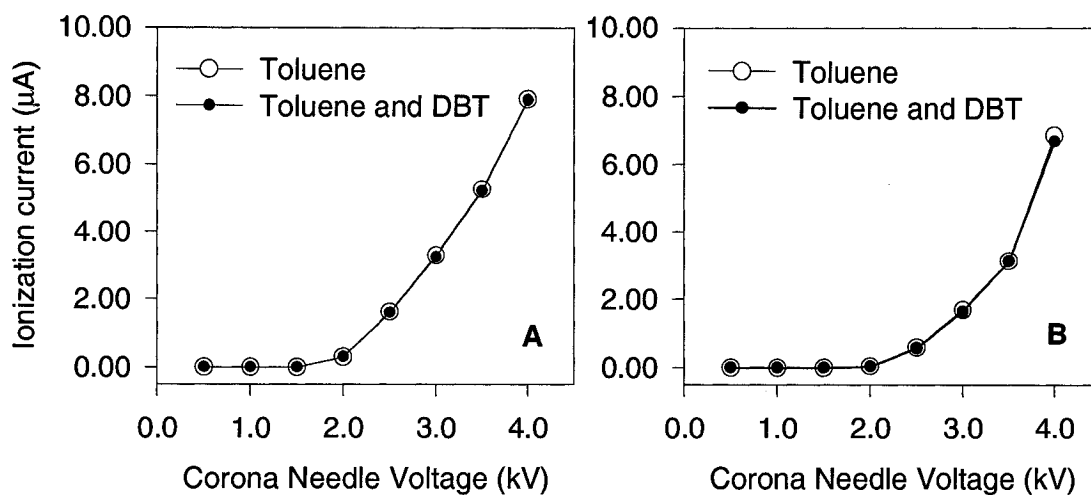


Figure 3.25. Ionization current as a function of the corona needle voltage for toluene alone and toluene with DBT (linear region, $[DBT] = 6.6 \times 10^{-6} \text{ mol L}^{-1}$) at different solvent flow rates: 0.02 mL min^{-1} (A) and 0.5 mL min^{-1} (B).

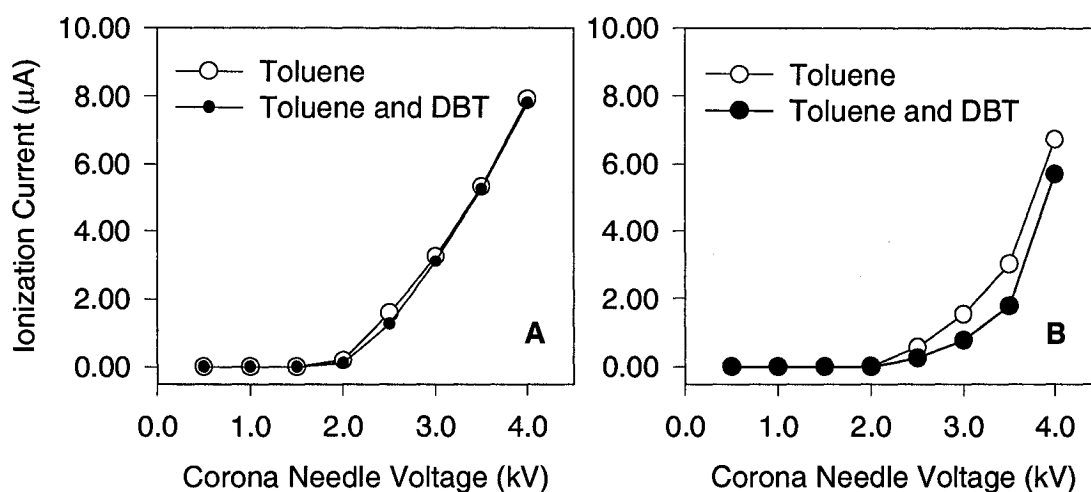


Figure 3.26. Ionization current as a function of the corona needle voltage for toluene alone and toluene with DBT (non-linear region, $[DBT] = 2.0 \times 10^{-2} \text{ mol L}^{-1}$) at different solvent flow rates: 0.02 mL min^{-1} (A) and 0.5 mL min^{-1} (B).

Each graph shows two ionization current curves, one for the solvent alone and the second for the solvent along with the analyte. The standard deviation for the ionization current was $\pm 0.04 \mu\text{A}$ in MeOH and MeCN, and $\pm 0.2 \mu\text{A}$ in toluene ($n = 3$) when the analyte was present. In almost all instances (except for high concentrations of DBT at the high solvent flow rate) the ionization currents in the solvent alone and in the presence of analyte were very similar. For concentrations of DBT in the non-linear region and at 0.5 mL min^{-1} , the ionization current in the presence of DBT was slightly lower than the ionization current in the solvent alone (Figures 3.22 B, 3.24 B and 3.26 B).

A possible explanation for effect observed in Figures 3.22 B, 3.24 B and 3.26 B could be that heavier $\text{M}^{+\bullet}$ ions, such as those of the analyte, travel more slowly than lighter ions towards the counter electrode and therefore, heavier species will stay longer in the vicinity of the corona needle. In this region, recombination of $\text{M}^{+\bullet}$ may occur according to $(\text{M}^{+\bullet} + \text{e}^- \rightarrow \text{M})$, thus reducing the number of electrons that flows towards the needle and the ionization current.

3.3.2.6. Total Ion Current Studies

The relative ionization efficiency of each PAC was determined in MeCN, MeOH and toluene to study ionization mechanisms. The ionization efficiency is given by the total ion counts (TIC). TIC corresponds to the sum of counts for $\text{M}^{+\bullet}$ and MH^+ ions for each PAC. The counts for $\text{M}^{+\bullet}$ and MH^+ ions in each solvent are shown in Tables 3.10 to 3.12 ($[\text{PAC}] = 1.0 \times 10^{-5} \text{ mol L}^{-1}$).

Toluene was used as a solvent of low ionization energy in an attempt to verify the idea that ionization efficiency was related to the ΔH of the simple charge exchange reaction ($\text{Solvent}^{+\bullet} + \text{Analyte} \rightarrow \text{Solvent} + \text{Analyte}^{+\bullet}$) (see below): MeCN [12.2] > MeOH [10.8] > toluene [8.8] (ionization energies in eV are shown in brackets).

Large differences exist in the ionization efficiency among solvents, both with regard to charge exchange and proton transfer. In general, the total ion counts ($\text{M}^{+\bullet} + \text{MH}^+$) for all analytes followed the order: toluene > MeCN > MeOH,

and this order seemed to apply both to the formation of $M^{+•}$ (with the exception of FLU) and MH^{+} (with the exception of PY).

Table 3.10. Species and total ion counts (TIC) for PACs in MeCN (relative standard deviation in % shown in parentheses, $n = 5$).

PAC	$M^{+•}$	MH^{+}	TIC
Pyrene	9.0e5 (10)	Not observed	9.0e5 (10)
Carbazole	1.9e6 (5)	3.9e6 (4)	5.8e6 (3)
Fluorenone	2.1e5 (14)	2.0e6 (11)	2.2e6 (10)
Dibenzothiophene	6.8e5 (11)	Not observed	6.8e5 (11)

Table 3.11. Species and total ion counts (TIC) for PACs in MeOH (relative standard deviation in % shown in parentheses, $n = 5$).

PAC	$M^{+•}$	MH^{+}	TIC
Pyrene	1.4e3 (8)	1.3e3 (7)	2.7e3 (7)
Carbazole	4.1e3 (7)	4.6e3 (8)	8.7e3 (5)
Fluorenone	2.9e3 (8)	9.7e4 (1)	1.0e5 (2)
Dibenzothiophene	2.6e3 (8)	Not observed	2.6e3 (8)

Table 3.12. Species and total ion counts (TIC) for PACs in toluene (relative standard deviation in % shown in parentheses, $n = 5$).

PAC	$M^{+•}$	MH^{+}	TIC
Pyrene	1.1e7 (9)	4.6e6 (9)	1.6e7 (7)
Carbazole	1.1e7 (7)	7.7e6 (4)	1.9e7 (4)
Fluorenone	1.5e5 (10)	1.9e7 (6)	1.9e7 (6)
Dibenzothiophene	6.6e6 (14)	3.6e5 (58)	7.0e6 (13)

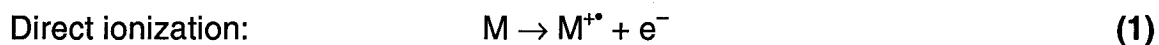
The total ion current studies show that the ionization efficiency of PACs is higher in toluene and lower in MeOH. To test the idea that toluene might significantly improve ionization, different amounts of toluene were added (2.5, 5 and 10% v/v) to solutions of DBT in MeOH ($[DBT] = 4 \times 10^{-5} \text{ mol L}^{-1}$). However, after the addition of toluene, no significant improvement ($\times 10$) of the total ion counts for DBT was obtained, the ion counts increased only slightly: 2 times (2.5% toluene), 2.5 times (5% toluene) and 4 times (10% toluene).

3.3.2.7. Ionization Mechanisms in APCI(+)

Introduction

Ionization in APCI occurs by ion/molecule reactions between analyte molecules and the components of a plasma. The plasma can be formed by either β -radiation from a ^{63}Ni source or a corona discharge. Both ionization methods provide similar spectra, however, the corona discharge produces higher ion currents (~ 100 times) and thus wider linear dynamic ranges than the ^{63}Ni source (Carroll *et al.* 1975).

A corona discharge forms in a very small volume, assumed to be spherical, at the tip of a sharp needle to which a very high voltage ($\sim 4.0 \text{ kV}$) is applied. The voltage applied to the corona needle can be either positive or negative. The plasma is formed by abstraction of electrons from molecules due to the high electric field present in the discharge (1) and by acceleration of the electrons in the high fields to velocities high enough to produce secondary ionization by collision with other molecules (2).



In a positive corona discharge, the electrons travel a short distance toward the needle and the molecular ions, $\text{M}^{+\bullet}$, migrate a much larger distance toward the counter electrode. This separation of charge allows ion/molecule reactions to occur in a large volume far from the corona needle (Figure 3.27).

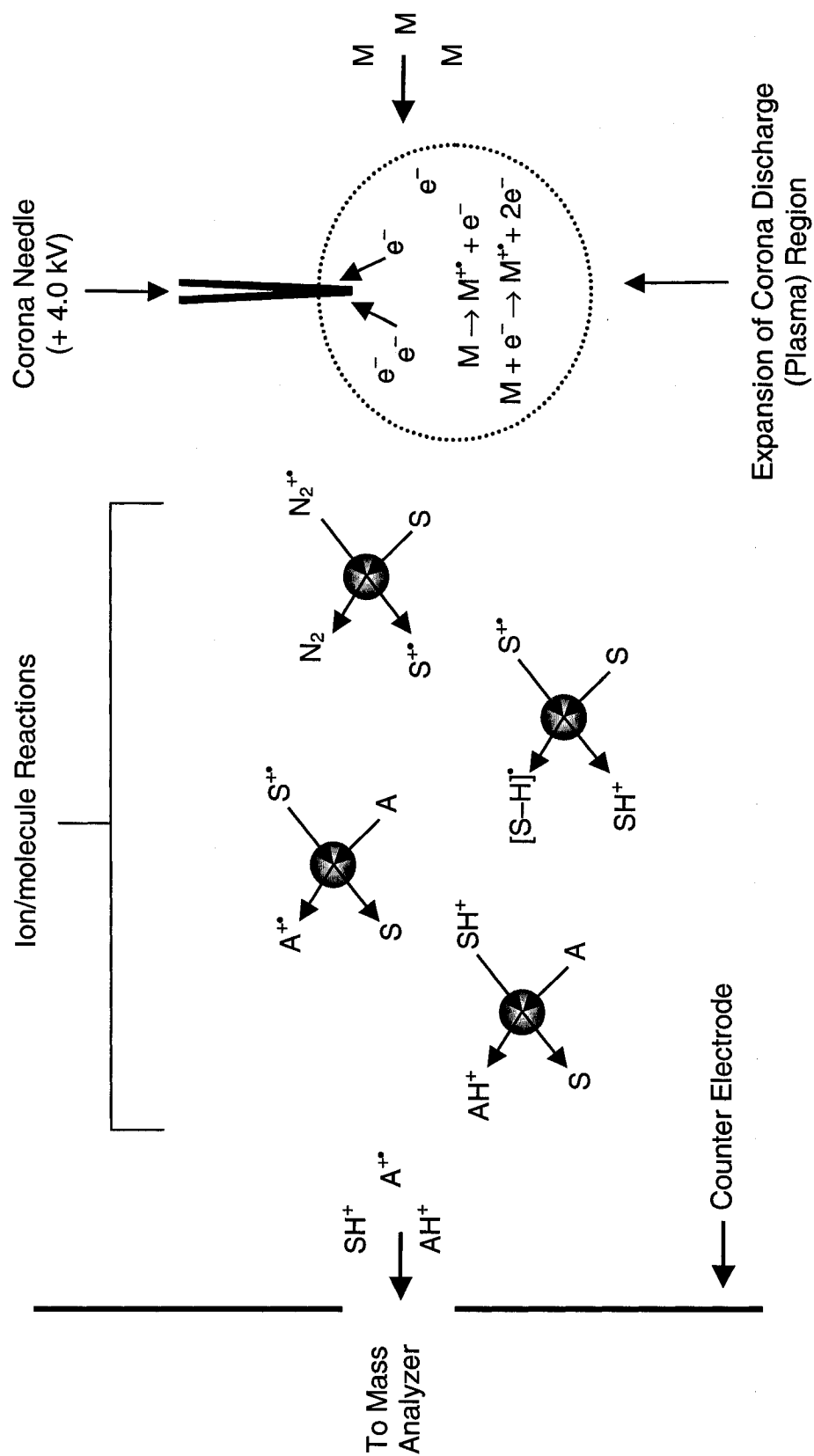
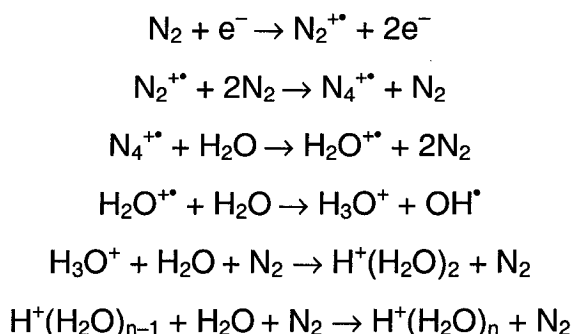


Figure 3.27. Ionization mechanisms in APCI(+) with nitrogen as source gas (M: molecule, A: analyte, S: solvent). (Not drawn to scale).

The classical ionization mechanism for APCI is proton transfer from a protonated solvent molecule (or cluster) and was first proposed by Horning and co-workers (Horning *et al.* 1973).

Using dry nitrogen gas they observed ions present in the plasma formed with a ^{63}Ni foil source. Assuming that any water clusters detected originated from traces of water present on the source walls, the authors rationalized the ions observed on the basis of the following sequence of reactions.



Later on the authors showed evidence for this mechanism and demonstrated that the mixture of ions detected depended directly on the distance of the corona discharge needle from the entrance aperture of the mass analyzer (Dzidic *et al.* 1976). Using a source with a corona discharge needle very close to the skimmer cone (0.5 mm), they observed ions with very short residence times in the source. Under these conditions and with pure N_2 gas, the base peak in the spectrum was $\text{N}_4^{+\bullet}$, and small amounts of $\text{H}_2\text{O}^{+\bullet}$, $\text{N}_2^{+\bullet}$ and N_3^+ were also identified. High energy species, such as $\text{H}_2\text{O}^{+\bullet}$, $\text{N}_4^{+\bullet}$, $\text{N}_2^{+\bullet}$ and N_3^+ were not observed with a source in which the corona needle was 4 mm from the skimmer cone (Carroll *et al.* 1975).

These studies show that high energy ions, for example $\text{N}_4^{+\bullet}$ and $\text{N}_2^{+\bullet}$ in a discharge in N_2 gas, are formed from the predominant molecular species present in the corona discharge region. These primary reagent ions migrate into other regions in the source and react with solvent, analyte or impurity molecules to form ions of lower energy (Figure 3.27). At atmospheric pressure, where there are many collisions, equilibrium is rapidly achieved and only ions of the lowest

energy are detected. In the sources cited above, equilibrium seemed to be observed only if the corona needle was at least 4 mm from the analyzer aperture.

There are several factors that make explanation of ionization mechanisms in APCI difficult under our present conditions. Both molecular ions, M^+ , and protonated molecules, AH^+ , are observed, indicating that there are at least two mechanisms for ionization, one (or more) involving charge exchange and one (or more) involving proton transfer. Assuming that there is a limited number of primary ions formed in the discharge, the number of analyte ions formed by charge exchange will depend on the mechanisms available to form ions of all types, not just on the energetics of the simple charge exchange reaction.

A second complication is that the ions in and near the corona discharge can not be observed in our current situation. As previously explained, the corona needle in the APCI ion source employed here is fixed in position. Since the distance from the corona needle to the skimmer cone is about 5 cm (Figure 1.5), only the ions that survive the entire journey through the ion source of the mass spectrometer, rather than the ions formed directly in the corona discharge, can be detected under the circumstances of this work. To illustrate this thought, background spectra in toluene, MeCN and MeOH are shown in Figures 3.28 through 3.30.

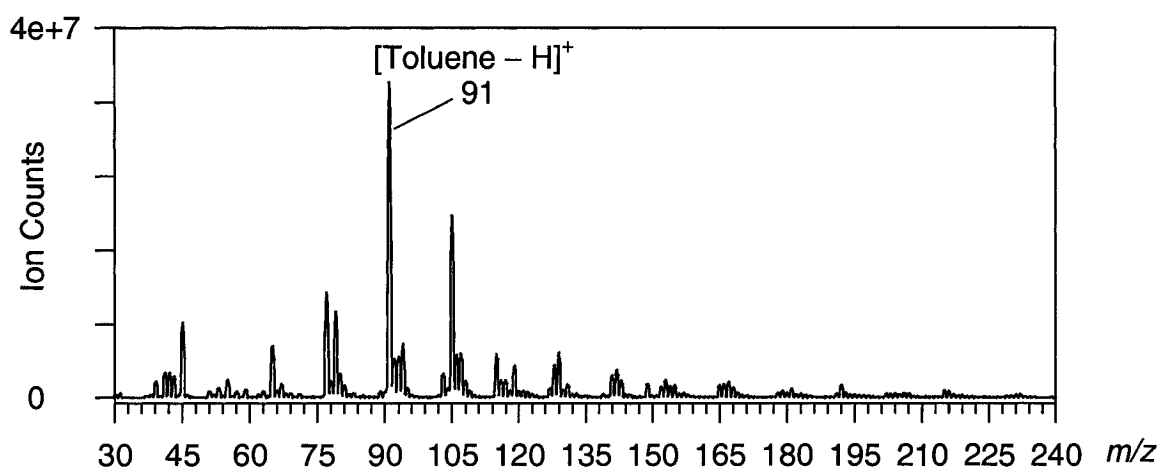


Figure 3.28. Background spectrum of toluene at 40 V cone. Conditions: solvent flow rate (0.5 mL min^{-1}), B (200 sLph), S (200 sLph) and N (45 sLph).

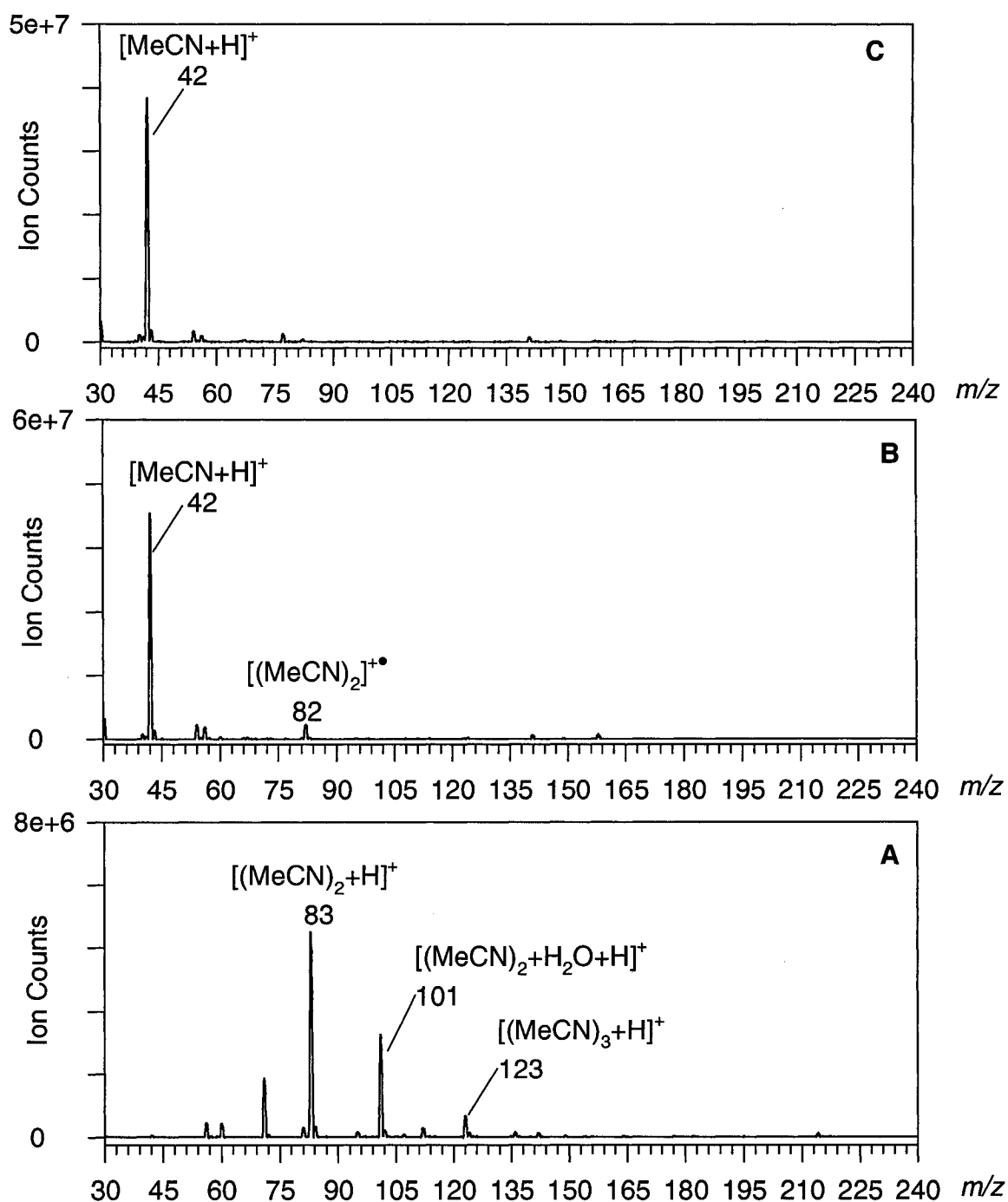


Figure 3.29. Background spectra of MeCN at 5 V (A), 30 V (B) and 40 V (C) cone. Conditions: solvent flow rate (0.5 mL min^{-1}), B (400 sLph), S (200 sLph) and N (45 sLph).

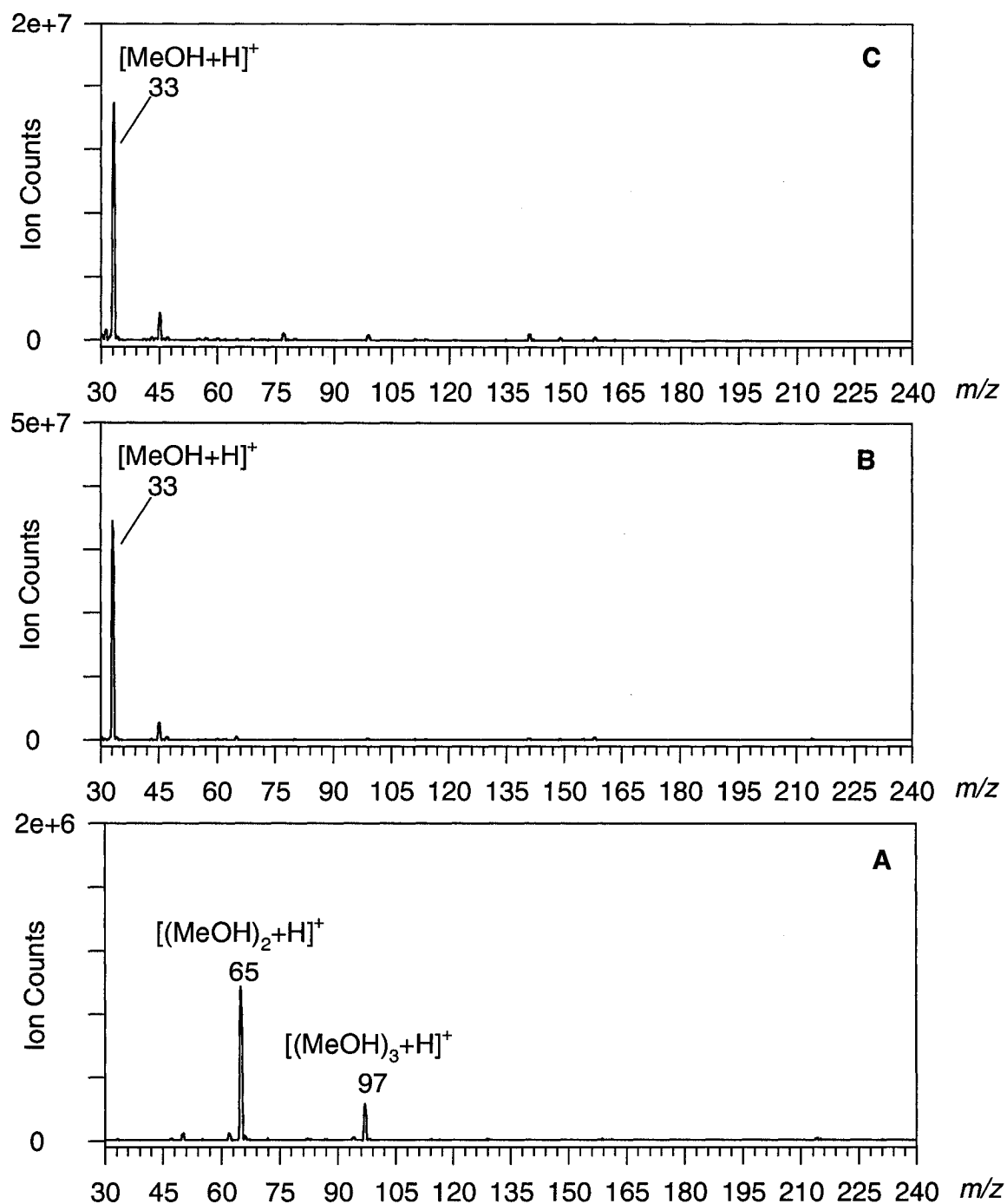


Figure 3.30. Background spectra of MeOH at 5 V (A), 30 V (B) and 40 V (C) cone. Conditions: solvent flow rate (0.5 mL min^{-1}), B (400 sLph), S (200 sLph) and N (45 sLph).

Protonated solvent molecules and their proton-bound clusters (the latter only observed at low cone voltages) were the major species observed in the background spectra of MeCN and MeOH (Figures 3.29 and 3.30, respectively). The ion counts for the molecular ions of MeCN and MeOH, which are of higher energy than the protonated solvent ions, were very low.

From the three solvents tested, toluene might be a special case in the sense that the major peak observed in its mass spectrum was [toluene – H]⁺, at m/z 91, with other major peaks at m/z 105, 77, 79 and 65, indicating fragmentation, addition and perhaps rearrangement reactions in the plasma (Figure 3.28). Like MeCN and MeOH, the ion counts for the molecular ion of toluene were very low.

Formation of primary ions (N_2^{+} and N_4^{+})

In the following discussion, N_2 is the source gas, A is the analyte, and S is the solvent. If primary ion formation occurs in a very small volume at the corona needle tip and the field strength is high enough to cause ionization of all molecules within that volume, the ions will be formed directly in proportion to their concentration. The concentration of solvent and analyte relative to that of N_2 can be calculated for MeCN, MeOH and toluene at different solvent flow rates (see Appendix A for details).

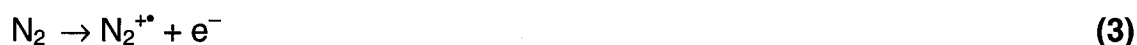
Relative concentrations, $[N_2] : [Solvent] : [Water] : [Analyte]$, for the various solvents at different solvent flow rates (based on the calculations shown in Appendix A) are shown in Table 3.13. Even at the highest flow rate used for MeOH, there are about 25 times as many N_2 molecules present as solvent molecules and 7×10^7 times as many N_2 molecules as analyte molecules (under the conditions used in the calculations).

Although conditions near the corona needle are such that all molecules within the plasma forming region can be ionized, primary ions will be formed directly in proportion to the concentration of N_2 , solvent, analyte and impurities.

Table 3.13. Concentration of solvent, water and analyte relative to N₂ for MeCN, MeOH and toluene at different solvent rates ([N₂]:[Solvent]:[Water]:[Analyte]).

Solvent flow rate:	MeCN
0.02 mL min ⁻¹	[1] : [1.14e-3] : [2.62e-7] : [5.95e-10]
0.10 mL min ⁻¹	[1] : [5.70e-3] : [1.32e-6] : [2.98e-9]
0.50 mL min ⁻¹	[1] : [2.85e-2] : [6.61e-6] : [1.49e-8]
	MeOH
0.02 mL min ⁻¹	[1] : [1.47e-3] : [2.62e-7] : [5.95e-10]
0.10 mL min ⁻¹	[1] : [7.36e-3] : [1.32e-6] : [2.98e-9]
0.50 mL min ⁻¹	[1] : [3.68e-2] : [6.61e-6] : [1.49e-8]
	Toluene
0.02 mL min ⁻¹	[1] : [5.60e-4] : [2.62e-7] : [5.95e-10]
0.10 mL min ⁻¹	[1] : [2.80e-3] : [1.32e-6] : [2.98e-9]
0.50 mL min ⁻¹	[1] : [1.40e-2] : [6.61e-6] : [1.49e-8]

Therefore, the major source of primary ions will be N₂ gas and the major primary ion formed in the corona discharge will be N₂⁺. This will happen even though the ionization energy of N₂ is higher than that of the analyte or the solvent. The thermodynamic properties relevant to ionization of the materials used in this study are shown in Table 3.14.



The positive radical ions of N₂ formed in the corona discharge by (3) and (4) may then undergo ion/molecule reactions to give N₄⁺ (5) as previously suggested (Horning *et al.* 1973 and Dzidic *et al.* 1976).



Table 3.14. Thermodynamic data for analytes, solvents and nitrogen gas.

Species	Ionization Energy ^a (IE) (eV)	Proton Affinity ^a (PA) (eV)	Bond Dissociation Energy of C _{sp3} -H Bonds ^d <i>D</i> (S—H) (eV)
PY	7.43	9.01 ^a / 9.14 ^b	—
CAR	7.6	9.05 ^b	—
FLU	8.36	8.98 ^b	—
DBT	8.44	8.56 ^b	—
Toluene	8.83	8.13 ^a / 8.28 ^b	3.8
MeOH	10.84	7.82 ^a / 7.72 ^b	4.2
MeCN	12.20	8.08 ^a / 8.08 ^b	4.1
N ₂	15.58 ^c	5.12	—
H	13.60	—	—

^a Values taken from <http://www.webbook.nist.gov>, access date: February 5, 2007.

^b Values calculated using the PBE1PBE/6-31+G(*d*)/B3LYP/6-31G(*d*) level of theory (Appendix B).

^c The recombination energy of N₂⁺⁺ is 15.3 eV (Harrison 1992 p 13)

^d Values obtained from (Luo 2003 pp 30–31, 57, 76). The C–H bond dissociation energy in benzene is 4.9 eV.

Formation of charge exchange reagent ion (S⁺⁺)

Primary reagent ions (N₂⁺⁺ and N₄⁺⁺) migrate to other regions in the ion source and will ionize those molecules with ionization energy lower than the recombination energy of N₂⁺⁺ by charge exchange (*e.g.* solvent and analyte molecules). Given that the concentration of solvent molecules in the ion source is much higher than the concentration of analyte molecules, the first step in forming the ions actually observed in the mass spectra is probably charge exchange to a solvent ion:



Reactions (6) and (7) must be very rapid and strongly exothermic since neither N_2^{+*} nor N_4^{+*} were observed in any mass spectra nor did Horning and associates observe such ions in spectra taken with a source in which the corona needle was separated by 4 mm or more from the analyzer entrance aperture (Carroll *et al.* 1975).

The observation that ionization efficiency varies greatly among solvents (Tables 3.10 through 3.12) indicates that a large majority of analyte molecules are not ionized directly by contact with N_2^{+*} or N_4^{+*} , even though such ionization is highly energetically favored (the recombination energy of N_2^{+*} is greater than the ionization energy of the analyte, see below). Thus the high-energy nitrogen ions must have been consumed by reactions (6) and (7) before having a chance to ionize the analyte. All the evidence presented by Harrison (Harrison 1992 pp 15–18) indicates that such ion/molecule reactions are quite fast, and thermochemical calculations show that reaction (6) is energetically favored.

The ΔH value for reaction (6) can be calculated as $\Delta H = IE(S) - RE(N_2^{+*})$, where $IE(S)$ is the ionization energy of the solvent and $RE(N_2^{+*})$ is the recombination energy of N_2^{+*} . The recombination energy is $-\Delta H$ for the ($M^{+*} + e^- \rightarrow M$) reaction. For monoatomic ions, the RE has the same value as the IE for the neutral species. For non-monoatomic ions the RE is somewhat less than the IE due to excess vibrational and rotational energies that result on recombination or, in some cases, formation of possible excited states (Harrison 1992 p 13). The RE of N_2^{+*} is known (15.3 eV). However, in the event that the RE is not known, *e.g.* for the solvent ions, the IE of the neutral species will be used as a good approximation of the RE, realizing that the IE is slightly higher than the RE value. Using the data in Table 3.14 and considering that $\Delta H = IE(S) - RE(N_2^{+*})$, the ΔH values for the charge exchange reaction between solvent molecules and N_2^{+*} are (in eV): -6.47 for toluene, -4.46 for MeOH and -3.10 for MeCN. These results indicate that the formation of the charge exchange reagent ion, S^{+*} , *via* reaction (6) is exothermic in all cases, though more favored in toluene and less in MeCN.

In order to determine if the interaction of N_4^{+*} with a solvent molecule leads to charge exchange, the ΔH for reaction (7) was calculated theoretically using the B3LYP/6–31G(*d*) method. So as to assess the reliability of the results obtained with this method, the ΔH for reaction (6) was also calculated and the values compared to those obtained experimentally from ionization energy data. Enthalpy values of the species involved in reactions (6) and (7) can be found in Appendix C.

The theoretical ΔH values for reactions (6) and (7) are shown in Table 3.15. The results reveal that both reactions are exothermic and thus, favoured in all solvents. Comparison between the experimental and theoretical ΔH values for reaction (6) shows that the theoretical values are 0.9 eV more negative than the experimental ones, although the trend among the solvents is the same: toluene > MeOH > MeCN.

Table 3.15. Theoretical ΔH values (in eV) for reactions (6) and (7).

Reaction	ΔH (eV) Toluene	ΔH (eV) MeOH	ΔH (eV) MeCN
$N_2^{+*} + S \rightarrow N_2 + S^{+*}$ (6)	-7.4^a (-6.5) ^b	-5.4^a (-4.5) ^b	-4.0^a (-3.1) ^b
$N_4^{+*} + S \rightarrow 2N_2 + S^{+*}$ (7)	-5.5^a	-3.5^a	-2.2^a

^a Calculated thermodynamic data are shown in Table C1 (Appendix C).

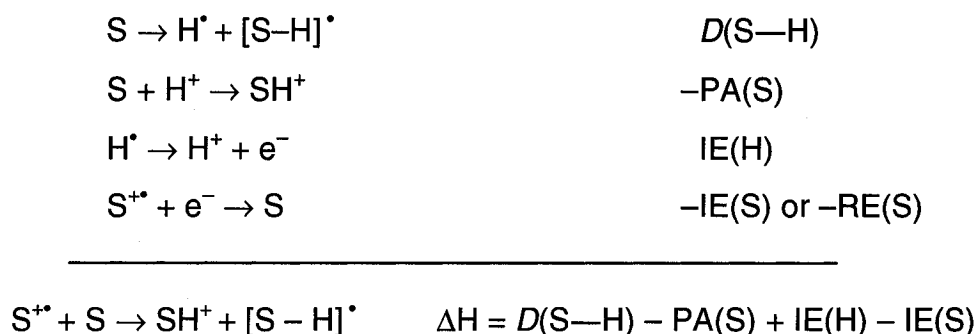
^b Numbers correspond to experimental ΔH values ($\Delta H = IE(S) - RE(N_2^{+*})$).

Formation of proton transfer reagent ion (SH^+)

The positive radical ions of the solvent formed by reactions (6) and (7) can then ionize other species present in the ion source by charge exchange. Given the higher concentration of solvent molecules compared to analyte molecules, S^{+*} will probably react with other solvent molecules by reaction (8).



Reaction (8) can take place by either proton transfer from $S^{+\bullet}$ to S or H atom transfer from S to $S^{+\bullet}$. The ΔH for the formation of protonated solvent molecules by (8) can be obtained using the thermochemical model proposed by Syage (Syage 2004).



In the above model $D(S-H)$ is the energy required for the homolytic cleavage of the lowest energy bond to hydrogen in a solvent molecule S, and $PA(S)$ is the proton affinity of the solvent. Note that for the last equation ($S^{+\bullet} + e^- \rightarrow S$) of the model, the negative of the ionization energy of the solvent is used given that $RE(S^{+\bullet})$ is not known. Therefore the ΔH values obtained with the IE will be less exothermic than they should be.

Using the values for $IE(H)$, $IE(S)$, $PA(S)$ and $D(S-H)$ listed in Table 3.14, the ΔH values (in eV) for reaction (8) are: -2.59 for MeCN, -0.87 for MeOH and $+0.43$ for toluene. Protonated solvent molecules should most easily form in MeCN and with most difficulty in toluene. This could explain why only SH^+ ions and their clusters, and not $S^{+\bullet}$ ions, are observed in the background spectra of MeCN and MeOH (Figures 3.29 and 3.30).

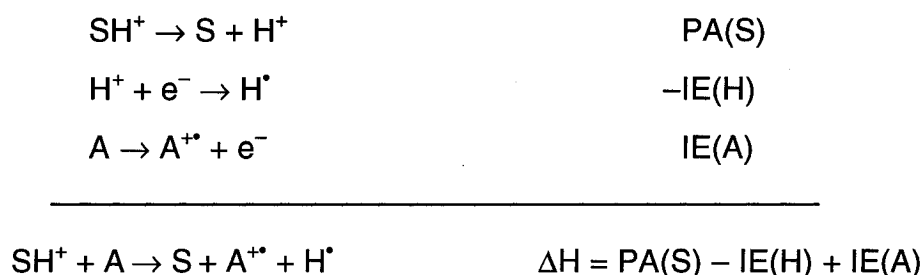
Formation of the molecular ion of the analyte ($A^{+\bullet}$)

To this point we have explained the formation of primary ($N_2^{+\bullet}$ and $N_4^{+\bullet}$) and secondary ($S^{+\bullet}$ and SH^+) reagent ions. In the following section the different pathways for the formation of the analyte ions, $A^{+\bullet}$ and AH^+ , will be studied. In general, there are at least five possible mechanisms leading to $A^{+\bullet}$:



As mentioned above, the observation that ionization efficiency differs markedly among solvents argues against both significant amounts of direct analyte ionization in the discharge (9) or analyte ionization by collision with a high-energy nitrogen ion ($N_2^{+\bullet}$ or $N_4^{+\bullet}$) (10). If either were the case, the ionization efficiency for each analyte would be the same in all solvents. Therefore, reactions (9) and (10) can be eliminated from consideration.

Formation of the positive radical ion of the analyte must thus proceed through some high-energy solvent species ($S^{+\bullet}$ and SH^+). The ΔH for reaction (11) was obtained using the following set of reactions to examine if SH^+ ions were able to ionize the analyte by charge exchange. The ΔH values obtained with this model are listed in Table 3.16.



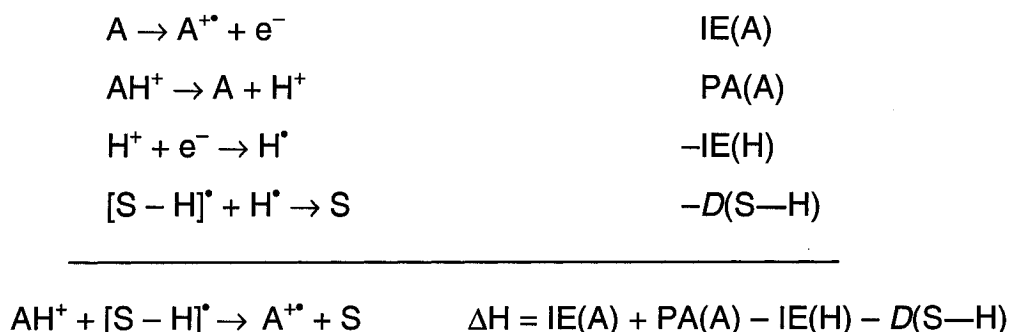
The results in Table 3.16 show that reaction (11) is highly endothermic for all of the analytes used in this study, with the most endothermic being for DBT in toluene or MeCN and the least being for PY in MeOH. However, all ΔH values for proton transfer *via* the pathway $SH^+ + A \rightarrow S + AH^+$ are exothermic (see below). Therefore, it is more likely that when an analyte molecule collides with a

protonated solvent molecule, proton transfer will take place. Consequently, reaction (11) is an unlikely pathway for forming A^+ .

Table 3.16. Experimental ΔH values (in eV) for reaction (11).

PAC	ΔH (eV) MeOH	ΔH (eV) MeCN	ΔH (eV) Toluene
PY	+1.66	+1.92	+1.97
CAR	+1.83	+2.09	+2.14
FLU	+2.59	+2.85	+2.90
DBT	+2.67	+2.93	+2.98

The positive radical ion of the analyte could also be formed by abstraction of an H atom from AH^+ by $[S - H]^*$ (12) according to the following scheme.

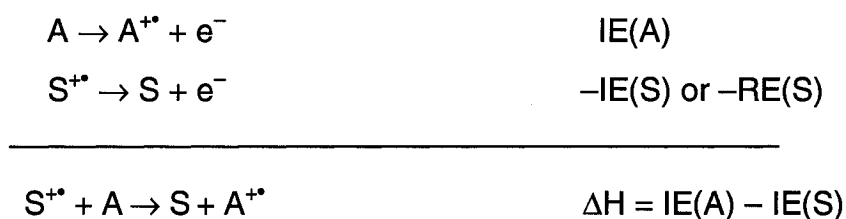


The ΔH values calculated using this model are listed in Table 3.17. For this scheme the order of decreasing reactivity with regard to solvent is MeOH > MeCN > toluene and with regard to analyte PY > CAR > DBT > FLU. The ΔH values for reaction (12) are exothermic, however, due to concentration considerations (relatively low concentration of AH^+), reaction (12) probably does not offer a major pathway for formation of A^+ .

Table 3.17. Experimental ΔH values (in eV) for reaction (12).

PAC	ΔH (eV) MeOH	ΔH (eV) MeCN	ΔH (eV) Toluene
PY	-1.22	-1.12	-0.82
CAR	-1.14	-1.04	-0.74
DBT	-0.79	-0.69	-0.39
FLU	-0.45	-0.35	-0.05

The positive radical ions of the analyte can be formed by charge exchange between analyte molecules and $S^{+\bullet}$ (13). Reaction (13) can be viewed as the sum of the following reactions. The ΔH values determined using this model are listed in Table 3.18.

**Table 3.18.** Experimental ΔH values (in eV) for reaction (13).

PAC	ΔH (eV) MeCN	ΔH (eV) MeOH	ΔH (eV) Toluene
PY	-4.77	-3.41	-1.40
CAR	-4.60	-3.24	-1.23
FLU	-3.84	-2.48	-0.47
DBT	-3.76	-2.40	-0.39

Reaction (13) for the analytes studied here is energetically favored, quite highly for most analytes. For a given solvent ($IE(S)$ is constant), the order of ease of ionization of the analyte should decrease as $IE(A)$ increases leading to the following order: PY > CAR > FLU > DBT which is different from the experimental order. For a given analyte ($IE(A)$ is constant), the ability of $S^{+\bullet}$ to

charge exchange with A should decrease as IE(S) decreases and the following order is obtained: $\text{MeCN}^{+\bullet} > \text{MeOH}^{+\bullet} > \text{toluene}^{+\bullet}$.

Given that reaction (13) is exothermic it might seem logical to assume that the major ion responsible for charge exchange with the analyte is the positive radical ion of the solvent, $\text{S}^{+\bullet}$. If these reactions are kinetically very fast, then all the solvents should provide approximately the same degree of analyte ionization — this is not observed. If, on the other hand, the amount of reaction is somehow limited by the energy available, then the expected order of ease of ionization by charge exchange should be: $\text{MeCN} > \text{MeOH} > \text{Toluene}$.

This was the order observed for MeCN and MeOH early in the study. However, when toluene was examined in an attempt to verify that ion production was related to the ΔH of the simple charge exchange reaction (13), the results showed that ionization was greatest in toluene, not least. Thus this simple picture was rejected.

Formation of the protonated molecule of the analyte (AH^+)

There are at least four possible mechanisms for the formation of AH^+ :



One way to create protonated analyte molecules is by transfer of an H atom from a solvent molecule to $\text{A}^{+\bullet}$ (14). The ΔH values for reaction (14) can be calculated using the following model and the results are listed in Table 3.19.



Table 3.19. Experimental ΔH values (in eV) for reaction (14).

PAC	ΔH (eV) Toluene	ΔH (eV) MeCN	ΔH (eV) MeOH
FLU	+0.05	+0.35	+0.45
DBT	+0.39	+0.69	+0.79
CAR	+0.74	+1.04	+1.14
PY	+0.82	+1.12	+1.22

The data in Table 3.19 show that reaction (14) is endothermic for all combinations. For the solvents, the order of decreasing ability to protonate is toluene > MeCN > MeOH, and for PACs the order is FLU > DBT > CAR > PY.

Another possible way to create protonated analyte molecules is by reaction (15). This reaction may occur either by transfer of H^+ from $A^{\bullet+}$ to A or by transfer of an H atom from A to $A^{\bullet+}$. The ΔH for reaction (15) can be calculated using the following model



The assumption that the $C_{sp^2}-H$ bond dissociation energy in the analyte ($D(A-H)$) is equal to that of benzene (4.9 eV as reported by Luo 2003 p 30) was made in the ΔH calculation for reaction (15). The thermochemical model provides positive ΔH values in all cases. The order of endothermicity for reaction (15) is [ΔH in brackets in eV]: PY [1.92] > CAR [1.84] > DBT [1.49] > FLU [1.15]. These values indicate that once A^+ is formed, it is unlikely to become converted to a protonated molecule either by reacting with a solvent molecule (14) or another analyte molecule (15).

Protonated analyte molecules can form from SH^+ by transfer of H^+ according to reaction (16). The proton transfer reaction can be considered to be the sum of the reactions given below. The ΔH values for this scheme are shown in Table 3.20.

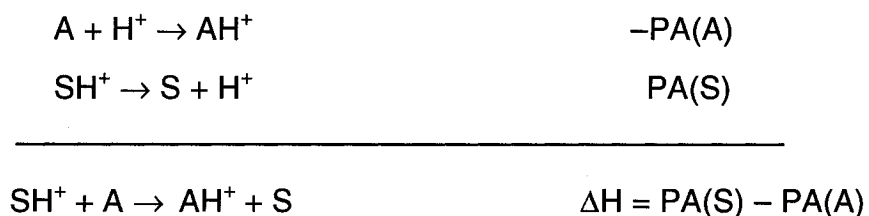


Table 3.20. Experimental ΔH values (in eV) for reaction (16).

PAC	ΔH (eV) MeOH	ΔH (eV) MeCN	ΔH (eV) Toluene
PY	-1.32	-1.06	-1.01
CAR	-1.23	-0.97	-0.92
FLU	-1.16	-0.90	-0.85
DBT	-0.74	-0.48	-0.43

For a given solvent ($PA(S)$ is constant), the order of ease of proton transfer should decrease as $PA(A)$ decreases. This leads to the following order: PY > CAR > FLU > DBT. For a given analyte ($PA(A)$ is constant), the ability of SH^+ to transfer a proton should decrease as $PA(S)$ increases, and therefore

reaction (16) is expected to be more highly favored in MeOH and less in MeCN or toluene.

The above calculations assumed that [toluene + H]⁺ is the reagent ion that would transfer a proton to an analyte molecule in a toluene-containing plasma. However, the chemistry of the ions in the plasma is probably more complex than portrayed by the above schemes, and this may be even more so for toluene where molecular rearrangement and loss of hydrogen can come into play.

Protonated analyte molecules could arise by transfer of H⁺ from S⁺ to analyte molecules according to reaction (17). The ΔH values for reaction (17) can be calculated using the set of equations given below. Experimental values for reaction (17) are displayed in Table 3.21.

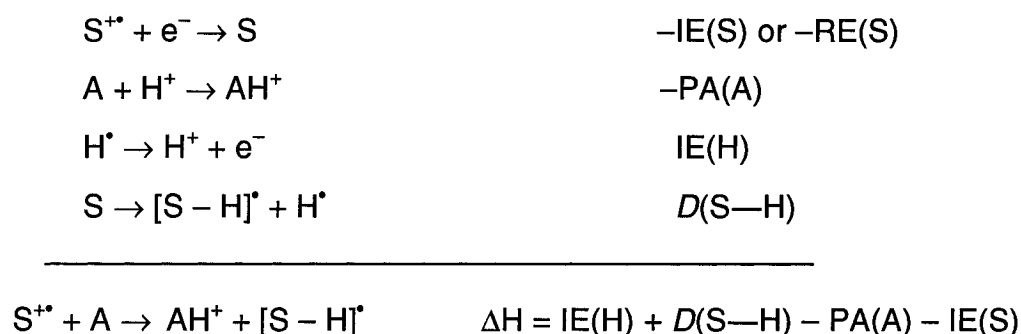


Table 3.21. Experimental ΔH values (in eV) for reaction (17).

PAC	ΔH (eV) MeCN	ΔH (eV) MeOH	ΔH (eV) Toluene
PY	-3.65	-2.19	-0.58
CAR	-3.56	-2.10	-0.49
FLU	-3.49	-2.03	-0.42
DBT	-3.07	-1.61	0.00

The above scheme shows that reaction (17) is exothermic for almost all PACs (except DBT in toluene). For the solvents, the order of decreasing ability

to protonate is MeCN > MeOH > toluene. For the analytes the expected order is PY > CAR > FLU > DBT.

These results show that A⁺ is possibly formed *via* reaction (13), while AH⁺ may be formed by reactions (16) and (17). The analyte and solvent orders observed in TIC studies are shown in Tables 3.22 and 3.23, respectively (Tables 3.22 and 3.23 display the same data as Tables 3.10 through 3.12).

Table 3.22. Ionization data—Solvent comparison for a given analyte.

Species	Order of Ionization Efficiency (Solvent Comparison) [the numbers in brackets are ion counts]
	PY
Total Ionization ^a	Toluene [1.6e7] > MeCN [9.0e5] > MeOH [2.7e3]
Formation of A ⁺	Toluene [1.1e7] > MeCN [9.0e5] > MeOH [1.4e3]
Formation of AH ⁺	Toluene [4.6e6] > MeOH [1.3e3] > MeCN [NO ^b]
	DBT
Total Ionization ^a	Toluene [7.0e6] > MeCN [6.8e5] > MeOH [2.6e3]
Formation of A ⁺	Toluene [6.6e6] > MeCN [6.8e5] > MeOH [2.6e3]
Formation of AH ⁺	Toluene [3.6e5] > MeCN [NO ^b] > MeOH [NO ^b]
	CAR
Total Ionization ^a	Toluene [1.9e7] > MeCN [5.8e6] > MeOH [8.7e3]
Formation of A ⁺	Toluene [1.1e7] > MeCN [1.9e6] > MeOH [4.1e3]
Formation of AH ⁺	Toluene [7.7e6] > MeCN [3.9e6] > MeOH [4.6e3]
	FLU
Total Ionization ^a	Toluene [1.9e7] > MeCN [2.2e6] > MeOH [1.0e5]
Formation of A ⁺	MeCN [2.1e5] > Toluene [1.5e5] > MeOH [2.9e3]
Formation of AH ⁺	Toluene [1.9e7] > MeCN [2.0e6] > MeOH [9.7e4]

^a Total ionization = [A⁺ + AH⁺]

^b Not observed

Table 3.23. Ionization data—Analyte comparison for a given solvent.

Species	Order of Ionization Efficiency (Analyte Comparison) [the numbers in brackets are ion counts]
Total Ionization ^a Formation of A ⁺ Formation of AH ⁺	Toluene FLU [1.9e7] = CAR [1.9e7] > PY [1.6e7] > DBT [7.0e6] CAR [1.1e7] = PY [1.1e7] > DBT [6.6e6] > FLU [1.5e5] FLU [1.9e7] > CAR [7.7e6] > PY [4.6e6] > DBT [3.6e5]
	MeCN CAR [5.8e6] > FLU [2.2e6] > PY [9.0e5] > DBT [6.8e5] CAR [1.9e6] > PY [9.0e5] > DBT [6.8e5] > FLU [2.1e5] CAR [3.9e6] > FLU [2.0e6] > PY [NO ^b] = DBT [NO ^b]
	MeOH FLU [1.0e5] > CAR [8.7e3] > PY [2.7e3] > DBT [2.6e3] CAR [4.1e3] > FLU [2.9e3] > DBT [2.6e3] > PY [1.4e3] FLU [9.7e4] > CAR [4.6e3] > PY [1.3e3] > DBT [NO ^b]

^a Total ionization = [A⁺ + AH⁺]^b Not observed

The solvent and analyte orders expected from thermochemical calculations for reactions (16) and (17) are listed in Table 3.24.

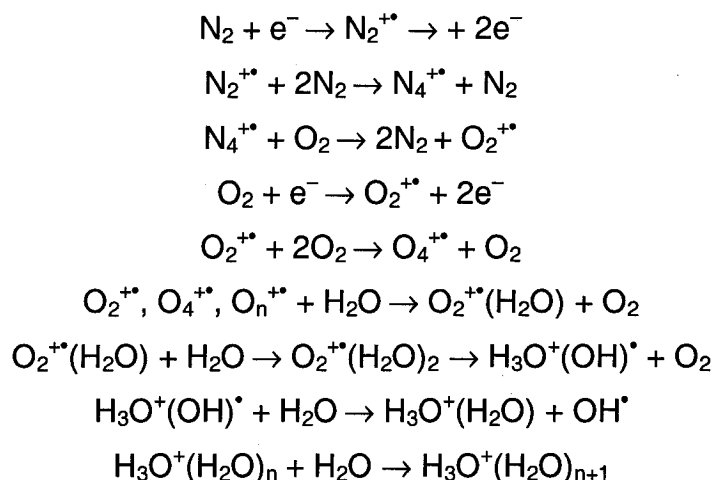
Table 3.24. Thermochemical model—Analyte and solvent comparison.

Reaction	Analyte order expected for a given solvent	Solvent order expected for all PACs
$S^{*+} + A \rightarrow S + A^{*+}$ (13)	PY > CAR > FLU > DBT	MeCN > MeOH > Toluene
$SH^+ + A \rightarrow AH^+ + S$ (16)	PY > CAR > FLU > DBT	MeOH > MeCN ~ Toluene
$S^{*+} + A \rightarrow AH^+ + [S - H]^*$ (17)	PY > CAR > FLU > DBT	MeCN > MeOH > Toluene

In general, the ion counts in toluene are an order of magnitude higher than in MeCN and those in MeCN are two orders of magnitude higher than in MeOH, and this seemed to apply to both charge exchange and proton transfer. For all compounds, toluene provides the best medium for proton transfer with MeOH providing a slight edge over MeCN on a relative basis, but not on an absolute basis. In all cases except FLU, toluene also provides greater charge exchange ionization on an absolute basis. The results obtained using the thermochemical model do not explain the large effect of the solvent on the ionization process or the solvent order obtained in total ion current studies (Toluene > MeCN > MeOH).

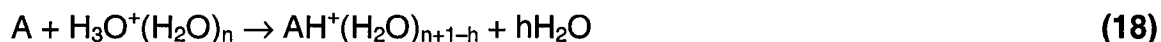
Effect of solvation on sensitivity in APCI

Kebarle and co-workers have pointed out that clustering (solvation) has a large effect on the sensitivities observed in APCI, where protonated water molecules are thought to be the reagent ions (Sunner *et al.* 1988a and Sunner *et al.* 1988b). They studied ionization mechanisms in APCI to explain the different sensitivities of nitrogen-, oxygen- and sulfur-containing bases to proton transfer. Since the source gas used in their work was air, they modified the ionization mechanism proposed by Horning to include oxygen (see page 106) and suggested that protonated water clusters were formed through oxygen as shown below:

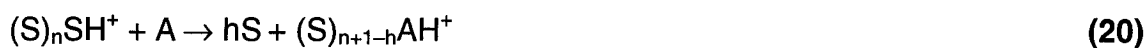


The authors noticed that nitrogen-containing bases with gas-phase basicities greater than 8.7 eV protonated readily, with high and similar sensitivities. The ionization efficiency of compounds with gas-phase basicities less than 8.7 eV (mostly oxygen-containing bases) was lower and increased with their gas-phase basicities. Other analytes for which the proton might attach to sulfur or carbon had much lower sensitivities which bore no relation to the gas-phase basicities. (Note: the gas-phase basicity or GB is the negative of the free energy change associated with the $A + H^+ \rightarrow AH^+$ reaction in the gas phase).

They explained the sensitivity order observed as being due to differences in solvation energies and gas-phase basicities. Under the conditions of their work, hydronium ion-water clusters are the main reagent ions. These protonate analyte molecules according to reaction (18) (A is the analyte). Reaction (18) will be exothermic or not depending on the energetics of the simple proton transfer reaction (*i.e.* $A + H_3O^+ \rightarrow AH^+ + H_2O$), the solvation energies of H_3O^+ and AH^+ , and the number of water molecules bound to H_3O^+ and AH^+ (*i.e.* the values of n and $n+1-h$).



Clustering might also have a similar effect on the ionization efficiency of the analytes used in our work. Two possible types of solvent clusters are of interest, solvated radical positive ions, $(S)_nS^{+\bullet}$ and solvated protonated clusters, $(S)_nSH^+$. The charge exchange and proton transfer reactions, when considering clusters, become (19) and (20), respectively. However, it should be mentioned that toluene might present a special case in that the ions and ion clusters might not resemble those in MeCN or MeOH (toluene is less polar than either MeCN or MeOH and thus, intermolecular interactions should be weaker in the case of toluene).



The effect of clustering on the energetics of the charge exchange reaction (19) will depend on the energetics of the simple charge exchange reaction ($S^{+\bullet} + A \rightarrow S + A^{+\bullet}$), the solvation bond strengths between S and $S^{+\bullet}$, and between S and $A^{+\bullet}$, and on the values of n and (n+1-h), *i.e.* the number of bonds formed. Similarly, the effect of solvation on the energetics of the proton transfer reaction (20) will depend on the energetics of the simple proton transfer reaction ($SH^+ + A \rightarrow S + AH^+$), the solvation bond strengths between S and SH^+ , and between S and AH^+ , and on the values of n and (n+1-h).

One might expect that solvation of solvent ions ($S^{+\bullet}$ and SH^+) would be highest in MeOH where hydrogen bonding should be significant and lowest in toluene, which is non polar and should exhibit no hydrogen bonding (MeCN would be intermediate). Thus the two ionization reactions should be most inhibited by solvation in MeOH and least in toluene, considering only the left hand side of reactions (19) and (20). If there were a compensating energy change on the right hand side from either strong solvation bonds to $A^{+\bullet}$ or AH^+ or a small value of h, then this would counteract the solvation inhibition mentioned above. One might expect that both solvation energy and (n+1-h) would follow the order: FLU > CAR > PY ~ DBT, based on polarity and the ability to form hydrogen bonds. This is the order observed for relative ability to become ionized by proton transfer, given by $MH^+ / (MH^+ + M^{+\bullet})$ (Figure 3.31), and it is also the general order observed in overall ion count.

None of the analyte molecules is very polar and none participate strongly in hydrogen bonding; however, FLU probably does hydrogen bond with protic solvents but to an extent smaller than an alcohol. It is interesting to note that the ion count for FLU in MeOH is much higher than that for any analyte. This may be due to stronger solvation of AH^+ , which in turn allows greater ionization. It would

seem reasonable to assume that differences in solvation between products and reactants in MeOH would be greater than those in MeCN, which in turn would be greater than those in toluene. This would explain the order observed in overall ionization efficiency.

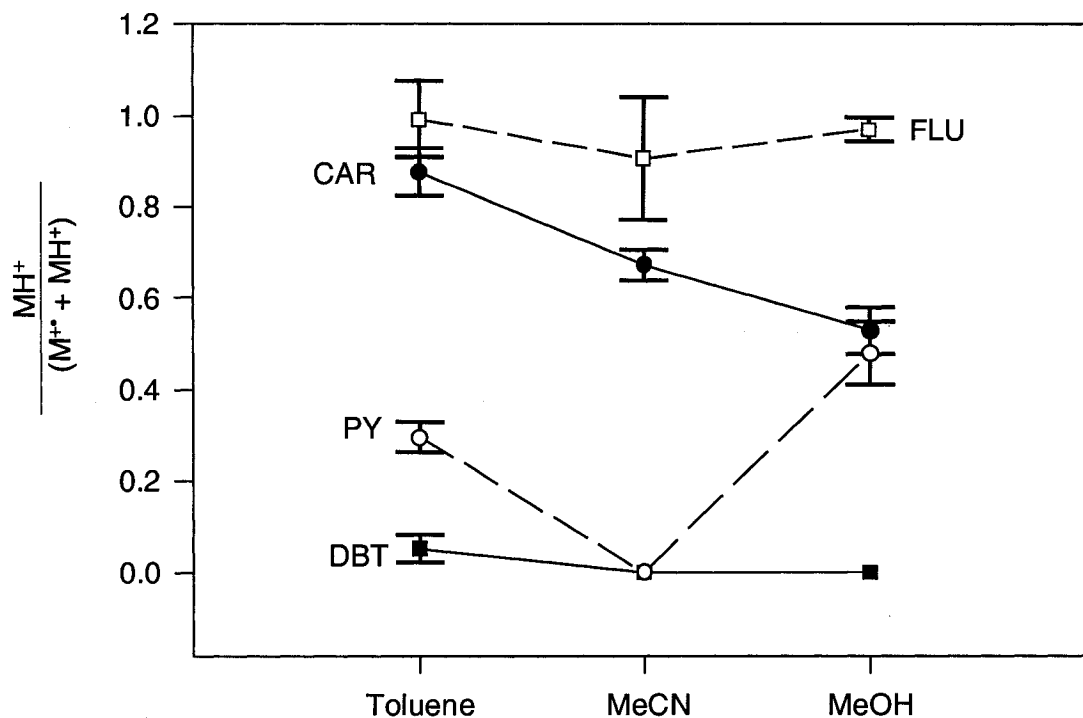


Figure 3.31. Efficiency of proton transfer vs. charge exchange for DBT, PY, FLU and CAR as a function of solvent.

3.3.2.8. Calculations using Gaussian

In the absence of ionization energy data for analyte and solvent clusters and in order to obtain the ΔH and ΔG values for the charge exchange (19) and the proton transfer (20) reactions when considering clustering, the enthalpy (H) and Gibbs energy (G) of analyte and solvent ions were estimated using Gaussian (T = 298.15 K, p = 1 atm).

The optimized geometries of toluene, (toluene)⁺, (toluene)H⁺, S, A, (S)_{n=0-2}S⁺, (S)_{n=0-2}SH⁺, (S)_{n=0,1}A⁺ and (S)_{n=0,1}AH⁺ (where A represent DBT, PY, CAR or FLU and S MeCN or MeOH) are shown in Figures 3.32 to 3.38. Selected

bond lengths and angles are also presented. For the neutral molecules of MeCN, MeOH, toluene, DBT, PY, CAR and FLU the calculated bond lengths and angles agree to within ± 0.01 Å and $\pm 0.9^\circ$, respectively, with experimental data (Schaffrin and Trotter 1970, Lee and Boo 1996a, Lee and Boo 1996b, Hazell *et al.* 1972 and <http://www.webbook.nist.gov>, access date: March 19, 2007).

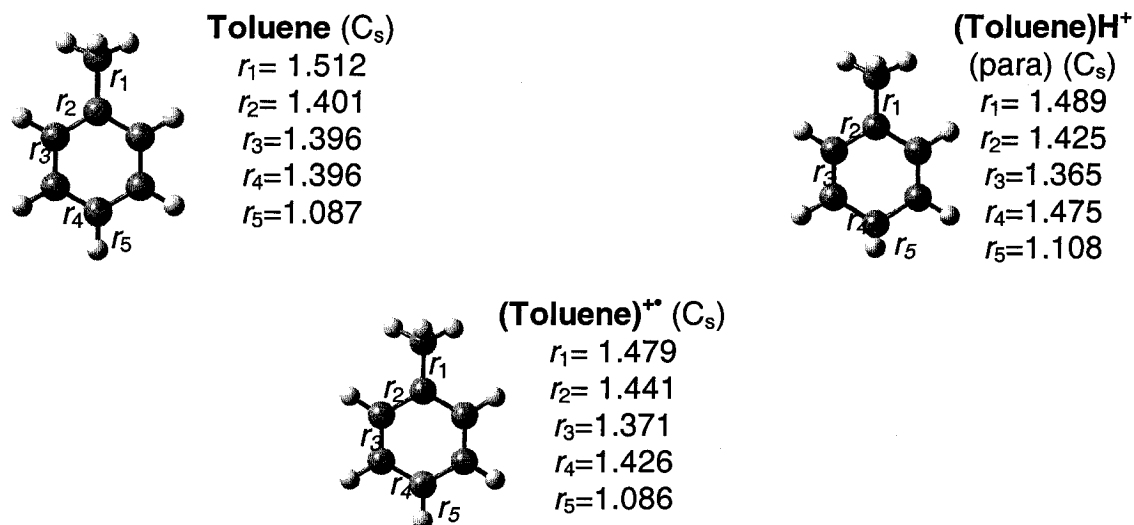


Figure 3.32. Optimized geometries of toluene, (toluene) H^+ and (toluene) $^{+•}$. Selected bond lengths in Å.

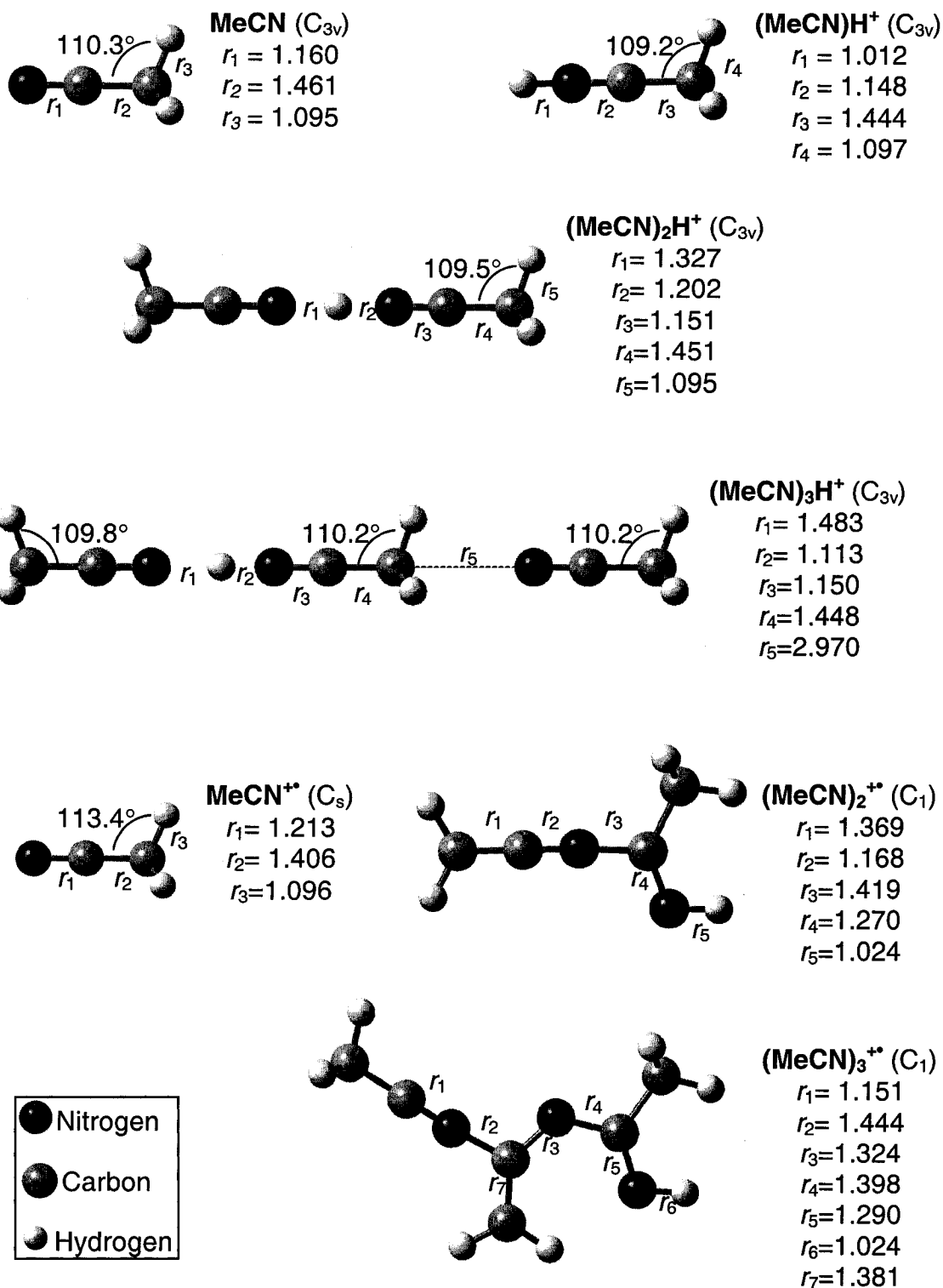


Figure 3.33. Optimized geometries of $(\text{MeCN})_n\text{H}^+$ and $(\text{MeCN})_n^{++}$ ($n=1-3$) clusters. Selected bond lengths are in Å and angles in degree.

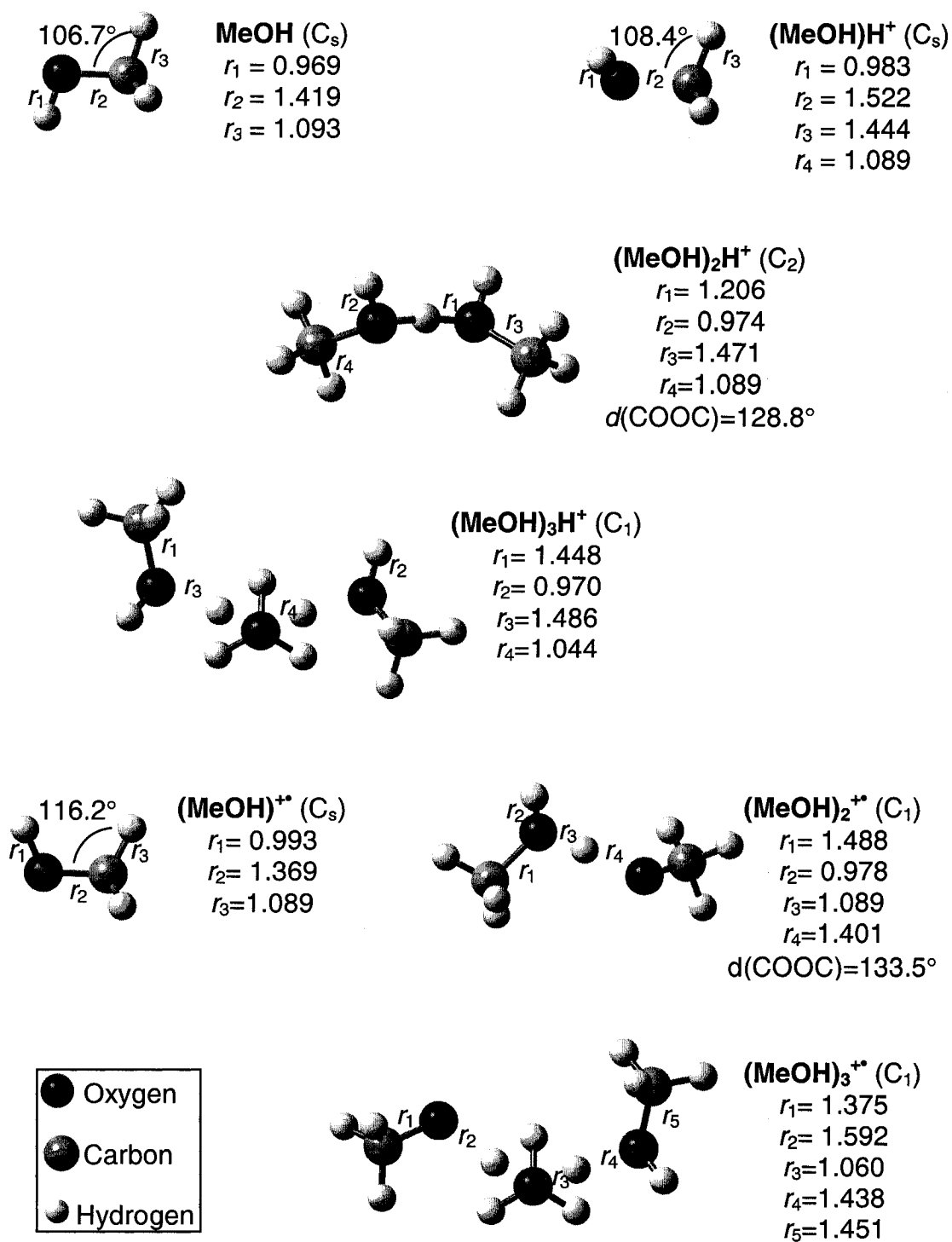


Figure 3.34. Optimized geometries of $(\text{MeOH})_n\text{H}^+$ and $(\text{MeOH})_n^{+\bullet}$ ($n=1-3$) clusters. Selected bond lengths in Å and angles in degree.

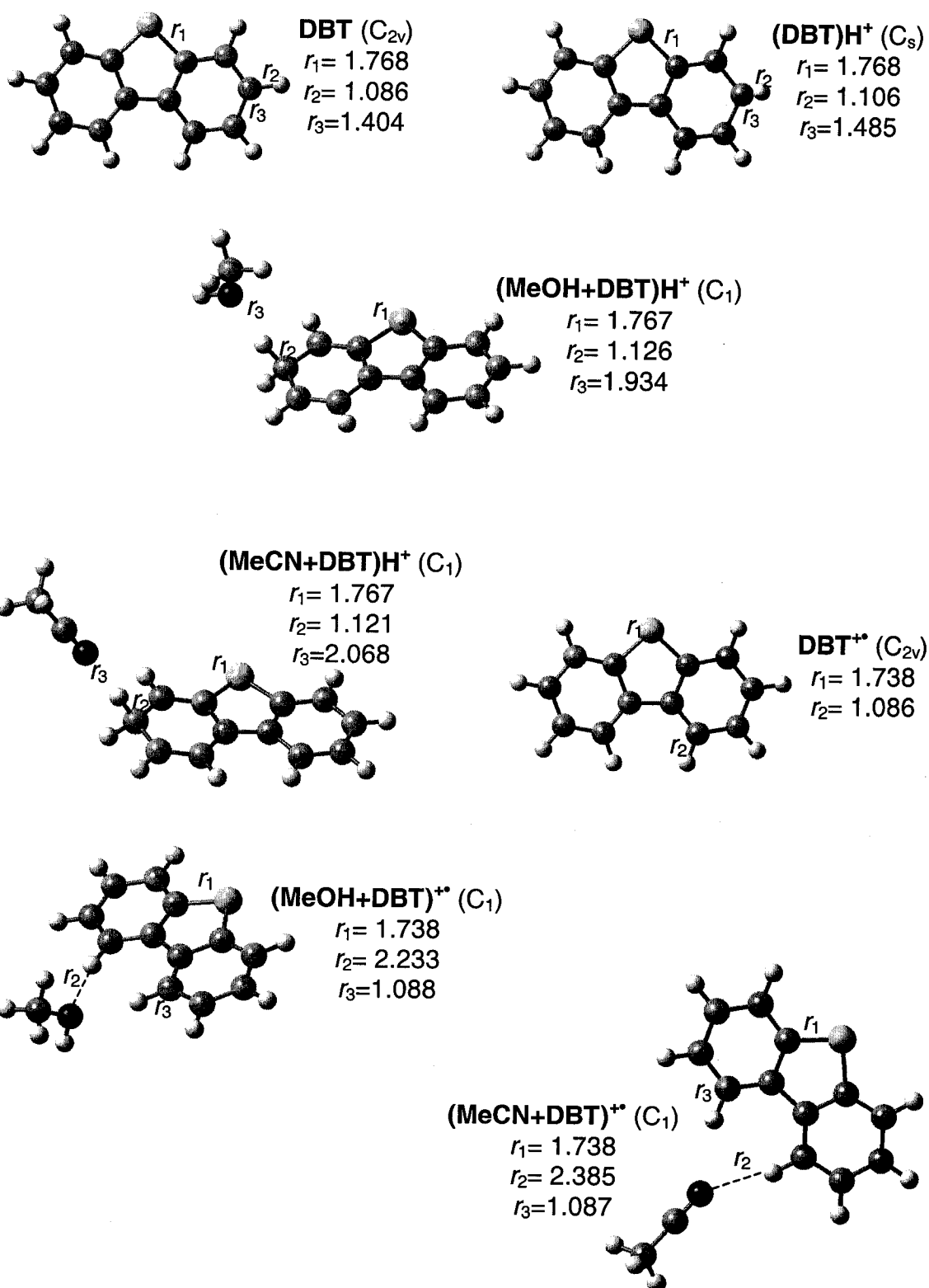


Figure 3.35. Optimized geometries of DBT species. Selected bond lengths in Å.

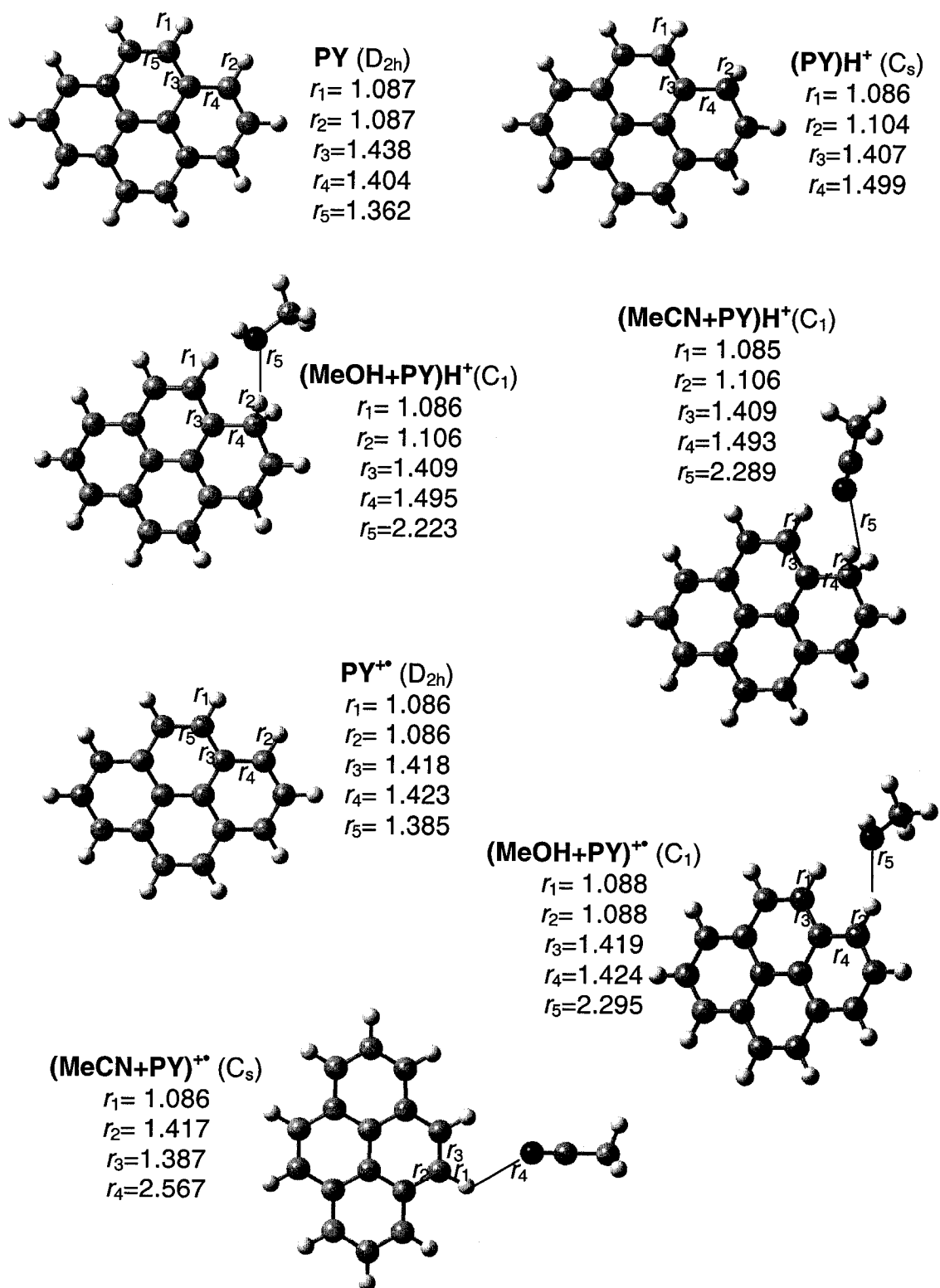


Figure 3.36. Optimized geometries of PY species. Selected bond lengths in Å.

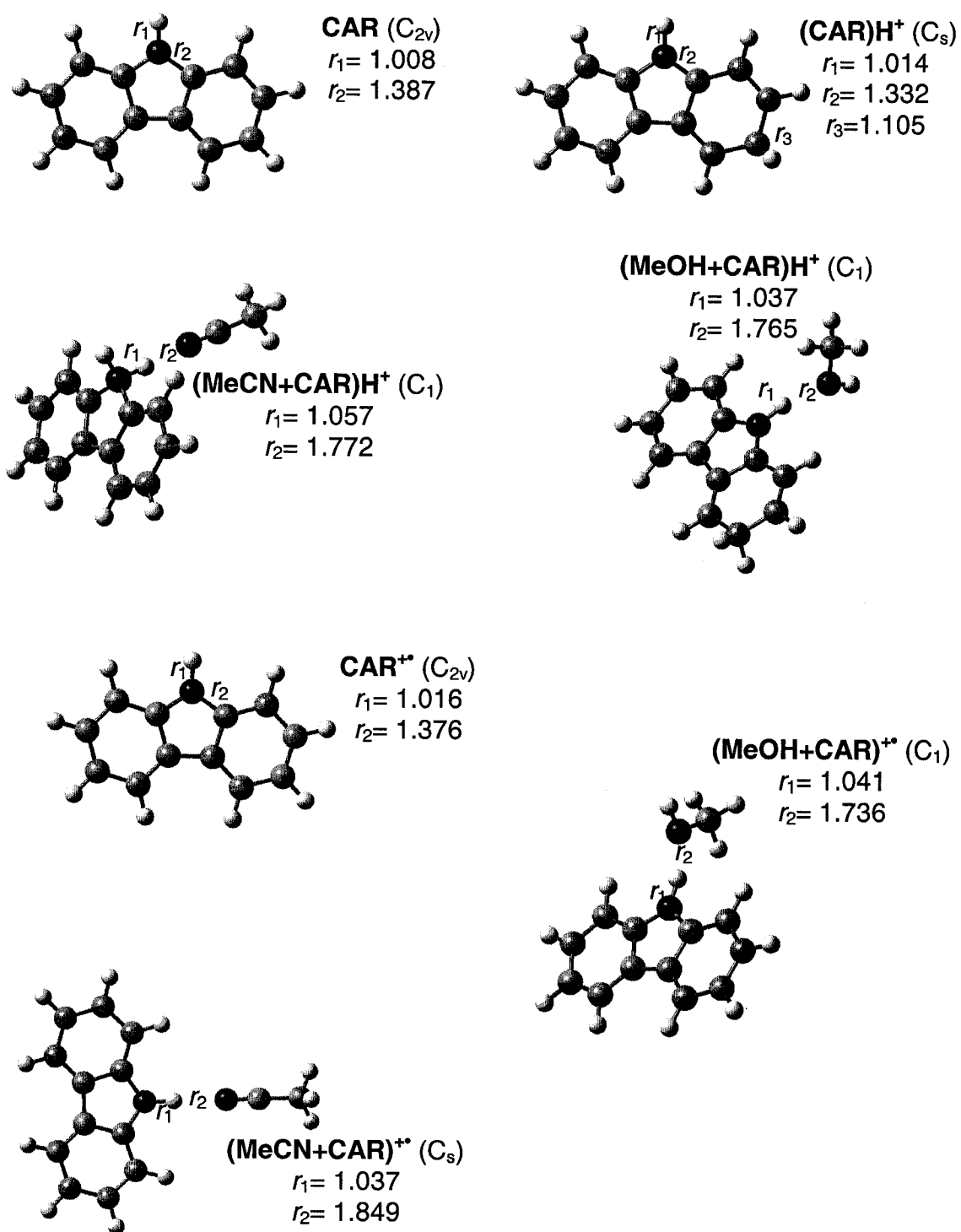


Figure 3.37. Optimized geometries of CAR species. Selected bond lengths in Å.

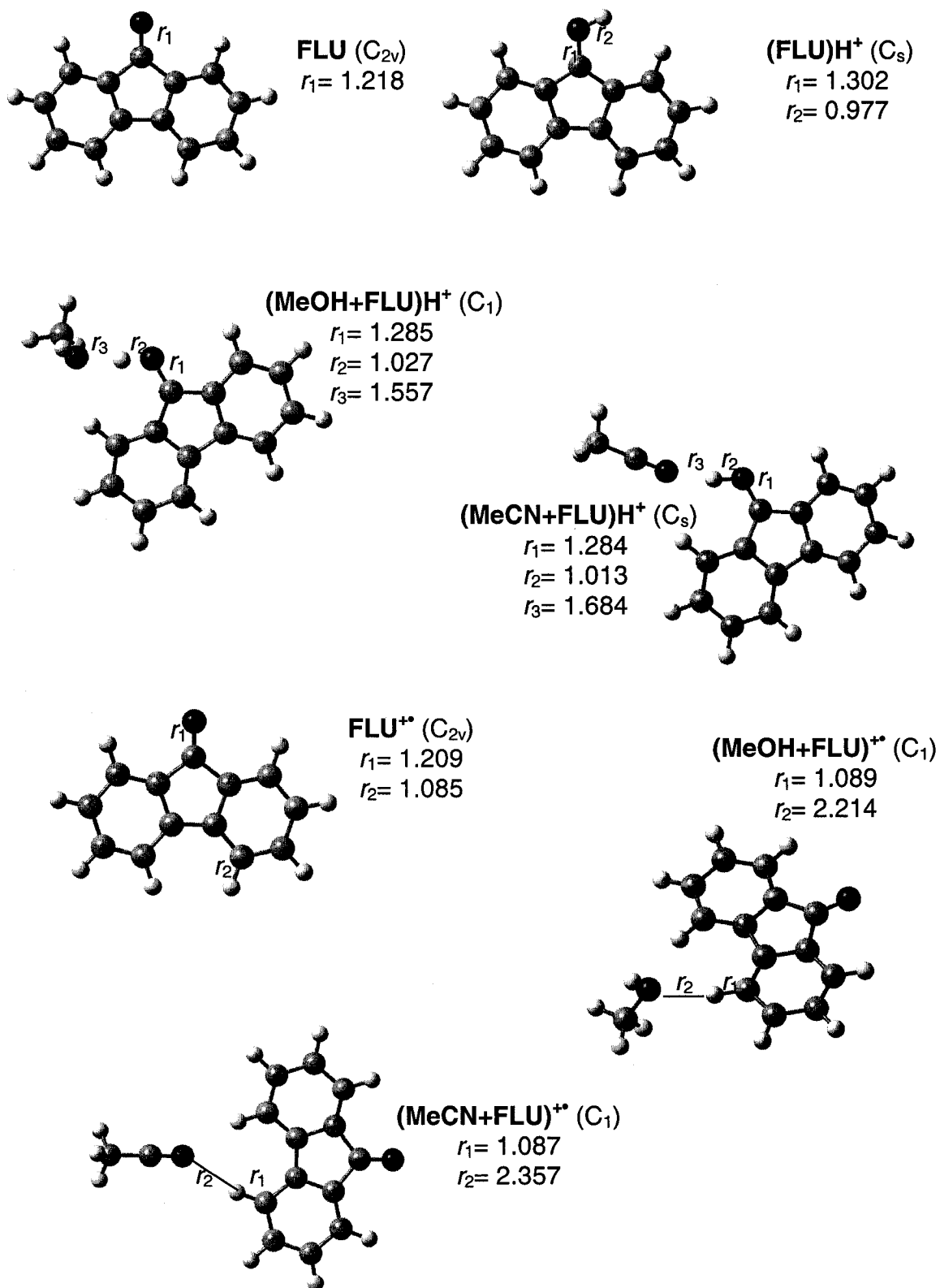


Figure 3.38. Optimized geometries of FLU species. Selected bond lengths in Å.

In Table 3.25, thermodynamic data for the $(S)_{n-1}H^+ + S \rightarrow (S)_nH^+$ ($n=1-3$) clustering reaction in the gas phase (S : MeCN or MeOH) are compared with available experimental values, in order to assess the reliability of the theoretical calculations. The term $\Delta E_{n-1,n}$ is the stabilization energy. The stabilization energy is the electronic energy (E) difference between the cluster and the isolated monomers, calculated as (3.2). The data show that although overestimated, the calculated $\Delta E_{n-1,n}$ values are, as a whole, in good agreement with the experimental $\Delta H^\circ_{n-1,n}$. All the clustering reactions are spontaneous, as indicated by their $\Delta G^\circ_{n-1,n}$ values. For MeCN and MeOH, $\Delta H^\circ_{n-1,n}$ and $\Delta G^\circ_{n-1,n}$ decrease monotonically with increasing n .

$$\Delta E_{n-1,n} = E((S)_nH^+) - E((S)_{n-1}H^+) - E(S) \quad (3.2)$$

In the case of AH^+ species, all possible isomers obtained by association of the proton with each carbon atom or heteroatom in the molecule were optimized in order to determine the preferred site of protonation for the model PACs and toluene. Protonation directly above the aromatic ring was also considered, but, in the optimized structure the proton was attached to one of the atoms of the aromatic ring, *i.e.* one of the previously considered structures.

The electronic energy (E) of AH^+ species for different sites of protonation is given in Table 3.26. The minimum-energy value for a given AH^+ species is underlined in the table. The calculations show that the favoured site of protonation for DBT and CAR is a carbon atom (not the heteroatom), whereas for FLU, the preferred site is oxygen. Toluene protonates preferentially on the *para* position, which is in agreement with previous studies (Devlin *et al.* 1975).

Calculated thermodynamic data for the $AH^+ + S \rightarrow (S)AH^+$ clustering reaction in the gas phase (S : MeCN or MeOH; A : DBT, PY, CAR or FLU) are shown in Table 3.27. Calculations show that all the clustering reactions, except for PY in MeOH, are spontaneous as indicated by their ΔG° values. The clustering reactions are more favoured for FLU and CAR and less for DBT and PY, both in MeOH and in MeCN.

Table 3.25. Thermodynamic quantities for the clustering reactions $(S)_{n-1}H^+ + S \rightarrow (S)_nH^+$ where S is either MeCN or MeOH. (Note: ΔE , ΔH° and ΔG° in kJ mol^{-1} , ΔS° in $\text{J mol}^{-1} \text{K}^{-1}$, E is the electronic energy in hartrees, $\Delta E_{n-1,n}$ is the stabilization energy calculated as $\Delta E_{n-1,n} = E((S)_nH^+) - E((S)_{n-1}H^+) - E(S)$).

Cluster	E^a (hartree)	$\Delta E_{n-1,n}^a$	Calc ^a $\Delta H^\circ_{n-1,n}$	Exp $\Delta H^\circ_{n-1,n}$	Calc ^a $\Delta G^\circ_{n-1,n}$	Exp $\Delta G^\circ_{n-1,n}$	Calc ^a $\Delta S^\circ_{n-1,n}$	Exp $\Delta S^\circ_{n-1,n}$
MeCN	-132.75493							
(MeCN)H ⁺	-133.06426	-812	-783		-785		+5	
(MeCN) ₂ H ⁺	-265.87135	-137	-140	-126 ^b	-109	-90 ^d	-103	-121 ^b
(MeCN) ₃ H ⁺	-398.64238	-42	-32	-39 ^b	-14	-15 ^d	-60	-79 ^b
MeOH	-115.71441							
(MeOH)H ⁺	-116.01574	-791	-756		-758		+7	
(MeOH) ₂ H ⁺	-231.78852	-153	-155	-138 ^c	-113	-100 ^c	-139	-128 ^c
(MeOH) ₃ H ⁺	-347.54262	-104	-93	-89 ^c	-60	-54 ^c	-112	-118 ^c

^a Values calculated with the B3LYP/6-31G(d) method (present work).

^b Values taken from Meot-Ner 1978 (estimated errors : 10 % for ΔH° and ΔG°).

^c Values taken from Kebarle and Grimsrud 1973 (estimated errors : 10 % for ΔH° and ΔG° and >10 % for ΔS°).

^d Values estimated from $\Delta G^\circ = \Delta H^\circ - T\Delta S^\circ$ using ΔH° and ΔS° as reported by Meot-Ner 1978.

Table 3.26. Electronic energy (E_e) for AH^+ species and (toluene) H^+ .

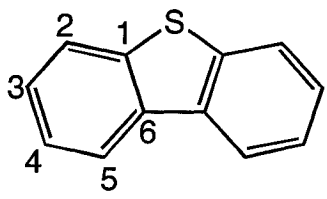
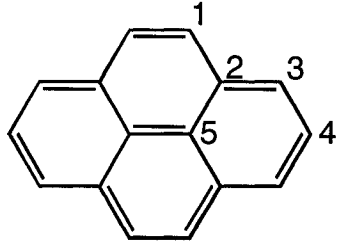
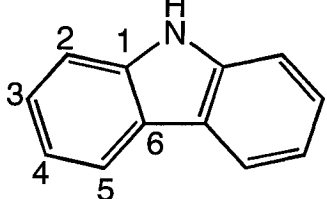
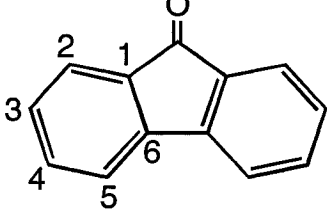
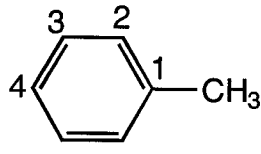
Molecule	Proton Site	Symmetry	$-E_e(h)$
	S	C_s	860.62336
	C1	C_1	860.62038
	C2	C_s	860.63635
	C3	C_s	<u>860.64035</u>
	C4	C_s	860.63998
	C5	C_s	860.63816
	C6	C_1	860.61704
	C1	C_s	616.11209
	C2	C_1	616.08295
	C3	C_s	<u>616.12944</u>
	C4	C_s	616.10509
	C5	C_1	616.08502
	N	C_s	517.81612
	C1	C_1	517.78885
	C2	C_s	517.81792
	C3	C_s	517.81527
	C4	C_s	<u>517.82359</u>
	C5	C_s	517.81292
	C6	C_1	517.78008
	O	C_s	<u>575.78652</u>
	C1	C_1	575.75397
	C2	C_s	575.74155
	C3	C_s	575.76277
	C4	C_s	575.74508
	C5	C_s	575.75637
	C6	C_1	575.72869
	C1	C_s	271.87291
	C2	C_1	271.88556
	C3	C_1	271.87969
	C4	C_s	<u>271.88742</u>

Table 3.27. Thermodynamic data for the $AH^+ + S \rightarrow (S)AH^+$ reaction where S: MeCN or MeOH and A: DBT, PY, CAR or FLU (ΔE° , ΔH° and ΔG° in kJ mol^{-1}).

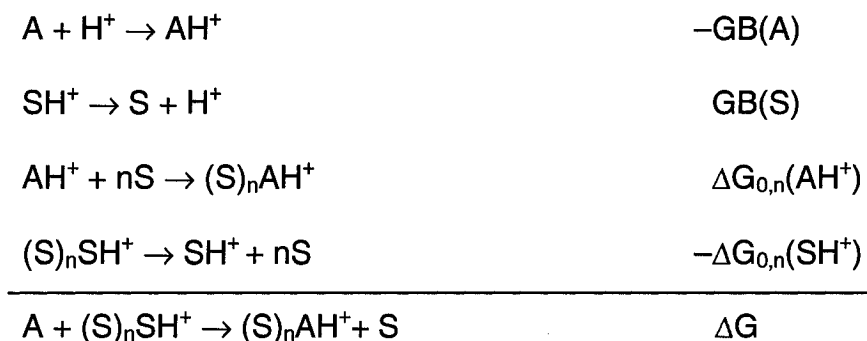
Solvent	PAC	ΔE°	ΔH°	ΔG°
MeCN	FLU	– 97.6	– 93.2	– 62.6
	CAR	– 71.0	– 61.1	– 33.4
	DBT	– 48.5	– 43.1	– 18.0
	PY	– 39.9	– 35.5	– 12.0
MeOH	FLU	– 99.2	– 94.2	– 53.1
	CAR	– 70.5	– 63.7	– 26.0
	DBT	– 40.9	– 36.2	– 4.5
	PY	– 38.4	– 31.1	+ 2.0

One might expect that the solvents MeCN and MeOH would form more stable clusters with themselves than with any of the PACs. In order to confirm this, similar calculations were carried out for the $SH^+ + nS \rightarrow (S)_nSH^+$ ($n = 1-2$) clustering reactions in MeCN and MeOH. The results are given in Table 3.28. The data show that all the solvent clustering reactions are spontaneous, and solvation of $(MeOH)H^+$ is more favourable than for $(MeCN)H^+$. In addition, the stabilities of MeCN and MeOH clusters increase with the number of solvent molecules bound to SH^+ (ΔH° and ΔG° increase with increasing n), at least for the values of n studied.

Table 3.28. Thermodynamic quantities for the $SH^+ + nS \rightarrow (S)_nSH^+$ ($n = 1-2$) clustering reaction where S: MeCN or MeOH (ΔE° , ΔH° and ΔG° in kJ mol^{-1}).

Solvent	Reaction	ΔE°	ΔH°	ΔG°
MeCN	$SH^+ + S \rightarrow (S)SH^+$	– 136.9	– 139.9	– 109.0
	$SH^+ + 2S \rightarrow (S)_2SH^+$	– 179.2	– 172.2	– 123.5
MeOH	$SH^+ + S \rightarrow (S)SH^+$	– 153.2	– 154.6	– 113.1
	$SH^+ + 2S \rightarrow (S)_2SH^+$	– 257.4	– 248.0	– 173.2

The proton transfer reaction considering solvation can be viewed as the sum of the following equations, where GB is the gas-phase basicity and $\Delta G_{0,n}$ is the solvation free energy.



The change in free energy, ΔG , for the above reaction depends on the difference of the gas-phase basicities of the solvent and the analyte, *i.e.* $[GB(S) - GB(A)]$, and the relative solvation free energies of AH^+ and SH^+ , *i.e.* $[\Delta G_{0,n}(AH^+) - \Delta G_{0,n}(SH^+)]$ as shown in equation (3.3):

$$\Delta G = [GB(S) - GB(A)] + [\Delta G_{0,n}(AH^+) - \Delta G_{0,n}(SH^+)] \quad (3.3)$$

Based on calculated thermodynamic data (Tables 3.27 and 3.28), solvation of SH^+ is preferred over solvation of AH^+ , *i.e.* $\Delta G_{0,1}(SH^+) > \Delta G_{0,1}(AH^+)$. Therefore, the solvation energy difference, $[\Delta G_{0,n}(AH^+) - \Delta G_{0,n}(SH^+)]$, will be positive and unfavourable in all situations. This endothermicity is expected to be larger in MeOH and for larger n values, explaining the much lower ionization efficiency of PACs in MeOH.

Moreover, the difference in solvation energy, $[\Delta G_{0,n}(AH^+) - \Delta G_{0,n}(SH^+)]$, is expected to be smaller (less positive) for compounds that form more stable clusters with the solvent. PACs such as FLU, CAR and azapyrene, as oppose to DBT and PY, can form stronger hydrogen bonds with the solvent because their

clusters can be stabilized by hydrogen bonding through the hydrogen atom attached to either oxygen or nitrogen (even though the preferable protonation site for CAR is on carbon, calculations predict that clusters of CAR and the solvent are stabilized by hydrogen bonding through the hydrogen attached to nitrogen and not to carbon). This would explain the higher sensitivity observed for FLU, CAR and azapyrene.

For the proton transfer reaction to be spontaneous, the unfavourable solvation energy difference, $[\Delta G_{0,n}(AH^+) - \Delta G_{0,n}(SH^+)]$, in equation (3.2) must be compensated for by the gas-phase basicity difference, $[GB(S) - GB(A)]$. For all PACs and solvents used in this study $GB(A) > GB(S)$. The gas-phase basicities of the solvents in eV are: MeOH [7.5] < MeCN [7.7] < toluene [7.8], which suggests that MeOH, having the lowest gas-phase basicity, provides the best medium for proton transfer (values taken from <http://www.webbook.nist.gov>, access date: February 5, 2007). This would help explain the relatively high sensitivity observed in MeOH for azapyrene. The counts for the MH^+ of the impurity in a sample of non-pure pyrene ($[PY] = 1.0 \times 10^{-5} \text{ mol L}^{-1}$) were about 30 times higher ($TIC = 9.0 \times 10^4$) than the total ion counts $[M^+ + MH^+]$ for PY in MeOH (Figure 3.5), and higher than the TIC for all PACs, except FLU ($TIC = 1.0 \times 10^5$) (Note: the total ion counts for pure and non-pure pyrene were very similar). The ion counts for the impurity in MeCN ($TIC = 1.0 \times 10^5$) and toluene ($TIC = 1.4 \times 10^5$) were lower than the total ion counts for any of the PACs studied here and its ionization efficiency was similar in the three solvents tested.

In the case of azapyrene, the simple proton transfer reaction is quite exothermic (the gas-phase basicity of a similar base, pyridine is 9.3 eV) and this compensates for the solvation energy difference. Although the gas-phase basicity of CAR is expected to be similar to that of azapyrene (indol and pyridine have similar gas-phase basicities ~ 9.3 eV), the ionization efficiency of CAR is lower than that of azapyrene. This is a consequence of the smaller difference in solvation energy, $[\Delta G_{0,n}(AH^+) - \Delta G_{0,n}(SH^+)]$, for azapyrene which can form more stable clusters than CAR, giving high sensitivity. In addition, azapyrene is

expected to ionize more efficiently than FLU because of its larger gas-phase basicity.

Kebarle and associates (Sunner *et al.* 1988a and Sunner *et al.* 1988b) also observed much higher sensitivities for nitrogen-containing bases such as amines and pyridines, that have high gas-phase basicities and that can form relatively stable AH^+ clusters. Compounds that protonate on oxygen, *e.g.* methanol and acetone can also form relatively stable clusters but their gas phase basicities are lower, resulting in lower sensitivities. On the other hand, the AH^+ of compounds that protonate on sulfur or carbon, such as dimethyl sulfide, thiophene, pyrrole and PAHs, form clusters of very low stability because of the poor ability of their conjugated acids to form hydrogen bonds. Consequently, the sensitivity observed for these analytes was much lower.

The calculated ΔH° and ΔG° values for the charge exchange (19) and the proton transfer (20) reactions are shown in Tables 3.29 to 3.36. In general, all reactions are exothermic for $n = 0$ and become less exothermic when increasing n (n is the number of solvent molecules attached to the solvent ions). This indicates that the solvated reagent ions, $(S)_nSH^+$ or $(S)_nS^{+*}$, are less efficient than the bare ions, SH^+ or S^{+*} , in ionizing the analyte.

In addition, when AH^+ or A^{+*} are solvated, the proton transfer and the charge exchange reactions become more exothermic than when the analyte ions are not attached to solvent molecules. When considering solvated analyte ions, $(S)AH^+$ or $(S)A^{+*}$, as opposed to bare ions, AH^+ or A^{+*} , the calculations predict a similar order to that obtained in TIC studies.

The order predicted by the calculations for the proton transfer reaction considering solvated analyte ions is (analyte comparison for a given solvent): $FLU > CAR > PY > DBT$, and without solvation is: $PY > CAR > FLU > DBT$ (both in MeCN and MeOH). As shown before, the orders observed in TIC studies are: $FLU > CAR > PY > DBT$ in MeOH, and $CAR > FLU > PY = DBT$ in MeCN, which agree much better with the theoretical order obtained assuming solvation.

Protonated molecules of FLU and CAR, which are expected to form stronger bonds with the solvent, are predicted to ionize more efficiently than PY or DBT.

For the charge exchange reaction, the expected order from theory is CAR > PY > DBT > FLU, with solvation, and PY > CAR > DBT > FLU, without solvation, either in MeOH or in MeCN. Again, the experimental order agrees much better with the theoretical one when solvation is assumed to happen than when it is not. The charge exchange reaction in MeCN followed the order CAR > PY > DBT > FLU, the same order predicted by calculations considering solvation. However, in the case of MeOH, the agreement with the experimental order (CAR > FLU > DBT > PY) is poor.

On the whole, thermodynamic data obtained with Gaussian indicates that solvated analyte ions and solvent ions are probably the species involved in the proton transfer and charge exchange reactions occurring in the APCI ion source.

Table 3.29. Thermodynamic data for the $A + (S)_nSH^+ \rightarrow AH^+ + (n+1)S$ ($n = 0-2$) proton transfer reaction in MeOH (ΔH° and ΔG° in eV).

Reaction	ΔH°	ΔG°	Order
$A + SH^+ \rightarrow AH^+ + S$ PY CAR FLU DBT	- 1.52 - 1.43 - 1.32 - 0.92	- 1.57 - 1.44 - 1.33 - 0.95	Calculations: PY>CAR>FLU>DBT TIC Studies: FLU>CAR>PY>DBT
$A + S_2H^+ \rightarrow AH^+ + 2S$ PY CAR FLU DBT	+ 0.08 + 0.17 + 0.28 + 0.68	- 0.39 - 0.27 - 0.15 + 0.22	
$A + S_3H^+ \rightarrow AH^+ + 3S$ PY CAR FLU DBT	+ 1.05 + 1.14 + 1.25 + 1.64	+ 0.23 + 0.36 + 0.47 + 0.85	

Table 3.30. Thermodynamic data for the $A + (S)_nSH^+ \rightarrow (S)AH^+ + nS$ ($n = 0-2$) proton transfer reaction in MeOH (ΔH° and ΔG° in eV).

Reaction	ΔH°	ΔG°	Order
$A + SH^+ \rightarrow (S)AH^+$			<p>Calculations: FLU>CAR>PY>DBT</p> <p>TIC Studies: FLU>CAR>PY>DBT</p>
FLU	-2.29	-1.88	
CAR	-2.09	-1.71	
PY	-1.84	-1.54	
DBT	-1.30	-0.99	
$A + S_2H^+ \rightarrow (S)AH^+ + S$			
FLU	-0.69	-0.70	
CAR	-0.48	-0.53	
PY	-0.24	-0.37	
DBT	+0.30	+0.18	
$A + S_3H^+ \rightarrow (S)AH^+ + 2S$			
FLU	+0.28	-0.08	
CAR	+0.48	+0.20	
PY	+0.73	+0.25	
DBT	+1.27	+0.80	

Table 3.31. Thermodynamic data for the $A + (S)_nS^{+*} \rightarrow A^{+*} + (n+1)S$ ($n = 0-2$) charge exchange reaction in MeOH (ΔH° and ΔG° in eV).

Reaction	ΔH°	ΔG°	Order
$A + S^{+*} \rightarrow A^{+*} + S$			<p>Calculations: PY>CAR>DBT>FLU</p> <p>TIC Studies: CAR>FLU>DBT>PY</p>
PY	-3.47	-3.47	
CAR	-3.23	-3.22	
DBT	-2.86	-2.87	
FLU	-2.52	-2.53	
$A + S_2^{+*} \rightarrow A^{+*} + 2S$			
PY	-1.70	-2.08	
CAR	-1.45	-1.83	
DBT	-1.08	-1.47	
FLU	-0.74	-1.14	
$A + S_3^{+*} \rightarrow A^{+*} + 3S$			
PY	-0.59	-1.34	
CAR	-0.35	-1.09	
DBT	+0.03	-0.73	
FLU	+0.37	-0.40	

Table 3.32. Thermodynamic data for the $A + (S)_nS^{+*} \rightarrow (S)A^{+*} + nS$ ($n = 0-2$) charge exchange reaction in MeOH (ΔH° and ΔG° in eV).

Reaction	ΔH°	ΔG°	Order
$A + S^{+*} \rightarrow (S)A^{+*}$			Calculations: CAR>PY>DBT>FLU TIC Studies: CAR>FLU>DBT>PY
CAR	-3.92	-3.54	
PY	-3.83	-3.51	
DBT	-3.26	-2.92	
FLU	-2.96	-2.61	
$A + S_2^{+*} \rightarrow (S)A^{+*} + S$			
CAR	-2.15	-2.15	
PY	-2.05	-2.12	
DBT	-1.48	-1.52	
FLU	-1.18	-1.22	
$A + S_3^{+*} \rightarrow (S)A^{+*} + 2S$			
CAR	-1.04	-1.41	
PY	-0.94	-1.38	
DBT	-0.37	-0.78	
FLU	-0.07	-0.48	

Table 3.33. Thermodynamic data for the $A + (S)_nSH^+ \rightarrow AH^+ + (n+1)S$ ($n = 0-2$) proton transfer reaction in MeCN (ΔH° and ΔG° in eV).

Reaction	ΔH°	ΔG°	Order
$A + SH^+ \rightarrow AH^+ + S$			Calculations: PY>CAR>FLU>DBT TIC Studies: CAR>FLU>PY=DBT
PY	-1.24	-1.29	
CAR	-1.15	-1.17	
FLU	-1.04	-1.05	
DBT	-0.65	-0.68	
$A + S_2H^+ \rightarrow AH^+ + 2S$			
PY	+0.21	-0.16	
CAR	+0.30	-0.04	
FLU	+0.41	+0.08	
DBT	+0.80	+0.45	
$A + S_3H^+ \rightarrow AH^+ + 3S$			
PY	+0.54	-0.01	
CAR	+0.63	+0.11	
FLU	+0.74	+0.22	
DBT	+1.14	+0.60	

Table 3.34. Thermodynamic data for the $A + (S)_nSH^+ \rightarrow (S)AH^+ + nS$ ($n = 0-2$) proton transfer reaction in MeCN (ΔH° and ΔG° in eV).

Reaction	ΔH°	ΔG°	Order
$A + SH^+ \rightarrow (S)AH^+$			<p>Calculations: FLU>CAR>PY>DBT</p> <p>TIC Studies: CAR>FLU>PY=DBT</p>
FLU	-2.01	-1.70	
CAR	-1.78	-1.51	
PY	-1.61	-1.42	
DBT	-1.09	-0.86	
$A + S_2H^+ \rightarrow (S)AH^+ + S$			
FLU	-0.56	-0.57	
CAR	-0.33	-0.38	
PY	-0.16	-0.29	
DBT	+0.36	+0.27	
$A + S_3H^+ \rightarrow (S)AH^+ + 2S$			
FLU	-0.22	-0.42	
CAR	+0.00	-0.23	
PY	+0.17	-0.14	
DBT	+0.69	+0.42	

Table 3.35. Thermodynamic data for the $A + (S)_nS^{*+} \rightarrow A^{*+} + (n+1)S$ ($n = 0-2$) charge exchange reaction in MeCN (ΔH° and ΔG° in eV).

Reaction	ΔH°	ΔG°	Order
$A + S^{*+} \rightarrow A^{*+} + S$			<p>Calculations: PY>CAR>DBT>FLU</p> <p>TIC Studies: CAR>PY>DBT>FLU</p>
PY	-4.83	-4.79	
CAR	-4.59	-4.54	
DBT	-4.22	-4.18	
FLU	-3.88	-3.84	
$A + S_2^{*+} \rightarrow A^{*+} + 2S$			
PY	-2.11	-2.55	
CAR	-1.87	-2.30	
DBT	-1.50	-1.94	
FLU	-1.15	-1.60	
$A + S_3^{*+} \rightarrow A^{*+} + 3S$			
PY	-1.49	-2.37	
CAR	-1.25	-2.12	
DBT	-0.88	-1.76	
FLU	-0.53	-1.42	

Table 3.36. Thermodynamic data for the $A + (S)_nS^{+*} \rightarrow (S)A^{+*} + nS$ ($n = 0-2$) charge exchange reaction in MeCN (ΔH° and ΔG° in eV).

Reaction	ΔH°	ΔG°	Order
$A + S^{+*} \rightarrow (S)A^{+*}$			Calculations: CAR>PY>DBT>FLU TIC Studies: CAR>PY>DBT>FLU
CAR	- 5.35	- 5.01	
PY	- 5.18	- 4.89	
DBT	- 4.65	- 4.36	
FLU	- 4.36	- 4.06	
$A + S_2^{+*} \rightarrow (S)A^{+*} + S$			
CAR	- 2.62	- 2.77	
PY	- 2.45	- 2.65	
DBT	- 1.93	- 2.11	
FLU	- 1.63	- 1.82	
$A + S_3^{+*} \rightarrow (S)A^{+*} + 2S$			
CAR	- 2.00	- 2.59	
PY	- 1.83	- 2.48	
DBT	- 1.31	- 1.94	
FLU	- 1.01	- 1.64	

3.3.3. MS/MS of Selected Sulfur Compounds

The collision induced dissociation (10–20 eV) mass spectra of MH^+ ions from organosulfur compounds generated under positive ion chemical ionization with methane as reagent gas show ions resulting from the loss of H^+ , HS^+ and CS (Hunt and Shabanowitz 1982). Many sulfur-containing compounds fragment in an EI mass spectrum by losses of 32 (S), 33 (HS^+), 34 (H_2S), 44 (CS), 45 (^+CHS) and 46 u (H_2CS), and these neutral losses are often structure-specific (Jacob 1990, pp 18–25). Therefore, MS/MS techniques could help identifying PASHs in the presence of other types of compounds and among other PASHs through characteristic fragmentation patterns.

The value of the MS/MS experiment is further enhanced if natural isotopic abundance ratios are considered when analyzing product-ion, precursor-ion and neutral loss mass spectra (Singleton and Cooks, 1983). Isotopic patterns of ions containing polyisotopic elements not only have characteristic peak height ratios but also are observed in the mass spectrum at particular m/z values. Therefore, the use of natural isotopic abundance ratios could permit greater certainty in the

identification and/or confirmation of the presence of PASHs in complex mixtures. The calculation of the fractional abundance in the isotope pattern of an ion in different mass spectra, both within a single spectrum and between two or more spectra, will be reviewed in the following section.

Natural Isotope Abundance in Various Types of Mass Spectra

Isotopes are atoms of the same element that differ in mass number due to differences in the number of neutrons in the nucleus. Carbon and hydrogen are examples of diisotopic, or X+1, elements that have one stable isotope (^{13}C or ^2H) that is 1 u heavier than the most abundant isotope (^{12}C or ^1H). However, hydrogen is usually treated as monoisotopic (X element) because the natural abundance of deuterium (0.015 %) is below the normal limits of detection (0.1 % of the base peak) (Smith and Busch 1999b, p 48). Stable sulfur isotopes are those with mass numbers 32, 33, 34 and 36, however ^{36}S is not usually included in isotopic calculations because of its low natural abundance (0.02%) (Gross 2004 p 70).

If a compound contains an element that has two or more stable isotopes, ionization will produce a group of peaks, known as an isotope pattern, that represents ions with the same elemental composition but a different isotopic composition. Since the fragmentation of ions in mass spectrometry yields a product ion and a neutral in an exactly 1:1 ratio according to (21), (22) and (23), the abundance of the ion detected after selection by Q3 can be predicted either by the theoretical abundance of the neutral fragment or the product ion (OE $^{+*}$: odd-electron ion, EE $^{+}$: even-electron ion, n: neutral fragment, R $^{\bullet}$: radical).



In all types of tandem mass spectrometry only the product ion is detected. In precursor-ion and neutral loss scans, the mass spectrometer records the m/z

value of the precursor-ion as Q1 scans, and reports this value. Therefore, precursor-ion spectra are reported as the m/z values of all precursor ions that give rise to a specific product ion and neutral loss spectra are reported as the m/z value of all the precursor ions that lose a specific neutral fragment. In product-ion scans Q1 does not scan and product-ion mass spectra are reported directly as the m/z value of the product ions of a specific precursor ion.

The fractional abundance or peak height ratios in the isotope pattern of an ion both within a single spectrum and among two or more spectra can be determined using (3.4), (3.5), (3.6) and (3.7). In these equations, **T** refers to a term of the expansion that gives the abundance of an ion or a neutral, **C** to the number of combinations for a specific isotope when comparing the precursor ion and the neutral fragment, **FA** to the natural fractional abundance of an isotope, **n** to the number of atoms in the precursor ion, **y** to the number of atoms in the product ion, **z** to the number of atoms in the neutral fragment and **n_T**, **y_T** and **z_T** to the total number of atoms of an element in the ion or neutral.

The first subscript (**i**) refers to the element number and the second (**q,r,s**) to the isotope number of that particular element. Therefore, there are **i** multiisotopic elements, **q** different isotopes of element 1, **r** different isotopes of element 2 and **s** different isotopes of element **i**. For example, (**n_T**)₁ is the total number of atoms of element 1 in the precursor ion, **z₁₂** is the number of atoms of isotope 2 of element 1 in the neutral fragment and **y₂₁** is the number of atoms of isotope 1 of element 2 in the product ion.

The terms provided by (3.4) give the fractional abundance for isotope patterns in simple mass spectra. In the case of precursor-ion mass spectra, the ratio of peak heights within a spectrum is given by the composition of the neutral fragment (3.6) and among spectra by the composition of the product ion (3.5). For neutral loss spectra, the fractional abundance within a spectrum is given by the composition of the product ion (3.5) and among spectra by the composition of neutral fragment (3.6). For product-ion spectra, the ratio of peak heights among spectra are given by the fractional abundances of the precursor-ions (3.4) and within spectra can be determined from (3.7). The product of the combinations

given by (3.7) is proportional to the number of ways of forming a neutral fragment from a selected precursor ion. Only those elements having more than one isotope in the precursor ion are incorporated in equation (3.7).

In theory there will be as many peaks in the isotope pattern of an ion as there are terms in the expansions given below. However, for instruments of unit mass resolution, such as quadrupoles, there will be only one peak in the isotope pattern for each appropriate nominal mass. Therefore, for quadrupoles the contributions of all the ions of a particular nominal mass must be summed to obtain the overall fractional abundance for that mass.

(3.4)

$$T = [(n_T)_1! (n_T)_2! \dots (n_T)_i!] \times \left[\frac{(FA_{11})^{n_{11}} (FA_{12})^{n_{12}} \dots (FA_{1q})^{n_{1q}} (FA_{21})^{n_{21}} (FA_{22})^{n_{22}} \dots (FA_{2r})^{n_{2r}} \dots (FA_{is})^{n_{is}}}{n_{11}! n_{12}! \dots n_{1q}! n_{21}! n_{22}! \dots n_{2r}! \dots n_{is}!} \right]$$

(3.5)

$$T = [(y_T)_1! (y_T)_2! \dots (y_T)_i!] \times \left[\frac{(FA_{11})^{y_{11}} (FA_{12})^{y_{12}} \dots (FA_{1q})^{y_{1q}} (FA_{21})^{y_{21}} (FA_{22})^{y_{22}} \dots (FA_{2r})^{y_{2r}} \dots (FA_{is})^{y_{is}}}{y_{11}! y_{12}! \dots y_{1q}! y_{21}! y_{22}! \dots y_{2r}! \dots y_{is}!} \right]$$

(3.6)

$$T = [(z_T)_1! (z_T)_2! \dots (z_T)_i!] \times \left[\frac{(FA_{11})^{z_{11}} (FA_{12})^{z_{12}} \dots (FA_{1q})^{z_{1q}} (FA_{21})^{z_{21}} (FA_{22})^{z_{22}} \dots (FA_{2r})^{z_{2r}} \dots (FA_{is})^{z_{is}}}{z_{11}! z_{12}! \dots z_{1q}! z_{21}! z_{22}! \dots z_{2r}! \dots z_{is}!} \right]$$

(3.7)

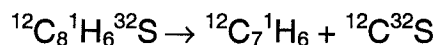
$$C_{11} \dots C_{1q} C_{21} \dots C_{2r} \dots C_{is} = \frac{n_{11}! \dots n_{1q}! n_{21}! \dots n_{2r}! \dots n_{is}!}{(n_{11} - z_{11})! z_{11}! \dots (n_{1q} - z_{1q})! z_{1q}! (n_{21} - z_{21})! z_{21}! \dots (n_{2r} - z_{2r})! z_{2r}! \dots (n_{is} - z_{is})! z_{is}!}$$

The loss of CS from the $M^{+•}$ ion of BT (C_8H_6S) (24) will be used as an example to illustrate the application of (3.4), (3.5), (3.6) and (3.7) for the calculation of isotopic abundance ratios within and among the different types of mass spectra.

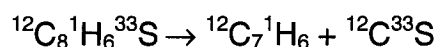
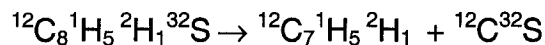
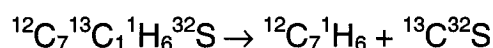
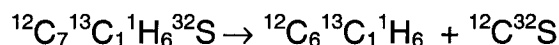


The following fragmentations can occur in the collision cell (q2) as a function of the setting in Q1 (Note: for simplicity, charges and dots signifying radical ions will be omitted and all masses will be given as nominal).

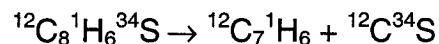
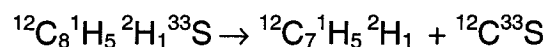
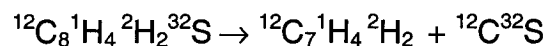
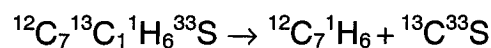
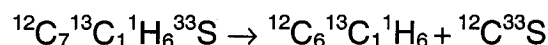
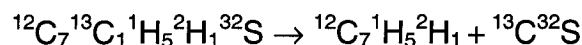
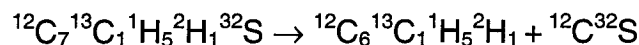
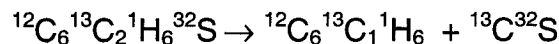
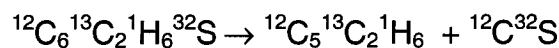
Q1 set to 134



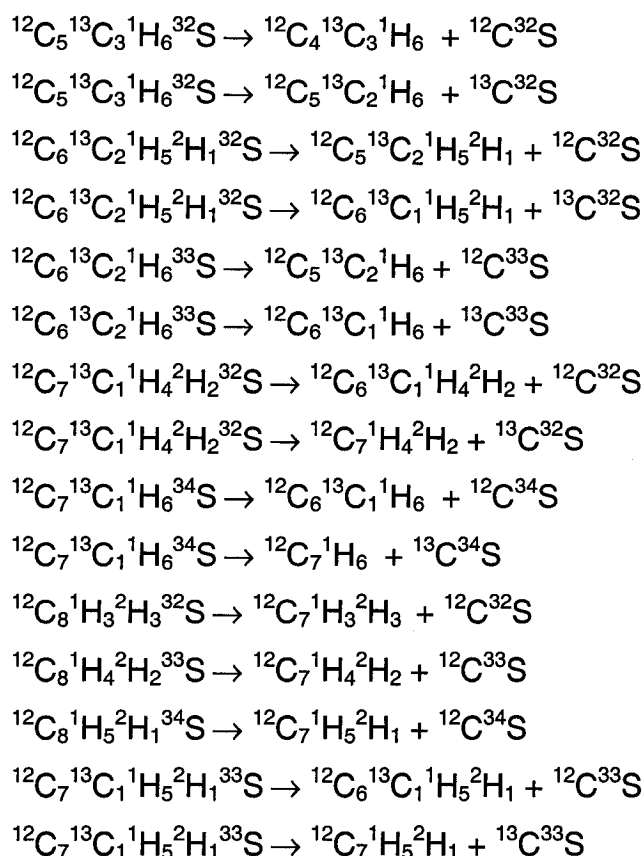
Q1 set to 135



Q1 set to 136



Q1 set to 137



In order to obtain precursor-ion mass spectra of reasonable intensity, Q3 could be set to three different m/z values: 90, 91 and 92. Three precursor-ion mass spectra are obtained, each containing an isotope cluster with three peaks (again of reasonable intensity), one for each precursor ion which produces one of the three different neutral fragments, *i.e.* 44, 45 or 46 u (Table 3.37) (Note: only those peaks having intensities greater than 0.1% of the base peak will be considered in this discussion).

One characteristic of precursor-ion spectra is that the isotope clusters of all spectra arise from the loss of the same neutral fragment or fragments. For example, the first peak of each spectrum ($134 \rightarrow 90$, $135 \rightarrow 91$, $136 \rightarrow 92$) arises from the loss of $^{12}\text{C}^{32}\text{S}$ and the second peak of each spectrum ($135 \rightarrow 90$, $136 \rightarrow 91$, $137 \rightarrow 92$) arises from the losses of $^{12}\text{C}^{33}\text{S}$ and $^{13}\text{C}^{32}\text{S}$ (Table 3.37).

Therefore, the ratios of peak heights within each precursor-ion spectrum are best calculated using the compositions of the neutral fragment (3.6).

Table 3.37. Fractional abundances (T) within precursor-ion mass spectrum.

Product Ion	<i>m/z</i>	Precursor Ion	<i>m/z</i>	Neutral Loss	<i>u</i>	<i>T</i>
$^{12}\text{C}_7^1\text{H}_6$	90	$^{12}\text{C}_8^1\text{H}_6^{32}\text{S}$	134	$^{12}\text{C}^{32}\text{S}$	44	9.3974e-1
$^{12}\text{C}_7^1\text{H}_6$	90	$^{12}\text{C}_7^{13}\text{C}_1^1\text{H}_6^{32}\text{S}$	135	$^{13}\text{C}^{32}\text{S}$	45	1.0164e-2
$^{12}\text{C}_7^1\text{H}_6$	90	$^{12}\text{C}_8^1\text{H}_6^{33}\text{S}$	135	$^{12}\text{C}^{33}\text{S}$	45	7.4198e-3
$^{12}\text{C}_7^1\text{H}_6$	90	$^{12}\text{C}_7^{13}\text{C}_1^1\text{H}_6^{33}\text{S}$	136	$^{13}\text{C}^{33}\text{S}$	46	8.0250e-5
$^{12}\text{C}_7^1\text{H}_6$	90	$^{12}\text{C}_8^1\text{H}_6^{34}\text{S}$	136	$^{12}\text{C}^{34}\text{S}$	46	4.2045e-2
$^{12}\text{C}_6^{13}\text{C}_1^1\text{H}_6$	91	$^{12}\text{C}_7^{13}\text{C}_1^1\text{H}_6^{32}\text{S}$	135	$^{12}\text{C}^{32}\text{S}$	44	9.3974e-1
$^{12}\text{C}_7^1\text{H}_5^2\text{H}_1$	91	$^{12}\text{C}_8^1\text{H}_5^2\text{H}_1^{32}\text{S}$	135	$^{12}\text{C}^{32}\text{S}$	44	
$^{12}\text{C}_6^{13}\text{C}_1^1\text{H}_6$	91	$^{12}\text{C}_6^{13}\text{C}_2^1\text{H}_6^{32}\text{S}$	136	$^{13}\text{C}^{32}\text{S}$	45	1.0164e-2
$^{12}\text{C}_7^1\text{H}_5^2\text{H}_1$	91	$^{12}\text{C}_7^{13}\text{C}_1^1\text{H}_5^2\text{H}_1^{32}\text{S}$	136	$^{13}\text{C}^{32}\text{S}$	45	
$^{12}\text{C}_6^{13}\text{C}_1^1\text{H}_6$	91	$^{12}\text{C}_7^{13}\text{C}_1^1\text{H}_6^{33}\text{S}$	136	$^{12}\text{C}^{33}\text{S}$	45	7.4198e-3
$^{12}\text{C}_7^1\text{H}_5^2\text{H}_1$	91	$^{12}\text{C}_8^1\text{H}_5^2\text{H}_1^{33}\text{S}$	136	$^{12}\text{C}^{33}\text{S}$	45	
$^{12}\text{C}_6^{13}\text{C}_1^1\text{H}_6$	91	$^{12}\text{C}_6^{13}\text{C}_2^1\text{H}_6^{33}\text{S}$	137	$^{13}\text{C}^{33}\text{S}$	46	8.0250e-5
$^{12}\text{C}_7^1\text{H}_5^2\text{H}_1$	91	$^{12}\text{C}_7^{13}\text{C}_1^1\text{H}_5^2\text{H}_1^{33}\text{S}$	137	$^{13}\text{C}^{33}\text{S}$	46	
$^{12}\text{C}_7^1\text{H}_5^2\text{H}_1$	91	$^{12}\text{C}_7^{13}\text{C}_1^1\text{H}_6^{34}\text{S}$	137	$^{12}\text{C}^{34}\text{S}$	46	4.2045e-2
$^{12}\text{C}_6^{13}\text{C}_1^1\text{H}_6$	91	$^{12}\text{C}_8^1\text{H}_5^2\text{H}_1^{34}\text{S}$	137	$^{12}\text{C}^{34}\text{S}$	46	
$^{12}\text{C}_5^{13}\text{C}_2^1\text{H}_6$	92	$^{12}\text{C}_6^{13}\text{C}_2^1\text{H}_6^{32}\text{S}$	136	$^{12}\text{C}^{32}\text{S}$	44	9.3974e-1
$^{12}\text{C}_6^{13}\text{C}_1^1\text{H}_5^2\text{H}_1$	92	$^{12}\text{C}_7^{13}\text{C}_1^1\text{H}_5^2\text{H}_1^{32}\text{S}$	136	$^{12}\text{C}^{32}\text{S}$	44	
$^{12}\text{C}_7^1\text{H}_4^2\text{H}_2$	92	$^{12}\text{C}_8^1\text{H}_4^2\text{H}_2^{32}\text{S}$	136	$^{12}\text{C}^{32}\text{S}$	44	
$^{12}\text{C}_5^{13}\text{C}_2^1\text{H}_6$	92	$^{12}\text{C}_5^{13}\text{C}_3^1\text{H}_6^{32}\text{S}$	137	$^{13}\text{C}^{32}\text{S}$	45	1.0164e-2
$^{12}\text{C}_6^{13}\text{C}_1^1\text{H}_5^2\text{H}_1$	92	$^{12}\text{C}_6^{13}\text{C}_2^1\text{H}_5^2\text{H}_1^{32}\text{S}$	137	$^{13}\text{C}^{32}\text{S}$	45	
$^{12}\text{C}_7^1\text{H}_4^2\text{H}_2$	92	$^{12}\text{C}_7^{13}\text{C}_1^1\text{H}_4^2\text{H}_2^{32}\text{S}$	137	$^{13}\text{C}^{32}\text{S}$	45	
$^{12}\text{C}_5^{13}\text{C}_2^1\text{H}_6$	92	$^{12}\text{C}_6^{13}\text{C}_2^1\text{H}_6^{33}\text{S}$	137	$^{12}\text{C}^{33}\text{S}$	45	7.4198e-3
$^{12}\text{C}_7^1\text{H}_4^2\text{H}_2$	92	$^{12}\text{C}_8^1\text{H}_4^2\text{H}_2^{33}\text{S}$	137	$^{12}\text{C}^{33}\text{S}$	45	
$^{12}\text{C}_6^{13}\text{C}_1^1\text{H}_5^2\text{H}_1$	92	$^{12}\text{C}_7^{13}\text{C}_1^1\text{H}_5^2\text{H}_1^{33}\text{S}$	137	$^{12}\text{C}^{33}\text{S}$	45	
$^{12}\text{C}_5^{13}\text{C}_2^1\text{H}_6$	92	$^{12}\text{C}_5^{13}\text{C}_3^1\text{H}_6^{33}\text{S}$	138	$^{13}\text{C}^{33}\text{S}$	46	8.0250e-5
$^{12}\text{C}_6^{13}\text{C}_1^1\text{H}_5^2\text{H}_1$	92	$^{12}\text{C}_6^{13}\text{C}_2^1\text{H}_5^2\text{H}_1^{33}\text{S}$	138	$^{13}\text{C}^{33}\text{S}$	46	
$^{12}\text{C}_7^1\text{H}_4^2\text{H}_2$	92	$^{12}\text{C}_7^{13}\text{C}_1^1\text{H}_4^2\text{H}_2^{33}\text{S}$	138	$^{13}\text{C}^{33}\text{S}$	46	
$^{12}\text{C}_5^{13}\text{C}_2^1\text{H}_6$	92	$^{12}\text{C}_6^{13}\text{C}_2^1\text{H}_6^{34}\text{S}$	138	$^{12}\text{C}^{34}\text{S}$	46	4.2045e-2
$^{12}\text{C}_6^{13}\text{C}_1^1\text{H}_5^2\text{H}_1$	92	$^{12}\text{C}_7^{13}\text{C}_1^1\text{H}_5^2\text{H}_1^{34}\text{S}$	138	$^{12}\text{C}^{34}\text{S}$	46	
$^{12}\text{C}_7^1\text{H}_4^2\text{H}_2$	92	$^{12}\text{C}_8^1\text{H}_4^2\text{H}_2^{34}\text{S}$	138	$^{12}\text{C}^{34}\text{S}$	46	

The fractional abundance for $^{12}\text{C}^{32}\text{S}$ is calculated using (3.6) as follows (Note: natural isotopic abundances used are: 0.9893 (^{12}C), 0.0107 (^{13}C), 0.999885 (^1H), 0.000115 (^2H), 0.9499 (^{32}S), 0.0075 (^{33}S) and 0.0425 (^{34}S) (de Laeter *et al.* 2003)).

$$T = [1!1!] \times \left[\frac{(0.9893)^1 (0.0107)^0 (0.9499)^1 (0.0075)^0 (0.0425)^0}{1!0!1!0!0!} \right] = 9.3974e-1$$

Fractional abundances of each of the peaks in the isotope clusters are listed in Table 3.37. In order to get the overall contributions, the fractional abundances of all species at a given mass must be summed. Therefore, there will be three peaks in the precursor-ion spectrum of m/z 90 at m/z values of 134, 135 and 136, with abundances of $9.3974e-1$, $1.7584e-2$ and $4.2126e-2$, respectively, and relative peak heights of 100.000 %, 1.871 % and 4.483 %. The precursor-ion spectrum of m/z 91 will also display three peaks with the same relative peak heights but the first peak of the isotope cluster will be observed at m/z 135.

Another characteristic of precursor-ion spectra is that every spectrum arises from the same fragment ion, in our case $C_7H_6^{+*}$. The ratios of peak heights among precursor-ion spectra are thus obtained using the composition of the product ions (3.5) (Table 3.38). For example, the fractional abundance of the product ion $^{12}C_6^{13}C_1^1H_5^2H_1^{+*}$ is calculated as follows

$$T = [7!6!] \times \left[\frac{(0.9893)^6 (0.0107)^1 (0.999885)^5 (0.000115)^1}{6!1!5!1!} \right] = 4.8423e-5$$

As shown in Table 3.38, the fractional abundances of the first peak of each precursor-ion spectrum ($134 \rightarrow 90$, $135 \rightarrow 91$, $136 \rightarrow 92$) are $9.2682e-1$, $7.0810e-2$ and $2.3254e-3$, respectively, and thus the ratios of peak heights among precursor-ion spectra will be 100.000 %, 7.640 % and 0.251 %.

For the BT example, constant neutral loss spectra are obtained by scanning Q1 and Q3 with a constant difference in mass of 44, 45 or 46 u. Three neutral loss spectra are produced, each containing the precursor ions that lose either 44, 45 or 46 u. Since the first peak (as well as the second peak, etc) of

each spectrum gives rise to the same product ion or ions, the peak height ratios within a neutral loss spectrum are most conveniently calculated from the expansion that pertains to the product ions (3.5) (Table 3.39).

Table 3.38. Fractional abundances (T) among precursor-ion mass spectra.

Neutral Loss	u	Precursor Ion	m/z	Product Ion	m/z	T
$^{12}\text{C}^{32}\text{S}$	44	$^{12}\text{C}_8^1\text{H}_6^{32}\text{S}$	134	$^{12}\text{C}_7^1\text{H}_6$	90	9.2682e-1
$^{13}\text{C}^{32}\text{S}$	45	$^{12}\text{C}_7^{13}\text{C}_1^1\text{H}_6^{32}\text{S}$	135	$^{12}\text{C}_7^1\text{H}_6$	90	
$^{12}\text{C}^{33}\text{S}$	45	$^{12}\text{C}_8^1\text{H}_6^{33}\text{S}$	135	$^{12}\text{C}_7^1\text{H}_6$	90	
$^{13}\text{C}^{33}\text{S}$	46	$^{12}\text{C}_7^{13}\text{C}_1^1\text{H}_6^{33}\text{S}$	136	$^{12}\text{C}_7^1\text{H}_6$	90	
$^{12}\text{C}^{34}\text{S}$	46	$^{12}\text{C}_8^1\text{H}_6^{34}\text{S}$	136	$^{12}\text{C}_7^1\text{H}_6$	90	
$^{12}\text{C}^{32}\text{S}$	44	$^{12}\text{C}_7^{13}\text{C}_1^1\text{H}_6^{32}\text{S}$	135	$^{12}\text{C}_6^{13}\text{C}_1^1\text{H}_6$	91	7.0170e-2
$^{12}\text{C}^{32}\text{S}$	44	$^{12}\text{C}_8^1\text{H}_5^2\text{H}_1^{32}\text{S}$	135	$^{12}\text{C}_7^1\text{H}_5^2\text{H}_1$	91	
$^{13}\text{C}^{32}\text{S}$	45	$^{12}\text{C}_6^{13}\text{C}_2^1\text{H}_6^{32}\text{S}$	136	$^{12}\text{C}_6^{13}\text{C}_1^1\text{H}_6$	91	
$^{12}\text{C}^{33}\text{S}$	45	$^{12}\text{C}_7^{13}\text{C}_1^1\text{H}_6^{33}\text{S}$	136	$^{12}\text{C}_6^{13}\text{C}_1^1\text{H}_6$	91	
$^{13}\text{C}^{32}\text{S}$	45	$^{12}\text{C}_7^{13}\text{C}_1^1\text{H}_5^2\text{H}_1^{32}\text{S}$	136	$^{12}\text{C}_7^1\text{H}_5^2\text{H}_1$	91	
$^{12}\text{C}^{33}\text{S}$	45	$^{12}\text{C}_8^1\text{H}_5^2\text{H}_1^{33}\text{S}$	136	$^{12}\text{C}_7^1\text{H}_5^2\text{H}_1$	91	6.3958e-4
$^{13}\text{C}^{33}\text{S}$	46	$^{12}\text{C}_6^{13}\text{C}_2^1\text{H}_6^{33}\text{S}$	137	$^{12}\text{C}_6^{13}\text{C}_1^1\text{H}_6$	91	
$^{12}\text{C}^{34}\text{S}$	46	$^{12}\text{C}_8^1\text{H}_5^2\text{H}_1^{34}\text{S}$	137	$^{12}\text{C}_6^{13}\text{C}_1^1\text{H}_6$	91	
$^{12}\text{C}^{34}\text{S}$	46	$^{12}\text{C}_7^{13}\text{C}_1^1\text{H}_6^{34}\text{S}$	137	$^{12}\text{C}_7^1\text{H}_5^2\text{H}_1$	91	
$^{13}\text{C}^{33}\text{S}$	46	$^{12}\text{C}_7^{13}\text{C}_1^1\text{H}_5^2\text{H}_1^{33}\text{S}$	137	$^{12}\text{C}_7^1\text{H}_5^2\text{H}_1$	91	
$^{12}\text{C}^{32}\text{S}$	44	$^{12}\text{C}_6^{13}\text{C}_2^1\text{H}_6^{32}\text{S}$	136	$^{12}\text{C}_5^{13}\text{C}_2^1\text{H}_6$	92	2.2768e-3
$^{12}\text{C}^{32}\text{S}$	44	$^{12}\text{C}_7^{13}\text{C}_1^1\text{H}_5^2\text{H}_1^{32}\text{S}$	136	$^{12}\text{C}_6^{13}\text{C}_1^1\text{H}_5^2\text{H}_1$	92	
$^{12}\text{C}^{32}\text{S}$	44	$^{12}\text{C}_8^1\text{H}_4^2\text{H}_2^{32}\text{S}$	136	$^{12}\text{C}_7^1\text{H}_4^2\text{H}_2$	92	
$^{13}\text{C}^{32}\text{S}$	45	$^{12}\text{C}_5^{13}\text{C}_3^1\text{H}_6^{32}\text{S}$	137	$^{12}\text{C}_5^{13}\text{C}_2^1\text{H}_6$	92	
$^{12}\text{C}^{33}\text{S}$	45	$^{12}\text{C}_6^{13}\text{C}_2^1\text{H}_6^{33}\text{S}$	137	$^{12}\text{C}_5^{13}\text{C}_2^1\text{H}_6$	92	
$^{13}\text{C}^{32}\text{S}$	45	$^{12}\text{C}_6^{13}\text{C}_2^1\text{H}_5^2\text{H}_1^{32}\text{S}$	137	$^{12}\text{C}_6^{13}\text{C}_1^1\text{H}_5^2\text{H}_1$	92	4.8423e-5
$^{12}\text{C}^{33}\text{S}$	45	$^{12}\text{C}_7^{13}\text{C}_1^1\text{H}_5^2\text{H}_1^{33}\text{S}$	137	$^{12}\text{C}_6^{13}\text{C}_1^1\text{H}_5^2\text{H}_1$	92	
$^{13}\text{C}^{32}\text{S}$	45	$^{12}\text{C}_7^{13}\text{C}_1^1\text{H}_4^2\text{H}_2^{32}\text{S}$	137	$^{12}\text{C}_7^1\text{H}_4^2\text{H}_2$	92	
$^{12}\text{C}^{33}\text{S}$	45	$^{12}\text{C}_8^1\text{H}_4^2\text{H}_2^{33}\text{S}$	137	$^{12}\text{C}_7^1\text{H}_4^2\text{H}_2$	92	
$^{12}\text{C}^{34}\text{S}$	46	$^{12}\text{C}_6^{13}\text{C}_2^1\text{H}_6^{34}\text{S}$	138	$^{12}\text{C}_5^{13}\text{C}_2^1\text{H}_6$	92	
$^{13}\text{C}^{33}\text{S}$	46	$^{12}\text{C}_5^{13}\text{C}_3^1\text{H}_6^{33}\text{S}$	138	$^{12}\text{C}_5^{13}\text{C}_2^1\text{H}_6$	92	2.2768e-3
$^{12}\text{C}^{34}\text{S}$	46	$^{12}\text{C}_7^{13}\text{C}_1^1\text{H}_5^2\text{H}_1^{34}\text{S}$	138	$^{12}\text{C}_6^{13}\text{C}_1^1\text{H}_5^2\text{H}_1$	92	
$^{13}\text{C}^{33}\text{S}$	46	$^{12}\text{C}_6^{13}\text{C}_2^1\text{H}_5^2\text{H}_1^{33}\text{S}$	138	$^{12}\text{C}_6^{13}\text{C}_1^1\text{H}_5^2\text{H}_1$	92	
$^{12}\text{C}^{34}\text{S}$	46	$^{12}\text{C}_8^1\text{H}_4^2\text{H}_2^{34}\text{S}$	138	$^{12}\text{C}_7^1\text{H}_4^2\text{H}_2$	92	
$^{13}\text{C}^{33}\text{S}$	46	$^{12}\text{C}_7^{13}\text{C}_1^1\text{H}_4^2\text{H}_2^{33}\text{S}$	138	$^{12}\text{C}_7^1\text{H}_4^2\text{H}_2$	92	

Thus, the neutral loss of 44 u mass spectrum will contain three peaks at m/z 134, 135 and 136, with fractional abundances of 9.2682e-1, 7.0810e-2 and 2.3254e-3, respectively, and relative peak heights of 100.000 %, 7.640 % and 0.251 %. The neutral loss mass spectrum of 45 u will also display three peaks

with the same relative peak heights but the first peak of the isotope cluster will be detected at one mass unit higher, *i.e.* 135 (Table 3.39).

Table 3.39. Fractional abundances (T) within neutral loss mass spectrum.

Neutral Loss u	Precursor Ion	m/z	Product Ion	m/z	T
$^{12}\text{C}^{32}\text{S}$	$^{12}\text{C}_8^1\text{H}_6^{32}\text{S}$	134	$^{12}\text{C}_7^1\text{H}_6$	90	9.2682e-1
$^{12}\text{C}^{32}\text{S}$	$^{12}\text{C}_7^{13}\text{C}_1^1\text{H}_6^{32}\text{S}$	135	$^{12}\text{C}_6^{13}\text{C}_1^1\text{H}_6$	91	7.0170e-2
$^{12}\text{C}^{32}\text{S}$	$^{12}\text{C}_8^1\text{H}_5^2\text{H}_1^{32}\text{S}$	135	$^{12}\text{C}_7^1\text{H}_5^2\text{H}_1$	91	6.3958e-4
$^{12}\text{C}^{32}\text{S}$	$^{12}\text{C}_6^{13}\text{C}_2^1\text{H}_6^{32}\text{S}$	136	$^{12}\text{C}_5^{13}\text{C}_2^1\text{H}_6$	92	2.2768e-3
$^{12}\text{C}^{32}\text{S}$	$^{12}\text{C}_7^{13}\text{C}_1^1\text{H}_5^2\text{H}_1^{32}\text{S}$	136	$^{12}\text{C}_6^{13}\text{C}_1^1\text{H}_5^2\text{H}_1$	92	4.8423e-5
$^{12}\text{C}^{32}\text{S}$	$^{12}\text{C}_8^1\text{H}_4^2\text{H}_2^{32}\text{S}$	136	$^{12}\text{C}_7^1\text{H}_4^2\text{H}_2$	92	1.8390e-7
$^{13}\text{C}^{32}\text{S}$	$^{12}\text{C}_7^{13}\text{C}_1^1\text{H}_6^{32}\text{S}$	135	$^{12}\text{C}_7^1\text{H}_6$	90	9.2682e-1
$^{12}\text{C}^{33}\text{S}$	$^{12}\text{C}_8^1\text{H}_6^{33}\text{S}$	135	$^{12}\text{C}_7^1\text{H}_6$	90	
$^{13}\text{C}^{32}\text{S}$	$^{12}\text{C}_6^{13}\text{C}_2^1\text{H}_6^{32}\text{S}$	136	$^{12}\text{C}_6^{13}\text{C}_1^1\text{H}_6$	91	7.0170e-2
$^{12}\text{C}^{33}\text{S}$	$^{12}\text{C}_7^{13}\text{C}_1^1\text{H}_6^{33}\text{S}$	136	$^{12}\text{C}_6^{13}\text{C}_1^1\text{H}_6$	91	
$^{13}\text{C}^{32}\text{S}$	$^{12}\text{C}_7^{13}\text{C}_1^1\text{H}_5^2\text{H}_1^{32}\text{S}$	136	$^{12}\text{C}_7^1\text{H}_5^2\text{H}_1$	91	6.3958e-4
$^{12}\text{C}^{33}\text{S}$	$^{12}\text{C}_8^1\text{H}_5^2\text{H}_1^{33}\text{S}$	136	$^{12}\text{C}_7^1\text{H}_5^2\text{H}_1$	91	
$^{13}\text{C}^{32}\text{S}$	$^{12}\text{C}_5^{13}\text{C}_3^1\text{H}_6^{32}\text{S}$	137	$^{12}\text{C}_5^{13}\text{C}_2^1\text{H}_6$	92	2.2768e-3
$^{12}\text{C}^{33}\text{S}$	$^{12}\text{C}_6^{13}\text{C}_2^1\text{H}_6^{33}\text{S}$	137	$^{12}\text{C}_5^{13}\text{C}_2^1\text{H}_6$	92	
$^{13}\text{C}^{32}\text{S}$	$^{12}\text{C}_6^{13}\text{C}_2^1\text{H}_5^2\text{H}_1^{32}\text{S}$	137	$^{12}\text{C}_6^{13}\text{C}_1^1\text{H}_5^2\text{H}_1$	92	4.8423e-5
$^{12}\text{C}^{33}\text{S}$	$^{12}\text{C}_7^{13}\text{C}_1^1\text{H}_5^2\text{H}_1^{33}\text{S}$	137	$^{12}\text{C}_6^{13}\text{C}_1^1\text{H}_5^2\text{H}_1$	92	
$^{13}\text{C}^{32}\text{S}$	$^{12}\text{C}_7^{13}\text{C}_1^1\text{H}_4^2\text{H}_2^{32}\text{S}$	137	$^{12}\text{C}_7^1\text{H}_4^2\text{H}_2$	92	1.8390e-7
$^{12}\text{C}^{33}\text{S}$	$^{12}\text{C}_8^1\text{H}_4^2\text{H}_2^{33}\text{S}$	137	$^{12}\text{C}_7^1\text{H}_4^2\text{H}_2$	92	
$^{13}\text{C}^{33}\text{S}$	$^{12}\text{C}_7^{13}\text{C}_1^1\text{H}_6^{33}\text{S}$	136	$^{12}\text{C}_7^1\text{H}_6$	90	9.2682e-1
$^{12}\text{C}^{34}\text{S}$	$^{12}\text{C}_8^1\text{H}_6^{34}\text{S}$	136	$^{12}\text{C}_7^1\text{H}_6$	90	
$^{13}\text{C}^{33}\text{S}$	$^{12}\text{C}_6^{13}\text{C}_2^1\text{H}_6^{33}\text{S}$	137	$^{12}\text{C}_6^{13}\text{C}_1^1\text{H}_6$	91	7.0170e-2
$^{12}\text{C}^{34}\text{S}$	$^{12}\text{C}_8^1\text{H}_5^2\text{H}_1^{34}\text{S}$	137	$^{12}\text{C}_6^{13}\text{C}_1^1\text{H}_6$	91	
$^{12}\text{C}^{34}\text{S}$	$^{12}\text{C}_7^{13}\text{C}_1^1\text{H}_6^{34}\text{S}$	137	$^{12}\text{C}_7^1\text{H}_5^2\text{H}_1$	91	6.3958e-4
$^{13}\text{C}^{33}\text{S}$	$^{12}\text{C}_7^{13}\text{C}_1^1\text{H}_5^2\text{H}_1^{33}\text{S}$	137	$^{12}\text{C}_7^1\text{H}_5^2\text{H}_1$	91	
$^{12}\text{C}^{34}\text{S}$	$^{12}\text{C}_6^{13}\text{C}_2^1\text{H}_6^{34}\text{S}$	138	$^{12}\text{C}_5^{13}\text{C}_2^1\text{H}_6$	92	2.2768e-3
$^{13}\text{C}^{33}\text{S}$	$^{12}\text{C}_5^{13}\text{C}_3^1\text{H}_6^{33}\text{S}$	138	$^{12}\text{C}_5^{13}\text{C}_2^1\text{H}_6$	92	
$^{12}\text{C}^{34}\text{S}$	$^{12}\text{C}_7^{13}\text{C}_1^1\text{H}_5^2\text{H}_1^{34}\text{S}$	138	$^{12}\text{C}_6^{13}\text{C}_1^1\text{H}_5^2\text{H}_1$	92	4.8423e-5
$^{13}\text{C}^{33}\text{S}$	$^{12}\text{C}_6^{13}\text{C}_2^1\text{H}_5^2\text{H}_1^{33}\text{S}$	138	$^{12}\text{C}_6^{13}\text{C}_1^1\text{H}_5^2\text{H}_1$	92	
$^{12}\text{C}^{34}\text{S}$	$^{12}\text{C}_8^1\text{H}_4^2\text{H}_2^{34}\text{S}$	138	$^{12}\text{C}_7^1\text{H}_4^2\text{H}_2$	92	1.8390e-7
$^{13}\text{C}^{33}\text{S}$	$^{12}\text{C}_7^{13}\text{C}_1^1\text{H}_4^2\text{H}_2^{33}\text{S}$	138	$^{12}\text{C}_7^1\text{H}_4^2\text{H}_2$	92	

The other feature of neutral loss spectra is that each spectrum arises from the same neutral fragment or fragments. For example, the first spectrum arises from the loss of $^{12}\text{C}^{32}\text{S}$ and the second spectrum arises from the losses of $^{13}\text{C}^{32}\text{S}$ and $^{12}\text{C}^{33}\text{S}$, *etc.* Therefore, the terms that provide the abundance ratios among

neutral loss spectra (Table 3.40) are obtained from the expansion that relates to the neutral fragment (3.6).

Table 3.40. Fractional abundances (T) among neutral loss mass spectra.

Product Ion	m/z	Precursor Ion	m/z	Neutral Loss u	T
$^{12}\text{C}_7^1\text{H}_6$	90	$^{12}\text{C}_8^1\text{H}_6^{32}\text{S}$	134	$^{12}\text{C}^{32}\text{S}$ 44	9.3974e-1
$^{12}\text{C}_6^{13}\text{C}_1^1\text{H}_6$	91	$^{12}\text{C}_7^{13}\text{C}_1^1\text{H}_6^{32}\text{S}$	135	$^{12}\text{C}^{32}\text{S}$ 44	
$^{12}\text{C}_7^1\text{H}_5^2\text{H}_1$	91	$^{12}\text{C}_8^1\text{H}_5^2\text{H}_1^{32}\text{S}$	135	$^{12}\text{C}^{32}\text{S}$ 44	
$^{12}\text{C}_5^{13}\text{C}_2^1\text{H}_6$	92	$^{12}\text{C}_6^{13}\text{C}_2^1\text{H}_6^{32}\text{S}$	136	$^{12}\text{C}^{32}\text{S}$ 44	
$^{12}\text{C}_6^{13}\text{C}_1^1\text{H}_5^2\text{H}_1$	92	$^{12}\text{C}_7^{13}\text{C}_1^1\text{H}_5^2\text{H}_1^{32}\text{S}$	136	$^{12}\text{C}^{32}\text{S}$ 44	
$^{12}\text{C}_7^1\text{H}_4^2\text{H}_2$	92	$^{12}\text{C}_8^1\text{H}_4^2\text{H}_2^{32}\text{S}$	136	$^{12}\text{C}^{32}\text{S}$ 44	
$^{12}\text{C}_7^1\text{H}_6$	90	$^{12}\text{C}_7^{13}\text{C}_1^1\text{H}_6^{32}\text{S}$	135	$^{13}\text{C}^{32}\text{S}$ 45	1.0164e-2
$^{12}\text{C}_6^{13}\text{C}_1^1\text{H}_6$	91	$^{12}\text{C}_6^{13}\text{C}_2^1\text{H}_6^{32}\text{S}$	136	$^{13}\text{C}^{32}\text{S}$ 45	
$^{12}\text{C}_7^1\text{H}_5^2\text{H}_1$	91	$^{12}\text{C}_7^{13}\text{C}_1^1\text{H}_5^2\text{H}_1^{32}\text{S}$	136	$^{13}\text{C}^{32}\text{S}$ 45	
$^{12}\text{C}_5^{13}\text{C}_2^1\text{H}_6$	92	$^{12}\text{C}_5^{13}\text{C}_3^1\text{H}_6^{32}\text{S}$	137	$^{13}\text{C}^{32}\text{S}$ 45	
$^{12}\text{C}_6^{13}\text{C}_1^1\text{H}_5^2\text{H}_1$	92	$^{12}\text{C}_6^{13}\text{C}_2^1\text{H}_5^2\text{H}_1^{32}\text{S}$	137	$^{13}\text{C}^{32}\text{S}$ 45	
$^{12}\text{C}_7^1\text{H}_4^2\text{H}_2$	92	$^{12}\text{C}_7^{13}\text{C}_1^1\text{H}_4^2\text{H}_2^{32}\text{S}$	137	$^{13}\text{C}^{32}\text{S}$ 45	
$^{12}\text{C}_7^1\text{H}_6$	90	$^{12}\text{C}_8^1\text{H}_6^{33}\text{S}$	135	$^{12}\text{C}^{33}\text{S}$ 45	7.4198e-3
$^{12}\text{C}_6^{13}\text{C}_1^1\text{H}_6$	91	$^{12}\text{C}_7^{13}\text{C}_1^1\text{H}_6^{33}\text{S}$	136	$^{12}\text{C}^{33}\text{S}$ 45	
$^{12}\text{C}_7^1\text{H}_5^2\text{H}_1$	91	$^{12}\text{C}_8^1\text{H}_5^2\text{H}_1^{33}\text{S}$	136	$^{12}\text{C}^{33}\text{S}$ 45	
$^{12}\text{C}_5^{13}\text{C}_2^1\text{H}_6$	92	$^{12}\text{C}_6^{13}\text{C}_2^1\text{H}_6^{33}\text{S}$	137	$^{12}\text{C}^{33}\text{S}$ 45	
$^{12}\text{C}_7^1\text{H}_4^2\text{H}_2$	92	$^{12}\text{C}_8^1\text{H}_4^2\text{H}_2^{33}\text{S}$	137	$^{12}\text{C}^{33}\text{S}$ 45	
$^{12}\text{C}_6^{13}\text{C}_1^1\text{H}_5^2\text{H}_1$	92	$^{12}\text{C}_7^{13}\text{C}_1^1\text{H}_5^2\text{H}_1^{33}\text{S}$	137	$^{12}\text{C}^{33}\text{S}$ 45	
$^{12}\text{C}_7^1\text{H}_6$	90	$^{12}\text{C}_7^{13}\text{C}_1^1\text{H}_6^{33}\text{S}$	136	$^{13}\text{C}^{33}\text{S}$ 46	8.0250e-5
$^{12}\text{C}_6^{13}\text{C}_1^1\text{H}_6$	91	$^{12}\text{C}_6^{13}\text{C}_2^1\text{H}_6^{33}\text{S}$	137	$^{13}\text{C}^{33}\text{S}$ 46	
$^{12}\text{C}_7^1\text{H}_5^2\text{H}_1$	91	$^{12}\text{C}_7^{13}\text{C}_1^1\text{H}_5^2\text{H}_1^{33}\text{S}$	137	$^{13}\text{C}^{33}\text{S}$ 46	
$^{12}\text{C}_5^{13}\text{C}_2^1\text{H}_6$	92	$^{12}\text{C}_5^{13}\text{C}_3^1\text{H}_6^{33}\text{S}$	138	$^{13}\text{C}^{33}\text{S}$ 46	
$^{12}\text{C}_6^{13}\text{C}_1^1\text{H}_5^2\text{H}_1$	92	$^{12}\text{C}_6^{13}\text{C}_2^1\text{H}_5^2\text{H}_1^{33}\text{S}$	138	$^{13}\text{C}^{33}\text{S}$ 46	
$^{12}\text{C}_7^1\text{H}_4^2\text{H}_2$	92	$^{12}\text{C}_7^{13}\text{C}_1^1\text{H}_4^2\text{H}_2^{33}\text{S}$	138	$^{13}\text{C}^{33}\text{S}$ 46	
$^{12}\text{C}_7^1\text{H}_6$	90	$^{12}\text{C}_8^1\text{H}_6^{34}\text{S}$	136	$^{12}\text{C}^{34}\text{S}$ 46	4.2045e-2
$^{12}\text{C}_7^1\text{H}_5^2\text{H}_1$	91	$^{12}\text{C}_7^{13}\text{C}_1^1\text{H}_6^{34}\text{S}$	137	$^{12}\text{C}^{34}\text{S}$ 46	
$^{12}\text{C}_6^{13}\text{C}_1^1\text{H}_6$	91	$^{12}\text{C}_8^1\text{H}_5^2\text{H}_1^{34}\text{S}$	137	$^{12}\text{C}^{34}\text{S}$ 46	
$^{12}\text{C}_5^{13}\text{C}_2^1\text{H}_6$	92	$^{12}\text{C}_6^{13}\text{C}_2^1\text{H}_6^{34}\text{S}$	138	$^{12}\text{C}^{34}\text{S}$ 46	
$^{12}\text{C}_6^{13}\text{C}_1^1\text{H}_5^2\text{H}_1$	92	$^{12}\text{C}_7^{13}\text{C}_1^1\text{H}_5^2\text{H}_1^{34}\text{S}$	138	$^{12}\text{C}^{34}\text{S}$ 46	
$^{12}\text{C}_7^1\text{H}_4^2\text{H}_2$	92	$^{12}\text{C}_8^1\text{H}_4^2\text{H}_2^{34}\text{S}$	138	$^{12}\text{C}^{34}\text{S}$ 46	

Therefore, the spectrum that arises from the loss of 44 u ($134 \rightarrow 90$) has a fractional abundance of 9.3974e-1, the spectrum for the loss of 45 u ($135 \rightarrow 90$) has a fractional abundance of 1.7584e-2, and that for the loss of 46 u ($136 \rightarrow 90$) has a fractional abundance of 4.2125e-2. The relative abundance among the three neutral loss spectra will be 100.000 %, 1.871 %, 4.483 %, respectively.

Table 3.41. Fractional abundances (T) of precursor ions.

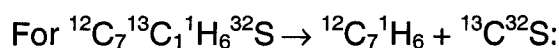
Product Ion	<i>m/z</i>	Neutral Loss	<i>u</i>	Precursor Ion	<i>m/z</i>	T
$^{12}\text{C}_7^1\text{H}_6$	90	$^{12}\text{C}^{32}\text{S}$	44	$^{12}\text{C}_8^1\text{H}_6^{32}\text{S}$	134	8.7097e-1
$^{12}\text{C}_7^1\text{H}_6$	90	$^{13}\text{C}^{32}\text{S}$	45	$^{12}\text{C}_7^{13}\text{C}_1^1\text{H}_6^{32}\text{S}$	135	7.5361e-2
$^{12}\text{C}_6^{13}\text{C}_1^1\text{H}_6$	91	$^{12}\text{C}^{32}\text{S}$	44	$^{12}\text{C}_7^{13}\text{C}_1^1\text{H}_6^{32}\text{S}$	135	7.5361e-2
$^{12}\text{C}_7^1\text{H}_6$	90	$^{12}\text{C}^{33}\text{S}$	45	$^{12}\text{C}_8^1\text{H}_6^{33}\text{S}$	135	6.8768e-3
$^{12}\text{C}_7^1\text{H}_5^2\text{H}_1$	91	$^{12}\text{C}^{32}\text{S}$	44	$^{12}\text{C}_8^1\text{H}_5^2\text{H}_1^{32}\text{S}$	135	6.0104e-4
$^{12}\text{C}_7^1\text{H}_6$	90	$^{13}\text{C}^{33}\text{S}$	46	$^{12}\text{C}_7^{13}\text{C}_1^1\text{H}_6^{33}\text{S}$	136	5.9502e-4
$^{12}\text{C}_6^{13}\text{C}_1^1\text{H}_6$	91	$^{12}\text{C}^{33}\text{S}$	45	$^{12}\text{C}_7^{13}\text{C}_1^1\text{H}_6^{33}\text{S}$	136	
$^{12}\text{C}_7^1\text{H}_6$	90	$^{12}\text{C}^{34}\text{S}$	46	$^{12}\text{C}_8^1\text{H}_6^{34}\text{S}$	136	3.8968e-2
$^{12}\text{C}_6^{13}\text{C}_1^1\text{H}_6$	91	$^{13}\text{C}^{32}\text{S}$	45	$^{12}\text{C}_6^{13}\text{C}_2^1\text{H}_6^{32}\text{S}$	136	2.8528e-3
$^{12}\text{C}_5^{13}\text{C}_2^1\text{H}_6$	92	$^{12}\text{C}^{32}\text{S}$	44	$^{12}\text{C}_6^{13}\text{C}_2^1\text{H}_6^{32}\text{S}$	136	
$^{12}\text{C}_7^1\text{H}_5^2\text{H}_1$	91	$^{13}\text{C}^{32}\text{S}$	45	$^{12}\text{C}_7^{13}\text{C}_1^1\text{H}_5^2\text{H}_1^{32}\text{S}$	136	5.2005e-5
$^{12}\text{C}_6^{13}\text{C}_1^1\text{H}_5^2\text{H}_1$	92	$^{12}\text{C}^{32}\text{S}$	44	$^{12}\text{C}_7^{13}\text{C}_1^1\text{H}_5^2\text{H}_1^{32}\text{S}$	136	
$^{12}\text{C}_7^1\text{H}_5^2\text{H}_1$	91	$^{12}\text{C}^{33}\text{S}$	45	$^{12}\text{C}_8^1\text{H}_5^2\text{H}_1^{33}\text{S}$	136	4.7455e-6
$^{12}\text{C}_7^1\text{H}_4^2\text{H}_2$	92	$^{12}\text{C}^{32}\text{S}$	44	$^{12}\text{C}_8^1\text{H}_4^2\text{H}_2^{32}\text{S}$	136	1.7282e-7
$^{12}\text{C}_7^1\text{H}_6$	90	$^{13}\text{C}^{34}\text{S}$	47	$^{12}\text{C}_7^{13}\text{C}_1^1\text{H}_6^{34}\text{S}$	137	3.3718e-3
$^{12}\text{C}_7^1\text{H}_5^2\text{H}_1$	91	$^{12}\text{C}^{34}\text{S}$	46	$^{12}\text{C}_7^{13}\text{C}_1^1\text{H}_6^{34}\text{S}$	137	
$^{12}\text{C}_6^{13}\text{C}_1^1\text{H}_6$	91	$^{13}\text{C}^{33}\text{S}$	46	$^{12}\text{C}_6^{13}\text{C}_2^1\text{H}_6^{33}\text{S}$	137	2.2524e-5
$^{12}\text{C}_5^{13}\text{C}_2^1\text{H}_6$	92	$^{12}\text{C}^{33}\text{S}$	45	$^{12}\text{C}_6^{13}\text{C}_2^1\text{H}_6^{33}\text{S}$	137	
$^{12}\text{C}_6^{13}\text{C}_1^1\text{H}_6$	91	$^{12}\text{C}^{34}\text{S}$	46	$^{12}\text{C}_8^1\text{H}_5^2\text{H}_1^{34}\text{S}$	137	2.6891e-5
$^{12}\text{C}_7^1\text{H}_5^2\text{H}_1$	91	$^{13}\text{C}^{33}\text{S}$	46	$^{12}\text{C}_7^{13}\text{C}_1^1\text{H}_5^2\text{H}_1^{33}\text{S}$	137	4.1061e-7
$^{12}\text{C}_6^{13}\text{C}_1^1\text{H}_5^2\text{H}_1$	92	$^{12}\text{C}^{33}\text{S}$	45	$^{12}\text{C}_7^{13}\text{C}_1^1\text{H}_5^2\text{H}_1^{33}\text{S}$	137	
$^{12}\text{C}_5^{13}\text{C}_2^1\text{H}_6$	92	$^{13}\text{C}^{32}\text{S}$	45	$^{12}\text{C}_5^{13}\text{C}_3^1\text{H}_6^{32}\text{S}$	137	6.1710e-5
$^{12}\text{C}_4^{13}\text{C}_3^1\text{H}_6$	93	$^{12}\text{C}^{32}\text{S}$	44	$^{12}\text{C}_5^{13}\text{C}_3^1\text{H}_6^{32}\text{S}$	137	
$^{12}\text{C}_6^{13}\text{C}_1^1\text{H}_5^2\text{H}_1$	92	$^{13}\text{C}^{32}\text{S}$	45	$^{12}\text{C}_6^{13}\text{C}_2^1\text{H}_5^2\text{H}_1^{32}\text{S}$	137	1.9687e-6
$^{12}\text{C}_5^{13}\text{C}_2^1\text{H}_5^2\text{H}_1$	93	$^{12}\text{C}^{32}\text{S}$	44	$^{12}\text{C}_6^{13}\text{C}_2^1\text{H}_5^2\text{H}_1^{32}\text{S}$	137	
$^{12}\text{C}_7^1\text{H}_4^2\text{H}_2$	92	$^{13}\text{C}^{32}\text{S}$	45	$^{12}\text{C}_7^{13}\text{C}_1^1\text{H}_4^2\text{H}_2^{32}\text{S}$	137	1.4953e-8
$^{12}\text{C}_6^{13}\text{C}_1^1\text{H}_4^2\text{H}_2$	93	$^{12}\text{C}^{32}\text{S}$	44	$^{12}\text{C}_7^{13}\text{C}_1^1\text{H}_4^2\text{H}_2^{32}\text{S}$	137	
$^{12}\text{C}_7^1\text{H}_4^2\text{H}_2$	92	$^{12}\text{C}^{33}\text{S}$	45	$^{12}\text{C}_8^1\text{H}_4^2\text{H}_2^{33}\text{S}$	137	1.3645e-9
$^{12}\text{C}_7^1\text{H}_3^2\text{H}_3$	93	$^{12}\text{C}^{32}\text{S}$	44	$^{12}\text{C}_8^1\text{H}_3^2\text{H}_3^{32}\text{S}$	137	2.6502e-11

A product-ion mass spectrum is obtained by selecting a single precursor ion in Q1 and scanning Q3 to record the *m/z* values of all the fragment ions. Since each product-ion spectrum arises from a unique precursor ion, the total intensity of all the peaks in the spectrum must reflect the abundance of the selected precursor ion. Therefore, in order to determine peak ratios in product-ion spectra, the fractional abundances of all the precursor ions involved are first calculated (Table 3.41). The fractional abundance of a precursor ion is calculated using (3.4). For $^{12}\text{C}_7^{13}\text{C}_1^1\text{H}_5^2\text{H}_1^{32}\text{S}^{+}$, this is done as follows

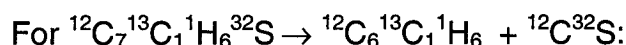
$$T = [8!6!1!] \times \left[\frac{(0.9893)^7 (0.0107)^1 (0.999885)^5 (0.000115)^1 (0.9499)^1 (0.0075)^0 (0.0425)^0}{7!1!5!1!1!0!0!} \right]$$

$$= 5.2005e-5$$

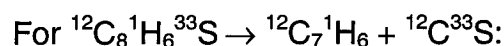
Once the precursor ion has been selected in Q1, the composition of that ion is fixed and the intensity ratios will depend only on the composition of the precursor ion with regard to number of isotopes and not on natural abundances. The number of ways to form the product ion or the neutral fragment from the precursor ion is calculated using equation (3.7). To obtain a better idea of how to use (3.7), the case in which Q1 is set to m/z 135 will be considered. The products of 135 are m/z 90 and 91 and the peak ratios in the spectrum are calculated from the following combinations (element 1 is carbon, element 3 is sulfur) (Table 3.41).



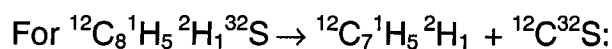
$$C_{11}C_{12}C_{31}C_{32}C_{33} = \frac{7!1!1!0!0!}{(7-0)!0!(1-1)!1!(1-1)!1!(0-0)!0!(0-0)!0!} = 1$$



$$C_{11}C_{12}C_{31}C_{32}C_{33} = \frac{7!1!1!0!0!}{(7-1)!1!(1-0)!0!(1-1)!1!(0-0)!0!(0-0)!0!} = 7$$



$$C_{11}C_{12}C_{31}C_{32}C_{33} = \frac{8!0!0!1!0!}{(8-1)!1!(0-0)!0!(0-0)!0!(1-1)!1!(0-0)!0!} = 8$$



$$C_{11}C_{12}C_{31}C_{32}C_{33} = \frac{8!0!1!0!0!}{(8-1)!1!(0-0)!0!(1-1)!1!(0-0)!0!(0-0)!0!} = 8$$

Table 3.42. Fractional abundances (T) in product-ion spectra.

Product Ion	m/z	NL	Precursor Ion	C	T
${}^{12}\text{C}_7{}^1\text{H}_6$	90	${}^{12}\text{C}^{32}\text{S}$	m/z 134 ${}^{12}\text{C}_8{}^1\text{H}_6{}^{32}\text{S}$	8/8	8.7097e-1
${}^{12}\text{C}_7{}^1\text{H}_6$	90	${}^{13}\text{C}^{32}\text{S}$	m/z 135 ${}^{12}\text{C}_7{}^{13}\text{C}_1{}^1\text{H}_6{}^{32}\text{S}$	1/8	9.4201e-3
${}^{12}\text{C}_6{}^{13}\text{C}_1{}^1\text{H}_6$	91	${}^{12}\text{C}^{33}\text{S}$	${}^{12}\text{C}_7{}^{13}\text{C}_1{}^1\text{H}_6{}^{32}\text{S}$	7/8	6.5941e-2
${}^{12}\text{C}_7{}^1\text{H}_6$	90	${}^{12}\text{C}^{32}\text{S}$	${}^{12}\text{C}_8{}^1\text{H}_6{}^{33}\text{S}$	8/8	6.8768e-3
${}^{12}\text{C}_7{}^1\text{H}_5{}^2\text{H}_1$	91	${}^{12}\text{C}^{32}\text{S}$	${}^{12}\text{C}_8{}^1\text{H}_5{}^2\text{H}_1{}^{32}\text{S}$	8/8	6.0104e-4
${}^{12}\text{C}_7{}^1\text{H}_6$	90	${}^{13}\text{C}^{33}\text{S}$	m/z 136 ${}^{12}\text{C}_7{}^{13}\text{C}_1{}^1\text{H}_6{}^{33}\text{S}$	1/8	7.4378e-5
${}^{12}\text{C}_6{}^{13}\text{C}_1{}^1\text{H}_6$	91	${}^{12}\text{C}^{33}\text{S}$	${}^{12}\text{C}_7{}^{13}\text{C}_1{}^1\text{H}_6{}^{33}\text{S}$	7/8	5.2064e-4
${}^{12}\text{C}_7{}^1\text{H}_6$	90	${}^{12}\text{C}^{34}\text{S}$	${}^{12}\text{C}_8{}^1\text{H}_6{}^{34}\text{S}$	8/8	3.8968e-2
${}^{12}\text{C}_6{}^{13}\text{C}_1{}^1\text{H}_6$	91	${}^{13}\text{C}^{32}\text{S}$	${}^{12}\text{C}_6{}^{13}\text{C}_2{}^1\text{H}_6{}^{32}\text{S}$	2/8	7.1320e-4
${}^{12}\text{C}_5{}^{13}\text{C}_2{}^1\text{H}_6$	92	${}^{12}\text{C}^{32}\text{S}$	${}^{12}\text{C}_6{}^{13}\text{C}_2{}^1\text{H}_6{}^{32}\text{S}$	6/8	2.1396e-3
${}^{12}\text{C}_7{}^1\text{H}_5{}^2\text{H}_1$	91	${}^{13}\text{C}^{32}\text{S}$	${}^{12}\text{C}_7{}^{13}\text{C}_1{}^1\text{H}_5{}^2\text{H}_1{}^{32}\text{S}$	1/8	6.5006e-6
${}^{12}\text{C}_6{}^{13}\text{C}_1{}^1\text{H}_5{}^2\text{H}_1$	92	${}^{12}\text{C}^{32}\text{S}$	${}^{12}\text{C}_7{}^{13}\text{C}_1{}^1\text{H}_5{}^2\text{H}_1{}^{32}\text{S}$	7/8	4.5504e-5
${}^{12}\text{C}_7{}^1\text{H}_5{}^2\text{H}_1$	91	${}^{12}\text{C}^{33}\text{S}$	${}^{12}\text{C}_8{}^1\text{H}_5{}^2\text{H}_1{}^{33}\text{S}$	8/8	4.7455e-6
${}^{12}\text{C}_7{}^1\text{H}_4{}^2\text{H}_2$	92	${}^{12}\text{C}^{32}\text{S}$	${}^{12}\text{C}_8{}^1\text{H}_4{}^2\text{H}_2{}^{32}\text{S}$	8/8	1.7282e-7
${}^{12}\text{C}_7{}^1\text{H}_6$	90	${}^{13}\text{C}^{34}\text{S}$	m/z 137 ${}^{12}\text{C}_7{}^{13}\text{C}_1{}^1\text{H}_6{}^{34}\text{S}$	1/8	4.2148e-4
${}^{12}\text{C}_6{}^{13}\text{C}_1{}^1\text{H}_6$	91	${}^{12}\text{C}^{34}\text{S}$	${}^{12}\text{C}_7{}^{13}\text{C}_1{}^1\text{H}_6{}^{34}\text{S}$	7/8	2.9503e-3
${}^{12}\text{C}_6{}^{13}\text{C}_1{}^1\text{H}_6$	91	${}^{13}\text{C}^{33}\text{S}$	${}^{12}\text{C}_6{}^{13}\text{C}_2{}^1\text{H}_6{}^{33}\text{S}$	2/8	5.6310e-6
${}^{12}\text{C}_5{}^{13}\text{C}_2{}^1\text{H}_6$	92	${}^{12}\text{C}^{33}\text{S}$	${}^{12}\text{C}_6{}^{13}\text{C}_2{}^1\text{H}_6{}^{33}\text{S}$	6/8	1.6893e-5
${}^{12}\text{C}_7{}^1\text{H}_5{}^2\text{H}_1$	91	${}^{12}\text{C}^{34}\text{S}$	${}^{12}\text{C}_8{}^1\text{H}_5{}^2\text{H}_1{}^{34}\text{S}$	8/8	2.6891e-5
${}^{12}\text{C}_7{}^1\text{H}_5{}^2\text{H}_1$	91	${}^{13}\text{C}^{33}\text{S}$	${}^{12}\text{C}_7{}^{13}\text{C}_1{}^1\text{H}_5{}^2\text{H}_1{}^{33}\text{S}$	1/8	5.1326e-8
${}^{12}\text{C}_6{}^{13}\text{C}_1{}^1\text{H}_5{}^2\text{H}_1$	92	${}^{12}\text{C}^{33}\text{S}$	${}^{12}\text{C}_7{}^{13}\text{C}_1{}^1\text{H}_5{}^2\text{H}_1{}^{33}\text{S}$	7/8	3.5928e-7
${}^{12}\text{C}_5{}^{13}\text{C}_2{}^1\text{H}_6$	92	${}^{13}\text{C}^{32}\text{S}$	${}^{12}\text{C}_5{}^{13}\text{C}_3{}^1\text{H}_6{}^{32}\text{S}$	3/8	2.3141e-5
${}^{12}\text{C}_4{}^{13}\text{C}_3{}^1\text{H}_6$	93	${}^{12}\text{C}^{32}\text{S}$	${}^{12}\text{C}_5{}^{13}\text{C}_3{}^1\text{H}_6{}^{32}\text{S}$	5/8	3.8569e-5
${}^{12}\text{C}_6{}^{13}\text{C}_1{}^1\text{H}_5{}^2\text{H}_1$	92	${}^{13}\text{C}^{32}\text{S}$	${}^{12}\text{C}_6{}^{13}\text{C}_2{}^1\text{H}_5{}^2\text{H}_1{}^{32}\text{S}$	2/8	4.9218e-7
${}^{12}\text{C}_5{}^{13}\text{C}_2{}^1\text{H}_5{}^2\text{H}_1$	93	${}^{12}\text{C}^{32}\text{S}$	${}^{12}\text{C}_6{}^{13}\text{C}_2{}^1\text{H}_5{}^2\text{H}_1{}^{32}\text{S}$	6/8	1.4765e-6
${}^{12}\text{C}_7{}^1\text{H}_4{}^2\text{H}_2$	92	${}^{13}\text{C}^{32}\text{S}$	${}^{12}\text{C}_7{}^{13}\text{C}_1{}^1\text{H}_4{}^2\text{H}_2{}^{32}\text{S}$	1/8	1.8691e-9
${}^{12}\text{C}_6{}^{13}\text{C}_1{}^1\text{H}_4{}^2\text{H}_2$	93	${}^{12}\text{C}^{32}\text{S}$	${}^{12}\text{C}_7{}^{13}\text{C}_1{}^1\text{H}_4{}^2\text{H}_2{}^{32}\text{S}$	7/8	1.3084e-8
${}^{12}\text{C}_7{}^1\text{H}_4{}^2\text{H}_2$	92	${}^{12}\text{C}^{33}\text{S}$	${}^{12}\text{C}_8{}^1\text{H}_4{}^2\text{H}_2{}^{33}\text{S}$	8/8	1.3645e-9
${}^{12}\text{C}_7{}^1\text{H}_3{}^2\text{H}_3$	93	${}^{12}\text{C}^{32}\text{S}$	${}^{12}\text{C}_8{}^1\text{H}_3{}^2\text{H}_3{}^{32}\text{S}$	8/8	2.6502e-11

In order to calculate the contribution of each product ion to its particular peak in the product-ion spectrum, the fractional abundance of the precursor ion (Column T in Table 3.41) is multiplied by the number of ways that product ion can be formed out of the total ways all product ions can be formed from a given precursor ion (Column C in Table 3.42).

The fractional abundances of all species at a given mass are summed in order to get the overall contributions. Calculated peak ratios within and among product-ion mass spectra are listed in Table 3.43.

Table 3.43. Relative peak heights within and among product-ion mass spectra.

Precursor Ion <i>m/z</i>	Product Ion <i>m/z</i>	T	Within (%)	Among (%)
134	90	8.7096e-1	100.000	100.000
135	90	1.6297e-2	24.491	9.511
	91	6.6542e-2	100.000	
136	90	3.9043e-2	100.000	4.877
	91	1.2451e-3	3.189	
	92	2.1854e-3	5.597	
137	90	4.2148e-4	14.130	0.400
	91	2.9828e-3	100.000	
	92	4.0890e-5	1.371	
	93	4.0058e-5	1.343	

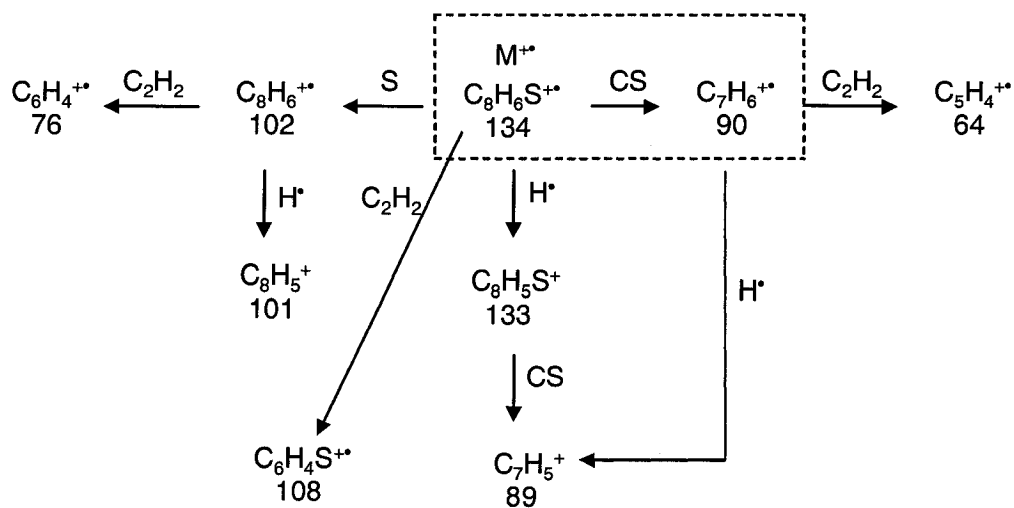
3.3.3.1. APCI(+)-MS/MS of Model Compounds

The fragmentation processes for BT, DBT, MDBT and DMDBT were studied by MS/MS in a QqQ instrument, and the results are reported here. In the majority of the cases, only the ions containing the most abundant isotopes (*i.e.* the monoisotopic peaks) were selected in the different MS/MS analyses.

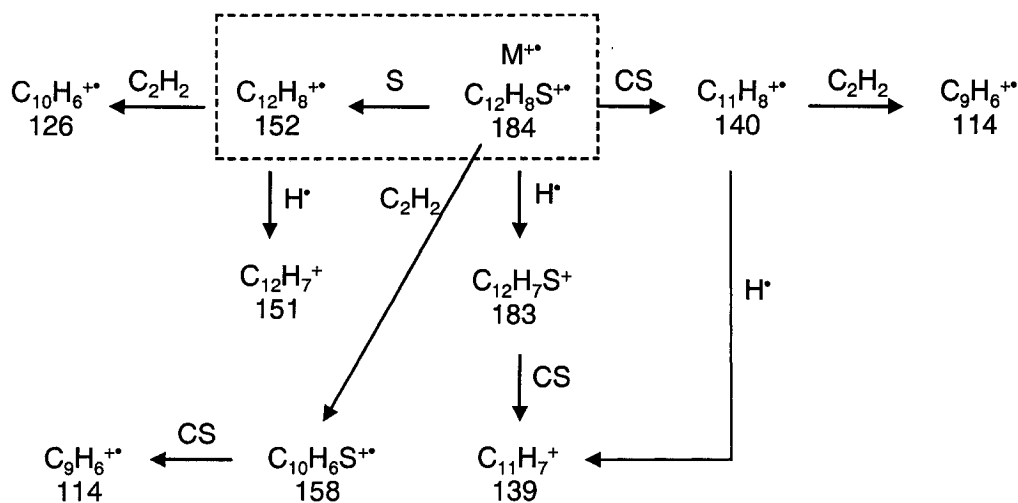
Fragmentation pathways observed for the model PASHs are shown in Schemes 3.1 to 3.4. In the schemes, the major fragmentations occurring in the APCI(+) ion source are delimited by boxes formed by broken lines.

The full-scan spectra of BT, DBT, MDBT and DMDBT are presented in Figures 3.39 I, 3.40 J, 3.41 L and 3.42 R, respectively. The M^{+} ions are observed in the mass spectra at *m/z* values that correspond to the integer for the

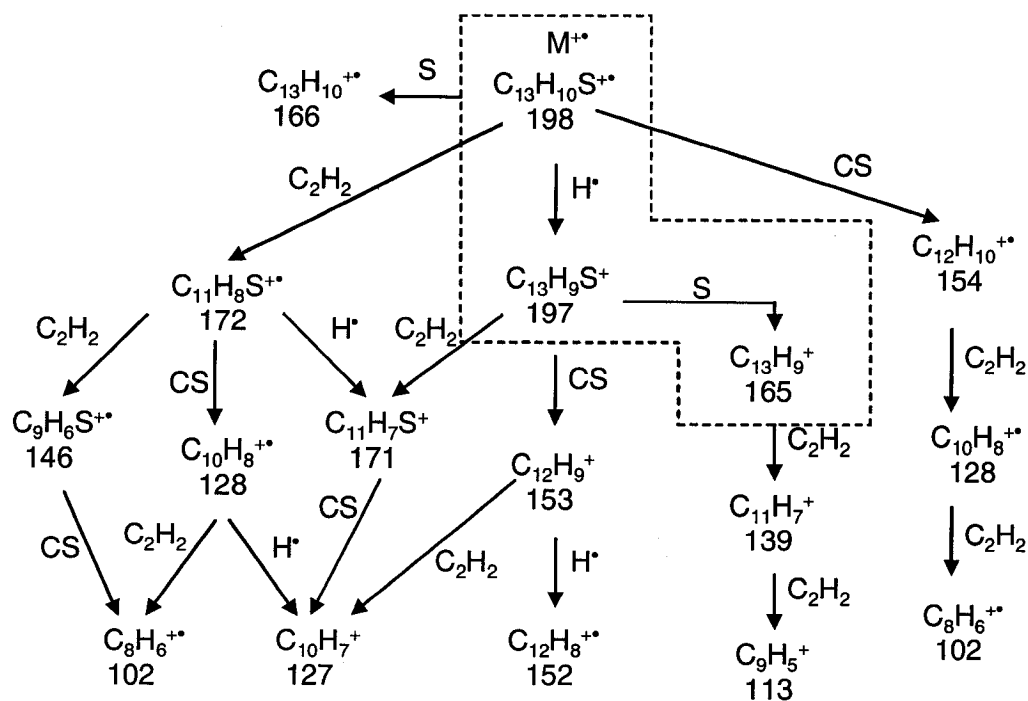
monoisotopic masses listed in Table 3.1, whilst the $[M - H]^+$ ions are detected at one mass unit less.



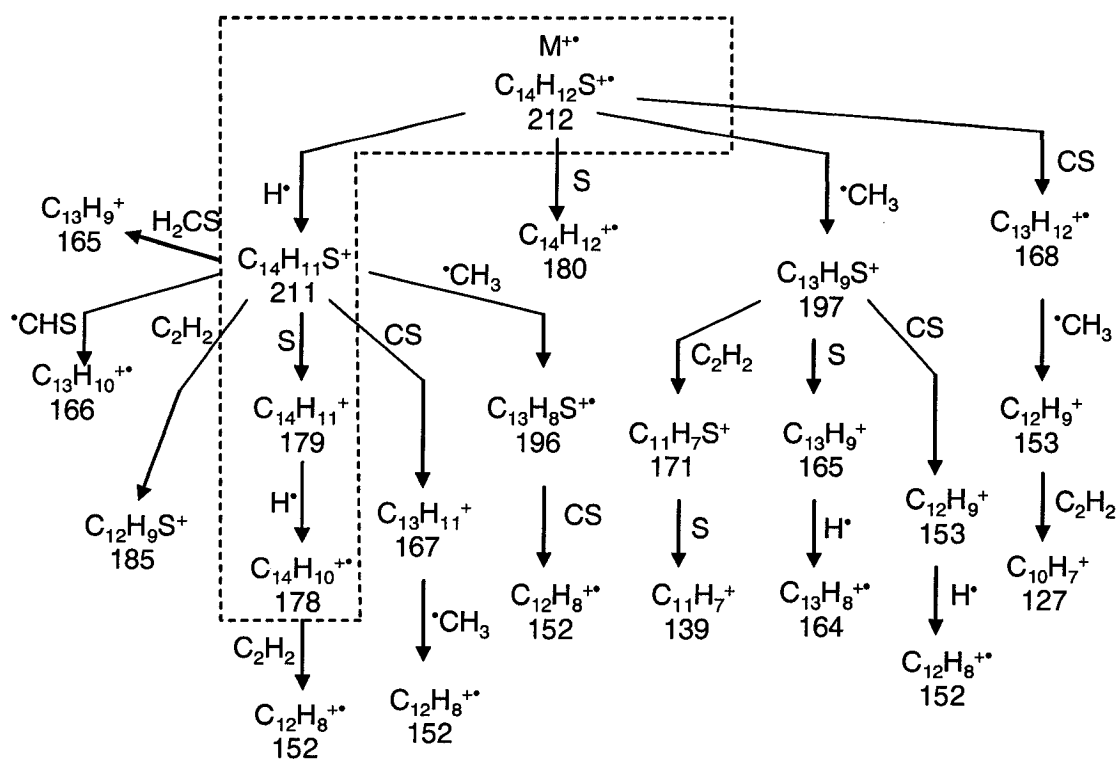
Scheme 3.1. Fragmentation pathways for BT.



Scheme 3.2. Fragmentation pathways for DBT.



Scheme 3.3. Fragmentation pathways for MDBT.



Scheme 3.4. Fragmentation pathways for DMDBT.

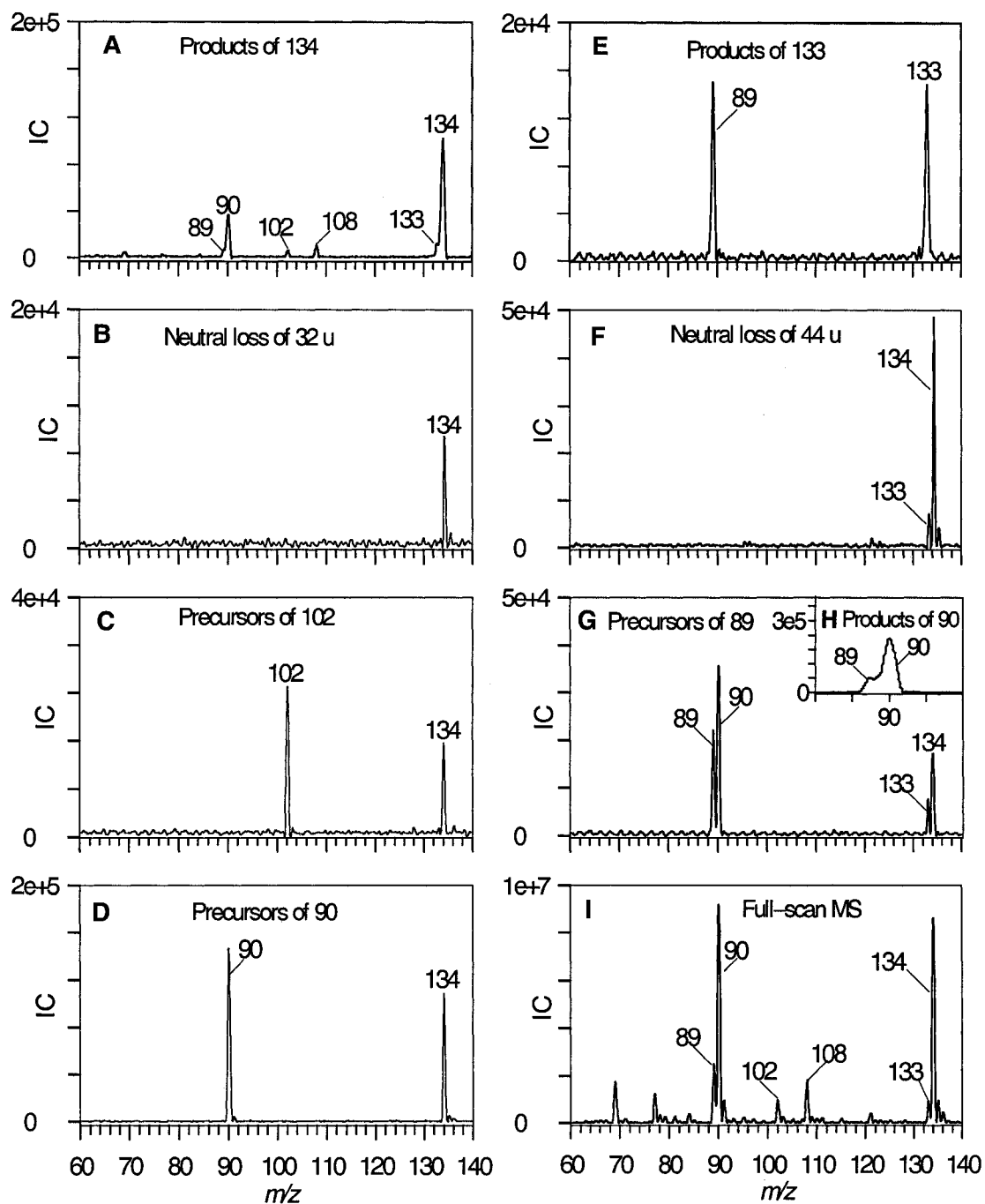


Figure 3.39. MS/MS and full-scan spectra of BT (IC: ion counts). Collision energy (eV) and cone voltage (V) for each experiment: 10, 55 (A); 10, 40 (B); 13, 43 (C); 11, 43 (D); 10, 50 (E); 10, 60 (F); 12, 43 (G); 10, 55 (H) and 50 V (I).

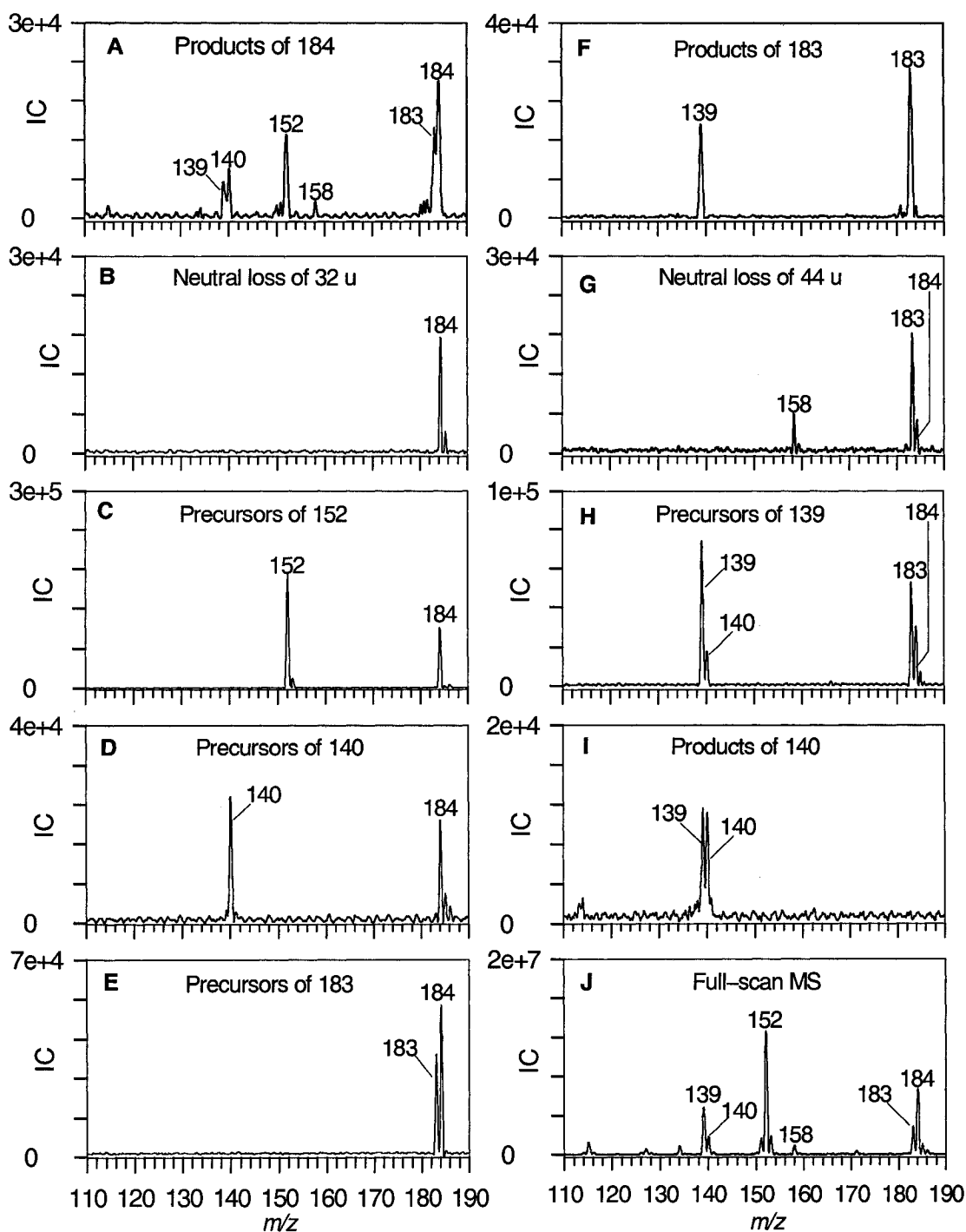


Figure 3.40. MS/MS and full-scan spectra of DBT (IC: ion counts). Collision energy (eV) and cone voltage (V) for each experiment: 15, 70 (A); 10, 40 (B); 20, 50 (C); 15, 55 (D); 10, 50 (E); 10, 50 (F); 10, 60 (G); 15, 55 (H); 20, 50 (I) and 60 V (J).

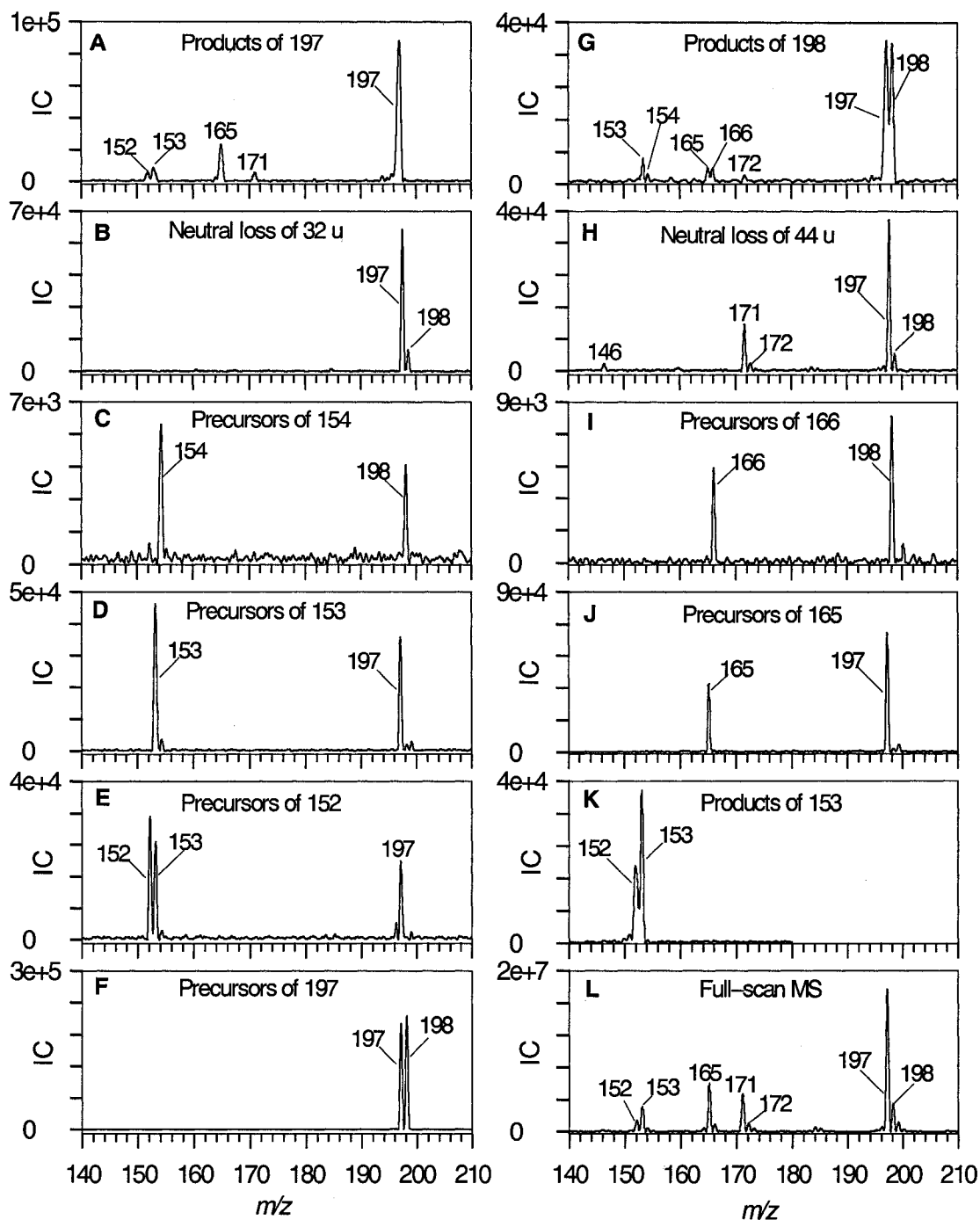


Figure 3.41. MS/MS and full-scan spectra of MDBT (IC: ion counts). Collision energy (eV) and cone voltage (V) for each experiment: 10, 60 (A); 15, 50 (B); 10, 60 (C); 10, 60 (D); 10, 60 (E), 10, 35 (F); 15, 45 (G); 15, 55 (H); 15, 50 (I); 15, 50 (J); 10, 60 (K) and 60 V (L).

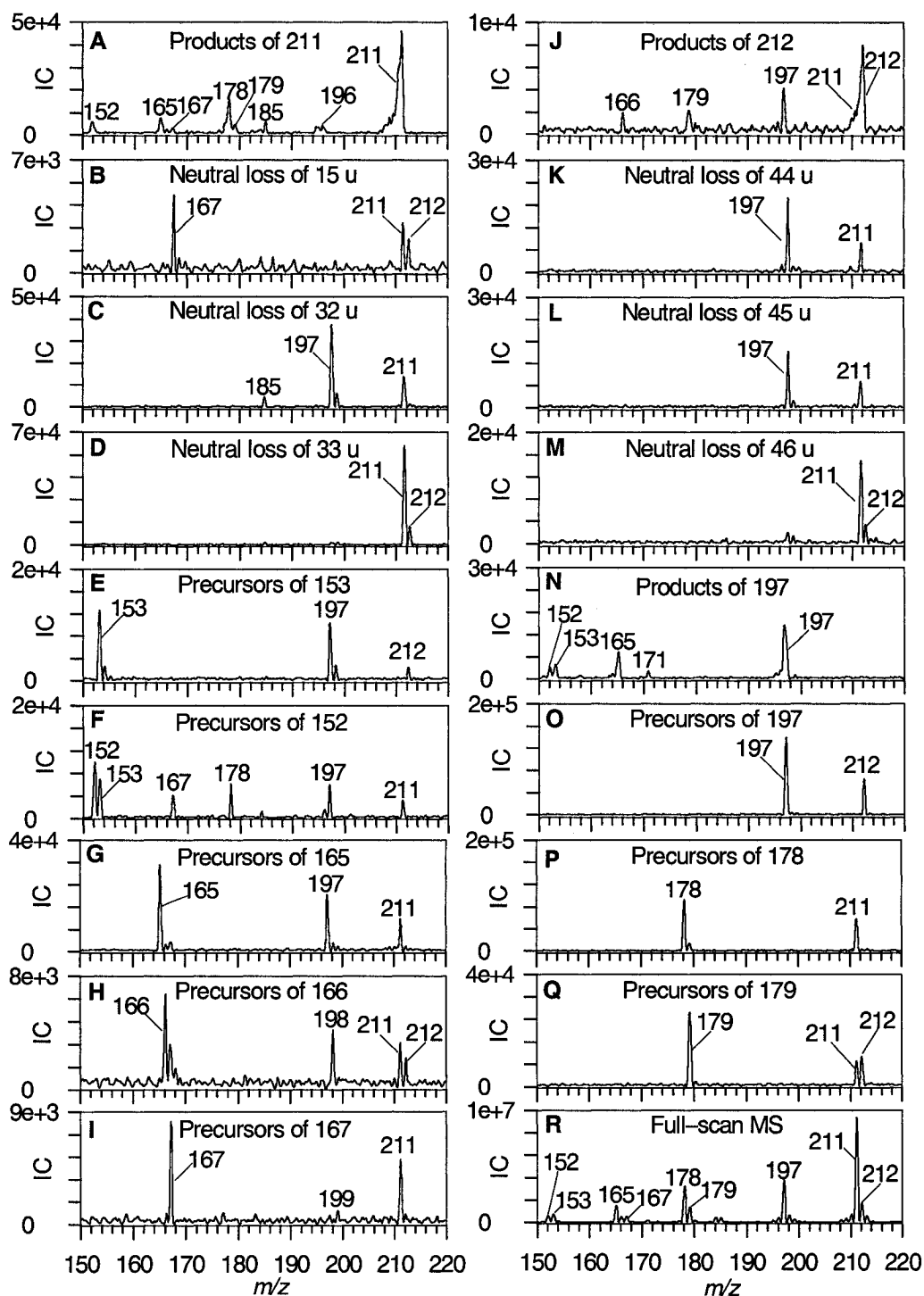


Figure 3.42. MS/MS and full-scan spectra of DMDBT. Collision energy (eV) and cone voltage (V): 20, 55 (A); 15, 60 (B); 20, 50 (C); 20, 50 (D); 10, 55 (E); 10, 55 (F); 15, 55 (G); 15, 55 (H); 15, 55 (I); 10, 60 (J); 20, 50 (K); 20, 50 (L); 20, 50 (M); 10, 60 (N); 15, 40 (O); 10, 55 (P); 10, 55 (Q) and 60 V (R).

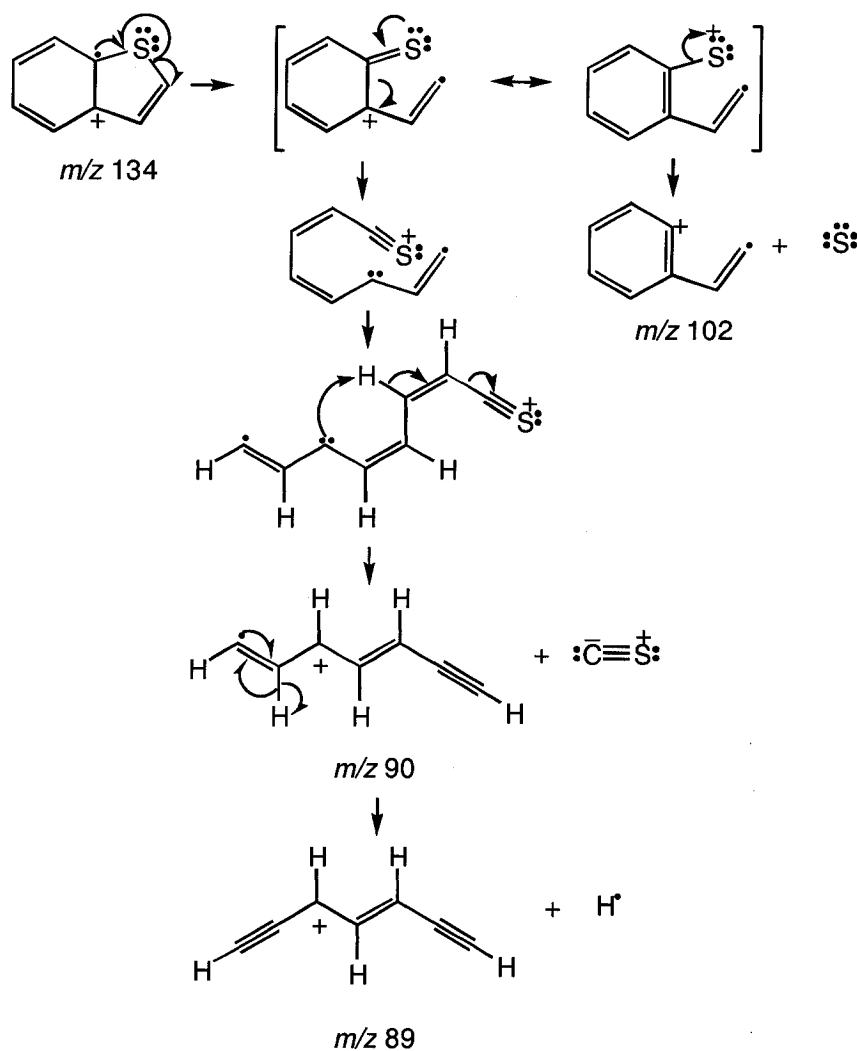
Model PASHs are ionized mainly by charge exchange. The major high mass species observed in the full-scan spectra of DBT and BT at different cone voltages was the $M^{+\bullet}$ ion (10 V–60 V). In the case of MDBT and DMDBT, $M^{+\bullet}$ was the main ion detected at lower cone voltages (10 V–40 V), while $[M - H]^+$ was the predominant species at higher cone voltages (50 V–60 V). In general, $M^{+\bullet}$ and $[M - H]^+$ ions fragmented to produce the neutral fragments S, CS, C_2H_2 and H^\bullet . However, the relative intensity of the product ions varied among spectra, giving rise to different fragmentation patterns for BT, DBT, MDBT and DMDBT.

Fragmentation pathways of the model compounds were confirmed by the results obtained in precursor-ion, product-ion and neutral loss mass spectra (Figures 3.39 to 3.42). Mechanisms for the formation of the major fragment ions observed in their mass spectra are shown in Schemes 3.5 to 3.11. All the proposed reactions are based on reasonable postulates but no additional studies were carried out to prove them. Mechanisms shown are those that involve the fewest number of steps and that produce ions in which the charge can be stabilized by conjugation. Given that the fragmentation behavior of these compounds becomes more complex in the order $BT < DBT < MDBT < DMDBT$, the fragmentation pattern of BT will be discussed first.

The peak at m/z 90 was the major fragment ion observed in the full-scan spectra of BT at different cone voltages (Figure 3.39 I). The product-ion of m/z 134 (Figure 3.39 A), the precursor-ion of m/z 90 (Figure 3.39 D) and the neutral loss of 44 u (Figure 3.39 F) mass spectra reveal that m/z 90 is formed from the $M^{+\bullet}$ ion of BT (m/z 134). The difference between the peaks detected at m/z 90 and 134 is 44 m/z which indicates the loss of CS from $M^{+\bullet}$. The neutral fragment CS also appears to be lost from the $[M - H]^+$ ion of BT (m/z 133) (Figures 3.39 E, F and G), though this fragmentation seems to be minor compared to the loss of CS from $M^{+\bullet}$ (Figure 3.39 F).

The fragmentation pathway that involves the loss of sulfur (32 u) from the $M^{+\bullet}$ ion of BT to produce the ion at m/z 102 is confirmed in the product-ion of m/z 134 (Figures 3.39 A), the neutral loss of 32 u (Figure 3.39 B) and the precursor-ion of m/z 102 (Figure 3.39 C) mass spectra, yet the loss of sulfur from

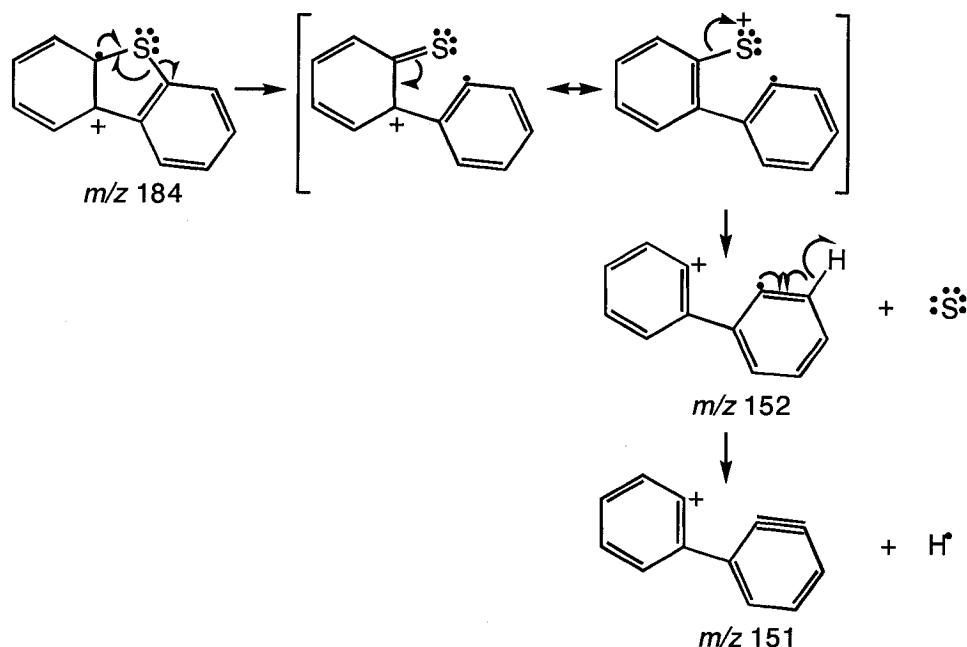
$M^{+\bullet}$ appears to be less significant than the loss of CS from the $M^{+\bullet}$ ion of BT given the much lower abundance of m/z 102 compared to m/z 90 (Figure 3.39 I). Possible fragmentation mechanisms leading to the ions observed at m/z 89, 90 and 102 for BT are shown in Scheme 3.5.



Scheme 3.5. Possible fragmentation mechanisms for BT.

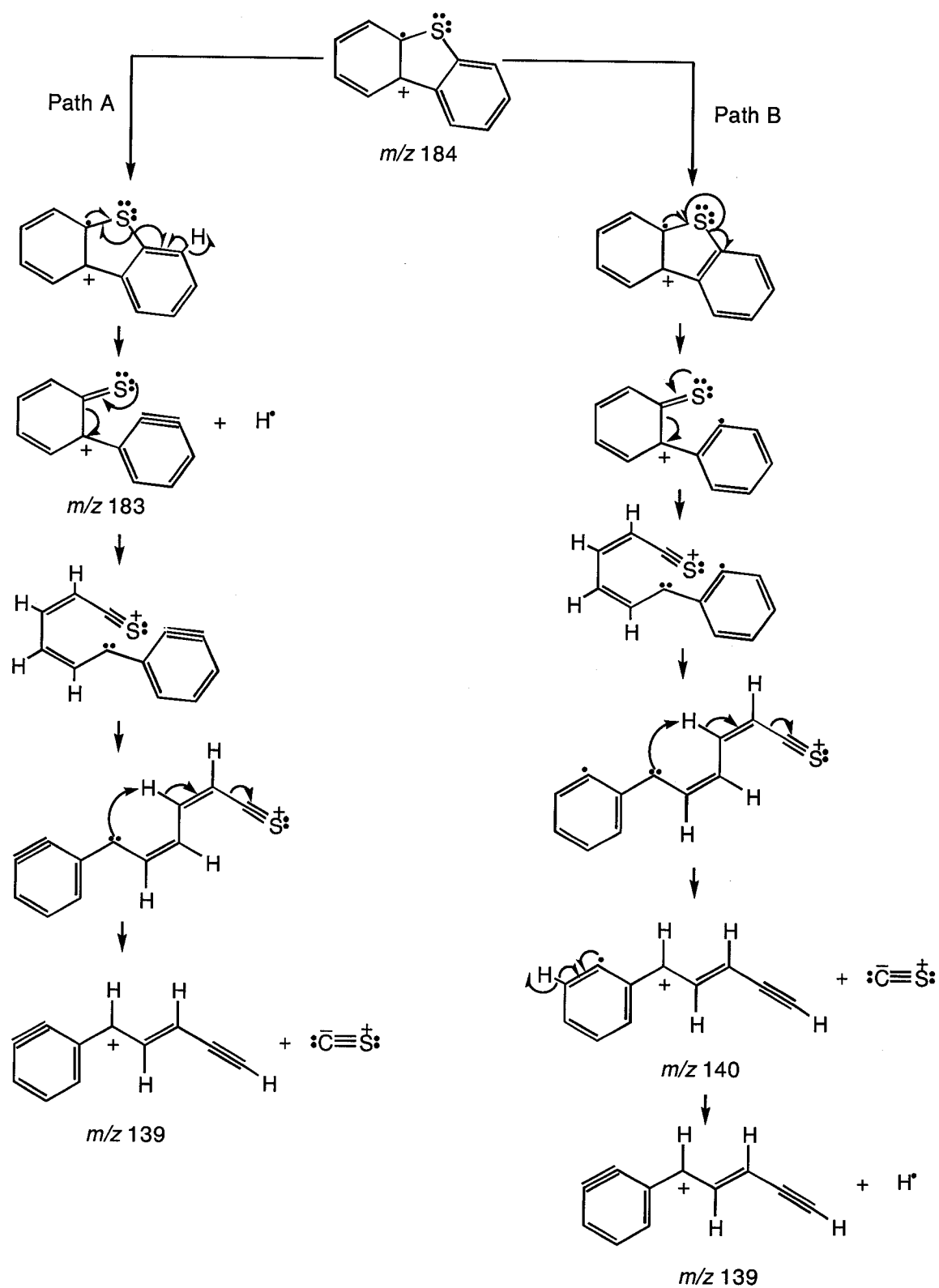
The main fragment ion in the full-scan spectra of DBT at different cone voltages is m/z 152, which indicates that sulfur (32 u) is the main neutral loss from DBT (Figure 3.40 J). The product-ion of m/z 184 (Figure 3.40 A), the neutral loss of 32 u (Figure 3.40 B) and the precursor-ion of m/z 152 (Figure 3.40 C) mass spectra confirm that sulfur is lost from the $M^{+\bullet}$ ion of DBT (m/z 184). A

possible fragmentation mechanism that explains the formation of the ions observed at m/z 152 and 151 is displayed in Scheme 3.6.



Scheme 3.6. Possible fragmentation reaction for DBT involving the loss of sulfur.

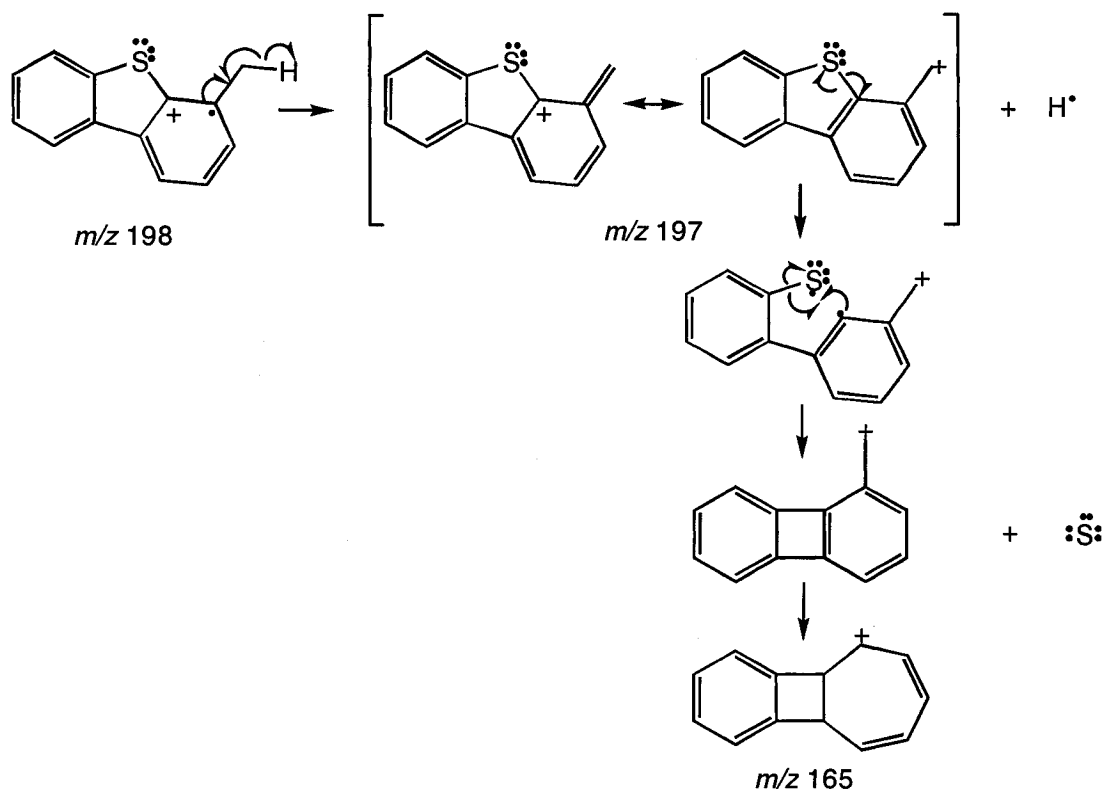
The second major fragment ion in the full-scan spectrum of DBT is observed at m/z 139 (Figure 3.40 J), which corresponds to the loss of CS from the $[\text{M} - \text{H}]^+$ ion of DBT (m/z 183) (Figures 3.40 F, G and H). The $[\text{M} - \text{H}]^+$ ion is formed by the loss of H^\bullet from the $\text{M}^{+\bullet}$ ion of DBT (Figures 3.40 A and E). A minor fragment ion at m/z 140, which is about 30 % of the peak at m/z 139 is also observed in Figure 3.40 J. The experimental 140 to 139 ratio (30 %) is higher than the theoretical value of 12 % based on natural isotopic abundances, indicating that about 18/30 (or 60 %) of the peak at m/z 140 is a fragment ion. Mass spectra in Figures 3.40 A, F and H show that the fragment at m/z 140 probably forms by the loss of CS from the $\text{M}^{+\bullet}$ ion of DBT. MS/MS scans show that the ion observed at m/z 139 can be formed from both m/z 140 and 183. Two possible routes (path A and path B) that could explain the formation of m/z 139 are shown in Scheme 3.7.



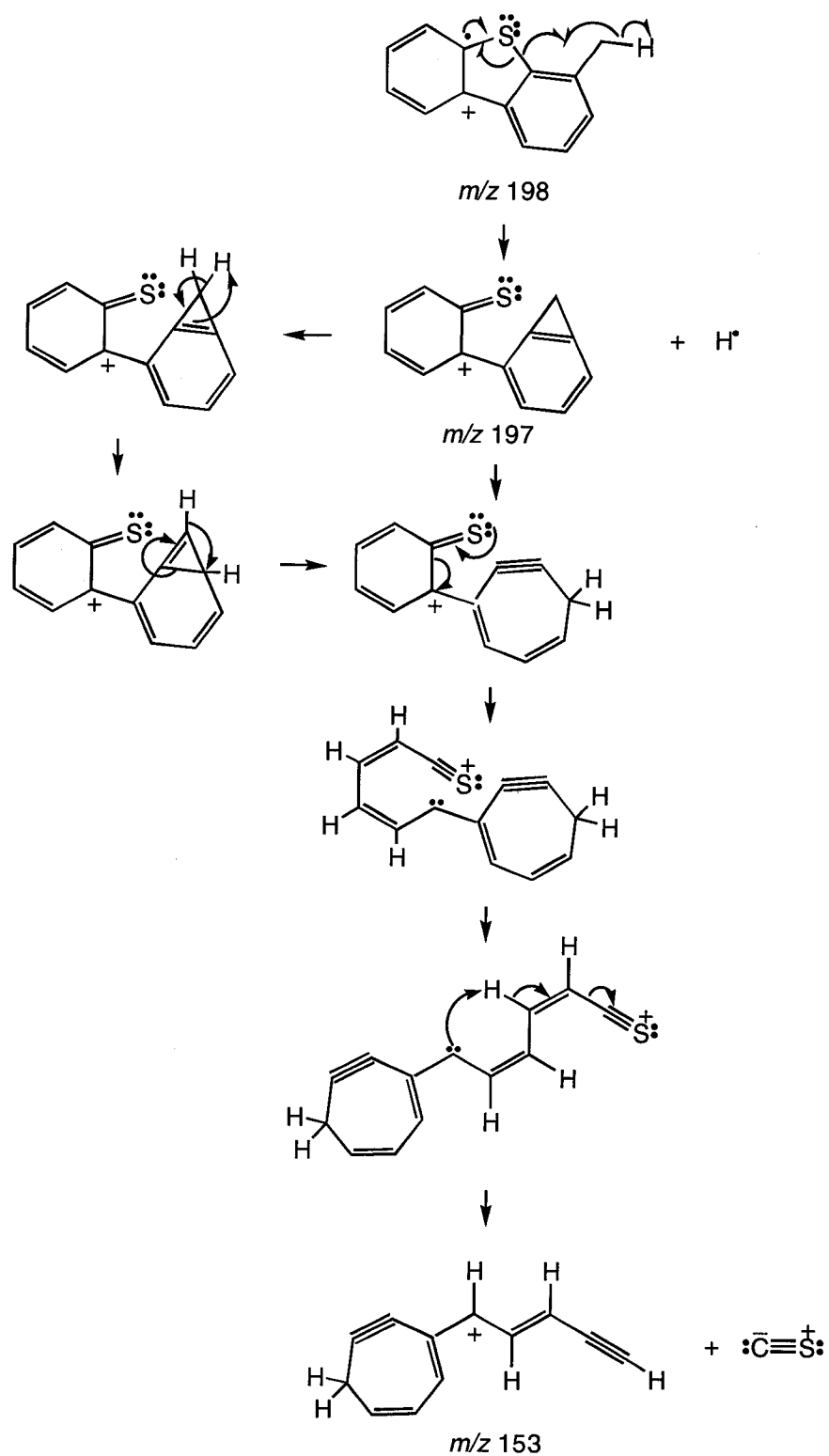
Scheme 3.7. Possible fragmentation pathways for DBT leading to the ions at m/z 183, 140 and 139.

As explained above, CS may be lost from both the $M^{+\bullet}$ and $[M - H]^+$ ions of DBT. Since, the neutral loss of 44 u mass spectrum (Figure 3.40 G) reveals that CS is mainly lost from the $[M - H]^+$ ion, path A (Scheme 3.7) is probably a more favored mechanism for the formation of the ion at m/z 139. For BT, which does not have a third fused ring, CS seems to be lost mainly from $M^{+\bullet}$ as opposed to $[M - H]^+$, even though the loss of CS from $[M - H]^+$ would involve one step less. Therefore, the major fragmentation path to produce the ion observed at m/z 89 in the spectra of BT is probably path B, rather than route A used by DBT.

The full-scan spectrum of MDBT at 60 V cone (Figure 3.41 L) reveals that m/z 165 and 153 are the two major product ions formed by the loss of neutral fragments containing sulfur. The ion observed at m/z 165 is produced by the loss of S from the $[M - H]^+$ ion of MDBT (Figures 3.41 A, J and B). The $[M - H]^+$ ion is generated from the $M^{+\bullet}$ of MDBT (Figures 3.41 F and G), most probably by benzylic bond cleavage. A possible fragmentation pathway that explains the formation of the ion at m/z 165 is shown in Scheme 3.8.



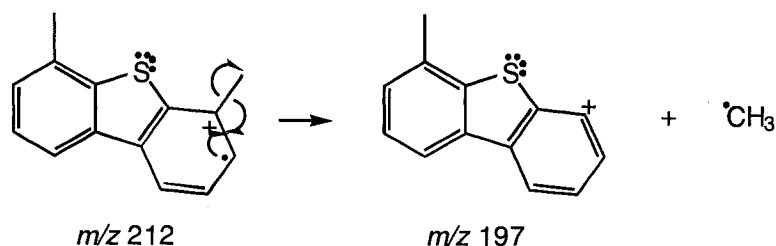
Scheme 3.8. Possible fragmentation pathway leading to m/z 165 for MDBT.



Scheme 3.9. Possible fragmentation pathway leading to m/z 153 for MDBT.

The fragment ion observed at m/z 153 is probably formed by the loss of CS from the $[M - H]^+$ peak (Figures 3.41 A, H and D). A plausible fragmentation mechanism for the formation of m/z 153 is shown in Scheme 3.9. This mechanism is very similar to that previously shown for DBT (path A in Scheme 3.7). The neutral fragments S and CS seem to be also lost from the $M^{+\bullet}$ of MDBT to generate the ions at m/z 154 and 166, respectively (Figures 3.41 C, I and G), yet these appear to be minor fragmentations.

The fragmentation processes for DMDBT are more complicated than those for BT and DBT and somewhat similar to MDBT. The $M^{+\bullet}$ ion of DMDBT (m/z 212) loses a hydrogen atom, probably by benzylic C–H bond cleavage, to produce $[M - H]^+$ at m/z 211 (Figure 3.42 J) and this is the most abundant fragment ion in the full-scan mass spectra of DMDBT (Figure 3.42 R). A methyl radical (15 u) is also lost from $M^{+\bullet}$ to yield a relatively abundant m/z 197 ion (Figures 3.42 J and O). However, the loss of hydrogen from $M^{+\bullet}$ by benzylic bond cleavage is more favorable than the loss of methyl radical from $M^{+\bullet}$ by phenylic bond cleavage (Scheme 3.10).



Scheme 3.10. Cleavage of the phenylic bond in DMDBT to form ion at m/z 197.

The benzyl cation (m/z 211) is more abundant than the phenyl cation (m/z 197) because the former is more stable. The positive charge on the phenyl ion is located in an empty sp^2 orbital lying in the plane of the ring and can not be resonance-stabilized since it does not overlap with the p -orbitals forming the π -bonds of the ring. The $[M - H]^+$ species of unalkylated PASHs form by phenylic

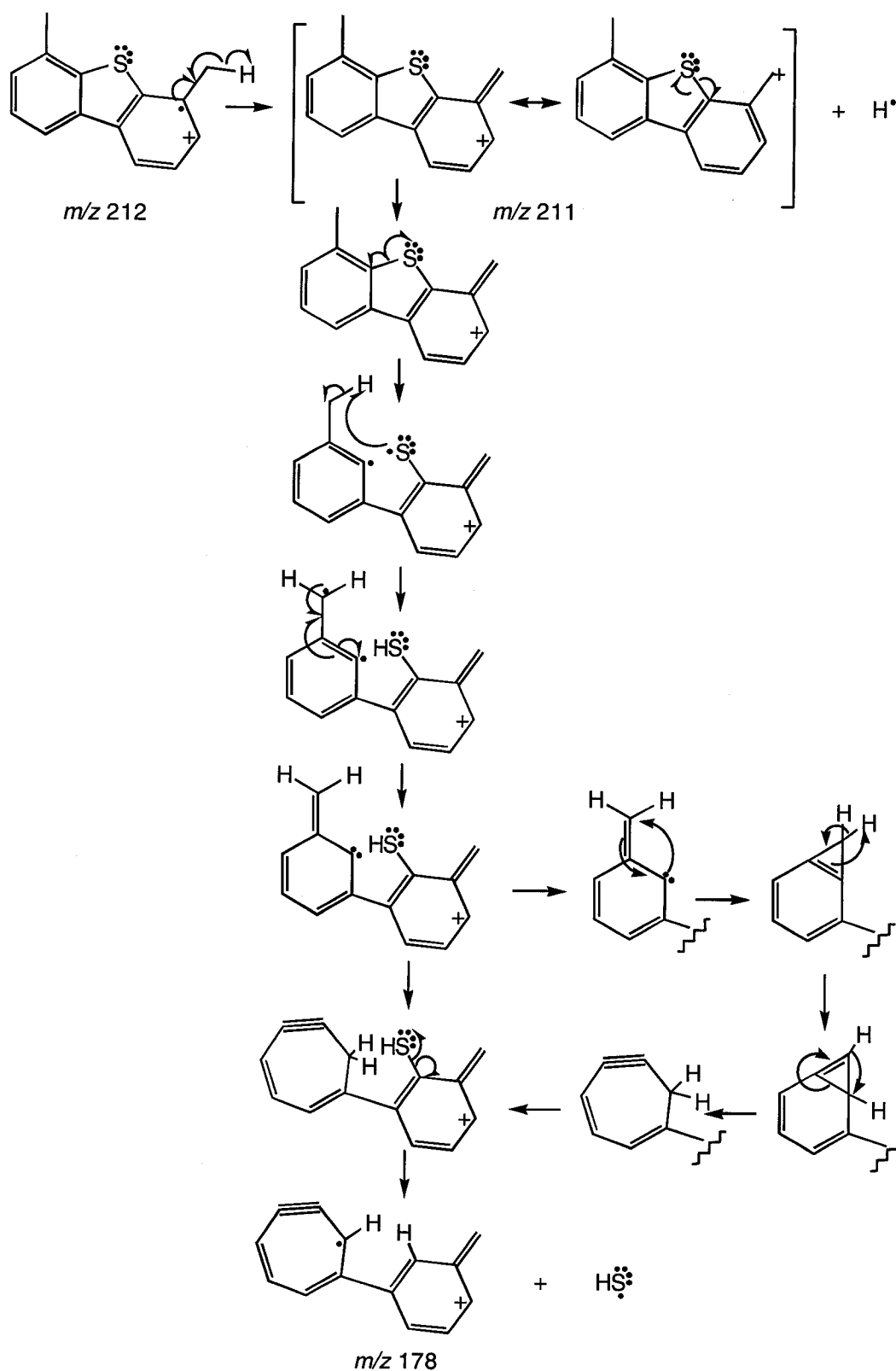
bond cleavage and this would also explain the much lower abundance of $[M - H]^+$ ions in the mass spectra of DBT and BT.

A methyl radical may be also lost from the $[M - H]^+$ ion (Figure 3.42 A and B), yet the loss of $\cdot\text{CH}_3$ from $M^{+\bullet}$ is much more favorable. The ion at m/z 197 formed by the loss of $\cdot\text{CH}_3$ from the $M^{+\bullet}$ peak of DMDBT fragments in a similar fashion to m/z 197 derived by the loss of hydrogen from the $M^{+\bullet}$ ion of MDBT (Figures 3.42 N and 3.41 A). In addition to the losses of H^\bullet and $\cdot\text{CH}_3$, the $M^{+\bullet}$ of DMDBT may also lose HS^\bullet (33 u) and H_2CS (46 u) to generate the ions observed at m/z 179 and m/z 166.

Ions detected at m/z 179 and 178 are formed by the loss of S (Figure 3.42 A, C and Q) and HS^\bullet (Figures 3.42 A, D and P), respectively, from $[M - H]^+$. The $[M - H]^+$ ion also appears to lose CS (Figures A, I and K), $\cdot\text{CHS}$ (Figures A, L and H) and H_2CS (Figures A, G and M). The second major product ion in the full-scan spectrum of DMDBT is m/z 165, which could arise by loss of H_2CS from $[M - H]^+$ (m/z 211) and/or loss of S from $[M - \text{CH}_3]^+$ (m/z 197).

A major fragmentation process for DMDBT appears to be the loss of HS^\bullet from $[M - H]^+$ to produce m/z 178. The decomposition of an even-electron ion, $[M - H]^+$, to produce an odd-electron ion and a radical, HS^\bullet , is not commonly observed because the fragmentation involves the separation of an electron pair, which is energetically unfavorable (McLafferty and Tureček 1993, p 55). Although unusual, the loss of HS^\bullet from the $[M - H]^+$ ion of DMDBT was observed in the present work and has been previously reported by Rudzinski and co-workers (Rudzinski *et al.* 2003).

Scheme 3.11 shows a possible fragmentation pathway leading to m/z 178. The loss of a radical from an even-electron ion may occur in some cases, for example, when a very stable ion is formed (Gross 2004, p 227). The fragmentation mechanism in Scheme 3.11 proposes that 178 could be stabilized due to delocalization of the positive charge on one ring and the radical site on the other.



Scheme 3.11. Possible fragmentation pathways for the formation of the ion at m/z 178 for DMDBT.

3.3.3.2. SRM Experiments

Taking into account natural isotopic abundance ratios in product-ion, precursor-ion and neutral loss mass spectra could further confirm fragmentation pathways. If the fragmentation process involves the loss of sulfur, then the use of natural isotopic ratios could permit the identification of sulfur-containing compounds in complex mixtures with greater certainty. The use of natural abundance ratios in the different types of MS/MS analyses will be illustrated using two compounds that lose neutral fragments containing sulfur very easily and in a clean way, *i.e.* very little loss of H⁺ occurs along with the loss of the sulfur-containing neutral fragment. The selected compounds are TA and MA.

The full-scan spectra of TA (Figures 3.43 D) shows that TA ionizes by charge exchange. The major neutral loss from the M⁺ ion of TA (m/z 216) is 32 u, most probably sulfur. TA, which has two sulfur atoms, shows two sequential losses of 32 u (Figure 3.43 C). The loss of sulfur from the M⁺ ion of TA generates the product ion at m/z 184 (Figures 3.42 A and B), and this is the major fragmentation pathway for TA.

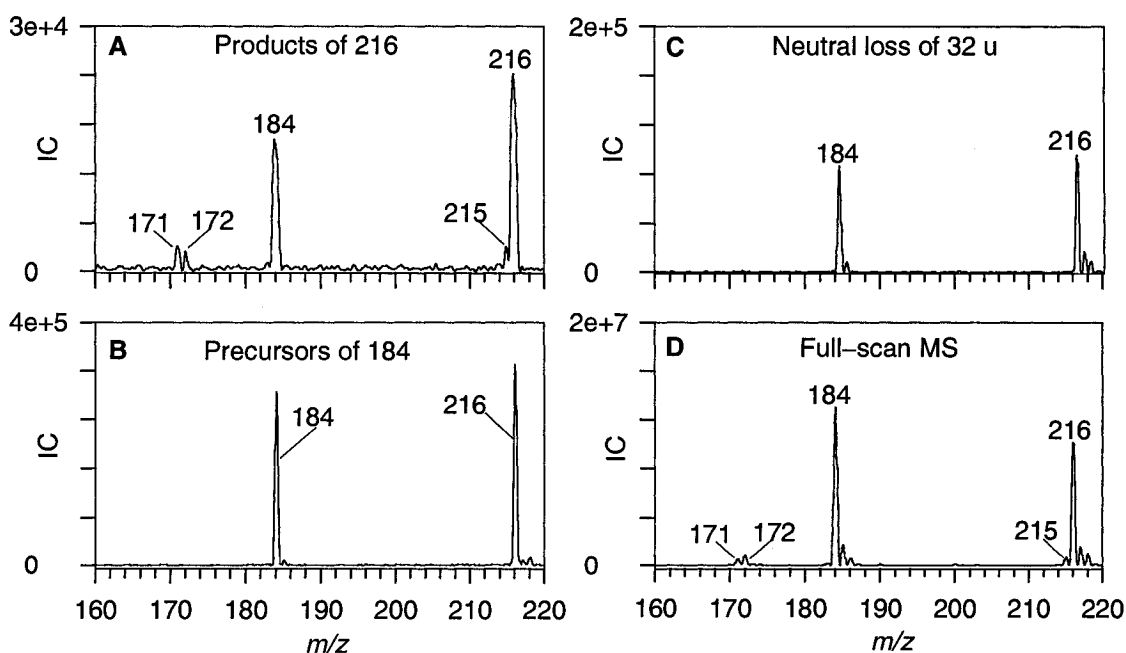


Figure 3.43. MS/MS and full-scan spectra of TA. Collision energy (eV) and cone voltage (V) for each experiment: 10, 60 (A); 20, 35 (B); 15, 55 (C) and 40 V (D).

MA, on the other hand, ionizes mainly by proton transfer (Figure 3.44 D). The major fragment ion observed in the full-scan spectrum of MA is m/z 94. The ion at m/z 94 is formed by the loss of 74 u (C_2H_2OS) from the MH^+ peak (m/z 168) of MA (Figures 3.44 A, B and C). As shown in the figures, 74 u is the major loss from MA.

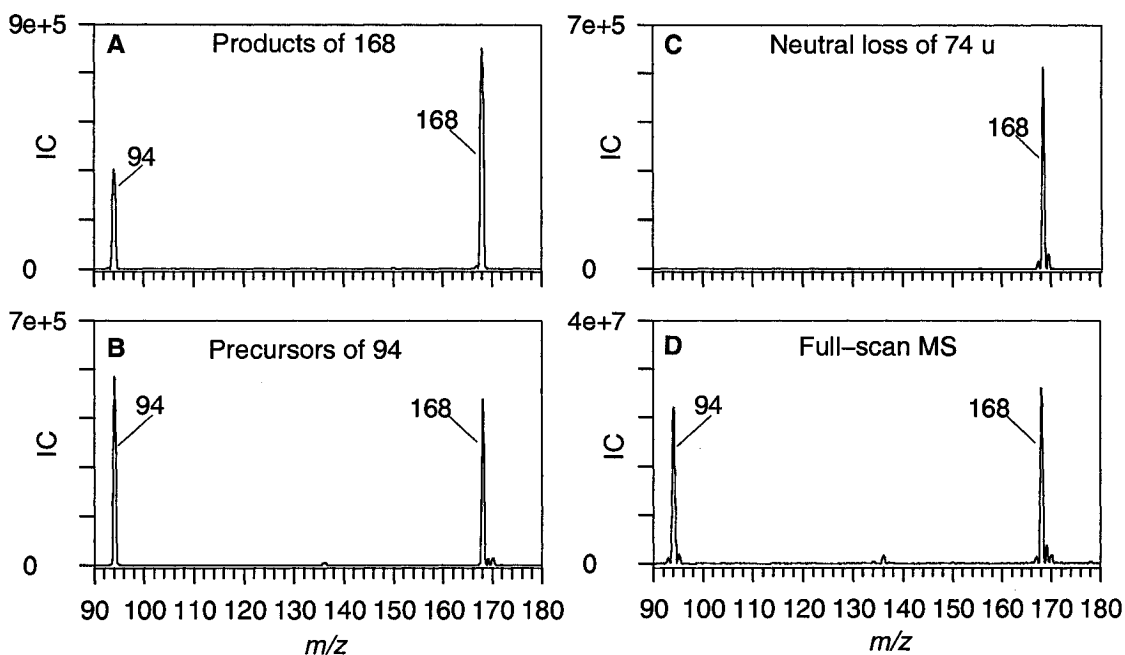


Figure 3.44. MS/MS and full-scan spectra of MA. Collision energy (eV) and cone voltage (V) for each experiment: 5, 25 (A); 5, 15 (B); 5, 20 (C) and 20 V (D).

SRM experiments were performed in a QqQ instrument to calculate peak height ratios in MS/MS spectra to confirm the fragmentation pathways $M^{+*} \rightarrow [M - 32]^{+*}$ for TA, and $MH^+ \rightarrow [M + H - 74]^+$ for MA. The theoretical and experimental abundance ratios for each MS/MS scan are displayed in Tables 3.44 to 3.49. Theoretical values can be calculated using (3.4), (3.5), (3.6) and (3.7). However, the values reported here were obtained using the program *IC Wizard* written by Dr. Louis Ramaley and that can be downloaded from: http://tarc.chemistry.dal.ca/soft_down.htm (access date: April 23, 2007). This program uses these equations in providing the results. The program *IC Wizard* is based on a treatment which considers combinations whereas the method developed by Rockwood (Rockwood *et al.* 2003) uses a matrix approach.

Table 3.44. Theoretical (T) and experimental (E) abundance ratios (%) within and among neutral loss spectra for TA (10 eV and 35 V cone).

MS/MS scan	Q1 (m/z)	Q3 (m/z)	Within Spectrum		Among Spectra	
			T	E (n = 5)	T	E (n = 5)
NL 32 u (³² S)	216	184	100.00	100.00	100.00	100.0
	217	185	13.86	14.07±0.08		
	218	186	5.36	5.17±0.06		
	219	187	0.62	0.60 ±0.02		
NL 33 u (³³ S)	217	184	100.00	100.0	0.79	1.8 ± 0.1
	218	185	13.86	25.9 ± 0.8		
	219	186	5.36	6 ± 1		
	220	187	0.62	1.2 ± 0.7		
NL 34 u (³⁴ S)	218	184	100.00	100.00	4.47	4.5 ± 0.1
	219	185	13.86	13 ± 1		
	220	186	5.36	4.6 ± 0.5		
	221	187	0.62	0.0		

Table 3.45. Theoretical (T) and experimental (E) abundance ratios (%) within and among product-ion spectra for TA (5 eV and 35 V cone).

MS/MS scan	Q1 (m/z)	Q3 (m/z)	Within Spectrum		Among Spectra	
			T	E (n = 5)	T	E (n = 5)
Products of 216	216	184	100.00	100.0	100.00	100.0
Products of 217	217	184	5.70	9.5 ± 0.3	14.65	15.4 ± 0.5
	217	185	100.00	100.0		
Products of 218	218	184	83.45	84 ± 3	9.94	9.9 ± 0.2
	218	185	2.04	4.7 ± 0.8		
	218	186	100.00	100.0		
Products of 219	219	184	0.00	1 ± 1	1.28	1.3 ± 0.1
	219	185	100.00	100		
	219	186	6.83	7 ± 1		
	219	187	99.91	99 ± 2		

Table 3.46. Theoretical (T) and experimental (E) abundance ratios (%) within and among precursor-ion spectra for TA (10 eV and 35 V cone).

MS/MS scan	Q1 (m/z)	Q3 (m/z)	Within Spectrum		Among Spectra	
			T	E (n = 5)	T	E (n = 5)
Precursors of 184	216	184	100.00	100.00	100.0	100.0
	217	184	0.79	1.8 ± 0.1		
	218	184	4.47	4.5 ± 0.1		
	219	184	0.00	0.06 ± 0.01		
Precursors of 185	217	185	100.00	100.0	13.86	14.1 ± 0.1
	218	185	0.79	3.4 ± 0.2		
	219	185	4.47	4.3 ± 0.3		
	220	185	0.00	0.3 ± 0.2		
Precursors of 186	218	186	100.00	100.00	5.36	5.2 ± 0.1
	219	186	0.79	0.9 ± 0.5		
	220	186	4.47	3.4 ± 0.4		
	221	186	0.00	0.0		
Precursors of 187	219	187	100.00	100	0.62	0.60 ± 0.02
	220	187	0.79	0.0		
	221	187	4.47	0.0		
	222	187	0.00	0.0		

Table 3.47. Theoretical (T) and experimental (E) abundance ratios (%) within and among product-ion spectra for MA (10 eV and 25 V cone).

MS/MS scan	Q1 (m/z)	Q3 (m/z)	Within Spectrum		Among Spectra	
			T	E (n = 5)	T	E (n = 5)
Products of 168	168	94	100.00	100.00	100.00	100.0
Products of 169	169	94	43.38	45.4 ± 0.4	9.96	10.4 ± 0.2
	169	95	100.00	100.0		
Products of 170	170	94	100.00	100.0	5.12	5.2 ± 0.1
	170	95	4.44	4.5 ± 0.4		
	170	96	4.36	4.4 ± 0.2		
Products of 171	171	94	32.32	32 ± 3	0.44	0.4 ± 0.1
	171	95	100.00	100		
	171	96	1.89	0.0		
	171	97	1.03	0.0		

Table 3.48. Theoretical (T) and experimental (E) abundance ratios (%) within and among neutral loss spectra for MA (5 eV and 15 V cone).

MS/MS scan	Q1 (m/z)	Q3 (m/z)	Within Spectrum		Among Spectra	
			T	E (n = 5)	T	E (n = 5)
NL 74 u	168	94	100.00	100.00	100.0	100.0
	169	95	6.95	6.96±0.04		
	170	96	0.21	0.22±0.01		
	171	97	0.00	0.01±0.01		
NL 75 u	169	94	100.00	100.0	3.01	3.1 ± 0.1
	170	95	6.95	7.6 ± 0.4		
	171	96	0.21	0.5 ± 0.2		
	172	97	0.00	0.2 ± 0.2		
NL 76 u	170	94	100.00	100.00	4.71	4.55 ± 0.05
	171	95	6.95	6.8 ± 0.4		
	172	96	0.21	0.2 ± 0.1		
	173	97	0.00	0.03 ± 0.06		
NL 77 u	171	94	100.00	100	0.11	0.11±0.01
	172	95	6.95	0.0		
	173	96	0.21	0.0		
	174	97	0.00	0.0		

Table 3.49. Theoretical (T) and experimental (E) abundance ratios (%) within and among precursor-ion spectra for MA (10 eV and 20 V cone).

MS/MS scan	Q1 (m/z)	Q3 (m/z)	Within Spectrum		Among Spectra	
			T	E (n = 5)	T	E (n = 5)
Precursors of 94	168	94	100.00	100.00	100.0	100.0
	169	94	3.01	3.21 ± 0.04		
	170	94	4.71	4.70 ± 0.04		
	171	94	0.11	0.13 ± 0.01		
Precursors of 95	169	95	100.00	100.0	6.95	6.96 ± 0.04
	170	95	3.01	3.4 ± 0.2		
	171	95	4.71	4.9 ± 0.1		
	172	95	0.11	0.3 ± 0.1		
Precursors of 96	170	96	100.00	100.00	0.21	0.22 ± 0.01
	171	96	3.01	2.5 ± 0.7		
	172	96	4.71	3.1 ± 0.8		
	173	96	0.11	0.0		
Precursors of 97	171	97	0.0	0.0	0.00	0.01 ± 0.01
	172	97	0.0	0.0		
	173	97	0.0	0.0		
	174	97	0.0	0.0		

Table 3.50. Experimental (E) abundance ratios (%) within and among product-ion spectra for MA at 10 eV and 20 eV collision energy (25 V cone).

MS/MS scan	Q1 (m/z)	Q3 (m/z)	Within Spectrum (n = 5)		Among Spectra (n = 5)	
			E (10 eV)	E (20 eV)	E (10 eV)	E (20 eV)
Products of 168	168	94	100.0	100.0	100.0	100.0
Products of 169	169	94	45.4 ± 0.4	55 ± 2	10.4 ± 0.2	10.9 ± 0.1
	169	95	100.0	100		
Products of 170	170	94	100.0	100.0	5.2 ± 0.1	5.3 ± 0.1
	170	95	4.5 ± 0.4	5.2 ± 0.3		
	170	96	4.4 ± 0.2	4.5 ± 0.2		
Products of 171	171	94	32 ± 3	42 ± 2	0.4 ± 0.1	0.6 ± 0.1
	171	95	100.0	100		
	171	96	0.0	0.0		
	171	97	0.0	0.0		

Table 3.51. Experimental (E) abundance ratios (%) within and among precursor-ion spectra for TA at 10 eV and 20 eV collision energy (35 V cone).

MS/MS scan	Q1 (m/z)	Q3 (m/z)	Within Spectrum (n = 5)		Among Spectra (n = 5)	
			E (10 eV)	E (20 eV)	E (10 eV)	E (20 eV)
Precursors of 184	216	184	100.00	100.0	100.0	100.0
	217	184	1.8 ± 0.1	3.4 ± 0.1		
	218	184	4.5 ± 0.1	4.7 ± 0.1		
	219	184	0.06±0.01	0.14±0.03		
Precursors of 185	217	185	100.0	100.0	14.1±0.1	14.1±0.1
	218	185	3.4 ± 0.2	7.4 ± 0.4		
	219	185	4.3 ± 0.3	4.4 ± 0.4		
	220	185	0.3 ± 0.2	0.4 ± 0.4		
Precursors of 186	218	186	100.00	100.0	5.2 ± 0.1	5.2 ± 0.1
	219	186	0.9 ± 0.5	2.7 ± 0.2		
	220	186	3.4 ± 0.4	3.9 ± 0.3		
	221	186	0.0	0.0		
Precursors of 187	219	187	100	100	0.60±0.02	0.61±0.02
	220	187	0.0	0.0		
	221	187	0.0	0.0		
	222	187	0.0	0.0		

The agreement between theoretical and experimental abundance ratios in Tables 3.44 through 3.49 is reasonably good for each type of MS/MS analysis. Major discrepancies are shown in bold characters in the tables. Although the values in bold differ from theory, the expected trends are still observed. Furthermore, the agreement between the experimental and theoretical values deteriorates at higher collision energies (20 eV) as shown in Tables 3.50 and 3.51 (note that values reported in Tables 3.44 to 3.49 were obtained at either 5 or 10 eV collision energy). In order to explain the differences observed between experiment and theory, the collision induced dissociation process (CID) will be reviewed first.

The overall CID process is assumed to have two steps (Douglas 1982). The first step corresponds to the collision between the ion and the target **(25)**. During this process (very fast 10^{-14} to 10^{-16} s) a fraction of the kinetic energy of the precursor ion (m_p^+) is converted to internal energy, bringing the ion into an excited state (m_p^{+*}). The second step involves the unimolecular decomposition of the activated ion to a product ion (m_f^+) and a neutral fragment (m_n) **(26)**.



The collision between the precursor ion and the target atom or molecule can be represented as shown in Figure 3.45, where m symbolizes mass, the subscripts p and t the precursor ion and the target, respectively, θ the scattering angle, P momentum, 1 the initial state and 2 the final state.

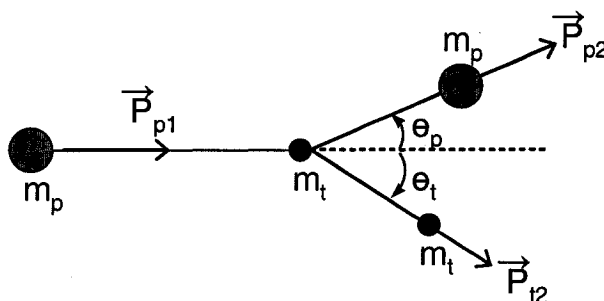


Figure 3.45. Collision process between an ion (m_p) and a neutral target (m_t).

Although the efficiency of the activation step is high (Douglas 1982), the conservation of total energy and momentum during inelastic collisions imply that only a small fraction of the kinetic energy of the precursor ion is actually converted to internal energy (Q). The limit of kinetic energy available for conversion (Q_{\max}) is a function of the scattering angle θ_p (3.8), and the maximum energy that can be converted is obtained when $\theta_p = 0^\circ$, a head-on collision (3.9) (E_{lab} is the kinetic energy of the precursor ion in the laboratory frame of reference) (de Hoffman *et al.* 1996 pp 48–50) (See Appendix E).

$$Q_{\max} = E_{\text{lab}} \left[\frac{(m_t - m_p)}{m_t} + \left(\frac{1}{m_t} \right) \left(\frac{m_p^2}{m_p + m_t} \right) (\cos^2 \theta_p) \right] \quad (3.8)$$

$$Q_{\max} = E_{\text{lab}} \left[\frac{m_t}{m_p + m_t} \right] \quad \text{for } \theta_p = 0^\circ \quad (3.9)$$

According to equation (3.9), an increase in the collision energy (E_{lab}) or in the collision gas mass should increase the energy available for conversion to internal energy of the precursor ion. Note that under the conditions used here, the maximum energy that can be converted in a head-on collision is only about one sixth of the precursor-ion kinetic energy ($m_p \sim 200$ u and collision gas is Ar, therefore $m_t = 40$ u). In addition, Q_{\max} is expected to decrease as a function of $1/m_p$, thus heavier precursor ions have less internal energy available for fragmentation during the collision process than lighter ones (Sleno and Volmer 2004).

In a QqQ instrument, a dc offset is generally applied on the rods of q2 to provide kinetic energy to activate the ions and cause fragmentation. For example, a 20 V offset will supply 20 eV of energy (in the laboratory frame of reference) for a singly charged ion. This offset can be changed manually to vary the degree of fragmentation. The kinetic energy imparted to the precursor ion by

means of the offset corresponds to E_{lab} , usually in the 5–30 eV range, and identified as the collision energy throughout this thesis.

Once in q2, some precursor ions may not hit any targets and hence leave q2 with their initial energy. However, most of them probably collide at least once with a neutral target. By doing so, they lose some of the initial energy to the target and if fragmentation does not occur, they will exit q2 with less energy. Moreover, the scattering angle θ_p varies during the collision process, and so will change the amount of energy transferred to the target and left to the ion after the collision. Equation (3.8) indicates that the maximum kinetic energy available for conversion (Q_{max}) decreases as θ_p increases and will go to zero when $\theta_p = 11.5^\circ$ ($m_t = 40$ u and $m_p = 200$ u).

The kinetic energy of the precursor ion after an inelastic collision with the target (E'_{lab}) can be calculated using equation (3.10), where $M = m_p + m_t$, E_{lab} is the precursor ion energy before collision, θ_p is the scattering angle of the precursor ion and Q is the energy converted to internal energy.

$$\frac{E'_{lab}}{E_{lab}} = \left[\frac{1}{M^2} \right] \left\{ m_p \cos \theta_p \pm \left[m_p^2 \cos^2 \theta_p + m_t^2 - m_p^2 - m_t M \frac{Q}{E_{lab}} \right]^{1/2} \right\}^2 \quad (3.10)$$

Equation (3.10) predicts that the precursor ions leaving q2 without fragmenting will have a wide energy distribution because of the range of scattering angles occurring during the activation step.

If the precursor ion fragments to a product ion of mass m_f with no kinetic energy release, the products will move at the same speed as the precursor and will have an energy E_{frag} given by (3.11). Therefore, fragment ions will have lower kinetic energies than the precursor because they are lighter (less mass, similar speed).

$$E_{frag} \approx E'_{lab} \left[\frac{m_f}{m_p} \right] \quad (3.11)$$

The overall ideas coming from these studies about ion activation by CID are that precursor and product ions emerging from q2 have a spread in energy arising from the range of scattering angles involved in the activation step with product ions having lower kinetic energy than the precursor ions. Since precursor and product ions coming from q2 have different kinetic energies one would expect significant differences in transmission efficiency and resolution in Q3.

The resolution (R_{\max}) that can be obtained in a quadrupole mass filter is inversely proportional to the energy of the ions (E_{ions}) according to equation (3.12), where n is the number of cycles spent by the ion in the quadrupole field, f is the frequency and L is the length of quadrupole rods (Dawson 1976 pp 22–24).

$$R_{\max} = \frac{f^2 L^2 m_{\text{ion}}}{22.4 E_{\text{ion}}} \approx \frac{n^2}{12.2} \quad (3.12)$$

Kinetic energy or ion velocity is not directly involved in determining resolution in quadrupole mass filters. However, if ion velocities are high enough so that ions pass through the quadrupole before undergoing a sufficient number of RF cycles, then the ion kinetic energy may affect resolution.

In order to slow down the ions coming from q2 and thus improve resolution in Q3, an offset opposite to that applied on q2 is normally required on Q3. This offset may be optimal for precursor ions that do not fragment but too high to permit entry of product ions into Q3, since products have lower kinetic energy. If, on the contrary, the offset in Q3 is lowered enough to allow the entry of all ions, then those ions with high kinetic energy will be traveling too fast and good resolution may not be obtained. Therefore, the setting of the dc offset on Q3 will be a compromise between resolution and sensitivity. The spread in energies observed for ions of a given mass exiting q2 will make determining the magnitude of this offset additionally difficult or impossible.

Although single mass spectra obtained using either Q1 or Q3 show that both mass filters are calibrated and properly tuned for unit mass resolution, when acquiring a product-ion mass spectrum, resolution is not unit mass (see the peak

at m/z 169 in Figures 3.46 A). The lowering of resolution appears as a broadening of the peaks, which increases as m/z increases, and an overlapping of peaks only one unit mass apart (m/z 94 and 95 in Figure 3.46 A). In Figure 3.46 A, the precursor ion (m/z 169) is observed to have the poorest resolution (widest peak) while the peaks of the products (m/z 94 and 95) are narrower. The peak shape of the precursor ions deteriorates as the collision energy increases from 5 eV (Figure 3.46 A) to 15 eV (Figure 3.46 B). This phenomenon can be explained as an effect of the offsets placed on Q1 and q2 and the spread in kinetic energy of the ions existing q2, which is expected to increase as the collision energy increases.

Unlike product-ion spectra, the peaks observed in precursor-ion or neutral loss spectra have unit mass resolution and their width does not change with mass (see the precursor-ion spectrum in Figure 3.46 C). However, when the collision energy is increased from 5 eV (Figure 3.46 C) to 20 eV, a false peak is observed at m/z 94 in the precursor-ion spectrum of m/z 95 (Figure 3.46 D), even though the resolution appears to be very good.

When acquiring a product-ion spectrum, Q1 is set to pass a given m/z ion continuously (Q1 is not scanned). Therefore, there is a constant flow of ions entering q2, exiting q2 and entering Q3. The width of the peaks recorded by the detector placed after Q3 is determined only by the resolution in Q3.

On the other hand, when obtaining either a precursor-ion or a neutral loss spectrum, Q1 is scanned and the source of ions entering q2 and Q3 is not continuous. Ions can only pass through q2 and Q3 if they are selected by Q1. If the resolution in Q1 is unit mass, the peaks observed by the detector after Q3 will also have unit mass width. This explains the much better (though apparent) resolution observed in precursor-ion or neutral loss spectra compared to product-ion spectra. However, if the resolution in Q3 is less than unit mass, ions of more than one mass value will traverse Q3 although it is set to pass a single mass. This will distort the isotope clusters in precursor and neutral loss spectra and give rise to false peaks, especially if the kinetic energy of the ions exiting q2 increases when higher collision energies are used (Figure 3.46 D).

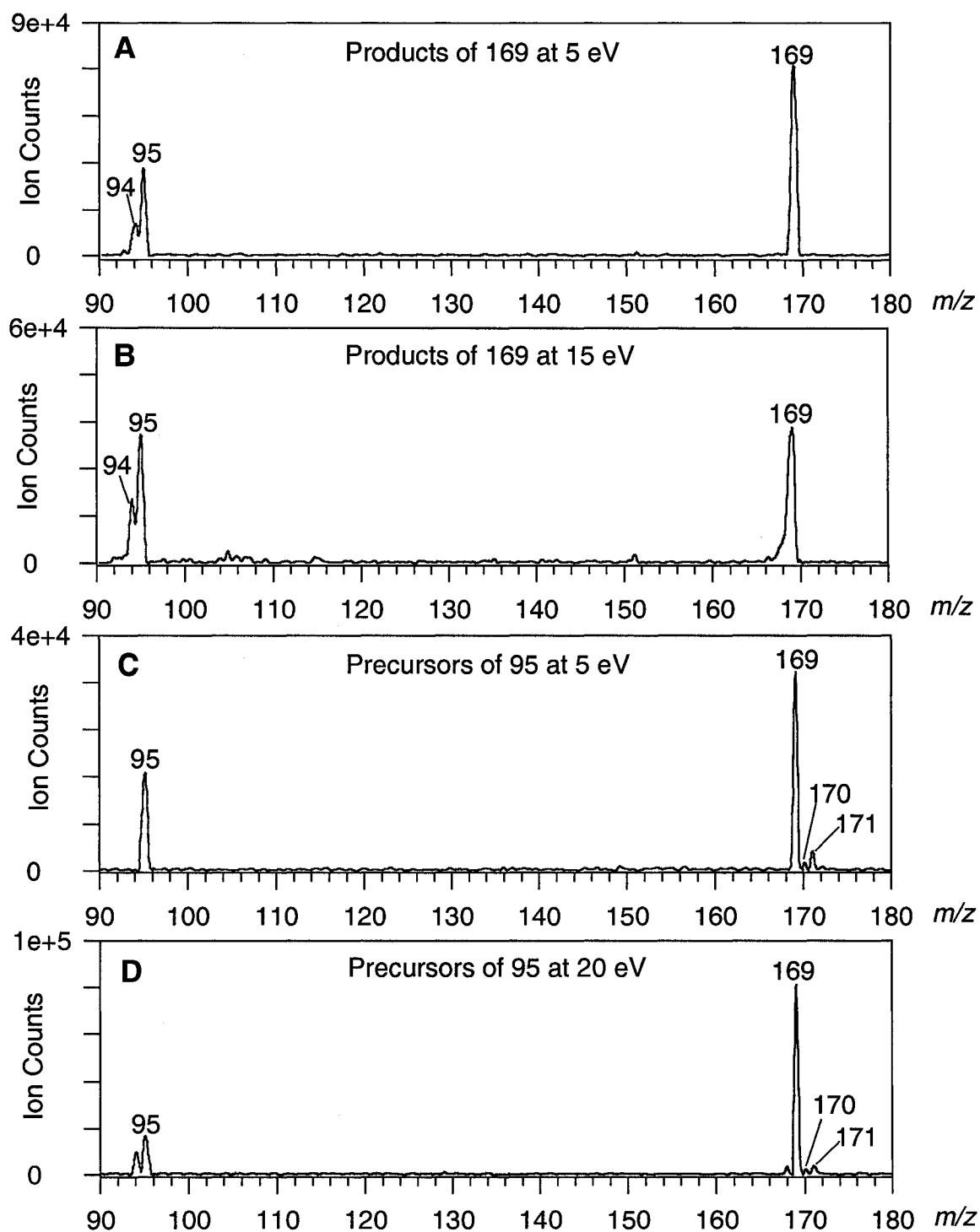


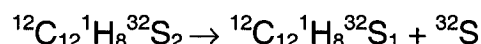
Figure 3.46. Product-ion mass spectra of m/z 169 (A and B) and precursor-ion mass spectra of m/z 95 (C and D) at different collision energies: 5 eV (A), 15 eV (B), 5 eV (C) and 20 eV (D) (MA, 15 V cone).

To investigate the problems that can arise due to poor resolution in Q3, the example of TA losing S will be examined **(27)**.

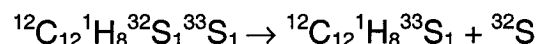
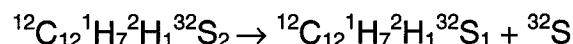
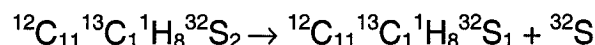


The following fragmentations can occur in q2 as a function of the setting in Q1 (Note: charges and dots that signify radical ions will be omitted and all masses will be given as nominal, for simplicity).

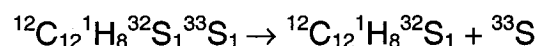
Q1 set to 216



Q1 set to 217

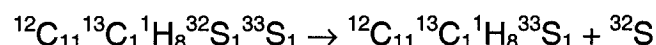
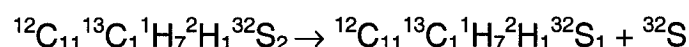


intensity split 1/2

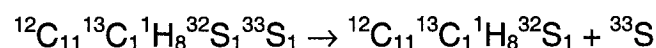


intensity split 1/2

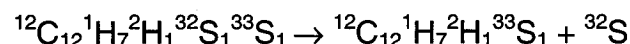
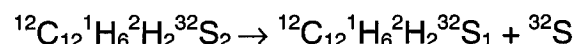
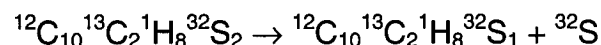
Q1 set to 218



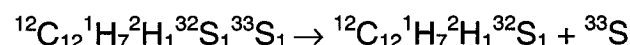
intensity split 1/2



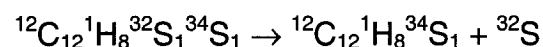
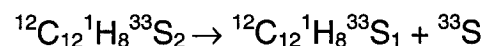
intensity split 1/2



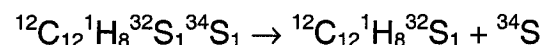
intensity split 1/2



intensity split 1/2

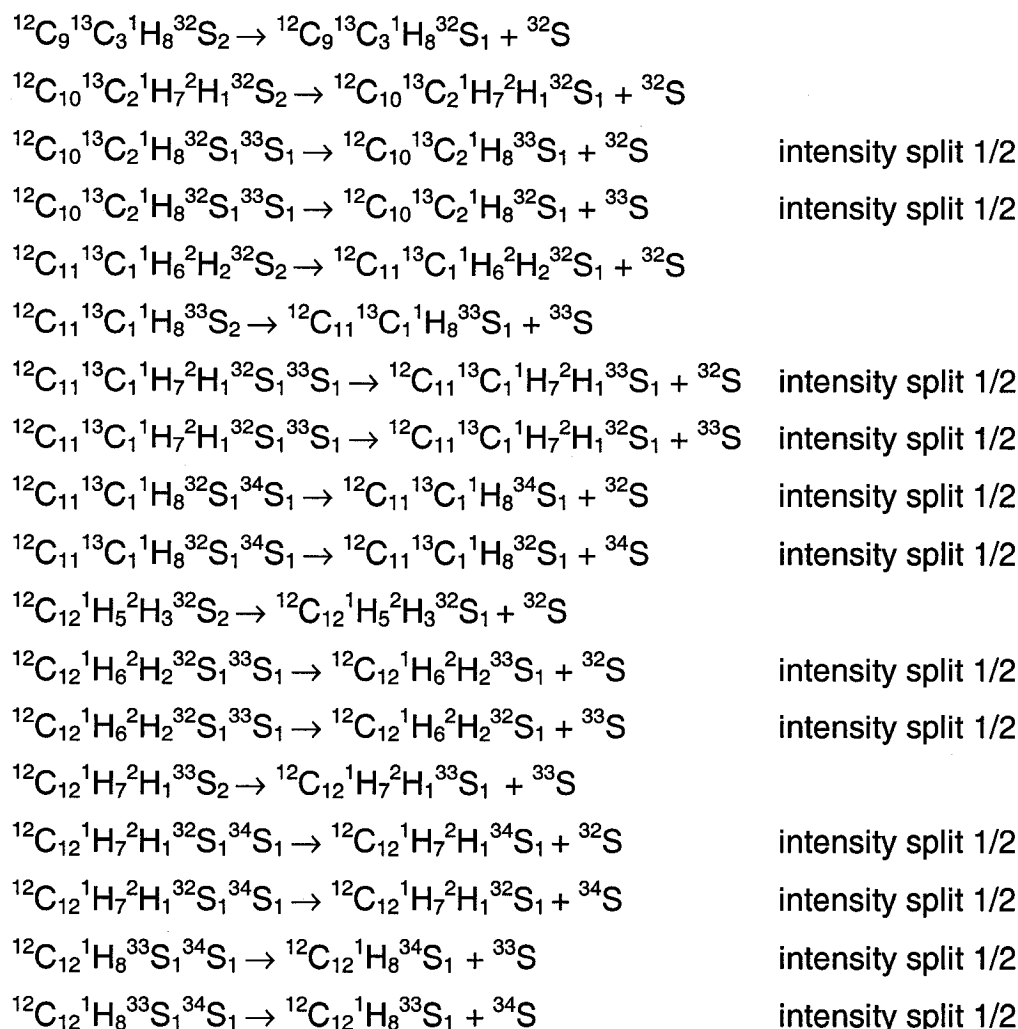


intensity split 1/2



intensity split 1/2

Q1 set to 219



The fractional abundances of all the precursor ions (T) are calculated using equation (3.4). The results are shown in Table 3.52. Natural isotopic abundances used in the calculations are: 0.9893 (^{12}C), 0.0107 (^{13}C), 0.999885 (^1H), 0.000115 (^2H), 0.9499 (^{32}S), 0.0075 (^{33}S) and 0.0425 (^{34}S) (de Laeter *et al.* 2003). For example, the fractional abundance for $^{12}\text{C}_{12}^1\text{H}_8^{32}\text{S}_2$ is calculated as follows,

$$T = \frac{12!8!2!}{12!0!8!0!2!0!0!} \times \left[\frac{(0.9893)^{12}(0.0107)^0(0.999885)^8(0.000115)^0(0.9499)^2(0.0075)^0(0.0425)^0}{12!0!8!0!2!0!0!} \right] = 7.9231\text{e-}1$$

Table 3.52. Fractional abundances (T) of all precursor ions.

Precursor Ions	Fractional Abundance (T)
<i>m/z</i> 216 $^{12}\text{C}_{12}^{1}\text{H}_8^{32}\text{S}_2$	7.9231e-1
<i>m/z</i> 217 $^{12}\text{C}_{11}^{13}\text{C}_1^{1}\text{H}_8^{32}\text{S}_2$ $^{12}\text{C}_{12}^{1}\text{H}_7^2\text{H}_1^{32}\text{S}_2$ $^{12}\text{C}_{12}^{1}\text{H}_8^{32}\text{S}_1^{33}\text{S}_1$	1.0283e-1 7.2900e-4 1.2511e-2
<i>m/z</i> 218 $^{12}\text{C}_{11}^{13}\text{C}_1^{1}\text{H}_7^2\text{H}_1^{32}\text{S}_2$ $^{12}\text{C}_{11}^{13}\text{C}_1^{1}\text{H}_8^{32}\text{S}_1^{33}\text{S}_1$ $^{12}\text{C}_{10}^{13}\text{C}_2^{1}\text{H}_8^{32}\text{S}_2$ $^{12}\text{C}_{12}^{1}\text{H}_6^2\text{H}_2^{32}\text{S}_2$ $^{12}\text{C}_{12}^{1}\text{H}_7^2\text{H}_1^{32}\text{S}_1^{33}\text{S}_1$ $^{12}\text{C}_{12}^{1}\text{H}_8^{33}\text{S}_2$ $^{12}\text{C}_{12}^{1}\text{H}_8^{32}\text{S}_1^{34}\text{S}_1$	9.4617e-5 1.6238e-3 6.1171e-3 2.9346e-7 1.1512e-5 4.9392e-5 7.0898e-2
<i>m/z</i> 219 $^{12}\text{C}_9^{13}\text{C}_3^{1}\text{H}_8^{32}\text{S}_2$ $^{12}\text{C}_{10}^{13}\text{C}_2^{1}\text{H}_7^2\text{H}_1^{32}\text{S}_2$ $^{12}\text{C}_{10}^{13}\text{C}_2^{1}\text{H}_8^{32}\text{S}_1^{33}\text{S}_1$ $^{12}\text{C}_{11}^{13}\text{C}_1^{1}\text{H}_6^2\text{H}_2^{32}\text{S}_2$ $^{12}\text{C}_{11}^{13}\text{C}_1^{1}\text{H}_8^{33}\text{S}_2$ $^{12}\text{C}_{11}^{13}\text{C}_1^{1}\text{H}_7^2\text{H}_1^{32}\text{S}_1^{33}\text{S}_1$ $^{12}\text{C}_{11}^{13}\text{C}_1^{1}\text{H}_8^{32}\text{S}_1^{34}\text{S}_1$ $^{12}\text{C}_{12}^{1}\text{H}_5^2\text{H}_3^{32}\text{S}_2$ $^{12}\text{C}_{12}^{1}\text{H}_6^2\text{H}_2^{32}\text{S}_1^{33}\text{S}_1$ $^{12}\text{C}_{12}^{1}\text{H}_7^2\text{H}_1^{33}\text{S}_2$ $^{12}\text{C}_{12}^{1}\text{H}_7^2\text{H}_1^{32}\text{S}_1^{34}\text{S}_1$ $^{12}\text{C}_{12}^{1}\text{H}_8^{33}\text{S}_1^{34}\text{S}_1$	2.2054e-4 5.6284e-6 9.6596e-5 3.8088e-8 6.4106e-6 1.4941e-6 9.2018e-3 6.7503e-11 4.6340e-9 4.5446e-8 6.5234e-5 5.5978e-4

In order to demonstrate that poor resolution in Q3 will have an affect on product-ion and neutral loss mass spectra, the abundance ratios within the precursors of *m/z* 184 and 185, and the neutral loss of 32 and 33 u mass spectra were calculated assuming poor resolution in Q3 (Tables 3.53 to 3.60). In the following discussion, it will be assumed that Q1 and Q3 are properly calibrated, that Q1 is tuned for unit mass resolution and only passes one mass, and that Q3 passes 10% of the two neighboring masses due to poor resolution.

In Tables 3.53, 3.55, 3.57 and 3.59, the Fragmentation and *m/z* Products (P) columns are self-explanatory (in the Fragmentation column the masses of the lightest isotopes are omitted for simplicity). The Status column indicates the

“closeness” of the product-ion mass to the setting of Q3. An “on” status signifies that the mass of the product ion is the same as the setting of Q3 and thus will pass unattenuated. An “overlap” status indicates a mass within one unit, plus or minus, of the setting of Q3, and an “off” status specifies a mass two or more units away from the setting. The Factor column indicates the fraction of the fractional abundance (T) to be attributed to that particular fragmentation (T values for each precursor ion are shown in Table 3.52). All “overlap” masses will have assigned an arbitrary factor of 0.1 (10 %) due to poor resolution. Additionally, any fragmentation that can produce two or more product ions will have a factor to take this into account (for the loss of one S atom from TA, which contains two sulfur atoms, this factor will be $\frac{1}{2}$). The Fractional Intensity column is the numerical value associated with the Factor column.

Table 3.53. Precursors of 184 (Q3 set to m/z 184, Q1 scanned, P: product ion).

Fragmentation	m/z P	Status	Factor	Fractional Intensity
Q1 at m/z 216: $C_{12}H_8S_2 \rightarrow C_{12}H_8S_1 + S$	184	on	T	7.9230e-1
Q1 at m/z 217: $C_{11}^{13}C_1H_8S_2 \rightarrow C_{11}^{13}C_1H_8S_1 + S$	185	overlap	(0.1)T	1.0283e-2
$C_{12}H_7^2H_1S_2 \rightarrow C_{12}H_7^2H_1S_1 + S$	185	overlap	(0.1)T	7.2900e-5
$C_{12}^1H_8S_1^{33}S_1 \rightarrow C_{12}H_8^{33}S_1 + S$	185	overlap	(0.1)(1/2)T	6.2557e-4
$C_{12}H_8S_1^{33}S_1 \rightarrow C_{12}H_8S_1 + ^{33}S$	184	on	(1/2)T	6.2557e-3
Q1 at m/z 218: $C_{11}^{13}C_1H_7^2H_1S_2 \rightarrow C_{11}^{13}C_1H_7^2H_1S_1 + S$	186	off	—	—
$C_{11}^{13}C_1H_8S_1^{33}S_1 \rightarrow C_{11}^{13}C_1H_8^{33}S_1 + S$	185	overlap	(0.1)(1/2)T	8.1192e-5
$C_{11}^{13}C_1H_8S_1^{33}S_1 \rightarrow C_{11}^{13}C_1H_8S_1 + ^{33}S$	186	off	—	—
$C_{10}^{13}C_2H_8S_2 \rightarrow C_{10}^{13}C_2^1H_8S_1 + S$	186	off	—	—
$C_{12}H_6^2H_2S_2 \rightarrow C_{12}H_6^2H_2S_1 + S$	186	off	—	—
$C_{12}H_7^2H_1S_1^{33}S_1 \rightarrow C_{12}H_7^2H_1^{33}S_1 + S$	186	off	—	—
$C_{12}H_7^2H_1S_1^{33}S_1 \rightarrow C_{12}H_7^2H_1S_1 + ^{33}S$	185	overlap	(0.1)(1/2)T	5.7559e-7
$C_{12}H_8^{33}S_2 \rightarrow C_{12}H_8^{33}S_1 + ^{33}S$	185	overlap	(0.1)T	4.9392e-6
$C_{12}H_8S_1^{34}S_1 \rightarrow C_{12}H_8^{34}S_1 + S$	184	on	(1/2)T	3.5449e-2
$C_{12}H_8S_1^{34}S_1 \rightarrow C_{12}H_8S_1 + ^{34}S$	186	off	—	—

The abundance ratios within a spectrum at low resolution are obtained by summing the fractional intensities at each setting of Q1 (“on” and “overlap”

masses). The theoretical intensity ratios (high resolution) have also been calculated by summing only those values that exactly match the setting of Q3 (“on” masses). The results obtained are displayed in Tables 3.54, 3.56, 3.58 and 3.60.

In the low resolution spectrum (Table 3.54) the isotopic mass at m/z 217, has a significant intensity distortion (low resolution: 2.176 % vs. high resolution: 0.790 %), which demonstrates that poor resolution in Q3 affects the appearance of the isotopic cluster. Note that the high resolution values are the same as the theoretical values shown in Table 3.46 as they must be.

Table 3.54. Fractional abundance within precursor-ion of m/z 184 spectrum at low and high resolution.

Q1 m/z	Low Resolution		High Resolution	
	Fractional Intensity	%	Fractional Intensity	%
216	7.9230e-1	100.000	7.9230e-1	100.000
217	1.7237e-2	2.176	6.2557e-3	0.790
218	3.5536e-2	4.485	3.5449e-2	4.474

A similar calculation was performed for the precursors of m/z 185 and the results obtained are shown in Tables 3.55 and 3.56. There is a peak at m/z 216 where no peak should be (Table 3.56), and this peak is a significant fraction of the base peak (about 70 %). A major intensity distortion is detected at m/z 218 at low resolution (low resolution: 4.631 % vs. high resolution: 0.790 %). The alteration of the relative peak heights in the spectrum for m/z 218 in Table 3.56 is even larger than the distortion previously reported for m/z 217 in Table 3.54 (m/z 218 in Table 3.56: 4.631 % vs. m/z 217 in Table 3.54: 2.176 %). Moreover, very similar results are obtained when comparing the relative intensities determined experimentally (Table 3.46), with the values calculated assuming poor resolution in Q3 (Table 3.56). Note that the relative intensity for m/z 218 in Table 3.56 (precursors of 185, under the E column, within spectrum) is 3.4 %, more than the 1.8 % for the 217 peak in the spectrum for the precursors of 184.

Table 3.55. Precursors of 185 (Q3 set to m/z 185, Q1 scanned, P: product ion).

Reaction	m/z P	Status	Factor	Fractional Intensity
Q1 at m/z 216:				
$C_{12}H_8S_2 \rightarrow C_{12}H_8S_1 + S$	184	overlap	(0.1)T	7.9230e-2
Q1 at m/z 217:				
$C_{11}^{13}C_1H_8S_2 \rightarrow C_{11}^{13}C_1H_8S_1 + S$	185	on	T	1.0283e-1
$C_{12}H_7^2H_1S_2 \rightarrow C_{12}H_7^2H_1S_1 + S$	185	on	T	7.2900e-4
$C_{12}^1H_8S_1^{33}S_1 \rightarrow C_{12}H_8^{33}S_1 + S$	185	on	(1/2)T	6.2557e-3
$C_{12}H_8S_1^{33}S_1 \rightarrow C_{12}H_8S_1 + ^{33}S$	184	overlap	(0.1)(1/2)T	6.2557e-4
Q1 at m/z 218:				
$C_{11}^{13}C_1H_7^2H_1S_2 \rightarrow C_{11}^{13}C_1H_7^2H_1S_1 + S$	186	overlap	(0.1)T	9.4616e-6
$C_{11}^{13}C_1H_8S_1^{33}S_1 \rightarrow C_{11}^{13}C_1H_8^{33}S_1 + S$	185	on	(1/2)T	8.1192e-4
$C_{11}^{13}C_1H_8S_1^{33}S_1 \rightarrow C_{11}^{13}C_1H_8S_1 + ^{33}S$	186	overlap	(0.1)(1/2)T	8.1192e-5
$C_{10}^{13}C_2H_8S_2 \rightarrow C_{10}^{13}C_2^1H_8S_1 + S$	186	overlap	(0.1)T	6.1171e-4
$C_{12}H_6^2H_2S_2 \rightarrow C_{12}H_6^2H_2S_1 + S$	186	overlap	(0.1)T	2.9346e-8
$C_{12}H_7^2H_1S_1^{33}S_1 \rightarrow C_{12}H_7^2H_1^{33}S_1 + S$	186	overlap	(0.1)(1/2)T	5.7559e-7
$C_{12}H_7^2H_1S_1^{33}S_1 \rightarrow C_{12}H_7^2H_1S_1 + ^{33}S$	185	on	(1/2)T	5.7559e-6
$C_{12}H_8^{33}S_2 \rightarrow C_{12}H_8^{33}S_1 + ^{33}S$	185	on	T	4.9392e-6
$C_{12}H_8S_1^{34}S_1 \rightarrow C_{12}H_8^{34}S_1 + S$	184	overlap	(0.1)(1/2)T	3.5449e-3
$C_{12}H_8S_1^{34}S_1 \rightarrow C_{12}H_8S_1 + ^{34}S$	186	overlap	(0.1)(1/2)T	3.5449e-3
Q1 at m/z 219:				
$C_9^{13}C_3H_8S_2 \rightarrow C_9^{13}C_3H_8S_1 + S$	187	off	—	—
$C_{10}^{13}C_2H_7^2H_1S_2 \rightarrow C_{10}^{13}C_2H_7^2H_1S_1 + S$	187	off	—	—
$C_{10}^{13}C_2H_8S_1^{33}S_1 \rightarrow C_{10}^{13}C_2H_8^{33}S_1 + S$	187	off	—	—
$C_{10}^{13}C_2H_8S_1^{33}S_1 \rightarrow C_{10}^{13}C_2H_8S_1 + ^{33}S$	186	overlap	(0.1)(1/2)T	4.8298e-6
$C_{11}^{13}C_1H_6^2H_2S_2 \rightarrow C_{11}^{13}C_1H_6^2H_2S_1 + S$	187	off	—	—
$C_{11}^{13}C_1H_8^{33}S_2 \rightarrow C_{11}^{13}C_1H_8^{33}S_1 + ^{33}S$	186	overlap	(0.1)T	6.4106e-7
$C_{11}^{13}C_1H_7^2H_1S^{33}S \rightarrow C_{11}^{13}C_1H_7^2H_1^{33}S + S$	187	off	—	—
$C_{11}^{13}C_1H_7^2H_1S^{33}S \rightarrow C_{11}^{13}C_1H_7^2H_1S + ^{33}S$	186	overlap	(0.1)(1/2)T	7.4705e-8
$C_{11}^{13}C_1H_8S_1^{34}S_1 \rightarrow C_{11}^{13}C_1H_8^{34}S_1 + S$	187	off	—	—
$C_{11}^{13}C_1H_8S_1^{34}S_1 \rightarrow C_{11}^{13}C_1H_8S_1 + ^{34}S$	185	on	(1/2)T	4.6009e-3
$C_{12}H_5^2H_3S_2 \rightarrow C_{12}H_5^2H_3S_1 + S$	187	off	—	—
$C_{12}H_6^2H_2S_1^{33}S_1 \rightarrow C_{12}H_6^2H_2^{33}S_1 + S$	187	off	—	—
$C_{12}H_6^2H_2S_1^{33}S_1 \rightarrow C_{12}H_6^2H_2S_1 + ^{33}S$	186	overlap	(0.1)(1/2)T	2.3170e-10
$C_{12}H_7^2H_1^{33}S_2 \rightarrow C_{12}H_7^2H_1^{33}S_1 + ^{33}S$	186	overlap	(0.1)T	4.5446e-9
$C_{12}H_7^2H_1S_1^{34}S_1 \rightarrow C_{12}H_7^2H_1^{34}S_1 + S$	187	off	—	—
$C_{12}H_7^2H_1S_1^{34}S_1 \rightarrow C_{12}H_7^2H_1S_1 + ^{34}S$	185	on	(1/2)T	3.2617e-5
$C_{12}H_8^{33}S_1^{34}S_1 \rightarrow C_{12}H_8^{34}S_1 + ^{33}S$	186	overlap	(0.1)(1/2)T	2.7989e-5
$C_{12}H_8^{33}S_1^{34}S_1 \rightarrow C_{12}H_8^{33}S_1 + ^{34}S$	185	on	(1/2)T	2.7989e-4

Table 3.56. Fractional abundance within precursor-ion of m/z 185 spectrum at low and high resolution.

Q1 m/z	Low Resolution		High Resolution	
	Fractional Intensity	%	Fractional Intensity	%
216	7.9230e-2	71.739	0.000	0.000
217	1.1044e-1	100.000	1.0982e-1	100.000
218	5.1149e-3	4.631	8.6707e-4	0.790
219	4.9469e-3	4.479	4.9134e-3	4.474

The relative intensity ratios in neutral loss spectra at low and high resolution were also calculated. Calculations were performed considering the loss of ^{32}S or ^{33}S . In the constant neutral loss spectra, Q1 and Q3 are both scanned with a constant difference of m/z 32 between them (if ^{32}S is lost). The results of the calculations are shown in Tables 3.57 to 3.60.

Table 3.57. Constant neutral loss of 32 (Q1 and Q3 are both scanned with a constant difference of m/z 32 between them, P: product ion).

Reaction	m/z P	Status	Factor	Fractional Intensity
Q1 at m/z 216, Q3 at m/z 184: $\text{C}_{12}\text{H}_8\text{S}_2 \rightarrow \text{C}_{12}\text{H}_8\text{S}_1 + \text{S}$	184	on	T	7.9230e-1
Q1 at m/z 217, Q3 at m/z 185: $\text{C}_{11}^{13}\text{C}_1\text{H}_8\text{S}_2 \rightarrow \text{C}_{11}^{13}\text{C}_1\text{H}_8\text{S}_1 + \text{S}$	185	on	T	1.0283e-1
$\text{C}_{12}\text{H}_7^2\text{H}_1\text{S}_2 \rightarrow \text{C}_{12}\text{H}_7^2\text{H}_1\text{S}_1 + \text{S}$	185	on	T	7.2900e-4
$\text{C}_{12}^1\text{H}_8\text{S}_1^{33}\text{S}_1 \rightarrow \text{C}_{12}\text{H}_8^{33}\text{S}_1 + \text{S}$	185	on	(1/2)T	6.2557e-3
$\text{C}_{12}\text{H}_8\text{S}_1^{33}\text{S}_1 \rightarrow \text{C}_{12}\text{H}_8\text{S}_1 + ^{33}\text{S}$	184	overlap	(0.1)(1/2)T	6.2557e-4
Q1 at m/z 218, Q3 at m/z 186: $\text{C}_{11}^{13}\text{C}_1\text{H}_7^2\text{H}_1\text{S}_2 \rightarrow \text{C}_{11}^{13}\text{C}_1\text{H}_7^2\text{H}_1\text{S}_1 + \text{S}$	186	on	T	9.4616e-5
$\text{C}_{11}^{13}\text{C}_1\text{H}_8\text{S}_1^{33}\text{S}_1 \rightarrow \text{C}_{11}^{13}\text{C}_1\text{H}_8^{33}\text{S}_1 + \text{S}$	185	overlap	(0.1)(1/2)T	8.1192e-5
$\text{C}_{11}^{13}\text{C}_1\text{H}_8\text{S}_1^{33}\text{S}_1 \rightarrow \text{C}_{11}^{13}\text{C}_1\text{H}_8\text{S}_1 + ^{33}\text{S}$	186	on	(1/2)T	8.1192e-4
$\text{C}_{10}^{13}\text{C}_2\text{H}_8\text{S}_2 \rightarrow \text{C}_{10}^{13}\text{C}_2^1\text{H}_8\text{S}_1 + \text{S}$	186	on	T	6.1171e-3
$\text{C}_{12}\text{H}_6^2\text{H}_2\text{S}_2 \rightarrow \text{C}_{12}\text{H}_6^2\text{H}_2\text{S}_1 + \text{S}$	186	on	T	2.9346e-7
$\text{C}_{12}\text{H}_7^2\text{H}_1\text{S}_1^{33}\text{S}_1 \rightarrow \text{C}_{12}\text{H}_7^2\text{H}_1^{33}\text{S}_1 + \text{S}$	186	on	(1/2)T	5.7559e-6
$\text{C}_{12}\text{H}_7^2\text{H}_1\text{S}_1^{33}\text{S}_1 \rightarrow \text{C}_{12}\text{H}_7^2\text{H}_1\text{S}_1 + ^{33}\text{S}$	185	overlap	(0.1)(1/2)T	5.7559e-7
$\text{C}_{12}\text{H}_8^{33}\text{S}_2 \rightarrow \text{C}_{12}\text{H}_8^{33}\text{S}_1 + ^{33}\text{S}$	185	overlap	(0.1)T	4.9392e-6
$\text{C}_{12}\text{H}_8\text{S}_1^{34}\text{S}_1 \rightarrow \text{C}_{12}\text{H}_8^{34}\text{S}_1 + \text{S}$	184	off	—	—
$\text{C}_{12}\text{H}_8\text{S}_1^{34}\text{S}_1 \rightarrow \text{C}_{12}\text{H}_8\text{S}_1 + ^{34}\text{S}$	186	on	(1/2)T	3.5449e-2

For the neutral loss of 32 u (Table 3.58), the low resolution spectrum is in good agreement with the high resolution spectrum. In addition, the experimental values for the neutral loss of 32 u (Table 3.44) are in good agreement with the theoretical values. For the neutral loss of 32 u, poor resolution in Q3 alters very little the peak height ratios within the neutral loss spectrum.

Table 3.58. Fractional abundance within constant neutral loss of 32 u spectrum at low and high resolution.

Q1 <i>m/z</i>	Low Resolution		High Resolution	
	Fractional Intensity	%	Fractional Intensity	%
216	7.9230e-1	100.000	7.9230e-1	100.000
217	1.1044e-1	13.939	1.0982e-1	13.860
218	4.2565e-2	5.372	4.2479e-2	5.361

Fractional abundance ratios within the neutral loss of 33 u mass spectrum are shown in Tables 3.59 and 3.60. Comparison between the results obtained at low and high resolutions show that the agreement is poor (Table 3.60). A peak at *m/z* 216 is the base peak in the low resolution spectrum, even though it should not be there. By assigning the peak at *m/z* 217 a value of 100.000 %, the spectrum is still very badly distorted. Assuming low resolution in Q3, the highest deviations from theory are obtained for the neutral loss of 33 u from 218. This is observed both in the spectrum determined experimentally (Table 3.44, neutral loss of 33 u, precursor ion 218) and in the low resolution spectrum (Table 3.60).

As these results illustrate, some spectra for the same fragmentation are badly distorted (for example, precursors of 185 and neutral loss of ³³S spectra) while others are distorted very little (precursors of 184 and neutral loss of ³²S spectra). The distortion appeared in the form of false peaks and alterations in the peak heights. The magnitude of the distortion will depend on the resolution (the offset program for Q3), the accuracy of the mass settings of the two mass filters (the calibration), the presence of ions that can interfere and the actual appearance of the mass spectrum.

Table 3.59. Constant neutral loss of 33 (Q1 and Q3 are both scanned with a constant difference of m/z 33 between them, P: product ion).

Reaction	m/z P	Status	Factor	Fractional Intensity
Q1 at m/z 216, Q3 at m/z 183: $C_{12}H_8S_2 \rightarrow C_{12}H_8S_1 + S$	184	overlap	(0.1)T	7.9230e-2
Q1 at m/z 217, Q3 at m/z 184: $C_{11}^{13}C_1H_8S_2 \rightarrow C_{11}^{13}C_1H_8S_1 + S$	185	overlap	(0.1)T	1.0283e-2
$C_{12}H_7^2H_1S_2 \rightarrow C_{12}H_7^2H_1S_1 + S$	185	overlap	(0.1)T	7.2900e-5
$C_{12}^1H_8S_1^{33}S_1 \rightarrow C_{12}H_8^{33}S_1 + S$	185	overlap	(0.1)(1/2)T	6.2557e-4
$C_{12}H_8S_1^{33}S_1 \rightarrow C_{12}H_8S_1 + ^{33}S$	184	on	(1/2)T	6.2557e-3
Q1 at m/z 218, Q3 at m/z 185: $C_{11}^{13}C_1H_7^2H_1S_2 \rightarrow C_{11}^{13}C_1H_7^2H_1S_1 + S$	186	overlap	(0.1)T	9.4616e-6
$C_{11}^{13}C_1H_8S_1^{33}S_1 \rightarrow C_{11}^{13}C_1H_8^{33}S_1 + S$	185	on	(1/2)T	8.1192e-4
$C_{11}^{13}C_1H_8S_1^{33}S_1 \rightarrow C_{11}^{13}C_1H_8S_1 + ^{33}S$	186	overlap	(0.1)(1/2)T	8.1192e-5
$C_{10}^{13}C_2H_8S_2 \rightarrow C_{10}^{13}C_2^1H_8S_1 + S$	186	overlap	(0.1)T	6.1171e-4
$C_{12}H_6^2H_2S_2 \rightarrow C_{12}H_6^2H_2S_1 + S$	186	overlap	(0.1)T	2.9346e-8
$C_{12}H_7^2H_1S_1^{33}S_1 \rightarrow C_{12}H_7^2H_1^{33}S_1 + S$	186	overlap	(0.1)(1/2)T	5.7559e-7
$C_{12}H_7^2H_1S_1^{33}S_1 \rightarrow C_{12}H_7^2H_1S_1 + ^{33}S$	185	on	(1/2)T	5.7559e-6
$C_{12}H_8^{33}S_2 \rightarrow C_{12}H_8^{33}S_1 + ^{33}S$	185	on	T	4.9392e-5
$C_{12}H_8S_1^{34}S_1 \rightarrow C_{12}H_8^{34}S_1 + S$	184	overlap	(0.1)(1/2)T	3.5449e-3
$C_{12}H_8S_1^{34}S_1 \rightarrow C_{12}H_8S_1 + ^{34}S$	186	overlap	(0.1)(1/2)T	3.5449e-3
Q1 at m/z 219, Q3 at m/z 186: $C_9^{13}C_3H_8S_2 \rightarrow C_9^{13}C_3H_8S_1 + S$	187	overlap	(0.1)T	2.2054e-5
$C_{10}^{13}C_2H_7^2H_1S_2 \rightarrow C_{10}^{13}C_2H_7^2H_1S_1 + S$	187	overlap	(0.1)T	5.6284e-7
$C_{10}^{13}C_2H_8S_1^{33}S_1 \rightarrow C_{10}^{13}C_2H_8^{33}S_1 + S$	187	overlap	(0.1)(1/2)T	4.8298e-6
$C_{10}^{13}C_2H_8S_1^{33}S_1 \rightarrow C_{10}^{13}C_2H_8S_1 + ^{33}S$	186	on	(1/2)T	4.8298e-5
$C_{11}^{13}C_1H_6^2H_2S_2 \rightarrow C_{11}^{13}C_1H_6^2H_2S_1 + S$	187	overlap	(0.1)T	3.8088e-9
$C_{11}^{13}C_1H_8^{33}S_2 \rightarrow C_{11}^{13}C_1H_8^{33}S_1 + ^{33}S$	186	on	T	6.4106e-6
$C_{11}^{13}C_1H_7^2H_1S^{33}S \rightarrow C_{11}^{13}C_1H_7^2H_1^{33}S + S$	187	overlap	(0.1)(1/2)T	7.4705e-8
$C_{11}^{13}C_1H_7^2H_1S^{33}S \rightarrow C_{11}^{13}C_1H_7^2H_1S + ^{33}S$	186	on	(1/2)T	7.4705e-7
$C_{11}^{13}C_1H_8S_1^{34}S_1 \rightarrow C_{11}^{13}C_1H_8^{34}S_1 + S$	187	overlap	(0.1)(1/2)T	4.6009e-4
$C_{11}^{13}C_1H_8S_1^{34}S_1 \rightarrow C_{11}^{13}C_1H_8S_1 + ^{34}S$	185	overlap	(0.1)(1/2)T	4.6009e-4
$C_{12}H_5^2H_3S_2 \rightarrow C_{12}H_5^2H_3S_1 + S$	187	overlap	(0.1)T	6.7503e-12
$C_{12}H_6^2H_2S_1^{33}S_1 \rightarrow C_{12}H_6^2H_2^{33}S_1 + S$	187	overlap	(0.1)(1/2)T	2.3170e-10
$C_{12}H_6^2H_2S_1^{33}S_1 \rightarrow C_{12}H_6^2H_2S_1 + ^{33}S$	186	on	(1/2)T	2.3170e-9
$C_{12}H_7^2H_1^{33}S_2 \rightarrow C_{12}H_7^2H_1^{33}S_1 + ^{33}S$	186	on	T	4.5446e-8
$C_{12}H_7^2H_1S_1^{34}S_1 \rightarrow C_{12}H_7^2H_1^{34}S_1 + S$	187	overlap	(0.1)(1/2)T	3.2617e-6
$C_{12}H_7^2H_1S_1^{34}S_1 \rightarrow C_{12}H_7^2H_1S_1 + ^{34}S$	185	overlap	0.1)(1/2)T	3.2617e-6
$C_{12}H_8^{33}S_1^{34}S_1 \rightarrow C_{12}H_8^{34}S_1 + ^{33}S$	186	on	(1/2)T	2.7989e-4
$C_{12}H_8^{33}S_1^{34}S_1 \rightarrow C_{12}H_8^{33}S_1 + ^{34}S$	185	overlap	(0.1)(1/2)T	2.7989e-5

Table 3.60. Fractional abundance within constant neutral loss of 33 u spectrum at low and high resolution.

Q1 <i>m/z</i>	Low Resolution			High Resolution	
	Fractional Intensity	% Base Peak 216	% Base Peak 217	Fractional Intensity	%
216	7.9230e-2	100.000	—	—	—
217	1.7237e-2	21.756	100.000	6.2557e-3	100.000
218	8.6598e-3	10.930	50.239	8.6707e-4	13.860
219	1.3176e-3	1.663	7.644	3.3539e-4	5.361

One approach to improving sensitivity and resolution in MS/MS is to scan the offset applied to Q3 with the fragment ion mass (Shushan *et al.* 1983), yet it is very difficult to arrange an optimal compromise between the offset and the ion mass over the entire mass range.

A second approach is to operate a conventional collision cell at higher pressures than typically used, 10 mTorr vs. 1 mTorr (Whalen *et al.* 1995). The effect of increasing the pressure of the collision gas in q2 is analogous to that observed in ion traps. Higher collision gas pressures would cause ions to migrate to the central axis, and exit q2 with narrower energy distributions, thus improving ion transmission and resolution. However, the major inconvenience of using high-pressure cells is that collisional cooling runs counter to efficient collisional activation. We tested the idea of using higher gas pressures in q2 to improve resolution. Although the pressures used by us ($2\text{e-}7$, $4\text{e-}7$ and $1\text{e-}6$ bar) were much lower than those usually employed in high-pressure cells, the intensity of the artificial peaks observed in precursor-ion spectra decreased when the collision gas pressure was increased.

In order to determine if better resolution and sensitivity could be achieved using an ion trap mass spectrometer, the product-ion mass spectra for TA and MA were obtained with the LCQ. The experimental and theoretical abundance ratios within and among product-ion mass spectra are shown in Tables 3.61 and 3.62. Mass spectra are displayed in Figures 3.47 and 3.48.

Table 3.61. Theoretical (T) and experimental (E) abundance ratios (%) within and among product-ion spectra for TA (LCQ).

MS/MS scan	Product Ion (m/z)	Within Spectrum		Among Spectra	
		T	E (n = 3)	T	E (n = 3)
Products of 216	184	100.00	100.0	100.00	100.0
Products of 217	184	5.70	8 ± 1	14.65	17.8 ± 0.4
	185	100.00	100		
Products of 218	184	83.45	91 ± 2	9.94	12.2 ± 0.9
	185	2.04	6 ± 1		
	186	100.00	100		
Products of 219	184	0.00	1 ± 1	1.28	1.8 ± 0.3
	185	100.00	100		
	186	6.83	20 ± 2		
	187	99.91	95 ± 4		

Table 3.62. Theoretical (T) and experimental (E) abundance ratios (%) within and among product-ion spectra for MA (LCQ).

MS/MS scan	Product Ion (m/z)	Within Spectrum		Among Spectra	
		T	E (n = 3)	T	E (n = 3)
Products of 168	94	100.00	100.0	100.00	100.0
Products of 169	94	43.38	45 ± 2	9.96	11 ± 1
	95	100.00	100		
Products of 170	94	100.00	100.0	5.12	4 ± 1
	95	4.44	3.4 ± 0.5		
	96	4.36	3.2 ± 0.5		
Products of 171	94	32.32	33 ± 2	0.44	0.3 ± 0.1
	95	100.00	100		
	96	1.89	1 ± 1		
	97	1.03	1 ± 1		

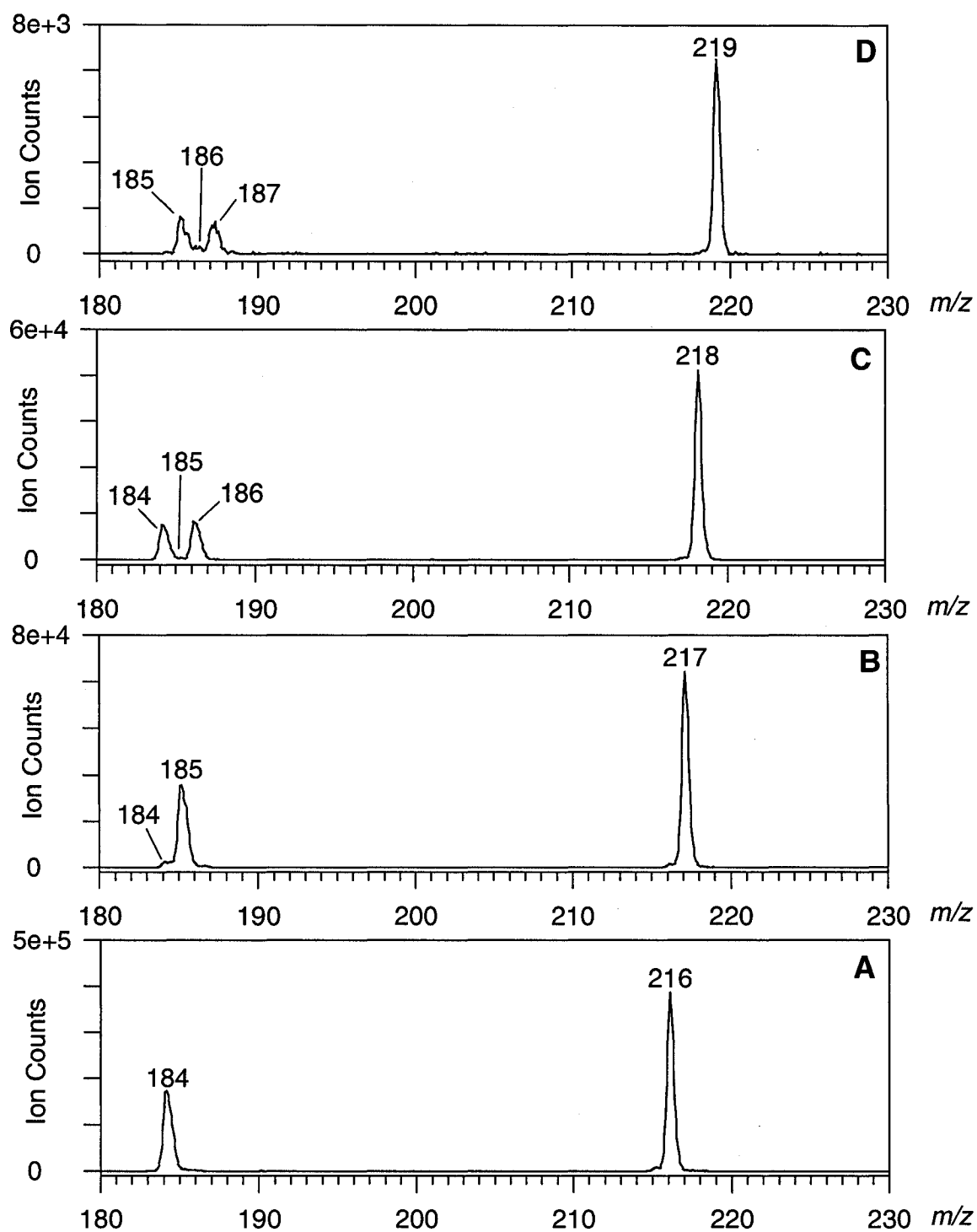


Figure 3.47. Product-ion mass spectra of TA obtained with the LCQ: products of m/z 216 (A), products of m/z 217 (B), products of m/z 218 (C) and products of m/z 219 (D).

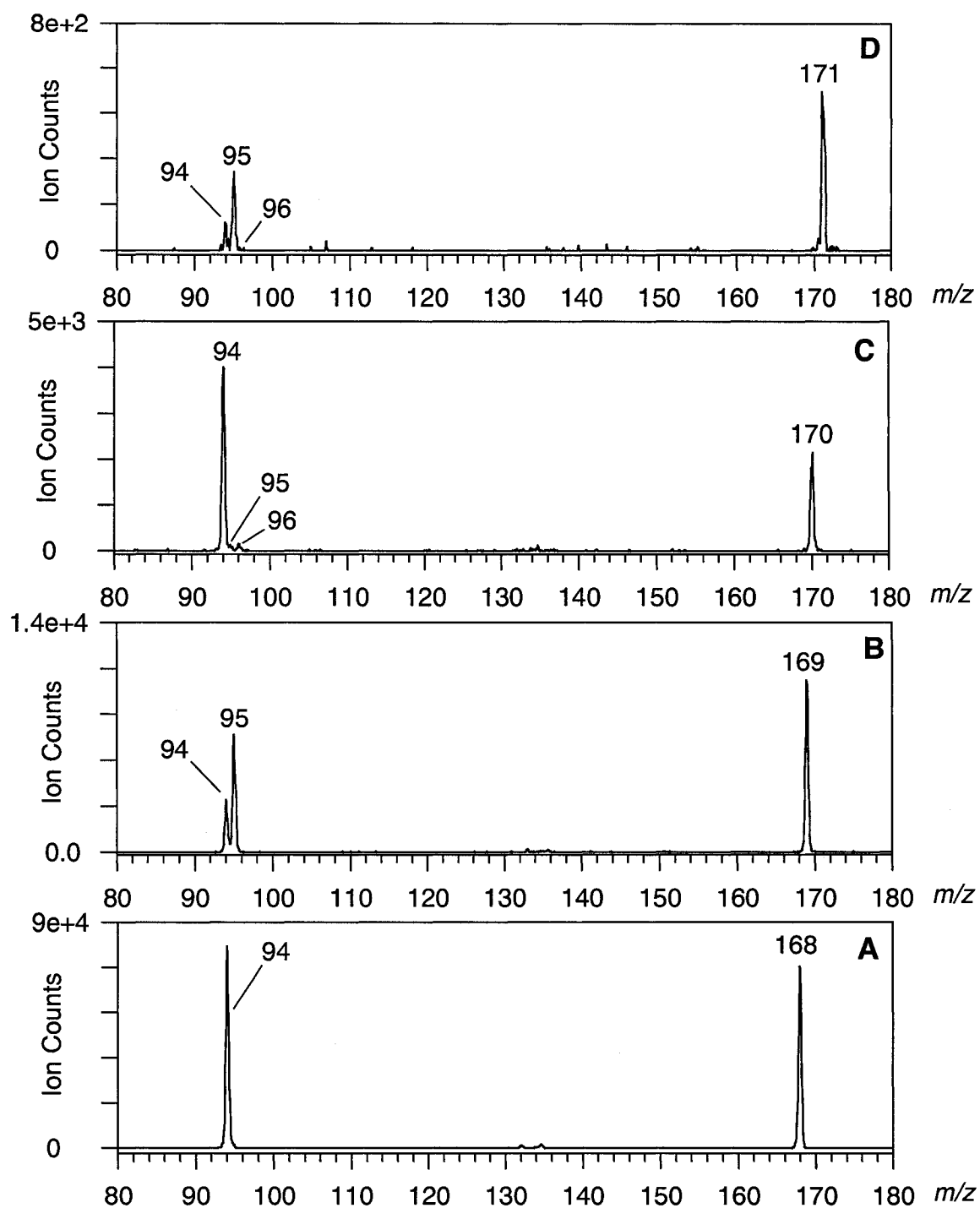


Figure 3.48. Product-ion mass spectra of MA obtained with the LCQ: products of m/z 168 (A), products of m/z 169 (B), products of m/z 170 (C) and products of m/z 171 (D).

Although there are some discrepancies between the theoretical and the experimental abundance ratios in Tables 3.61 and 3.62, the expected trends are still observed. In general, better agreement between experiment and theory was obtained with the QqQ instrument (Tables 3.45 and 3.47). However, higher sensitivity was achieved with the LCQ instrument for the product-ions of m/z 219 and 171 in full-scan mode (Figures 3.47 D and 3.48 D, respectively). In some cases, spectra recorded with the LCQ showed peaks that were poorly resolved, and this problem could not be solved. Although the LCQ could be tuned for maximum sensitivity, the resolution could not be improved by either decreasing the scan rate or changing the tuning parameters. The ion accumulation time and the concentration of analyte were also varied but no improvement in resolution was achieved either.

4.1. Conclusions

This thesis has been a study of methods based on chromatography, mass spectrometry and tandem mass spectrometry for improving the detection of sulfur-containing compounds from petroleum.

Chromatography

Several adsorbents derived from reduced metals supported on silica gel and alumina or ion-exchanged into zeolite Y were tested in order to separate sulfur-containing compounds from similar compounds such as PAHs. Of the adsorbents investigated, the most promising was the reduced form of $\text{PdCl}_2/\text{SiO}_2$. This material retained DBT more strongly than PHEN, yet could be used with MeCN and was easily regenerated with hydrogen and heat. Moreover, as the reduced form of the adsorbent was used, PASHs did not elute as Pd(II) complexes. However, complete separation between PHEN and DBT was not achieved and preparation of adsorbent with optimum % by weight of PdCl_2 depends on the amount of sulfur-containing compounds or total amount of PACs in the samples to be analyzed. Nevertheless, the use of a PdCl_2 adsorbent shows promise as a pre-concentration reagent.

Mass Spectrometry

Both ESI and APCI were examined as possible means by which to analyze PASHs in the presence of other compounds that do not contain sulfur. In general, APCI(+) provided an order of magnitude better sensitivity than ESI(+) for DBT and PY under normal conditions.

In ESI, ionization of DBT, TA and PY was mainly by charge exchange, an unusual observation since MH^+ are the ionic species normally observed in positive-ion ESI. The ionization efficiency of DBT and PY under standard ESI conditions was low and the ion counts for both compounds were similar. In an attempt to enhance the detection of DBT in the presence of PY, the possibility of

forming adduct ions by complexation reactions of PASHs with Ag(I) was studied but no improvement in sensitivity was obtained for DBT.

In APCI studies, both M^{+} and MH^{+} species were observed for DBT, CAR, FLU and PY in MeCN, MeOH and toluene, and the ion yield was mainly dependent on solvent and cone voltage. LODs were determined at different solvent flow rates both in MeCN and in MeOH and better LODs were obtained in MeCN.

The behavior observed at the low and high concentration ranges of the calibration curves agrees with the model which postulates that a maximum number of reagent ions exist in the plasma and that saturation begins to occur when the analyte uses up a significant fraction of all the available reagent ions.

In general, linear ranges extended to higher concentrations at lower solvent flow rates both in MeCN and in MeOH. This observation was explained as an effect of the analyte concentration in the ion source. Since the number of reagent ions available for ionizing the analyte is very similar at different solvent flow rates and more analyte molecules are present in the ion source at higher solvent flow rates, saturation of the analyte response is expected to occur at lower concentrations (or sooner) at higher solvent flow rates.

In addition, an increase in sensitivity was observed at higher probe temperatures, an expected result since vaporization is more efficient at higher probe temperatures and the number of analyte ions will increase with the increase of molecules in the vapor phase.

To test the idea that a maximum number of reagent ions are formed in the corona discharge, the ionization current was measured under different conditions. In general, the ionization current did not vary to a large extent, and this result demonstrated that the number of reagent ions in the plasma is very similar at different solvent flow rates and different solvents.

The results in which two analytes were studied in the same sample (ion competition data) is also consistent with the model which proposes that a limited number of reagent ions is formed in the corona discharge and that competition arises when a considerable fraction of reagent ions is used to ionize two (or

more) analytes present all together in the ion source. Although interference was greater at higher concentrations (non-linear region), there was more interference in MeOH, as compared to MeCN, in the linear region. Both PY and CAR were more successful than DBT in reacting with reagent ions, while FLU seemed less able to compete with DBT. This is consistent with the expected order of ease of charge exchange for the model analytes: PY ~ CAR < FLU ~ DBT.

For analytical purposes in reverse phase LC the above observations indicate that MeCN is superior to MeOH as a solvent (with regard to APCI response but not necessarily with regard to chromatographic behavior) since it provides better LODs and less interference between analytes in the linear response region. For the best LODs in MeCN, high solvent flow rates should be used but if high sensitivity is not a problem a low solvent flow rate would provide savings in solvent, a wider linear range and less deviation from linearity at high concentrations. In the case of complex samples where chromatography does not resolve compounds, care should be taken to operate in the linear response region, especially for quantitative purposes.

The ionization efficiency of analytes (TIC studies) differed markedly among solvents and followed the order: toluene > MeCN > MeOH. This result was explained considering the effect of solvation on the energetics of the charge exchange and proton transfer reactions. Solvation of solvent ions (S^{+*} and SH^+) is expected to be highest in MeOH and lowest in toluene. Therefore, the two ionization mechanisms should be most inhibited by solvation in MeOH and least in toluene, assuming that analyte ionization occurs *via* interaction with solvent ions. Since ionization current values do not explain the large differences observed among solvents in total ion current studies, the number of ions formed in the corona discharge is probably not as important in the formation of the analyte ions as is the nature of the reagent ions.

The higher ionization efficiency in MeOH of the impurity found in pyrene (azapyrene) relative to other PACs suggests that, on an absolute basis, MeOH provides the best medium for proton transfer, and that the ionization of nitrogen-containing bases that protonate on nitrogen is not affected by solvation to a large

extent whereas compounds that protonate on carbon (CAR, DBT and PY) will be much more affected, regardless of their relatively high gas-phase basicities.

The ΔH and ΔG values for the charge exchange and the proton transfer reactions when considering clustering were estimated using the B3LYP/6-31G(d) method. For the clustering reaction $(S)_{n-1}H^+ + S \rightarrow (S)_nH^+$ (where S is either MeCN or MeOH), calculated values were compared with available experimental data and while estimated values were overestimated, the agreement between experiment and theory was reasonably good.

In general, the order obtained in TIC studies (analyte comparison for a given solvent) agrees much better with the order estimated when considering solvated analyte ions, $(S)AH^+$ or $(S)A^{+*}$, as opposed to bare ions, AH^+ or A^{+*} . When comparing both solvents for a given analyte, calculated thermodynamic data show that $MeCN^{+*}$ is a better charge exchange reagent than $MeOH^{+*}$ and that the effect of solvation seems to be less in MeCN. For proton transfer, the two solvents seem closer, although solvation appears to give the edge to MeCN again. However, the differences observed among solvents in TIC studies are larger than the differences predicted by the calculations.

Tandem Mass Spectrometry

MS/MS in a QqQ instrument was used to study fragmentation processes of PASHs and the results show that MS/MS offers the ability to confirm the structure of PASHs through characteristic fragmentation patterns. For the model compounds, the major fragmentations involving the loss of neutral fragments that contain sulfur were $[M - CS]^{+*}$ for BT, $[M - S]^{+*}$ for DBT, $[M - H - S]^+$ for DMDBT and $[M - H - S - H]^{+*}$ for DMDBT. The characteristic fragmentation pattern of the sulfur compounds used as standards may offer the possibility of distinguishing substituted DBTs in the 4 and 6 positions from other DBTs since sulfur appears to be lost mainly from $[M - H]^+$ as opposed to M^{+*} when there is an alkyl group in the 4 and 6 positions of DBT.

SRM experiments were performed using TA and MA to demonstrate the use of natural abundance ratios in MS/MS as a means of identifying sulfur

compounds with greater certainty. Although theoretical and experimental abundance ratios differed in some cases, especially at high collision energies, the expected trends were still observed. Some spectra for the same fragmentation were badly distorted while others were distorted very little. The distortion appeared as variations in the peak heights and in the form of artificial peaks. The extent of the distortion will depend on the resolution (the collision energy and the offset program for Q3), the accuracy of the mass settings of Q1 and Q3, the presence of ions from impurities that can interfere and the relative intensities of the various peaks in the isotope cluster. Spectra obtained from monoisotopic precursor ions and monoisotopic neutral losses were less distorted and they did not display artificial peaks at low masses. Moreover, any false peaks that would arise at high masses in the isotopic cluster were likely to be of very low intensity and thus of little importance. This is because for the common elements present in the compounds studied (C, H, O N and S) the lowest mass isotope is also the most abundant.

4.2. Future Work

The overall goal of the present research is to develop a useful protocol to identify and determine sulfur-containing compounds in complex mixtures. To fully achieve this, it will be necessary to:

- Determine by experiment the ability of various forms of the $\text{PdCl}_2/\text{SiO}_2$ adsorbent to concentrate PASHs in petroleum samples prior to SFC, HPLC, or GC separation and analysis, and if successful, to develop a working system that incorporates the adsorbent.
- Study in detail the fragmentation mechanisms of other PASHs with a different substitution pattern and apply this knowledge to the determination of PASHs using the appropriate chromatography, ionization method and MS/MS technique.

- Investigate which MS/MS technique —constant neutral loss, precursor-ion or product-ion scans— would be best used in the analysis of PASHs in complex mixtures.

A product-ion scan is useful for identifying specific compounds whereas constant neutral loss and precursor-ion scans permit identifying compound classes. However, the possibility of identifying compound classes using a product-ion scan exists if SRM is performed, *i.e.* if Q1 is set to pass a precursor ion that is characteristic of sulfur-containing compounds and Q3 is set to pass a unique product ion also characteristic of sulfur-containing compounds.

A precursor-ion scan detects all precursor ions that fragment to give a common product ion. However, for example, not all $[M - 32]^+$ ions are common to all sulfur-containing compounds (except those that are isomers), and a common fragment ion such as CHS^+ (m/z 45) (Roussis *et al.* 2003 p 298) may not form directly from the M^{+} or the $[M - H]^+$ of the sulfur compound making compound identification difficult.

In a constant neutral loss scan, neither Q1 nor Q3 are set to a specific m/z value. Therefore, this type of scan is especially attractive since the neutral losses of, for example, S or CS, are specific for sulfur-containing compounds. PASHs could be identified not only selectively, *i.e.* in the presence of other compounds that do not contain sulfur, but also specifically, *i.e.* in the presence of other PASHs that have a different substitution pattern or arrangement of groups around the sulfur atom, in a unique experiment. In addition, peak height ratios within a constant neutral loss spectrum may provide more information for compound identification based on isotopic abundance calculations than peak height ratios within a precursor-ion spectrum, since in the former, the fractional abundance ratios within the isotopic pattern are given by the composition of the product ion, which gives more information about the compound than the neutral fragment. However, in the case of unresolved chromatographic peaks, a constant neutral loss scan may not confirm entirely the identity of co-eluting compounds and in this case, a product-ion scan may be necessary for compound identification.

Furthermore, the fragmentation behavior of sulfur-containing compounds for which the neutral fragments S, HS[•], CS, *etc.* are lost from different precursor ions, [M – H]⁺ and/or M⁺⁺, can be more easily confirmed by calculating the isotopic abundance ratios within a precursor-ion spectrum rather than within a neutral loss spectrum, since the peak height ratios in a precursor-ion spectrum are more conveniently calculated considering the composition of the neutral fragment.

- Examine the possibility that the use of the MS/MS technique will permit identifying organosulfur compounds in complex mixtures with little or no preliminary chromatographic separation. Determine the circumstances under which this can be achieved.
- Determine the optimum conditions for mass spectrometric detection of sulfur-containing compounds using various operating modes and chromatographic techniques, for example, GC/EI/MS/MS, SFC/APCI/MS/MS, HPLC/APCI/MS/MS, HPLC/ESI/MS/MS, and apply two dimensional chromatography, for example SFC/GC, to perform high resolution separations of sulfur-containing compounds in petroleum samples.

Appendix A. Calculation of Flow Rates

Considering that the total gas flow rate is 500 sLph at 25 °C (298.15 K), the molar volume for an ideal gas is 24.8 L mol⁻¹ at 25 °C and 1 bar, the solvent flow rate is 0.5 mL min⁻¹, the analyte concentration is 1e-5 mol L⁻¹ and assuming that no more than 0.008 % of water on a volume basis is present in the solvent, then the flow rate (FR) in mol min⁻¹ for N₂ gas, each solvent, analyte and water can be calculated as follows

$$\text{Gas FR} = (500 \text{ L h}^{-1}) / (24.8 \text{ L mol}^{-1}) / (60 \text{ min h}^{-1}) = 0.336 \text{ mol min}^{-1}$$

$$\text{MeCN FR} = (0.5 \text{ mL min}^{-1})(0.786 \text{ g mL}^{-1}) / (41.0 \text{ g mol}^{-1}) = 9.58\text{e-}3 \text{ mol min}^{-1}$$

$$\text{MeOH FR} = (0.5 \text{ mL min}^{-1})(0.791 \text{ g mL}^{-1}) / (32.0 \text{ g mol}^{-1}) = 1.24\text{e-}2 \text{ mol min}^{-1}$$

$$\text{Toluene FR} = (0.5 \text{ mL min}^{-1})(0.865 \text{ g mL}^{-1}) / (92.1 \text{ g mol}^{-1}) = 4.71\text{e-}3 \text{ mol min}^{-1}$$

$$\text{Water FR} = (0.5 \text{ mL min}^{-1})(0.008 \%)(0.055 \text{ mol mL}^{-1}) = 2.22\text{e-}6 \text{ mol min}^{-1}$$

$$\text{Analyte FR} = (0.5 \text{ mL min}^{-1})(1\text{e-}5 \text{ mol L}^{-1}) / (1000 \text{ mL L}^{-1}) = 5.00\text{e-}9 \text{ mol min}^{-1}$$

The relative concentration of water was also calculated although water was not added on purpose to any solution. The major source of water in the ion source was assumed to be as an impurity in the solvent. Densities and molecular weights of interest are listed in Table A1.

Table A1. Density and molecular weight of MeCN, MeOH, toluene and water.

Species	Density ^a (g mL ⁻¹)	M.W. (g mol ⁻¹)
MeCN	0.786	41.0
MeOH	0.791	32.0
Toluene	0.865	92.1
Water	1.000	18.0

^a Taken from the Aldrich Handbook of Fine Chemicals 2007.

Appendix B. Calculation of Proton Affinities

The proton affinity (PA) values for DBT, CAR and FLU are not reported in the literature. Therefore, PA values for these compounds were estimated using the Gaussian suite of programs. One advantage of determining proton affinities *via* computational methods is that absolute rather than relative values of the proton affinity are obtained (Deakyne 2003). However, we can not apply high levels of theory, such as Gaussian-2, which provide excellent results, due to the lack of computational resources and the relatively large systems under investigation. Since calculations based on density functional theory are known to produce reliable estimations of thermochemical data (Rabuck and Scuseria 1999), we used the B3LYP and the PBE1PBE methods to calculate the proton affinity of model PACs. PBE1PBE is the generalized-gradient-approximation-exchange-correlation functional of Perdew, Burke and Ernzerhof (Perdew *et al.* 1996).

The proton affinity is defined as the negative of the enthalpy change for the reaction $A + H^+ \rightarrow AH^+$ and, can be computed as

$$PA(A) = -\Delta H = -\left[(E_e(AH^+) - E_e(A)) + (ZPE(AH^+) - ZPE(A)) - \frac{5}{2}RT \right]$$

where A and AH^+ denote the analyte and its protonated form, respectively; E_e is the electronic energy and ZPE is the zero point energy (Chandra and Goursot 1996). The last term in the equation incorporates the correction for translational and rotational energy changes assuming classical behaviour ($3/2 RT$) and the ΔnRT term needed to change an energy to enthalpy supposing ideal gas behaviour ($R = 8.3144 \text{ kJ mol}^{-1} \text{ K}^{-1}$, $T = 298.15 \text{ K}$).

The geometries of the A and AH^+ species were optimized at the B3LYP/6-31G(d) level of theory. The structure of the protonated molecule used in the calculations was that with the lowest energy from all the possible AH^+ isomers.

Single-point energy calculations were done on the optimized geometries of A and AH^+ using both the B3LYP and the PBE1PBE methods. The electronic energy of A and AH^+ species was estimated using the B3LYP method and the following basis sets: 6-31G(d), 6-31+G(d), 6-311G and 6-311+G(d,p). When using the PBE1PBE method, only the 6-31+G(d) basis set was employed. The zero-point energy value obtained at the B3LYP/6-31G(d) level was scaled using a factor of 0.9804, as recommended by Foresman (Foresman 1996).

The proton affinities of compounds such as thiophene, pyrrole, acetonitrile, cyclopentanone, benzophenone, phenanthrene, anthracene, toluene and methanol were calculated in order to compare estimates with experimental values reported in the literature. The calculated and experimental proton affinities of model compounds are reported in Table B1. The average absolute deviation (ave. abs. dev.), the maximum positive deviation (max. dev. (+)) and the maximum negative deviation (max. dev. (-)) for each method are also listed in Table B1. The deviation is the difference between the experimental and the theoretical values (deviation = experiment – theory). The average absolute deviation is the average of the absolute values of each deviation.

In general, the agreement between experiment and theory was better when the PBE1PBE/6-31+G(d)//B3LYP/6-31G(d) level of theory was used. Therefore, proton affinity values obtained using the PBE1PBE method were the ones employed to calculate the ΔH of reactions (12), (14), (15), (16) and (17).

Table B1. Proton affinities of model compounds at the B3LYP and the PBE1PBE levels of theory and different basis sets.

Species	B3LYP			PBE1PBE 6-31+G(d)	Expt ^a
	6-31G(d)	6-31+G(d)	6311G	6-311+G(d,p)	
DBT	8.85	8.66	8.56	8.64	–
CAR	9.35	9.12	9.09	9.10	–
FLU	9.24	9.02	9.03	9.11	–
PY	9.45	9.24	9.20	9.21	9.01
Thiophene	8.78	8.61	8.55	8.59	8.45
Pyrrole	9.37	9.14	9.12	9.09	9.07
Cyclopentanone	8.67	8.48	8.49	8.60	8.54
Benzophenone	9.47	9.24	9.29	9.35	9.14
Phenanthrene	8.95	8.73	8.70	8.71	8.56
Anthracene	9.13	9.30	9.26	9.29	9.09
Acetonitrile	8.20	8.05	8.27	8.16	8.08
Methanol	7.92	7.71	8.04	7.82	7.82
Toluene	8.52	8.34	8.30	8.33	8.13
Ave. abs. dev.	0.26	0.14	0.14	0.13	–
Max. dev. (+)	–	0.11	0.05	0.00	–
Max. dev. (–)	0.44	0.23	0.22	0.21	–

^a Values taken from <http://www.webbook.nist.gov>, access date: February 5, 2007

Appendix C. Summary of Thermodynamic Data

Table C1. Summary of thermodynamic properties for the species of N₂, MeCN, MeOH and toluene at the B3LYP/6–31G(d) level of theory.

Species	S ^a	– E _e ^a	ZPE ^a	– H ^a	– G ^a
N ₂	D _{∞h}	109.52413	0.005599	109.51522	109.53698
N ₂ ⁺	D _{∞h}	108.94639	0.005340	108.93776	108.96018
N ₄ ⁺	D _{∞h}	218.53984	0.012471	218.52066	218.55415
MeCN	C _{3v}	132.75493	0.04564	132.70475	132.73227
[MeCN+H] ⁺	C _{3v}	133.06426	0.05627	133.00310	133.03119
[(MeCN) ₂ +H] ⁺	C _{3v}	265.87135	0.10032	265.76113	265.80499
[(MeCN) ₃ +H] ⁺	C _{3v}	398.64238	0.14852	398.47818	398.54276
MeCN ⁺	C _s	132.32017	0.04008	132.27502	132.30518
[(MeCN) ₂] ⁺	C ₁	265.18088	0.092813	265.07981	265.11981
[(MeCN) ₃] ⁺	C ₁	397.96184	0.14280	397.80735	397.85849
MeOH	C _s	115.71441	0.051471	115.65870	115.68566
[MeOH+H] ⁺	C _s	116.01574	0.064360	115.94684	115.97459
[(MeOH) ₂ +H] ⁺	C ₂	231.78852	0.11578	231.66444	231.70334
[(MeOH) ₃ +H] ⁺	C ₁	347.54262	0.17097	347.35868	347.41187
MeOH ⁺	C _s	115.33088	0.047532	115.27896	115.30681
[(MeOH) ₂] ⁺	C ₁	231.11312	0.10187	231.00297	231.04362
[(MeOH) ₃] ⁺	C ₁	346.87137	0.15617	346.70239	346.75645
Toluene	C _s	271.56665	0.12833	271.43118	271.46884
[Tol H] ⁺ <i>ortho</i>	C _s	271.88530	0.13854	271.73988	271.77629
[Tol+H] ⁺ <i>meta</i>	C ₁	271.87969	0.13862	271.73339	271.77159
[Tol+H] ⁺ <i>para</i>	C _s	271.88742	0.13858	271.74116	271.77977
[Tol+H] ⁺ <i>ipso</i>	C _s	271.87291	0.13981	271.72574	271.76332
[Toluene] ⁺	C _s	271.25774	0.12631	271.12378	271.16411

^a Electronic energies (E_e), enthalpies (H), Gibbs free energies (G) and zero point energies (ZPE) in hartrees; S stands for symmetry.

Table C2. Summary of thermodynamic properties for the species of DBT, PY, CAR and FLU at the B3LYP/6–31G(*d*) level of theory.

Species	S ^a	– E _e ^a	ZPE ^a	– H ^a	– G ^a
DBT	C _{2v}	860.30686	0.16166	860.13513	860.17914
[DBT+H] ⁺ C3	C _s	860.64035	0.17254	860.45723	860.50293
[DBT] ⁺⁺	C _{2v}	860.03147	0.16068	859.86046	859.90559
[DBT+MeOH+H] ⁺	C ₁	976.37033	0.22510	976.12973	976.19029
[DBT+MeOH] ⁺⁺	C ₁	975.76299	0.21381	975.53382	975.59310
[DBT+MeCN+H] ⁺	C ₁	993.41376	0.21874	993.17838	993.24207
[DBT+MeCN] ⁺⁺	C ₁	992.80419	0.20714	992.58094	992.64437
PY	D _{2h}	615.77313	0.20769	615.55448	615.59938
[PY+H] ⁺ C3	C _s	616.12944	0.21946	615.89854	615.94584
[PY] ⁺⁺	D _{2h}	615.52138	0.20791	615.30239	615.34820
[PY +MeOH+H] ⁺	C ₁	731.85846	0.27223	731.56908	731.63073
[PY +MeOH] ⁺⁺	C ₁	731.25126	0.26098	730.97407	731.03523
[PY +MeCN+H] ⁺	C ₁	748.89957	0.26567	748.61680	748.68268
[PY +MeCN] ⁺⁺	C _s	748.29087	0.25424	748.01972	748.08444
CAR	C _{2v}	517.47062	0.17694	517.28381	517.32699
[CAR +H] ⁺ C4	C _s	517.82359	0.18907	517.62444	517.66875
[CAR] ⁺⁺	C _{2v}	517.20918	0.17648	517.02285	517.06665
[CAR +MeOH+H] ⁺	C ₁	633.56487	0.24265	633.30740	633.36431
[CAR +MeOH] ⁺⁺	C ₁	632.95167	0.23010	632.70701	632.76404
[CAR +MeCN+H] ⁺	C ₁	650.60558	0.23781	650.35247	650.41375
[CAR +MeCN] ⁺⁺	C _s	649.99407	0.22346	649.75531	649.81621
FLU	C _{2v}	575.43704	0.16999	575.25656	575.30149
[FLU +H] ⁺ O	C _s	575.78652	0.18254	575.59314	575.63918
[FLU] ⁺⁺	C _{2v}	575.14946	0.16938	574.96930	575.01552
[FLU +MeOH+H] ⁺	C ₁	691.53873	0.23612	691.28771	691.34505
[FLU +MeOH] ⁺⁺	C ₁	690.88264	0.22271	690.64419	690.70424
[FLU +MeCN+H] ⁺	C _s	708.57864	0.22909	708.33340	708.39528
[FLU +MeCN] ⁺⁺	C ₁	707.92416	0.21602	707.69163	707.75578

^a Electronic energies (E_e), enthalpies (H), Gibbs free energies (G) and zero point energies (ZPE) in hartrees; S stands for symmetry.

Appendix D. Examples of Potential Energy Curves

Potential energy surfaces were constructed using the N–N distance (R_1) and the proton–nitrogen distance (R_2) (Figure D1) with the aim of locating the optimum N–N distance that would generate the minimum-energy geometry for the $(\text{MeCN})_2\text{H}^+$ cluster.

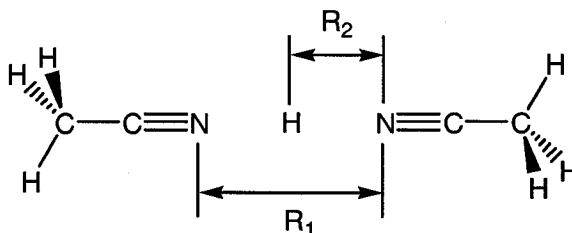


Figure D1. Coordinates used to obtain potential energy curves for $[(\text{MeCN})_2\text{H}]^+$.

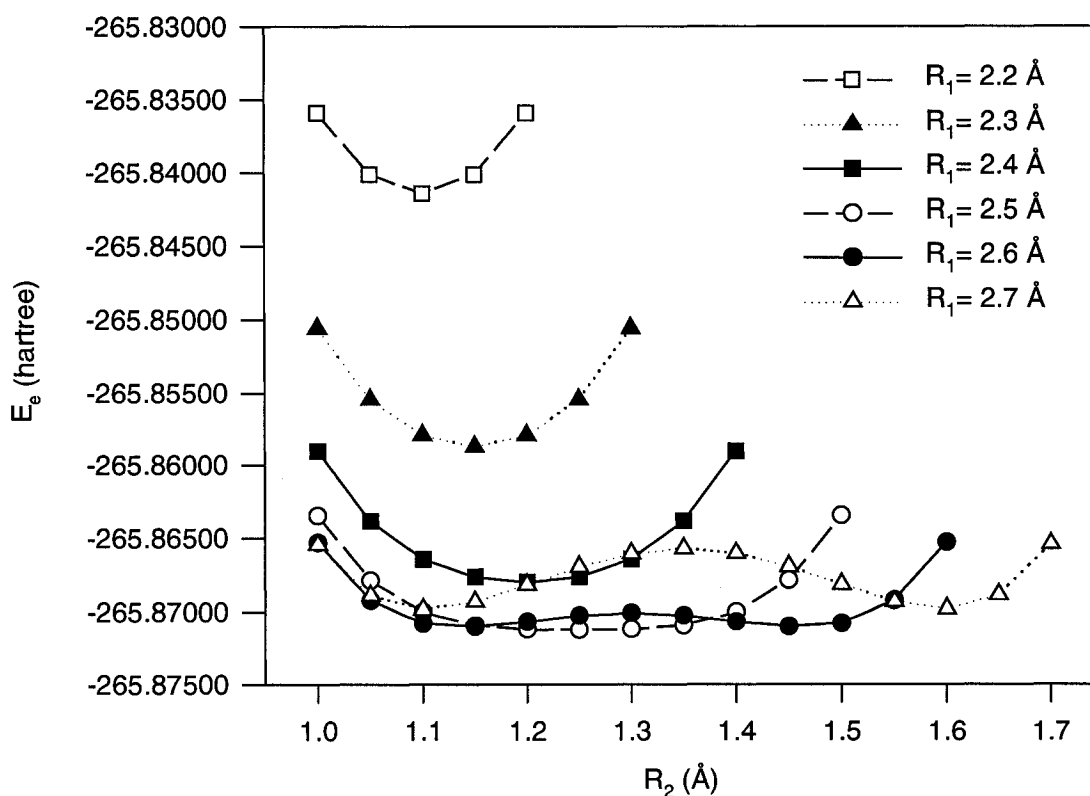


Figure D2. Potential energy surfaces for $[(\text{MeCN})_2\text{H}]^+$ as a function of the N–H distance (R_2) and parametric in the N–N distance (R_1).

The calculated potential energy curves for several values of R_1 are displayed in Figure D2. For each curve in the figure, R_1 is kept constant while R_2 is augmented in 0.05 Å increments. The potential energy surface has several local minima for R_1 values lower than 2.5 Å. For R_1 values greater than 2.5 Å, the energy of the system increases and curves have symmetric double-well shapes. The global minimum is obtained for $R_1=2.5$ Å, which agrees with the results obtained by Hirao *et al.* (Hirao *et al.* 1982a) using the HF/4–31G level of theory.

A flat potential energy curve is produced by rotating the two methyl groups in $[(\text{MeCN})_2+\text{H}]^+$ (figure not shown). The methyl groups are 7.7 Å apart in $[(\text{MeCN})_2+\text{H}]^+$. Similar results were obtained for the $[(\text{MeCN})_3+\text{H}]^+$ cluster, indicating that the energy of the $(\text{MeCN})_{n=2,3}\text{H}^+$ clusters is practically unaffected by rotation of the methyl groups.

Potential energy surfaces were also constructed for two possible $[(\text{MeOH})_2+\text{H}]^+$ cluster ions (Figure D3). Each curve in the figure was obtained by varying the dihedral angle C–O...O–C from 0 to 180°. The minimum-energy structure is obtained when the dihedral angle is about 130° for one of the $[(\text{MeOH})_2+\text{H}]^+$ isomers.

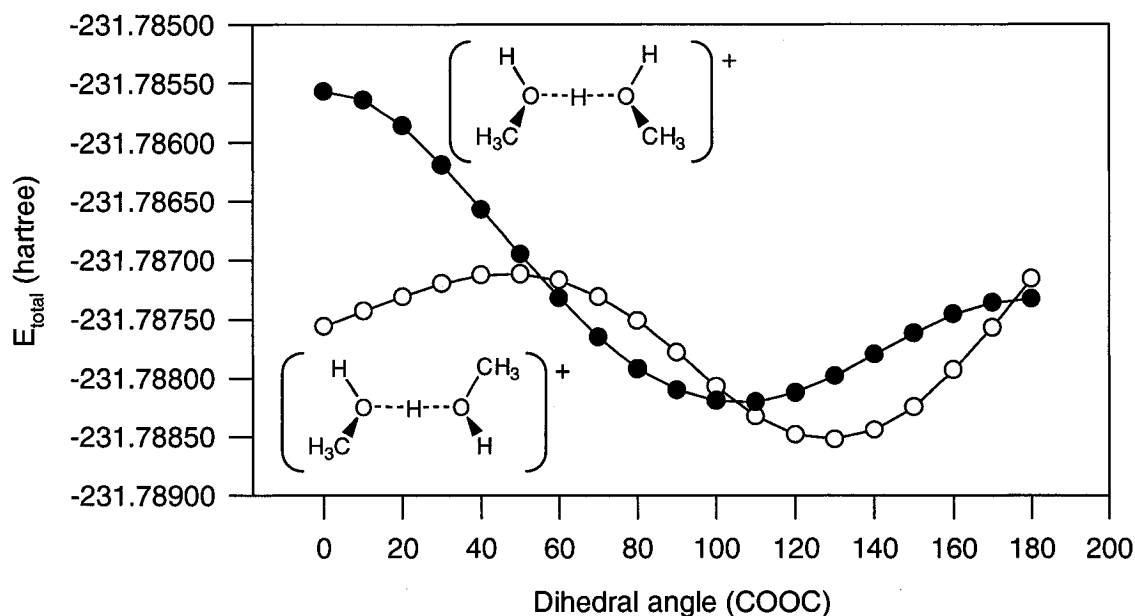


Figure D3. Potential energy curves for two $[(\text{MeOH})_2+\text{H}]^+$ isomers.

Appendix E. Derivation of Equations (3.8), (3.9) and (3.10)

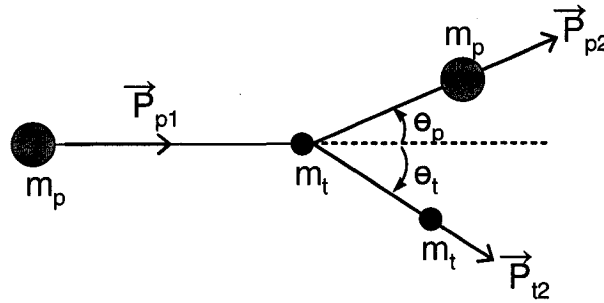
Two types of collisions can occur in a gas cell (q2): elastic and inelastic. In an elastic collision none of the kinetic energy of the colliding particles is converted into internal energy and in an inelastic collision some of the kinetic energy is converted. In either case, both momentum and total energy are conserved.

In the following discussion t represents the target, p the precursor ion, θ the scattering angle, m mass, v velocity, P momentum and T kinetic energy, 1 denotes initial state (before collision) and 2 final state (after collision). Momentum and velocity are vector quantities while kinetic energy is normally considered a scalar.

$$P = mv$$

$$T = \frac{mv^2}{2}$$

The collision can be depicted as follows



The law of conservation of momentum for a collision of two particles can be written as

$$P_{p1} + P_{t1} = P_{p2} + P_{t2}$$

The kinetic energy of the target at room temperature (300 K) is approximately

$$T_t \cong kTemp = \left(1.38e-23 \frac{J}{K} \right) (300 K) = 4.14e-21 J$$

A typical kinetic energy (collision energy in the lab frame) for a precursor ion is 20 eV or

$$T_p = (20 \text{ V})(1.60 \times 10^{-19} \text{ C}) = 3.20 \times 10^{-18} \text{ J}$$

The ratio of velocities of the colliding particles is given by (assuming that the precursor ion has a mass of 200 u and that the target is an argon atom)

$$\frac{v_p}{v_t} = \left(\frac{m_t T_p}{m_p T_t} \right)^{\frac{1}{2}} = \left(\frac{40 \times 3.20 \times 10^{-18}}{200 \times 4.14 \times 10^{-21}} \right)^{\frac{1}{2}} = 12.4$$

The velocity of the precursor ion is about ten times higher than the velocity of the target atom. Therefore the target can be considered to be at rest and under this condition the law of conservation of momentum becomes

$$P_{p1} = P_{p2} + P_{t2}$$

The law of conservation of momentum along the x and y axes can be written as [1] and [2], respectively (see the collision diagram above)

$$P_{p1} = P_{p2} \cos \theta_p + P_{t2} \cos \theta_t \quad (\text{along x axis}) \quad [1]$$

$$0 = P_{p2} \sin \theta_p - P_{t2} \sin \theta_t \quad (\text{along y axis}) \quad [2]$$

From the equation for the components of momentum along the y axis [2] and considering that $\sin^2 \theta + \cos^2 \theta = 1$,

$$P_{p2}^2 (1 - \cos^2 \theta_p) = P_{t2}^2 (1 - \cos^2 \theta_t)$$

$$P_{t2}^2 \cos^2 \theta_t = P_{t2}^2 - P_{p2}^2 + P_{p2}^2 \cos^2 \theta_p \quad [3]$$

From the equation for the components of momentum along the x axis [1],

$$P_{t2} \cos \theta_t = P_{p1} - P_{p2} \cos \theta_p$$

$$P_{t2}^2 \cos^2 \theta_t = P_{p1}^2 - 2 P_{p1} P_{p2} \cos \theta_p + P_{p2}^2 \cos^2 \theta_p \quad [4]$$

Equating [3] and [4] and after rearrangement,

$$P_{t2}^2 = P_{p1}^2 + P_{p2}^2 - 2 P_{p1} P_{p2} \cos \theta_p \quad [5]$$

Equation [5] applies both to elastic and inelastic collisions. For an inelastic collision, the conservation of total energy can be written as [6], where Q is the internal energy converted from kinetic energy.

$$T_{p1} = T_{p2} + T_{t2} + Q \quad [6]$$

Since $T = P^2/2m$, equation [6] becomes [7]

$$Q = \frac{P_{p1}^2}{2m_p} - \frac{P_{p2}^2}{2m_p} - \frac{P_{t2}^2}{2m_t} \quad [7]$$

P_{t2}^2 can be eliminated from [7] using [5] derived above

$$Q = \left(\frac{P_{p1}^2}{2} \right) \left(\frac{1}{m_p} - \frac{1}{m_t} \right) - \left(\frac{P_{p2}^2}{2} \right) \left(\frac{1}{m_p} + \frac{1}{m_t} \right) + \frac{P_{p1} P_{p2} \cos \theta_p}{m_t} \quad [8]$$

To determine the maximum value of Q as a function of the scattering angle, the equation for Q as a function of P_{p2} [8] can be differentiated and set equal to zero (it will be assumed that P_{p1} and θ_p are constant).

$$\frac{dQ}{dP_{p2}} = -P_{p2} \left(\frac{1}{m_p} + \frac{1}{m_t} \right) + \frac{P_{p1} \cos \theta_p}{m_t} \quad [9]$$

When [9] is set equal to zero

$$P_{p2} = \left[\frac{m_p}{(m_p + m_t)} \right] P_{p1} \cos \theta_p \quad \text{for } Q = Q_{\max} \quad [10]$$

$$P_{p2}^2 = \left[\frac{m_p^2}{(m_p + m_t)^2} \right] P_{p1}^2 \cos^2 \theta_p \quad \text{for } Q = Q_{\max} \quad [11]$$

Equations [10] and [11] can be substituted into [8] to eliminate P_{p2}

$$Q_{\max} = \left(\frac{P_{p1}^2}{2} \right) \left[\frac{(m_t - m_p)}{m_p m_t} + \left(\frac{1}{m_t} \right) \left(\frac{m_p}{(m_p + m_t)} \right) (\cos^2 \theta_p) \right] \quad [12]$$

Equation [12] can be recast in terms of energies since $P^2 = 2Tm$ to obtain (3.8). (In (3.8) T_{p1} has been substituted for E_{lab}).

$$Q_{\max} = E_{lab} \left[\frac{(m_t - m_p)}{m_t} + \left(\frac{1}{m_t} \right) \left(\frac{m_p^2}{(m_p + m_t)} \right) (\cos^2 \theta_p) \right] \quad (3.8)$$

The maximum in Q_{\max} occurs at $\theta_p = 0$, $\cos^2 \theta_p = 1$, which simplifies to (3.9).

$$Q_{\max} = E_{lab} \left[\frac{m_t}{m_p + m_t} \right] \quad \text{for } \theta_p = 0^\circ \quad (3.9)$$

The equation above for Q [8] can be solved for P_{p2} to give the quadratic (after some rearrangement)

$$\left[\frac{(m_p + m_t)}{m_p} \right] P_{p2}^2 - 2P_{p1} \cos \theta_p P_{p2} - \left[\frac{(m_p + m_t)}{m_p} \right] P_{p1}^2 + 2m_t Q = 0 \quad [13]$$

Using the quadratic formula to solve for P_{p2} gives [14]

$$P_{p2} = \left[\frac{P_{p1}}{(m_p + m_t)} \right] \left\{ m_p \cos \theta_p \pm \left[m_p^2 \cos^2 \theta_p + m_t^2 - m_p^2 - \frac{2m_p m_t (m_p + m_t) Q}{P_{p1}^2} \right]^{1/2} \right\} \quad [14]$$

This result indicates that there will be two values of P_{p2} at each value of P_{p1} , θ_p and Q . It also shows that Q cannot exceed Q_{\max} [12] or the value of the square root term in [14] becomes negative. The equation above for P_{p2} [14] can be converted into (3.10) by considering that

$$\frac{P_{p2}^2}{P_{p1}^2} = \frac{T_{p2}}{T_{p1}} \quad P_{p1}^2 = 2m_p T_{p1}$$

In (3.10), $M = m_p + m_t$, $E'_{lab} = T_{p2}$ and $E_{lab} = T_{p1}$.

$$\frac{E'_{lab}}{E_{lab}} = \left[\frac{1}{M^2} \right] \left\{ m_p \cos \theta_p \pm \left[m_p^2 \cos^2 \theta_p + m_t^2 - m_p^2 - m_t M \frac{Q}{E_{lab}} \right]^{1/2} \right\}^2 \quad (3.10)$$

Equation [14] can be used to calculate values of P_{p2} for various values of P_{p1} , θ_p and Q . P_{t2} can be calculated from the law of conservation of energy [15]

$$P_{t2} = \left[P_{p1}^2 \left(\frac{m_t}{m_p} \right) - P_{p2}^2 \left(\frac{m_t}{m_p} \right) - 2m_t Q \right]^{1/2} \quad [15]$$

and θ_t can be calculated from [16].

$$\sin \theta_t = \left(\frac{P_{p2}}{P_{t2}} \right) \sin \theta_p \quad [16]$$

When $Q = Q_{\max}$, there will only be one value for P_{p2} , P_{t2} , and θ_t , since the square root term becomes zero under these circumstances. Q_{\max} decreases as θ_p increases and goes to zero when

$$\cos \theta_p = \left[1 - \left(\frac{m_t}{m_p} \right)^2 \right]^{\frac{1}{2}} \quad [17]$$

Therefore the least internal energy is available at the maximum scattering angle [17] and the available energy increases as the scattering angle decreases (for both values of P_{p2}). For values of $Q < Q_{\max}$, there will be two values of P_{p2} , P_{t2} , and θ_t for every value of Q . When the positive root of the quadratic equation (3.10) is used the results apply to more glancing angles of collision, and when the negative value is used, more direct collisions are involved.

Reference List

- Abian, J. **1999** The coupling of gas and liquid chromatography with mass spectrometry, *J. Mass Spectrom.* 34, 157–168.
- Aebersold R. and Goodlett, R. **2001** Mass spectrometry in proteomics, *Chem. Rev.* 101, 269–295.
- Aksenov, V. S. and Kamyarov, V. F. **1980** Regularities in composition and structures of native sulfur compounds from petroleum. In *Organic sulfur chemistry*, edited by Freidlina R. K. and Skorova A. E., Pergamon Press: Oxford.
- Anacleto, J. F.; Ramaley L.; Benoit, F. M.; Boyd, R. K. and Quilliam, M. A. **1995** Comparison of Liquid Chromatography/Mass Spectrometry Interfaces for the Analysis of Polycyclic Aromatic Hydrocarbons, *Anal. Chem.* 67, 4145–4154.
- Andersson, J. T. **1987** Retention properties of a palladium chloride/silica sorbent for the liquid chromatographic separation of polycyclic aromatic sulfur heterocycles, *Anal. Chem.* 59, 2207–2209.
- Andersson J. T.; Hegazi, A. H. and Roberz, B. **2006** Polycyclic aromatic sulfur heterocycles as information carriers in environmental studies, *Anal. Bioanal. Chem.* 386, 891–905.
- Ardrey, B. **2003** In *Liquid chromatography–Mass spectrometry: an introduction*, Analytical Techniques in the Sciences, John Wiley: NY.
- Ashcroft, A. E. **1997** In *Ionization methods in organic mass spectrometry*, RSC Analytical Spectroscopic Monographs, edited by Barnett N. W., The Royal Society of Chemistry: Cambridge.
- Babich, I. V. and Moulijn, J. A. **2003** Science and technology of novel processes for deep desulfurization of oil refinery streams: a review, *Fuel* 82, 607–631.
- Becke, A. D. **1993** A new mixing of Hartree–Fock and local density-functional theory *J. Chem. Phys.* 98, 1372–1377.
- Bej, S. K. **2004a** Revamping of diesel hydrodesulfurizers: options available and future research needs, *Fuel Processing Technology* 85, 1503–1517.

Bej, S. K.; Maity S. K.; Turaga U. T. **2004b** Search for an efficient 4,6-DMDBT Hydrodesulfurization catalyst: a review of recent studies, *Energy & Fuels* 18, 1227–1237.

Boyd, S. L. and Boyd, R. B. **2007** A density functional study of methanol clusters, *J. Chem. Theory Comput.* 3, 54–61.

Breyse, M.; Djega–Mariadassou, G.; Pessayre, S.; Geantet, C.; Vrinat M.; Pérot, G.; Lemaire M. **2003** Deep desulfurization: reactions, catalysts and technological challenges, *Catalysis Today* 84, 129–138.

Busch, K. L.; Glish G. L.; McLuckey, S. A. **1988** In *Mass spectrometry/mass spectrometry: techniques and applications of tandem mass spectrometry*, VCH Publishers: NY.

Carroll, D. I.; Dzidic, I.; Stillwell, R. N.; Haegele, K. D. and Horning, E. C. **1975** Atmospheric pressure ionization mass spectrometry: a corona discharge ion source for use in liquid chromatography-mass spectrometer-computer analytical system, *Anal. Chem.* 47, 2369–2373.

Chambers, D. M.; Goeringer, D. E.; McLuckey, S. A.; Glish, G. L. **1993** Matrix-assisted laser desorption of biological molecules in the quadrupole ion trap mass spectrometer, *Anal. Chem.* 65, 14–20.

Chandra, A. K. and Goursot, A. **1996** Calculation of proton affinities using density functional procedures: a critical study *J. Phys. Chem.* 100, 11596–11599.

Cheskis, S.; Atar, E. and Amirav A. **1993** Pulsed-flame photometer: a novel gas chromatography detector, *Anal. Chem.* 65, 539–555.

Christie, T.; Brathwaite, B. and Thompson, B. **2002** Mineral commodity report 23–zeolites, *New Zealand Mining* 31, 16–24.

Cole, R. B. **1997** In *Electrospray ionization mass spectrometry: fundamentals, instrumentation, and applications*, John Wiley: NY.

Dandeneau, R. D. and Zerenner, E. H. **1979** An investigation of glasses for capillary chromatography, *Journal of High Resolution Chromatography and Chromatography Communications* 2, 351–356.

Dawson, P. H. 1976 In *Quadrupole mass spectrometry and its applications*, Elsevier: NY.

de Hoffmann, E.; Charette, J.; Stroobant, V. 1996 In *Mass spectrometry principles and applications*, John Wiley: NY, 2nd edition.

de Laeter, J. R.; Böhlke, J. K.; de Bièvre; Hidaka, H.; Peiser, H. S.; Rosman, K. J. R. and Taylor, P. D. P. 2003 Atomic weights of the elements: Review 2000 (IUPAC technical report) *Pure Appl. Chem.* 75, 683–800.

de Zeeuw J. and Luong J. 2002 Development in stationary phase technology for gas chromatography, *Trends in analytical chemistry* 21, 594–607.

Deakyne, C. A. 2003 Proton affinities and gas phase-basicities: theoretical methods and structural effects, *Int. J. of Mass Spectrom.* 227, 601–616.

Dempster, A. J. 1918 A new method of positive ray analysis, *Phys. Rev.* 11, 316–324.

Devlin, J. L.; Wolf, J. F.; Taft, R. W. and Hehre, W. J. 1975 The proton affinities of toluene, *J. Am. Chem. Soc.* 98, 1990–1992.

Douglas, D. J. 1982 Mechanism of the collision induced dissociation of polyatomic ions studied by triple quadrupole mass spectrometry, *J. Phys. Chem.* 86, 185–191.

Dressler, M. 1986 In *Selective gas chromatographic detectors*, Journal of Chromatography Library Volume 36, Elsevier: Amsterdam.

Dzidic, I.; Carroll, D. I.; Stillwell, R. N. and Horning, E. C. 1976 Comparison of positive ions formed in nickel-63 and corona discharge ion sources using nitrogen, argon, isobutene, ammonia and nitric oxide as reagents in atmospheric pressure ionization mass spectrometry, *Anal. Chem.* 48, 1763–1768.

Ettre, L. S. 2000 Starting a new century, *J. Chromatogr. Sci.* 38, 89–90.

Fenn, J. B.; Mann, M.; Meng, C. K.; Wong, S. F. and Whitehouse, C. M. 1989 Electrospray ionization for mass spectrometry of large molecules, *Science* 246, 64–71.

Fjeldsted, J. C. and Lee, M. L. **1984** Capillary supercritical fluid chromatography, *Anal. Chem.* 56, 619A–628A.

Foresman, J. B. **1996** In *Exploring chemistry with electronic structure methods*, Pittsburgh, PA: Gaussian Inc., 2nd edition.

Fujikawa, T. **2006** Highly active CoMo HDS catalyst for the production of clean diesel fuels, *Catalysis Surveys from Asia* 10, 89–97.

Gaussian **2003**, Revision B.05, Frisch, M. J.; Trucks, G. W.; Schlegel, H. B.; Scuseria, G. E.; Robb, M. A.; Cheeseman, J. R.; Montgomery, Jr., J. A.; Vreven, T.; Kudin, K. N.; Burant, J. C.; Millam, J. M.; Iyengar, S. S.; Tomasi, J.; Barone, V.; Mennucci, B.; Cossi, M.; Scalmani, G.; Rega, N.; Petersson, G. A.; Nakatsuji, H.; Hada, M.; Ehara, M.; Toyota, K.; Fukuda, R.; Hasegawa, J.; Ishida, M.; Nakajima, T.; Honda, Y.; Kitao, O.; Nakai, H.; Klene, M.; Li, X.; Knox, J. E.; Hratchian, H. P.; Cross, J. B.; Adamo, C.; Jaramillo, J.; Gomperts, R.; Stratmann, R. E.; Yazyev, O.; Austin, A. J.; Cammi, R.; Pomelli, C.; Ochterski, J. W.; Ayala, P. Y.; Morokuma, K.; Voth, G. A.; Salvador, P.; Dannenberg, J. J.; Zakrzewski, V. G.; Dapprich, S.; Daniels, A. D.; Strain, M. C.; Farkas, O.; Malick, D. K.; Rabuck, A. D.; Raghavachari, K.; Foresman, J. B.; Ortiz, J. V.; Cui, Q.; Baboul, A. G.; Clifford, S.; Cioslowski, J.; Stefanov, B. B.; Liu, G.; Liashenko, A.; Piskorz, P.; Komaromi, I.; Martin, R. L.; Fox, D. J.; Keith, T.; Al-Laham, M. A.; Peng, C. Y.; Nanayakkara, A.; Challacombe, M.; Gill, P. M. W.; Johnson, B.; Chen, W.; Wong, M. W.; Gonzalez, C. and Pople, J. A. Gaussian, Inc., Pittsburgh PA, 2003

Harrison, A. G. **1992** In *Chemical ionization mass spectrometry*, CRC Press: Boca Raton, FL, 2nd edition.

Hayen, H.; Jachmann, N.; Vogel, M. and Karst, U. **2002** LC–Electron Capture APCI–MS for the Determination of Nitroaromatic Compounds, *Analyst* 127, 1027–1030.

Hazell, A. C.; Larsen, F. K. and Lehmann, M. S. **1972** A neutron diffraction study of the crystal structure of pyrene, C₁₆H₁₀, *Acta Cryst.* B28, 2977–2984.

Hernández–Maldonado, A. J. and Yang, R. T. **2003** Desulfurization of commercial liquid fuels by selective adsorption via π –complexation with Cu(I)–Y zeolite, *Ind. Eng. Chem. Res.* 42, 3103–3110.

Hirao, K.; Yamabe, S. and Sano, M. **1982a** Theoretical study on the stability and structure of H⁺(HCN)_n and M⁺(CH₃CN)_n (M⁺ = H⁺, Li⁺, and Na⁺) clusters, *J. Phys. Chem.* 86, 2626–2632.

Hirao, K.; Sano, M. and Yamabe, S. **1982b** Theoretical study on the gas-phase solvation of the proton by methanol and dimethyl ether, *Chem. Phys. Letters* 87, 181–185.

Hogenboom, A. C.; Niessen, W. M; Brinkman, U. A. **1998** Rapid target analysis of microcontaminants in water by on-line single-short-column liquid chromatography combined with atmospheric pressure chemical ionization ion-trap mass spectrometry, *J. Chromatogr. A* 794, 201–210.

Horning, E. C.; Horning, M. G.; Carroll, D. I.; Dzidic, I. and Stillwell, R. N. **1973** New picogram detection system based on a mass spectrometer with an external ionization source at atmospheric pressure, *Anal. Chem.* 45, 936–943.

Hunt, D. F. and Shabanowitz, J. **1982** Determination of organosulfur compounds in hydrocarbon matrices by collision activated dissociation mass spectrometry, *Anal. Chem.* 54, 574–578.

Iler, R. K. **1979** In *The chemistry of silica*, John Wiley & Sons, Inc: NY.

Jacob, J. **1990** In *Sulfur analogues of polycyclic aromatic hydrocarbons (thiaarenes)*, Cambridge University Press: Cambridge.

Janoschek, R. **2001** Quantum Chemical B3LYP/cc-pvqz computation of ground-state structures and properties of small molecules with atoms of $Z \leq 18$ (hydrogen to argon), *Pure Appl. Chem.* 73, 1521–1553.

Kaduk, J. A. and Faber, J. **1995** Crystal structure of zeolite Y as a function of ion exchange, *The Rigaku Journal* 12, 14–34.

Kaiser, R. E. Jr.; Louris, J. N.; Amy, J. W. and Cooks, R. G. **1989** Extending the mass range of the quadrupole ion trap using axial modulation, *Rapid Commun. Mass Spectrom.* 3, 225–229.

Karas, M.; Bachmann, D. and Hillenkamp, F. **1985** Influence of the wavelength in high-irradiance ultraviolet laser desorption mass spectrometry of organic molecules, *Anal. Chem.* 57, 2935–2939.

Kebarle, P. and Grimsrud, E. P. **1973** Gas phase ion equilibria studies of the solvation of the hydrogen ion by methanol, dimethyl ether, and water. Effect of hydrogen bonding, *J. Am. Chem. Soc.* 95, 7939–7943.

Kebarle, P. and Tang, L. **1993** From ions in solution to ions in the gas phase-the mechanism of electrospray mass spectrometry, *Anal. Chem.* 65, 972A–986A.

Kirkland, J. J. **1971** High speed liquid-partition chromatography with chemically bonded organic stationary phases, *J. Chromatogr. Sci.* 9, 206–214.

Kolakowski, B. M. **1999** Studies of the response to polycyclic aromatic compounds of liquid introduction—atmospheric pressure ionization mass spectrometry, Ph.D. Thesis.

Kolakowski, B. M.; Grossert J. S.; Ramaley L. **2004** Studies on the positive-ion mass spectra from atmospheric pressure chemical ionization of gases and solvents used in liquid chromatography and direct liquid injection, *J. Am. Soc. Mass Spectrom.* 15, 311–324.

Kropp, K. G. and Fedorak, P. M. **1998** A review of the occurrence, toxicity, and biodegradation of condensed thiophenes found in petroleum, *Can. J. Microbiol.* 44, 605–622.

Lee, C.; Yang, W. and Parr, R. G. **1988** Development of the Colle–Salvetti correlation-energy formula into a functional of the electron density *Phys. Rev. B* 37, 785–789.

Lee, S. Y. and Boo, B. H. **1996a** Molecular structures and vibrational spectra of pyrrole and carbazole by density functional theory and conventional *ab initio* calculations, *J. Phys. Chem.* 100, 15073–15078.

Lee, S. Y. and Boo, B. H. **1996b** Molecular structure and vibrational spectra of 9-fluorenone. Density functional theory study, *Bull. Korean Chem. Soc.* 17, 760–764 (Journal written in English).

Louris, J. N.; Cooks, R. G.; Syka, J. E. P.; Kelley, P. E.; Stafford, G. C., Jr. and Todd, J. F. J. **1987** Instrumentation, applications, and energy deposition in quadrupole ion-trap tandem mass spectrometry, *Anal. Chem.* 59, 1677–1685.

Luo, Y. R. **2003** In *Handbook of bond dissociation energies in organic compounds*, CRC Press: Boca Raton, FL.

Ma, X.; Sakanishi; Mochida I. **1994** Hydrodesulfurization reactivities of various sulfur compounds in diesel fuel, *Ind. Eng. Chem. Res.* 33, 218–222.

Ma, X.; Sakanishi; Mochida I. **1996** Hydrodesulfurization reactivities of various sulfur compounds in vacuum gas oil, *Ind. Eng. Chem. Res.* 35, 2487–2494.

Ma, X.; Sun L.; Song, C. **2002** A new approach to deep desulfurization of gasoline, diesel fuel and jet fuel by selective adsorption for ultra-clean fuels and for fuel cell applications, *Catalysis Today* 77, 107–116.

March, R. E.; McMahon, A. W.; Allinson, E. T.; Londry, F. A.; Alfred, R. L.; Todd, J. F. J. and Vedel, F. **1990** Resonance excitation of ions stored in a quadrupole ion trap. Part II. Further simulation studies, *Int. J. Mass Spectrom. Ion Processes* 99, 109–124.

Martin, A. J. P. and Synge, R. L. M. **1941** A new form of chromatogram employing two liquid phases. I. A theory of chromatography. II. Application to the microdetermination of the higher monoamino acids in proteins. *Biochem. J.* 35 1358–1368.

McKinley, S. G. and Angelici R. J. **2003a** Deep desulfurization by selective adsorption of dibenzothiophenes on $\text{Ag}^+/\text{SBA-15}$ and Ag^+/SiO_2 , *Chem. Commun.*, 2620–2621.

McKinley, S. G. and Angelici R. J. **2003b** Extraction of dibenzothiophenes from petroleum feedstocks using ruthenium complex in aqueous solution, *Energy & Fuels* 17, 1480–1486.

McLafferty, F. W. and Tureček, F. **1993** In *Interpretation of mass spectra*, Mill Valley: CA, 4th edition.

Meot-Ner (Mautner), M. **1978** Solvation of the proton by HCN and CH_3CN . Condensation of HCN with ions in the gas phase, *J. Am. Chem. Soc.* 100, 4694–4699.

Miller, P. E. and Denton, M. B. **1986** The quadrupole mass filter: basic operating concepts, *J. Chem. Edu.* 63, 617–622.

Munson, B. **2000** Development of chemical ionization mass spectrometry, *Int. J. Mass Spectrom.* 200, 243–251.

Munson, M. S. B. and Field, F. H. **1966** Chemical ionization mass spectrometry. I. General introduction, *J. Am. Chem. Soc.* 88, 2621–2630.

Nadkarni, R. A. **2003** Advances in elemental analysis of hydrocarbons products. In *Analytical advances for hydrocarbon research*. Chapter 2, edited by Hsu, C. S., Kluwer Academic/Plenum Publishers: NY.

Nero, V. P. **2003** Mass spectrometric analyses for elemental sulfur and sulfur compounds in petroleum products and crude oils. In *Analytical advances for hydrocarbon research*. Chapter 8, edited by Hsu, C. S., Kluwer Academic/Plenum Publishers: NY.

Niessen W. M. A. **1999** In *Liquid chromatography–mass spectrometry*, Chromatographic Sciences Series Volume 79, Marcel Dekker: NY, 2nd edition.

Niessen, W. M. A. **2001** Principles and instrumentation of gas chromatography–mass spectrometry. In *Current practice of gas chromatography–mass spectrometry*, Chromatographic Sciences Series Volume 86, edited by Niessen W. M. A., Marcel Dekker: NY.

Nishioka, M.; Campbell, R. M.; Lee, M. L.; Castle, R. N. **1986** Isolation of sulfur heterocycles from petroleum- and coal-derived materials by ligand exchange chromatography, *Fuel* 65, 270–273.

Nishioka, M. **1988** Aromatic sulfur compounds other than condensed thiophenes in fossil fuels: enrichment and identification, *Energy and Fuels* 2, 214–219.

Novotny, M.; Springston, S. R.; Peaden, P. A.; Fjeldsted, J. C.; Lee, M. L. **1981** Capillary supercritical fluid chromatography, *Anal. Chem.* 53, 407A–414A.

Paul, W. and Steinwedel, H. **1953** A new mass spectrometer without magnetic field, *Zeitschrift fuer Naturforschung* 8a, 448–450.

Perspective **2003** Sulfur in fuels: more stringent sulfur specifications for fuels are driving innovation, *Applied Catalysis A: General* 248, 1–7.

Payne, A. H. and Glish, G. L. **2005** Tandem mass spectrometry in quadrupole ion trap and ion cyclotron resonance mass spectrometers, *Methods in Enzymology* 402, 109–148.

Perdew, J. P; Burke, K. and Ernzerhof, M. **1996** Generalized gradient approximation made simple, *Phys. Rev. Letters* 77, 3865–3868.

Pyell, U.; Schober, S. and Stork, G. **1997** Ligand-exchange chromatographic separation of polycyclic aromatic hydrocarbons and polycyclic aromatic sulfur heterocycles on a chelating silica gel loaded with palladium (II) or silver (I) cations, *Fresenius J. Anal. Chem.* 359, 538–541.

Rabuck, A. D. and Scuseria, G. E. **1999** Assessment of recently developed density functional for the calculation of enthalpies of formation in challenging cases, *Chem. Phys. Letters* 309, 450–456.

Ramaley, L. and Campbell, J. L. **2000** Two-dimensional chromatographic array detector using laser induced fluorescence with autoranging, *Instrum. Sci. & Technol.* 28, 189–204.

Ramamurthy, V. **2000** Controlling photochemical reactions via confinement: zeolites, *Journal of Photochemistry and Photobiology C: Photochemistry Reviews* 1, 145–166.

Rodriguez, J. A.; Chaturvedi, S. and Jirsak, T. **1998** The bonding of sulfur to pd surfaces: photoemission and molecular orbital studies, *Chem. Phys. Letters* 296, 421–428.

Roussis, S. G. and Fedora, J. W. **2002** Quantitative Determination of Polar and Ionic Compounds in Petroleum Fractions by Atmospheric Pressure Chemical Ionization and Electrospray Ionization Mass Spectrometry, *Rapid Commun. Mass Spectrom.* 16, 1295–1303.

Roussis, S. G.; Fedora, J. W.; Fitzgerald, W. P.; Cameron, A. S. and Proulx, R. **2003** Advanced molecular characterization by mass spectrometry: applications for petroleum and petrochemicals. In *Analytical advances for hydrocarbon research*, chapter 13, edited by Hsu, C. S., Kluwer Academic/Plenum Publishers: NY.

Rudzinski, W. E. **2003a** Chromatographic separation and atmospheric pressure ionization/mass spectrometry analysis of nitrogen, sulfur and oxygen containing compounds in crude oils. In *Analytical advances for hydrocarbon research*, chapter 13, edited by Hsu, C. S., Kluwer Academic/Plenum Publishers: NY.

Rudzinski, W. E., Zhang, Y. and Luo X. **2003b** Mass spectrometry of polyaromatic sulfur compounds in the presence of palladium (II) *J. Mass Spectrom.* 38, 167–173.

Ryhage, R. **1964** Use of a mass spectrometer as a detector and analyzer for effluents emerging from high temperature gas liquid chromatography columns, *Anal. Chem.* 36, 759–764.

Sanagi M. M. and Smith, R. M. **1988** In *Supercritical fluid chromatography*, chapter 3, edited by Smith R. M., RSC Chromatography Monographs, The Royal Society of Chemistry: London.

Schaffrin, R. M. and Trotter, J. **1970** Structure of dibenzothiophen, *J. Chem. Soc. (A): Inorg. Phys. Theor.* 9, 1561–1565.

Scott, R. P. W. **1986** In *Liquid chromatography detectors*, Journal of Chromatography Library Volume 33, Elsevier: Amsterdam, 2nd edition.

Scott, R. P. W. **1998** In *Introduction to analytical gas chromatography*, Chromatographic Sciences Series Volume 76, Marcel Dekker: NY, 2nd edition.

Shushan, B.; Douglas, D. J.; Davidson, W. R. and Nacson, S. **1983** The role of kinetic energy in triple quadrupole collision induced dissociation (CID) experiments, *Int. J. Mass Spectrom. and Ion Phys.* 46, 71–74.

Singleton K. E.; Cooks, R. G.; Wood K. V. **1983** Utilization of natural isotopic abundance ratios in tandem mass spectrometry, *Anal. Chem.* 55, 762–764.

Skoog, D. A. and Leary, J. J. **1992** In *Principles of instrumental analysis*, Saunders College Publishing: NY, 4th edition.

Sleno, L. and Volmer D. A. **2004** Ion activation methods for tandem mass spectrometry, *J. Mass Spectrom.* 39, 1091–1112.

Smith, R. M. J. **1999a** Supercritical fluids in separation science — the dreams, the reality and the future, *Chromatogr. A* 856, 83–115.

Smith, R. M. and Busch, K. L. **1999b** In *Understanding mass spectra — a basic approach*, John Wiley: NY.

Song, C. **2003** An overview of new approaches to deep desulfurization for ultra-clean gasoline, diesel fuel and jet fuel, *Catalysis Today* 86, 211–263.

Sparkman, O. D. **2000** In *Mass spectrometry desk reference*, Global View Publishing: Pittsburgh, PA, 1st edition.

Speight, J. G. **1980** In *The chemistry and technology of petroleum*, Chemical Industries Volume 3, Marcel Dekker:NY.

Stafford, G. C., Jr.; Kelley, P. E.; Syka, J. E. P.; Reynolds, W. E.; Todd, J. F. J. **1984** Recent improvements in and analytical applications of advanced ion trap technology, *International Journal of Mass Spectrometry and Ion Processes* 60, 85-98.

Stafford, G. **2002** Ion trap mass spectrometry: a personal perspective, *J. Am. Soc. Mass Spectrom.* 13, 589–596.

Sunner, J.; Nicol, G. and Kebarle, P. **1988a** Factors determining relative sensitivity of analytes in positive mode atmospheric pressure ionization mass spectrometry, *Anal. Chem.* 60, 1300–1307.

Sunner, J.; Michael, G. I. and Kebarle, P. **1988b** Sensitivity enhancements obtained at high temperatures in atmospheric pressure ionization mass spectrometry, *Anal. Chem.* 60, 1308–1313.

Syage, J. A. **2004** Mechanism of $[M+H]^+$ formation in photoionization mass spectrometry, *J. Am. Soc. Mass Spectrom.* 15, 1521–1533.

Takeuchi, T. **2003** Capillary columns in liquid chromatography, *Anal. Bioanal. Chem.* 375, 26–27.

Thompson, C. J. **1980** Identification of sulfur compounds in petroleum and alternative fossil fuels. In *Organic sulfur chemistry*, edited by Freidlina R. K. and Skorova A. E., Pergamon Press: Oxford.

Thomson, B. A. **1998** Atmospheric pressure ionization and liquid chromatography/mass spectrometry — together at last, *J. Am. Soc. Mass Spectrom.* 9, 187–193.

Thomson, J. J. **1913** Rays of positive electricity and their application to chemical analysis, Longmass Green: London.

van Berkel, G. J.; Glish, G. L.; McLuckey, S. A. **1990** Electrospray ionization combined with ion trap mass spectrometry, *Anal. Chem.* 62, 1284–1295.

van Berkel, G. J.; McLuckey, S. A. and Glish, G. L. **1991** Electrospray ionization of porphyrins using a quadrupole ion trap for mass analysis, *Anal. Chem.* 63, 1098–1109.

van Berkel, G. J. and Asano, K. G. **1994** Chemical derivatization for electrospray ionization mass spectrometry. 2. Aromatic and highly conjugated molecules, *Anal. Chem.* 66, 2096–2102.

van Deemter, J. J.; Zuiderweg, F. J. and Klinkenberg, A. **1956** Longitudinal diffusion and resistance to mass transfer as causes of nonideality in chromatography, *Chem. Eng. Sc.* 5, 271–289.

Volmer, D. A. and Sleno, L. **2005a** Mass analyzers: an overview of several designs and their applications, Part I, *Spectroscopy* 20, 20–26.

Volmer, D. A. and Sleno, L. **2005b** Mass analyzers: an overview of several designs and their applications, Part II, *Spectroscopy* 20, 90–94.

Whalen, K.; Grossert, J. S. and Boyd, R. K. **1995** Ion dissociation reactions induced in a high pressure quadrupole collision cell, *Rapid Commun. Mass Spectrom.* 9, 1366–1375.

Yamashita, M. and Fenn, J. B. **1984** Electrospray ion source. Another variation on the free-jet theme. *J. Phys. Chem.* 88, 4451–4459.

Yan, X. J. **1999** Detection by ozone-induced chemiluminescence in chromatography, *Chromatogr. A* 842, 267–308.

Yan, X. **2002** Sulfur and nitrogen chemiluminescence detection in gas chromatographic analysis, *J. Chromatogr. A* 976, 3–10.

Yancey, J. A. **1994** Review of liquid phases in gas chromatography, part I: intermolecular forces, *Journal of Chromatographic Science* 32, 349–357.

Yang, R. T. **2003a** In *Adsorbents: fundamentals and applications*, John Wiley & Sons, Inc: NY.

Yang, R. T.; Hernández-Maldonado, A. J. and Yang, F. H. **2003b** Desulfurization of transportation fuels with zeolites under ambient conditions, *Science* 301, 79–81.

Zeleny, J. **1917** Electric discharge from points, *Phys. Rev.* 9, 562–563.